Study of the Helicity Dependence of π^0 Photoproduction on Proton at MAMI

Dissertation

submitted to attain the academic degree
"Doctor of Natural Sciences"
at the Faculty of Physics, Mathematics and Computer Science:
Johannes Gutenberg University Mainz

Linturi, James Mugambi

born in Meru, Kenya

Mainz, August 2015

Study of the Helicity Dependence of π^0 Photoproduction on Proton at MAMI

James Mugambi Linturi

PhD Defense Date: October 29, 2015

D77 Mainzer Dissertation

ABSTRACT

The excitation spectrum is one of the fundamental properties of every spatially extended system. The excitations of the building blocks of normal matter, i.e., protons and neutrons (nucleons), play an important role in our understanding of the low energy regime of the strong interaction. Due to the large coupling, perturbative solutions of quantum chromodynamics (QCD) are not appropriate to calculate long-range phenomena of hadrons. For many years, constituent quark models were used to understand the excitation spectra. Recently, calculations in lattice QCD make first connections between excited nucleons and the fundamental field quanta (quarks and gluons).

Due to their short lifetime and large decay width, excited nucleons appear as resonances in scattering processes like pion nucleon scattering or meson photoproduction. In order to disentangle individual resonances with definite spin and parity in experimental data, partial wave analyses are necessary. Unique solutions in these analyses can only be expected if sufficient empirical information about spin degrees of freedom is available.

The measurement of spin observables in pion photoproduction is the focus of this thesis. The polarized electron beam of the Mainz Mictrotron (MAMI) was used to produce high-intensity, polarized photon beams with tagged energies up to 1.47 GeV. A frozen-spin Butanol target in combination with an almost 4π detector setup consisting of the Crystal Ball and the TAPS calorimeters allowed the precise determination of the helicity dependence of the $\gamma p \to \pi^0 p$ reaction. In this thesis, as an improvement of the target setup, an internal polarizing solenoid has been constructed and tested. A magnetic field of 2.32 T and homogeneity of 1.22×10^{-3} in the target volume have been achieved.

The helicity asymmetry E, i.e., the difference of events with total helicity $1/2$ and $3/2$ divided by the sum, was determined from data taken in the years 2013-14. Subtraction of background events arising from nucleons bound in Carbon and Oxygen was an important part of the analysis. The results for the asymmetry E are compared to existing data and predictions from various models. The results show a reasonable agreement to the models in the energy region of the $\Delta(1232)$-resonance but large discrepancies are observed for energy above 600 MeV. The expansion of the present data in terms of Legendre polynomials, shows the sensitivity of the data to partial wave amplitudes up to F-waves. Additionally, a first, preliminary multipole analysis of the present data together with other results from the Crystal Ball experiment has been performed.

ZUSAMMENFASSUNG

Das Anregungsspektrum ist eine der fundamentalen Eigenschaften jedes räumlich ausgedehnten Systems. Die Spektren der Grundbausteine der Materie, also der Protonen und Neutronen (Nukleonen), spielen eine wichtige Rolle beim Verständnis der starken Wechselwirkung bei niedrigen Energien. Wegen der starken Kopplung sind Techniken, die auf einer Störungsentwicklung aufbauen, keine geeigneten Ansätze zur Berechnung von hadronischer Phänomene bei großen Abständen. Über viele Jahre wurden Konstituentenquarkmodelle entwickelt, um Anregungen von Hadronen zu beschreiben. Seit einigen Jahren ist es im Rahmen Gitter-QCD möglich, erste Verbindungen zwischen angeregten Nukleonen und den fundamentalen Feldquanten (Quarks und Gluonen) herzustellen.

Wegen der kurzen Lebensdauer und der großen Zerfallsbreite, treten angeregte Nukelonen als Resonanzen in Streuprozessen wie der Pion-Nukleon Streuung oder der Photoproduktion von Mesonen in Erscheinung. Um einzelne Resonanzen mit definiertem Spin und Parität in experimentellen Daten zu identifizieren sind Partialwellenanalysen notwendig. Eindeutige Lösungen solcher Analysen kann man allerdings nur dann erwarten, wenn ausreichend Information über Spin-Freiheitsgrade vorhanden ist.

Die Messung von spinabhängigen Observablen der Photoproduktion von Pionen ist ein Schwerpunkt dieser Arbeit. Der polarisierte Elektronenstrahl des Mainzer Mikrotons (MAMI) wird zur Erzeugung hoch intensiver, polarisierter und energiemarkierter Photonenstrahlen bis zu 1,47 GeV verwendet. Ein "frozen-spin" Butanol Target in Kombination mit einem Detektorsystem, das fast den gesamten Raumwinkel abdeckt und aus den Crystal Ball und TAPS Kalorimetern aufgebaut ist, erlaubte die präzise Bestimmung der Helizitätsabhängigkeit der $\gamma p \to \pi^0 p$ Reaktion. Als Verbesserung des Targets wurde im Rahmen dieser Arbeit ein supraleitender Solenoid als interner Polarisationsmagnet entwickelt und getestet. Dabei wurde ein Magnetfeld von 2,32 T bei einer Homogenität von $1,22 \times 10^{-3}$ über dem Targetvolumen erreicht.

Die Helizitätsasymmetrie E, also die Differenz der Zählraten bei Gesamthelizität 1/2 und 3/2 dividiert durch die Summe, wurde mit Daten aus den Jahren 2013-15 bestimmt. Die Ergebnisse werden mit existierenden Daten sowie mit Modellvorhersagen verglichen. Im Bereich der $\Delta(1232)$ Resonanz findet man eine gute Übereinstimmung mit Modellen, oberhalb von 600 MeV werden die Abweichungen dagegen groß. Eine Entwicklung der gewonnenen Daten nach Legendre-Polynomen zeigt eine Empfindlichkeit auf Partialwellenamplituden bis zu F-Wellen. Darüber hinaus wurden die neuen Daten in

einer ersten vorläufigen Partialwellenanalyse zusammen mit anderen Daten des Crystal Ball Experiments verwendet.

Contents

List of Figures

List of Tables

Chapter 1

Introduction

In order to understand the structure of matter, knowledge about its constituents and how they interact with each other is important. The standard model of particle physics explains that matter is made up of quarks and leptons which interact through electromagnetic, strong and weak interactions via exchange of gauge bosons. Photons are exchanged in an electromagnetic interaction, $W^{\pm}$ and Z^0 bosons are exchanged in the weak interaction and gluons are the force carriers in the strong interaction. Quarks bind together to form hadrons via strong force transmitted by gluons. Hadrons are classified into: mesons, (e.g., pion, eta, eta'...) and baryons, (e.g., nucleons, Δ ...). Mesons are bound states consisting of a quark-antiquark pair in a sea of gluons while baryons (including nucleons) are bound states composed of three quarks in a sea of gluons and quark-antiquark pairs.

Quantum chromodynamics (QCD), a fundamental theory that describes the quark-gluon interactions, explains that quarks exist in charge states known as "colors". Due to SU(3) gauge symmetry of QCD there are three color charges: red, green and blue with each having its anti-color (anti-red, anti-blue and anti-green). In nature, only colorless states are observed as free particles. This means that, (i) each quark in a baryon must have a different color to produce a colorless state, and (ii) mesons have a colored quark and anti-colored anti-quark such that they cancel out. This is observed when the nucleon ground states are excited by supplying energy to them. The

excited states are short-lived and lose their energy by emitting a colorless state typically mesons [1].

In QCD the quark-quark interaction potential depends on the distance between the quarks and the energy. At very large energy ($\geq$1 GeV) and short distances, the couplings between quarks and gluons and the couplings of gluons to themselves become very small such that the quarks move almost freely inside a nucleon. This makes it possible to use perturbation theory to describe precisely the interactions of quarks and gluons at distances much smaller than the typical hadron size; a phenomenon known as *asymptotic freedom*. In this range, the strong interaction has been well-described by QCD using perturbation theory and tested experimentally.

However, at low energy ($\leq$1 GeV) and large distance scales found within the nucleon and its excited states, the quark-gluon coupling becomes very large. This means that the quarks and gluons are confined and no matter how much energy is injected into a nucleon, it is impossible to isolate either a quark or a gluon. This results in a phenomenon known as *confinement*. In this region, perturbative QCD has failed to describe the mechanism of mass generation and quark-gluon confinement. Therefore, other non-perturbative methods like phenomenological models or, recently, Lattice based calculations have been used to describe the strong interaction in the low energy regime [1]. The phenomena of confinement and asymptotic freedom are illustrated in figure 1.1 where the quark-gluon coupling constant α_S is plotted a function of momentum transfer [2]. The coupling constant α_S becomes smaller and relatively constant at high momenta but increases exponentially towards unity at low momenta.

Lattice gauge theory, proposed by K. Wilson in 1974, provides such a method: Lattice QCD (LDCD) [3]. LQCD discretizes the QCD Lagrangian in a space-time lattice with spacing a in a volume V and evaluates it numerically. The results are then extrapolated to continuum $a \to 0$. The disadvantage of LQCD is that it is limited by the availability of the computational resources and the efficiency of algorithms. Thus, the LQCD results come with both statistical and systematic errors [4]. However, due to the rapid growth of computational power and development of more efficient al-

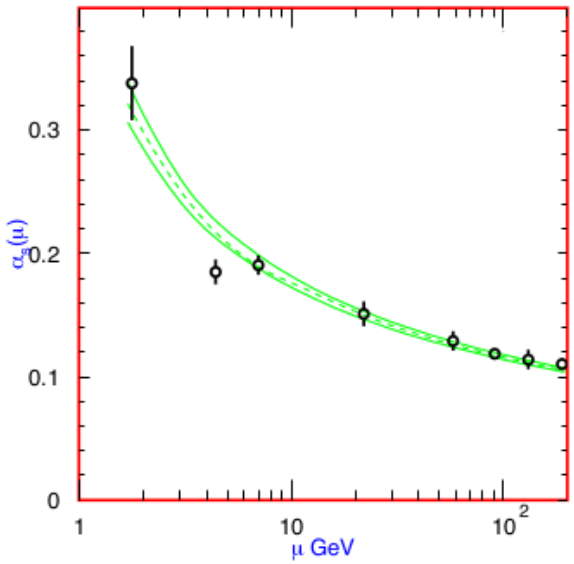

Figure 1.1: The strong coupling constant as a function of the momentum transfer μ [2]. Coupling constant is higher at low momentum transfer due to the confinement of quarks and low at higher momentum transfer which is the range of the asymptotic freedom.

gorithms, the extraction of precise results should be possible in the future. Even though recent LQCD calculations have provided results for both the ground state and the excited states of the nucleon in the non-perturbative region [5], the excitation spectrum of the nucleons is still not well understood. Therefore, experimental study of these excitation spectra is important.

Experimentally, a nucleon (proton or neutron) can be excited from its ground state using a beam of mesons (pion, kaon..), baryons, leptons or photons. The nucleon excited states lose their energy to go back to their ground state by emitting a meson. The nucleon excited states have been studied in large number of formation and production experiments [6, 7, 8]. Information on the nucleon spectrum is based on experiments that were performed using a beam of long-lived mesons (such pions and kaons) on nucleons. Unlike in atomic spectroscopy, where their resonances are well understood and can be observed, nucleon spectroscopy is more complicated. This is because the excited nucleon states have short life-times $\tau \approx 10^{-24}$ s corresponding to widths ($\Gamma = \frac{1}{\tau}$) of ≈ 100 MeV. Furthermore, the spacing of

the resonances is often less than Γ such that they overlap in the mass spectrum with increasing excitation energy. This makes it difficult to identify and study individual states as shown in figure 1.2, where only the lowest

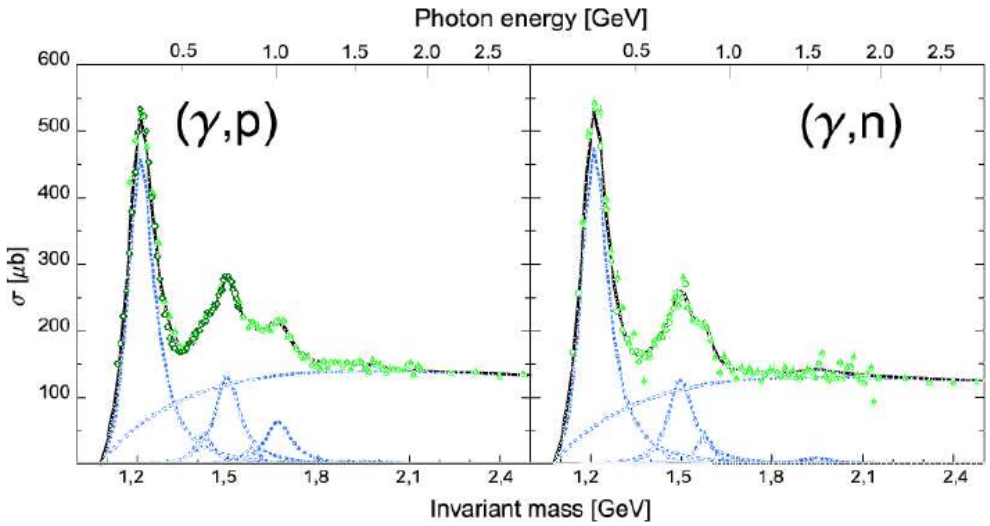

Figure 1.2: Total photoabsorption cross section on the proton (left) and the neutron (right). Points are measured data, curves are the Breit-Wigner shape fits on the nucleon resonances ($P_{33}(1232)$, $P_{11}(1440)$, $D_{13}(1520)$, $S_{11}(1535)$ and $F_{15}(1680)$ (only for protons) and $F_{37}(1950)$) and a smoothly varying background [9].

excited state, the Δ-resonance ($P_{33}(1232)$), corresponds to an isolated peak in the spectrum. At masses around 500 MeV, several resonances ($P_{11}(1440)$, $D_{13}(1520)$ and $S_{11}(1535)$) contribute to the broad structure observed in the spectrum. The measurement of the photoabsorption cross section alone does not allow a detailed investigation of the overlapping resonances. Effort must be made to extract and explain these resonances through measurement of polarization observables (discussed in 2.2) in addition to the photoabsorption cross section.

Various models have been used to explain the known low-lying resonances and predict the still unknown ones. The most used models are the constituent quark models [10, 11, 12, 13], which describe the baryons as three quark bound states. The constituent quark models build hadrons from the valence degrees of freedom interacting through phenomenological potential at large

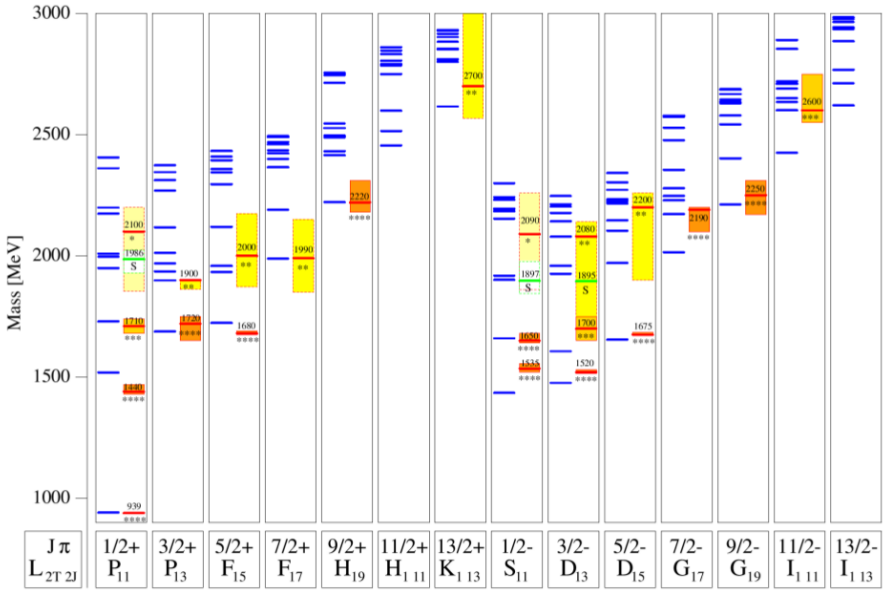

Figure 1.3: The nucleon excitation spectrum predicted by the Bonn model [14]. Predicted states are in blue while experimentally observed states are in red.

distances. An example of such a model is the Bonn model which is a relativistic covariant quark model. It uses a linearly rising potential which ensures that quark confinement is fulfilled within the model [14]. Figure 1.3 shows a comparison of the predicted nucleon excitation spectrum in blue lines and experimentally observed resonances in red lines for the Bonn model. The model predicts more resonances than observed experimentally. Also, the lattice QCD calculations have predicted a number of excited states similar to those predicted by the Bonn model at low masses [5]. Figure 1.4 shows nucleon and Δ spectra from lattices at a pion mass, m_π, of 396 MeV.

A comparison of the number of excited states predicted in both models to the one observed experimentally shows inconsistency. This results in the problem of "missing resonances". This inconsistency is commonly attributed to the fact that the number of degrees of freedom is too high in models. While a reduction of the number of degrees of freedom by, e.g., assuming quark-diquark structures decreases the number of nucleon states there are

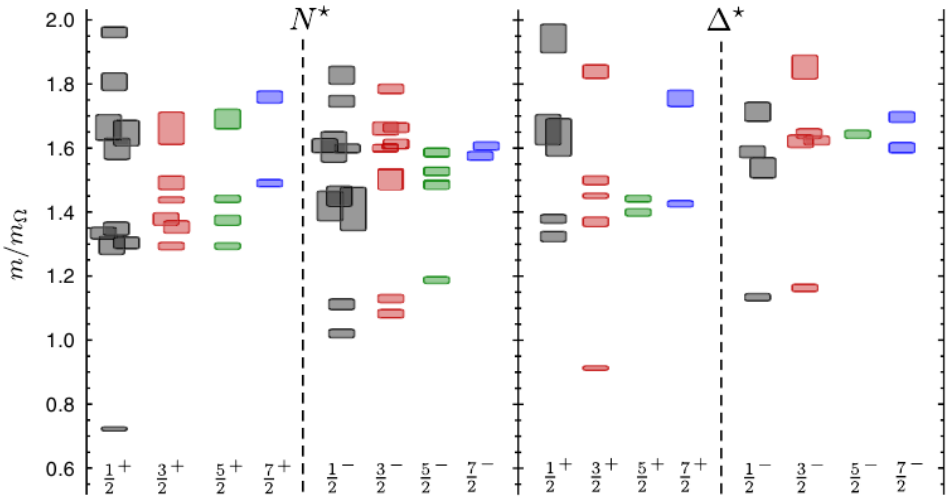

Figure 1.4: Nucleon and Δ resonance from lattice QCD at a pion mass, m_π, of 396 MeV. Masses are shown in ratios of the Ω baryon mass [5].

still more than those observed experimentally. On the other hand, the existing experimental data is dominated by πN scattering data. Perhaps some of the unobserved excited states either do not couple or have a small coupling to πN [9]. This suggests the importance of investigating the baryon resonance spectrum using multiple production mechanisms like photo and electroproduction experiments.

In particular, photoproduction of mesons allows access to the electromagnetic transition amplitudes of the resonances, which are important parameters in the investigation of the resonances. In the last two decades, photoproduction experiments at JLab in the USA; MAMI in Mainz, Germany; ELSA in Bonn, Germany; the GRAAL experiment at the ESRF in Grenoble, France; and Spring8 in Osaka, Japan have substantially improved the knowledge of nucleon resonances. Either evidence for unknown resonances was found or the properties of already known resonances could be extracted more precisely from the photoproduction data. An overview of the current status on the nucleon and the Δ-resonances below $W = 2$ GeV is shown in figure 1.5. According to the Particle Data Group (PDG) review [4], three or four stars are assigned only to the resonances which are confirmed by in-

dependent analyses and which are derived from analyses based on complete information, i.e., for analyses based on three observables in πN scattering or eight properly chosen observables in photoproduction (see chapter 2). In addition, these resonances have to be seen in one of their strongest decay modes. One or two star ratings indicate that the evidence of existence of the resonance is still poor.

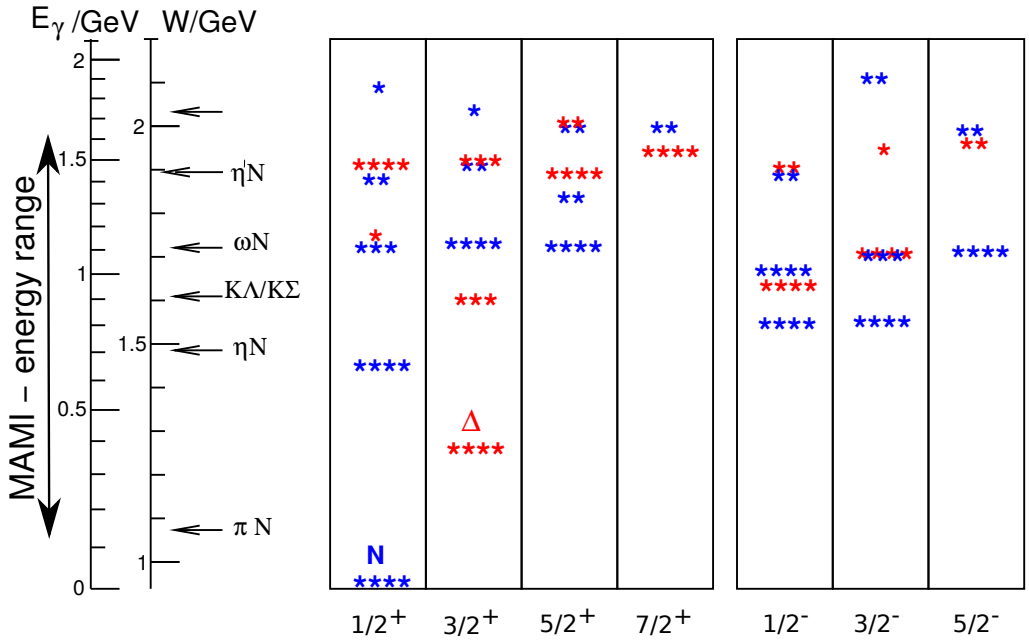

Figure 1.5: Summary of the nucleon (blue) and Δ (red) resonances below $W = 2$ GeV, which is the energy range at the Mainz Microtron (MAMI) [4].

Most of the photoproduction information on the nucleon excited spectrum has been obtained through the study of the various final state channels, e.g., $\gamma p \to \pi^0 p$, $\gamma p \to \eta p$, $\gamma p \to \eta' p$, etc. However, the most studied photoproduction reaction is $\gamma p \to \pi^0 p$. Figure 1.6 shows the differential cross section in π^0 photoproduction in the energy range $E_\gamma = 225 - 1525$ MeV. A comparison of the experimental differential cross section to partial wave analysis models of MAID [15], SAID [16] and Bonn Gatchina [17] (discussed in chapter 2) shows a good angular description of the data at all energy bins. However, the electromagnetic multipoles prediction indicates a large discrepancy between the three models [18] as shown in figure 1.7. Except M_{1+}-multipole, other

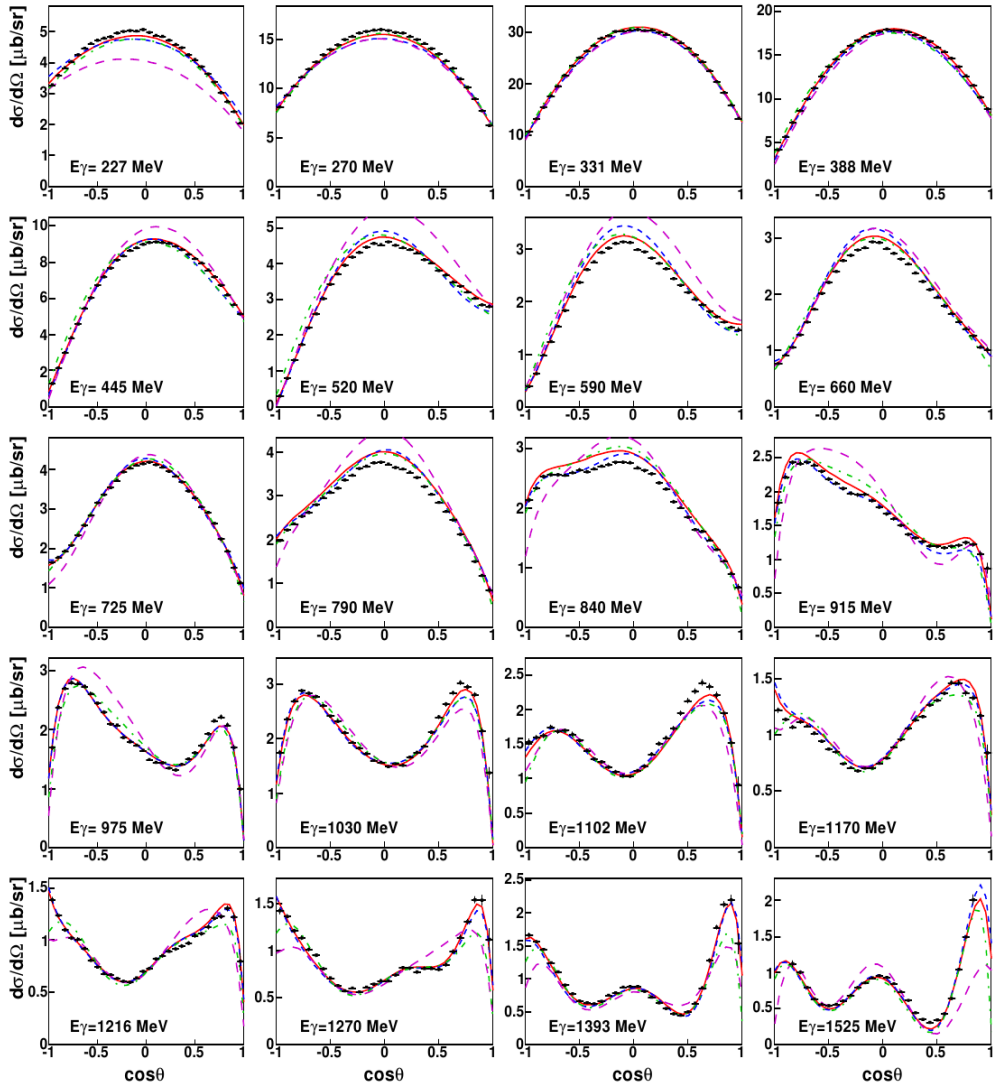

Figure 1.6: The differential cross sections on $\gamma p \to \pi^0 p$ from [19] compared to existing PWA solutions from SAID-CM12 [16] (blue dashed line), MAID2007 [15] (magenta long-dashed line), and Bonn- Gatchina BG2014-02 [17] (green dash-dotted line) and to a new SAID PR15 solution [16] (red solid line) obtained after adding the present data points into the fit.

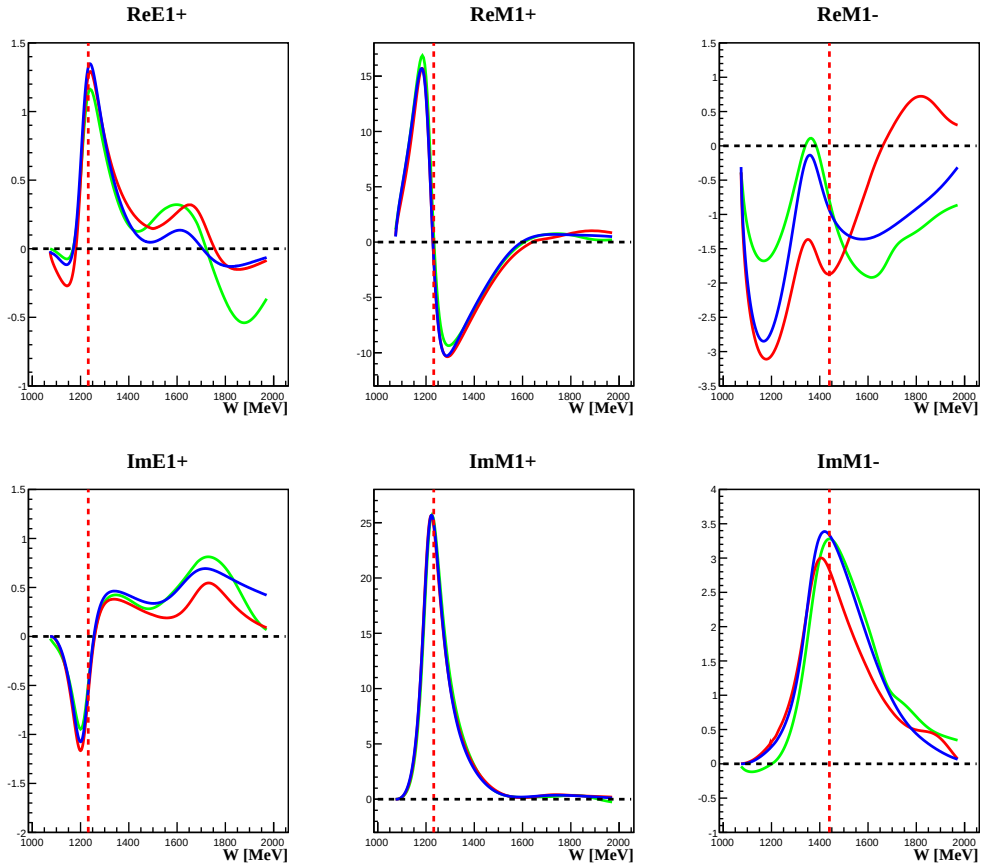

Figure 1.7: E_{1+}, M_{1+}, and M_{1-} electromagnetic multipoles for the reaction $\gamma p \to \pi^0 p$ as a function of photon beam energy from MAID2007 [15] (red), BnGa2014-02 [17] (green) and SAIDCM-12 [16] (blue) partial wave analysis models. Top and bottom rows are the real and imaginary parts of the multipoles, respectively. The dotted red line shows the position of the $\Delta(1232)3/2^+$ resonance for E_{1+} and M_{1+} and Roper resonance N(1440)$1/2^+$ for M_{1-}.

multipoles (E_{1+} and M_{1-}) show large discrepancies between themselves even though they well-describe the measured differential cross section data. This shows that other than measuring the cross section measurement it is important to experimentally measure the polarization observables in order to allow detailed, and unambiguous, extraction of the multipole contributions to the excited nucleon resonances.

This can be determined by performing a partial wave analysis using the angular dependence of the photoproduction observables in a combined fit. The fit is dependent on how a model describes the resonant and the non-resonant background terms in the scattering amplitudes. Therefore, inclusion of polarization observable data from different experiments will act as a constraint to the partial wave models. This thesis presents the measurement of helicity dependence of π^0 photoproduction via extraction of the helicity asymmetry E at the Mainz Microtron (MAMI) in the photon energy range $E_\gamma = 210 - 1440$ MeV. The helicity asymmetry E data will provide new information about the nucleon excited states.

1.1 Thesis Organization

This thesis presents the mechanism of pseudoscalar meson photoproduction including polarization observables in chapter 2. Chapter 3 describes the experimental setup at the A2 experimental hall at MAMI. Chapter 4 presents the operation of the frozen spin target and development of an internal polarizing magnet. The detector calibration and data analysis are discussed in chapters 5 and 6, respectively. The results are presented in chapter 7 while summary and conclusions follows thereafter in chapter 8.

Chapter 2

Photoproduction

This chapter presents the theoretical background of photoproduction experiments. Section 2.1 describes the photoproduction of pseudoscalar mesons. The polarization observables are described in section 2.2. The partial wave analysis models are discussed in section 2.3 and previous studies on π^0 photoproduction in section 2.4.

2.1 Photoproduction of Pseudoscalar Mesons

A photoproduction reaction involves a real photon γ, and a target nucleon N, which is in the ground state. After the reaction a meson m, and a baryon N', are produced in the final state as shown in figure 2.1. The reaction in figure 2.1 can be expressed as:

$$\gamma(\vec{k}) + N(\vec{p_i}) = m(\vec{q}) + N'(\vec{p_f}) \tag{2.1}$$

where the parameters in parenthesis are the four momenta vector for each particle. The four momenta vector for the reaction particles can be expressed

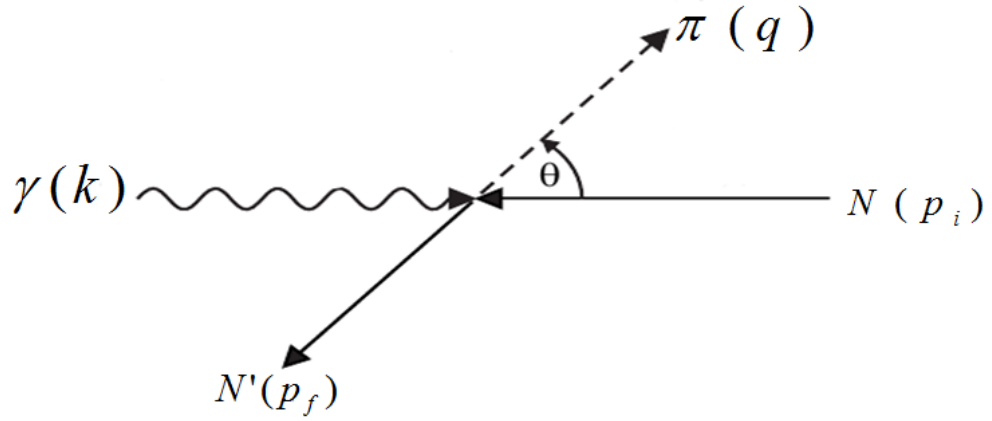

Figure 2.1: Schematic diagram of a meson photoproduction reaction.

in-terms of the Mandelstam invariant variables [20]:

$$\begin{aligned} s &= (k + p_i)^2 = (q + p_f)^2, \\ u &= (k - p_f)^2 = (q - p_i)^2, \\ t &= (q - k)^2 = (p_i - p_f)^2 \end{aligned} \tag{2.2}$$

where s is the square of the energy of the reaction and t is the square of the momentum transfer. The sum of the Mandelstam variables is equal to the square of the sum of all particle masses involved in the reaction given as:

$$s + t + u = 2M_N^2 + m_m^2 \tag{2.3}$$

where M_N and m_m are the nucleon and meson masses, respectively. In the center of mass (c.m.) frame, equation (2.2) can be written as:

$$s = W^2 = (E_i + k_0)^2, \tag{2.4}$$

$$u = M^2 + k^2 - 2k_0E_f - 2|\vec{q}||\vec{k}|x, \tag{2.5}$$

$$t = m_m + k^2 - 2k_0E_m + 2|\vec{q}||\vec{k}|x, \tag{2.6}$$

$$x = \cos\theta = \frac{\vec{q} \cdot \vec{k}}{|\vec{q}||\vec{k}|} \tag{2.7}$$

where θ is the c.m. scattering angle and W is the total c.m. energy [20]. For a photoproduction reaction, $k^2 = 0$. Therefore, the energies of the reaction particles in the c.m. frame can be expressed as:

$$E_\gamma = \frac{W^2 - M^2}{2W}, \tag{2.8}$$

$$E_i = \frac{W^2 + M^2}{2W}, \tag{2.9}$$

$$E_m = \frac{W^2 + m_m - M^2}{2W}, \tag{2.10}$$

$$E_f = \frac{W^2 - m_m + M^2}{2W}. \tag{2.11}$$

In scattering theory, the transition of a particle from an initial state $|i\rangle$ into a final state $|f\rangle$ is described by the scattering matrix S_{fi}. For a photoproduction reaction represented by equation (2.1), S_{fi} is given as:

$$S_{fi} = \frac{1}{(2\pi)^2}\delta^4(p_f + q - p_i - k)\sqrt{\frac{M_N^2}{4E_\gamma E_i E_m E_f}} \cdot i\mathcal{M}_{fi}. \tag{2.12}$$

The invariant matrix element $\mathcal{M}_{fi}$ describing the transition from initial to final state can be decomposed as:

$$i\mathcal{M}_{fi} = \bar{U}(p_f)\epsilon_\mu \mathcal{O}^\mu U(p_i) \tag{2.13}$$

where $\bar{U}(p_i)$ and $\bar{U}(p_f)$ are the Dirac spinors for the initial and final nucleon respectively, ϵ_μ is the photon polarization vector, and $\mathcal{O}^\mu$ describes the current operator produced by strongly interacting hadrons given as:

$$\mathcal{O}^\mu = \sum_{j=1}^{8} A_j(s, t, u, k^2) M_j \tag{2.14}$$

where M_j are operators that depend on the four momenta and polarization vector of the photon. A_j are the invariant amplitudes which incorporate the transition dynamics [20]. For photoproduction reactions where $k^2 = 0$, the

matrix $\mathcal{M}_{fi}$ can be written as:

$$i\mathcal{M}_{fi} = \bar{U}_f(p_f)\sum_{j=1}^{4} A_j(s,t,u,k^2)M_j U_i(p_i). \tag{2.15}$$

The invariant amplitude A_j can be expressed more conveniently in terms of amplitudes corresponding to a definite parity and angular momentum state. Thus, the matrix element $\mathcal{M}_{fi}$ can be expressed in terms of Pauli σ-matrices and the Dirac spinors:

$$\mathcal{M}_{fi} = \frac{4\pi W}{M_N}\chi_f \mathcal{F}\chi_i \tag{2.16}$$

where χ_i and χ_f are the initial and final nucleon spinors and $\mathcal{F}$ is a 2×2 matrix defined in terms of Chew, Goldberg, Low and Nambu (CGLN) amplitudes $\mathcal{F}_i$ [21] by:

$$\mathcal{F} = i\vec{\sigma}\cdot\vec{b}\mathcal{F}_1 + \vec{\sigma}\cdot\hat{q}\vec{\sigma}\cdot(\hat{k}\times\vec{b})\mathcal{F}_2 + i\vec{\sigma}\cdot\hat{k}\hat{q}\cdot\vec{b}\mathcal{F}_3 + i\vec{\sigma}\cdot\hat{q}\hat{q}\cdot b\mathcal{F}_4 \tag{2.17}$$

where $\hat{k}$ and $\hat{q}$ are the photon and meson unit vectors, respectively, $b = \epsilon_\mu$ for photoproduction reactions, and $\vec{\sigma}$ is the vector containing Pauli matrices.

The CGLN amplitudes can be expressed in terms of electric and magnetic multipoles since they are a function of spin and parity:

$$\begin{aligned}
\mathcal{F}_1(\theta) &= \sum_{l=0}^{\infty}[lM_{l+} + E_{l+}]P'_{l+1}(x) + [(l+1)M_{l-} + E_{l-}]P'_{l-1}(x), \\
\mathcal{F}_2(\theta) &= \sum_{l=1}^{\infty}[(l+1)M_{l+} + lM_{l-}]P'_l(x), \\
\mathcal{F}_3(\theta) &= \sum_{l=1}^{\infty}[E_{l+} - M_{l+}]P''_{l+1}(x) + [E_l - M_{l-}]P''_{l-1}(x), \\
\mathcal{F}_4(\theta) &= \sum_{l=2}^{\infty}[M_{l+} - E_{l+} - M_{l-} - E_l]P''_{l-1}(x)
\end{aligned} \tag{2.18}$$

where P'_l and P''_l are the first and second derivatives of Legendre polyno-

mials and $x = \cos(\theta)$. The sign index in photon magnetic multipole $M_{l\pm}$ and electric multipole $E_{l\pm}$ indicates that the nucleon spin is either added or subtracted from l to obtain the total angular momentum of the intermediate state ($J = l + 1/2$). Inverting equations in (2.18), the electromagnetic multipoles can be written [22]:

$$E_{l+} = \int_{-1}^{1} \frac{dx}{2(l+1)}(P_l\mathcal{F}_1 - P_{l+1}\mathcal{F}_2 + \frac{l}{2l+1}(P_{l-1} - P_{l+1})\mathcal{F}_3 + \frac{l+1}{2l+3}(P_l - P_{l+2})\mathcal{F}_4),$$

$$E_{l-} = \int_{-1}^{1} \frac{dx}{2l}(P_l\mathcal{F}_1 - P_{l-1}\mathcal{F}_2 - \frac{l+1}{2l+1}(P_{l-1} - P_{l+1})\mathcal{F}_3 + \frac{l}{2l-1}(P_l - P_{l-2})\mathcal{F}_4),$$

$$M_{l+} = \int_{-1}^{1} \frac{dx}{2(l+1)}(P_l\mathcal{F}_1 - P_{l+1}\mathcal{F}_2 - \frac{1}{2l+1}(P_{l-1} - P_{l+1})\mathcal{F}_3),$$

$$M_{l-} = \int_{-1}^{1} \frac{dx}{2l}(-P_l\mathcal{F} + 1 - P_{l-1}\mathcal{F}_2 + \frac{1}{2l+1}(P_{l-1} - P_{l+1})\mathcal{F}_3).$$

In the initial state, the photon has a angular momentum l_γ which couples electromagnetically to the nucleon with spin $J_N(J = 1/2)$ and parity $P_N = +1$ to produce a resonance with spin J_N^* and parity P_N^* as shown in figure 2.2. In the intermediate state it follows that:

$$|l_\gamma - J_N| \leq J_{N^*} \leq |l_\gamma + J_N|, \tag{2.19}$$

$$P_{N^*} = P_N \cdot P_\gamma = P_\gamma. \tag{2.20}$$

When a resonance decays to the nucleon ground state via emission of a meson with spin ($S_m = 0$), parity ($P_m = -1$) and relative angular momentum ($l_m = 0$) then the selection rules in equation (2.20) must be fulfilled [9]:

$$|l_m - 1/2| \leq J_{N^*} \leq |l_m + 1/2|, \tag{2.21}$$

$$P_{N^*} = P_N \cdot P_m \cdot (-1)^{l_m} = (-1)^{l_m+1}. \tag{2.22}$$

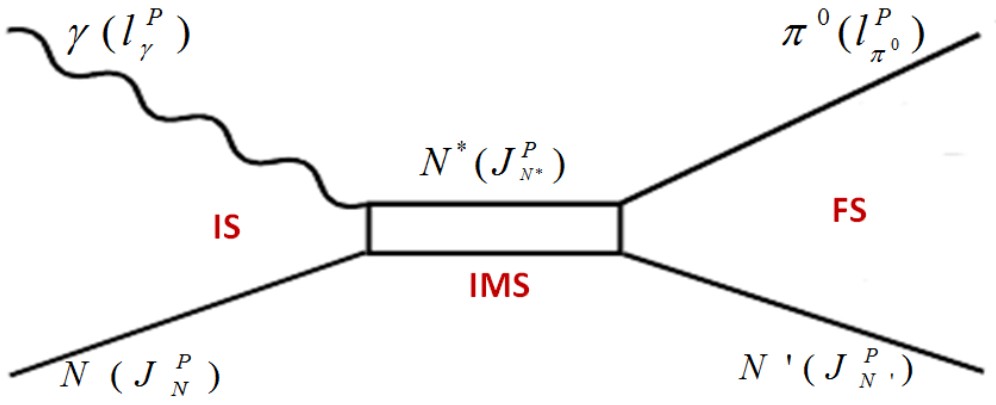

Figure 2.2: A schematic diagram for photoproduction of a meson via excitation of a nucleon [9]. IS- initial state, IMS- intermediate state and FS - final state.

This gives the following conditions for parity and angular momentum conservation

$$P_\gamma = P_{N^*} = (-1)^{l_m+1}, \tag{2.23}$$

$$l_\gamma \pm 1/2 = J_{N^*} = l_m \pm 1/2 \tag{2.24}$$

where the two "±" in equation (2.24) are independent. Therefore, angular momentum and parity conservation allows two conditions to be fulfilled. For magnetic multipoles (ML) with parity $P_\gamma = (-1)^{l+1}$;

$$ML : l_\gamma = l_m, \tag{2.25}$$

and electric multipole (EL) with parity $P_\gamma = (-1)^l$;

$$EL : l_\gamma = l_m \pm 1. \tag{2.26}$$

This means that each resonance can be excited by one electric and one magnetic multipole. However, for $J_{N^*} = 1/2$ resonances can only be excited by one multipole [9]. Table 2.1 gives a summary of the lowest order multi-

poles with the corresponding angular distributions of the cross sections. The

L	Photon M-pole	Initial state (l^P_γ, J^P_N)	Interm. state J^P_{N*}	Final state (J^P_N, l^P_m)	Multi-pole	$\frac{k*}{q*}\frac{d\sigma}{d\Omega}$
1	E1	$(1^-, \frac{1}{2}^+)$	$\frac{1}{2}^-$	$\frac{1}{2}^+, 0^-$	E_{0+}	$\lvert E_{0+}\rvert^2$
			$\frac{3}{2}^-$	$\frac{1}{2}^+, 2^-$	E_{2-}	$\lvert E_{2-}\rvert^2(5-3x^2)$
1	M1	$(1^+, \frac{1}{2}^+)$	$\frac{1}{2}^+$	$\frac{1}{2}^+, 1^+$	M_{1-}	$\lvert M_{1-}\rvert^2$
			$\frac{3}{2}^+$	$\frac{1}{2}^+, 1^+$	M_{1+}	$\lvert M_{1+}\rvert^2(5-3x^2)$
2	E2	$(2^+, \frac{1}{2}^+)$	$\frac{3}{2}^+$	$\frac{1}{2}^+, 1^+$	E_{1+}	$\frac{9}{2}\lvert E_{1+}\rvert^2(1+x^2)$
			$\frac{5}{2}^+$	$\frac{1}{2}^+, 3^+$	E_{3-}	$\frac{9}{2}\lvert E_{3-}\rvert^2(1+6x^2-5x^4)$
2	M2	$(2^-, \frac{1}{2}^+)$	$\frac{3}{2}^-$	$\frac{1}{2}^+, 2^-$	M_{2-}	$\frac{9}{2}\lvert M_{2-}\rvert^2(1+x^2)$
			$\frac{5}{2}^-$	$\frac{1}{2}^+, 2^-$	M_{2+}	$\frac{9}{2}\lvert M_{2+}\rvert^2(1+6x^2-5x^4)$

Table 2.1: Lowest order multipole amplitudes for the photoproduction of pseudoscalar mesons ($x = \cos\theta$) [9].

angular distributions reflect the quantum numbers of the excited state when the cross section is dominated by a resonance. In π^0-photoproduction, for example, the $\Delta(1232)3/2^+$ resonance is excited through the M_{1+}-multipole which exhibits the characteristic $(5 - 3\cos\theta^2)$ dependence. The angular distribution of π^0-photoproduction differential cross section data close to resonance at 331 MeV shown in figure 2.3 depicts this dependence, which is in good agreement with the expectation for the M_{1+}-multipole shown in figure 1.7. The angular distribution of the cross section depends on the combination of the spin of the resonance and the order of the photon multipoles but not the combinations of the parities of the resonance and multipole. For example the $3/2^-$ and $3/2^+$ resonances have the same angular dependence even though they are excited by electric and magnetic multipoles, respectively [9]. This shows that the cross section alone can not provide an unambiguous extraction of the multipole contributions to the excited nucleon resonances. To resolve these ambiguities, measurements of polarization observables are necessary.

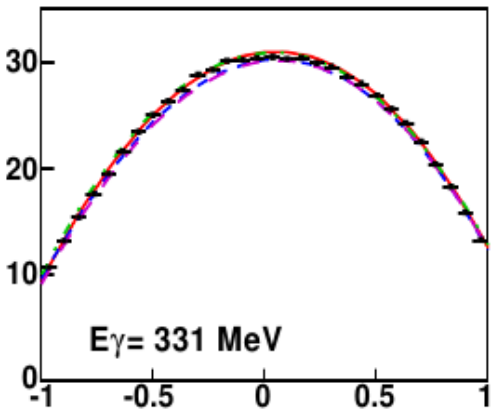

Figure 2.3: The differential cross section on $\gamma p \to \pi^0 p$ from [19] compared to existing PWA solutions from SAID-CM12 [16] (blue dashed line), MAID2007 [15] (magenta long-dashed line), and Bonn- Gatchina BG2014-02 [17] (green dash-dotted line) and to a new SAID PR15 solution [16] (red solid line) obtained after adding the present data points into the fit.

2.2 Polarization Observables

Meson photoproduction experiments can be performed with three types of polarization: photon beam polarization, nucleon target polarization and polarization of the recoil nucleon. The target polarization will be described in the frame $\{x, y, z\}$ as shown in figure 2.4 with z-axis pointing in the direction of the photon momentum $\hat{\vec{k}}$, the y-axis perpendicular to the reaction plane, $\hat{\vec{y}} = \hat{\vec{k}} \times \hat{\vec{q}} / \sin\theta$, and x-axis given by $\hat{\vec{x}} = \hat{\vec{y}} \times \hat{\vec{z}}$. The frame $\{x', y', z'\}$ is used for recoil nucleon polarization, where the z'-axis is defined by the momentum of the outgoing meson $\hat{\vec{q}}$, the y'-axis is the same as target polarization and the x'-axis is given by $\hat{\vec{x'}} = \hat{\vec{y'}} \times \hat{\vec{z'}}$. The photon polarization can either be linear or circular. For linear polarization ($P_T = 1$) in the reaction plane $(\hat{\vec{x}}, \hat{\vec{z}}), \varphi = 0$ and perpendicularly in the direction $\hat{\vec{y}}, \varphi = \pi/2$. For right-handed(or left handed) circular polarization $P_\odot = +1(-1)$ [23].

Using the coordinate definition in figure 2.4 for the three polarization combinations, a general polarized cross section can be defined

$$\frac{d\sigma}{d\Omega}^{(B,T,R)}(P^\gamma, P^N, P^R) = \frac{k}{q}|\langle P^R|\mathcal{F}_{CGLN}|P^T\rangle|^2 \tag{2.27}$$

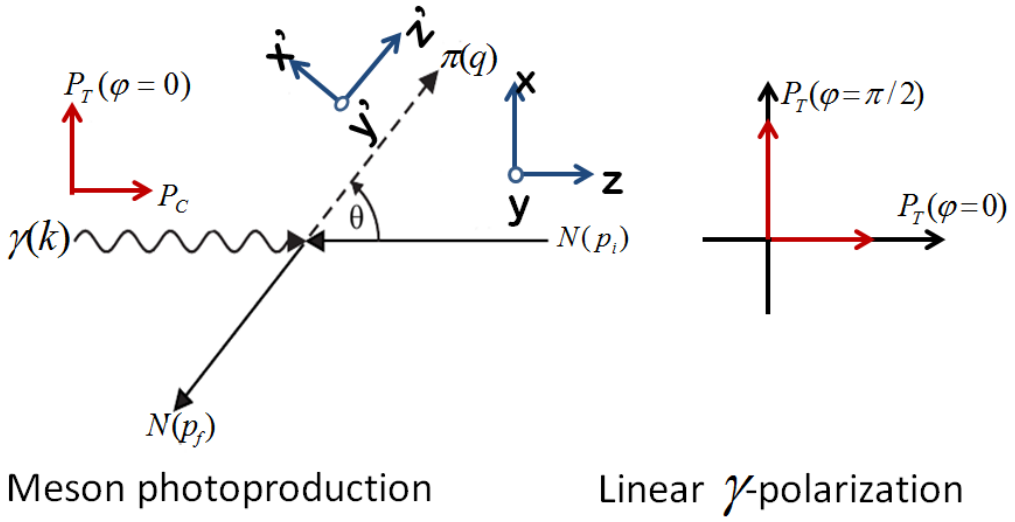

Figure 2.4: Coordinate system for target, beam and nucleon recoil experiments.

where P^γ is the direction of the photon spin polarization, P^R is the direction of the recoil nucleon spin and P^T is the direction of the initial state nucleon spin [24]. The combination of the polarization spins and the CGLN amplitudes results in 16 measurable observables in the photoproduction of pseudoscalar mesons. They are: the unpolarized differential cross-section σ_o, three single-polarization observable (Σ, T, and P), three sets of four asymmetries involving either a combination of the; beam and target (E, F, G, H) polarization, target-recoil ($O_{x'}, O_{z'}, C_{x'}, C_{z'}$), and beam-recoil ($T_{x'}, T_{z'}, L_{x'}, L_{z'}$) [25, 26, 27]. Table 2.2 summarizes all the 16 polarization observables depending on the polarization combination.

In this work an experiment was performed with both target and photon beam polarization. Therefore, the polarized differential cross section for meson photoproduction with the beam-target polarization is:

$$\begin{aligned}\frac{d\sigma}{d\Omega} &= \sigma_o\{1 - P^\gamma_{lin}\Sigma\cos 2\phi + P^T_x(-P^\gamma_{lin}H\sin 2\phi + P^\gamma_{cir}F) \\ &+P^T_y(T - P^\gamma_{lin}P\cos 2\phi) + P^T_z(-P^\gamma_{lin}G\sin 2\phi - P^\gamma_{cir}E)\}.\end{aligned} \tag{2.28}$$

Photon polarization		Target polarization	Recoil nucleon polarization	Target and recoil polarization
		X Y Z	X' Y' Z'	X' X' Z' Z' X Z X Z
unpolarized	σ_0	- T -	- P -	T_x L_x T_z L_z
linear	Σ	H -P G	O_x -T O_z	$-L_z$ T_z L_x $-T_x$
circular	-	F - E	C_x - C_z	

Table 2.2: Polarization observables in the photoproduction of the pseudoscalar mesons; Unpolarized cross section, three single polarization and twelve double polarization observables [27].

The measurement of the helicity asymmetry E using circularly polarized photon beam and a longitudinally polarized target is the main objective of this thesis. Therefore equation (2.28) can be written as

$$\frac{d\sigma}{d\Omega} = \sigma_o\{1 - P_z^T P_{cir}^{\gamma} E\}. \tag{2.29}$$

The helicity asymmetry E describes the coupling of a meson total spin $1/2$ or $3/2$ to the photon and the target nucleon and it gives the static properties of the nucleon in the low energy regime [8]. It can be expressed in terms of CGLN amplitudes as:

$$E\sigma_o = Re\{|\mathcal{F}_1|^2 + |\mathcal{F}_2|^2 - 2cos\theta\mathcal{F}_2\mathcal{F}_1^* + \sin^2\theta(\mathcal{F}_1\mathcal{F}_4^* + \mathcal{F}_2\mathcal{F}_3^*)\} \cdot \rho \tag{2.30}$$

where $\rho = \frac{q}{k}$ is a phase space factor given by meson and photon momenta q and k [28].

2.2.1 The "Complete Experiment" and Single Energy Analyses

Pseudoscalar meson photoproduction has 8 spin degrees of freedom, and due to parity conservation it can be described by four complex amplitudes $\mathcal{F}_i$ at each photon energy and scattering angle. Since the 1970s, efforts have been made on how to determine the complex amplitudes for pseudoscalar meson

photoproduction from a "complete" set of experiment unambiguously. A "complete experiment" is a set of measurements that is sufficient to predict all other possible experiments, provided that the measurements are free of uncertainties. Therefore in principle it is an academic problem, which can be solved by a mathematical algorithm. In practice, however, either a very high statistical precision would be required, which is very unlikely, or further measurements of other observables would be necessary [26, 23].

After various studies [27, 25, 29, 30] it became clear that at least eight carefully chosen observables are sufficient for an unambiguous determination of the complex amplitudes. From a complete set of 8 measured observables, one can determine the moduli of 4 amplitudes and 3 relative phases. However, there is always an overall phase which is unknown and can not be determined by additional measurements. Thus, analysis of nucleon resonances, through the determination of amplitudes of the "complete" experiment, is not very useful because the overall phase which is dependent on energy can not be resolved either by experiment or theory without strong model dependence [23]. The solution is to perform a truncated partial wave analysis on the observables themselves, where the overall unknown phase is only dependent on the energy and can be constrained by theory without strong model dependence. This is achieved by expanding all the observables $O_i(W,\theta)$ in terms of either Legendre polynomials or $\cos\theta$ as:

$$O_i(W,\theta) = \frac{q}{k}\sin^{\alpha_i}\theta \sum_{k=0}^{2l_{max}+\beta_i} A_k^i(W) P_k(\cos\theta). \tag{2.31}$$

The coefficient $A_k^i(W)$ in equation (2.31) can be expanded in a finite series of bilinear products of electric and magnetic multipoles up to $L = L_{max}$ as:

$$A_k^i(W) = \sum_{l,l'=0}^{l_{max}} \sum_{k,k'=0}^{4} \alpha_{l,l'}^{k,k'} \mathcal{M}_{l,k}(W) \mathcal{M}^*_{l',k'}(W) \tag{2.32}$$

where k, k' are the four possible electric and magnetic multipoles for each πN angular momentum $l \geq 2$, namely $\mathcal{M}_{l,k} = \{E_{l+}, E_{l-}, M_{l+}, M_{l-}\}$. For an S,

P truncation ($l_{max} = 1$) there are 4 complex multipoles $E_{0+}, E_{1-}, M_{1+}, M_{1-}$ leading to seven real parameters and an arbitrary phase which can be set to zero for the beginning [23].

2.3 Partial Wave Analyses (PWA) using Models

Besides the direct extraction of partial wave amplitudes from the measurement of observables at each single energy (see 2.2.1), often models are used to parameterize the energy dependence analysis. Various PWA formalisms have been developed by different analysis groups even though only a few have a comprehensive PWA based on a large database from experiments. These groups use different techniques to parametrize the nucleon resonance parameters and background contributions. Generally the background contributions are modeled by the Born terms and the vector-meson contribution while the resonant contribution is modeled by a Breit-Wigner parametrization. Other methods use K-Matrix formalism to model the overlapping resonances in the same partial wave and provide a good way of ensuring that the amplitudes preserve the unitarity [8]. In order to extract the nucleon resonance parameters, a fit is performed on the experimental data. Some of the PWA models are: MAID [31, 32, 33, 34], SAID [35, 36, 37, 38], Bonn-Gatchina [39, 40], the Giessen coupled-channel analysis [41, 42] and the excited baryon analysis center at Jefferson lab [43, 44]. A brief description of the PWA models used for comparison with the data in this work are given in the following subsections.

2.3.1 MAID (Unitary Isobar Model)

The MAID Isobar model was developed by the University of Mainz. Its first model MAID1998 was developed with a limited set of nucleon resonances described by Breit-Wigner forms and a non-resonant background constructed from the Born terms and the t-channel contributions. Each partial wave

was unitarized up to the pion threshold by use of the Watson theorem [31]. Since then the model has been upgraded to the current MAID2007 [33]. In MAID2007, the background contributions are complex functions defined according to K-matrix theory as:

$$t^{B,\alpha}_{\gamma\pi}(W,Q^2) = \nu^{B,\alpha}_{\gamma\pi}(W,Q^2)[1 + it^{\alpha}_{\pi N}(W)], \tag{2.33}$$

where the pion-nucleon elastic scattering amplitudes, $t^{\alpha}_{\pi N} = [\eta_\alpha exp(2i\delta_\alpha)]/2i$ are described by phase shifts δ_α and the inelasticity parameter η_α. The resonance contributions use the same equation as for MAID98 [31] and is given as:

$$t^{R,\alpha}_{\gamma\pi}(W,Q^2) = \bar{\mathcal{A}}^{R}_{\alpha}(W,Q^2)\frac{f_{\gamma N}(W)\Gamma_{tot}M_R f_{\pi N}(W)}{M_R^2 - W^2 - iM_R\Gamma_{tot}}e^{i\phi R} \tag{2.34}$$

where $f_{\pi N}$ is the Breit-Wigner factor describing the decay of a resonance with total width $\Gamma_{tot}(W)$, partial πN width $\Gamma_{\pi N}$ and spin J [33]. This model contains thirteen resonances of four-star below 2 GeV and gives the predictions of the multipoles, amplitudes, cross sections and polarization observables for photo and electroproduction on their website [15].

2.3.2 SAID Model

The SAID (Scattering Analysis Interactive Dial-in) model is based on the K-matrix approach, which includes the most important final state, phase space and threshold effects. The parameterization of the wave amplitudes are written in terms of polynomials used in [35]. This has been modified in [38] to fit the increasingly precise data. The modification included the third term as:

$$M = (Born + A)(1 + iT_{\pi N}) + BT_{\pi N} + (C + iD)(I_M T_{\pi N} - |T_{\pi N}|^2), \tag{2.35}$$

where $T_{\pi N}$ is the elastic πN scattering partial wave amplitude associated with the pion photoproduction multipole amplitude M. The factors A through D are parameterized in terms of simple polynomials with correct threshold

behaviors. Similar to MAID, SAID maintains an extensive database of elastic πN scattering, amplitudes and observable prediction on a website [16].

2.3.3 Bonn-Gatchina (BnGa) Model

This model is developed by the university of Bonn Germany and St. Petersburg in Russia. It uses the K-matrix parameterization deriving the background terms from phenomenology. The Analysis uses large experimental data base to constrain the PWA solutions [39]. Unlike in MAID and SAID, BnGa model is not constrained to πN scattering only but also includes the multi-particle final states like $p\pi^0\pi^0$ and $p\pi^0\eta$. A detailed description of this model can be found in [39, 40]. The group maintains a database of PWA amplitude, cross sections, multipoles and polarization observable of different decay channels [17].

2.4 Previous Studies on π^0 Photoproduction

The study of the $\gamma p \to \pi^0 p$ reaction has been investigated mainly through cross section measurements since the early 1960's [45, 46, 47, 48, 49, 50, 51, 52]. The most resent cross section data on π^0 covering a wide kinematic and energy range are presented in [50, 51, 19, 52]. Figure 2.5 shows the total cross section for the reaction $\gamma p \to \pi^0 p$ from CBELSA/TAPS [49] and recent A2Mainz data [19]. The first peak in the cross section corresponds to the Δ-resonance region $\Delta(1232)3/2^+$ dominated by the total spin 3/2. The second peak corresponds to the second resonance. In this region several nucleon resonances dominate with $N(1535)1/2^-$ and $N(1520)3/2^-$ having the largest contribution. The third peak around 1.65 GeV corresponds to the third resonance region where the main contributions are due to $N(1700)3/2^-$, $N(1680)5/2^+$ and $N(1650)1/2^-$ resonances each contributing $\approx 35\%$, $\approx 25\%$ and $\approx 20\%$, respectively [49, 19].

Due to the fact that the resonances overlap, the total cross section data is insufficient in the study of nucleon resonances. As discussed in 2.1 polarization observables can be used to constrain the partial wave analyses models.

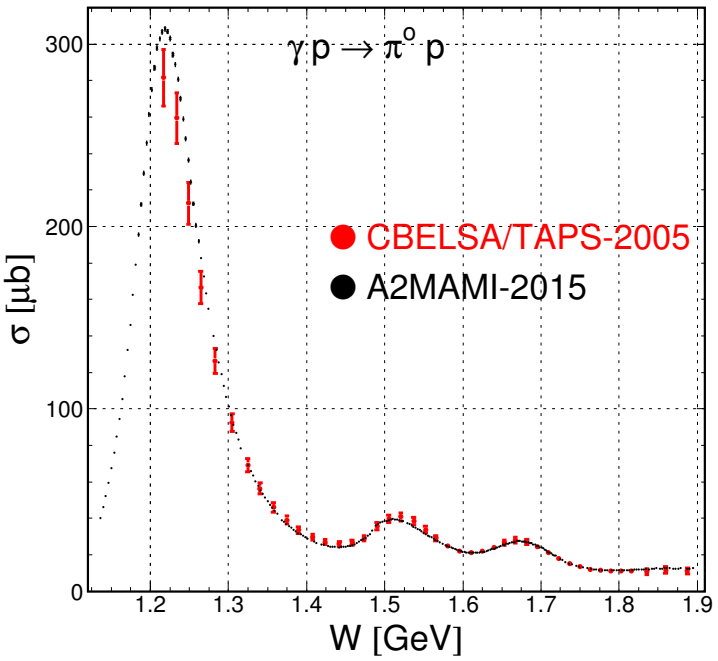

Figure 2.5: Total cross section for the reaction $\gamma p \to \pi^0 p$ from A2MAMI [19] (black) and CBELSA/TAPS [49] (red).

In the last decade, the development of the technologies to polarize both the beam and target has enabled the measurement of both single and double polarization observables. The measurements have been carried out in various experimental lab facilities: the Crystal Ball/TAPS experiment at MAMI in Germany, the CLAS facility at JLab in the USA, the Crystal Barrel/TAPS experiment at ELSA in Germany and the GRAAL experiment in Grenoble, France. The most studied polarization observable in $\gamma p \to \pi^0 p$ is the beam asymmetry Σ. It has been studied for different beam energies in MAMI, ELSA and GRAAL [53, 54, 55]. Single polarization observables T and P have been presented in [56, 57]. Double polarization observables H and G have been reported [57, 58] for the beam energy range $E_\gamma = 600 - 2300$ MeV at CBELSA/TAPS.

The helicity dependence differential cross section on π^0 photoproduction has been measured in the energy range $E_\gamma = 310 - 540$ [59] and $E_\gamma = 550 - 790$ [48] at MAMI. The cross section was evaluated by taking the

difference between the total events for parallel and anti-parallel nucleon-photon spin configurations. This, ensured that the background contribution of the reactions on carbon and oxygen nuclei from butanol target could be fully separated from the polarized hydrogen nuclei contribution. However, the cross section data was limited in angular coverage by covering only angles around 90^0.

Recently, measurement of helicity asymmetry E has been performed at the CBELSA/TAPS experiment covering photon beam energy of $E_\gamma = 600-2300$ MeV with bins $\geq$100 MeV and covering a polar angle between 0^o to 180^o [60]. The results, covering a few energy bins, are presented in [60] and shown in figure 2.6. It is clear that the angular dependence of helicity asymmetry E reflects the contribution of several weak resonances as detailed in [60] which were not visible in the photoproduction cross section. The comparison of the experimental results with the partial wave analysis predictions show large discrepancies even in the region of four star resonances N(1440)$1/2^+$, N(1535)$1/2^-$ and N(1520)$3/2^-$.

Also, the helicity asymmetry E on π^0 photoproduction has been measured in JLab for the energy range $E_\gamma = 550 - 2400$ MeV with energy binning of 50 MeV and polar angle coverage between 7^o to 145^o [61]. The results were compared to PWA predictions of SAID and MAID2007 models which indicate some discrepancies.

From the existing data, it is clear that abundant cross section data for π^0 photoproduction exist. However, there exist less data on polarization observables. In particular, there exist no data for helicity asymmetry E below $E_\gamma \leq 550$ MeV. Also, both measurements in [60] and [61] show unexpected discrepancy with the models and they are covering large energy bins. Therefore, study of the helicity asymmetry E in the energy range $E_\gamma = 210 - 1410$ MeV, will not only provide new data with finer energy binning (30 MeV) but also act as a check for the existing data. In addition, the data will be an input to the partial wave analysis models. This will help in constraining the models and understanding the discrepancy existing between data and the PWA models.

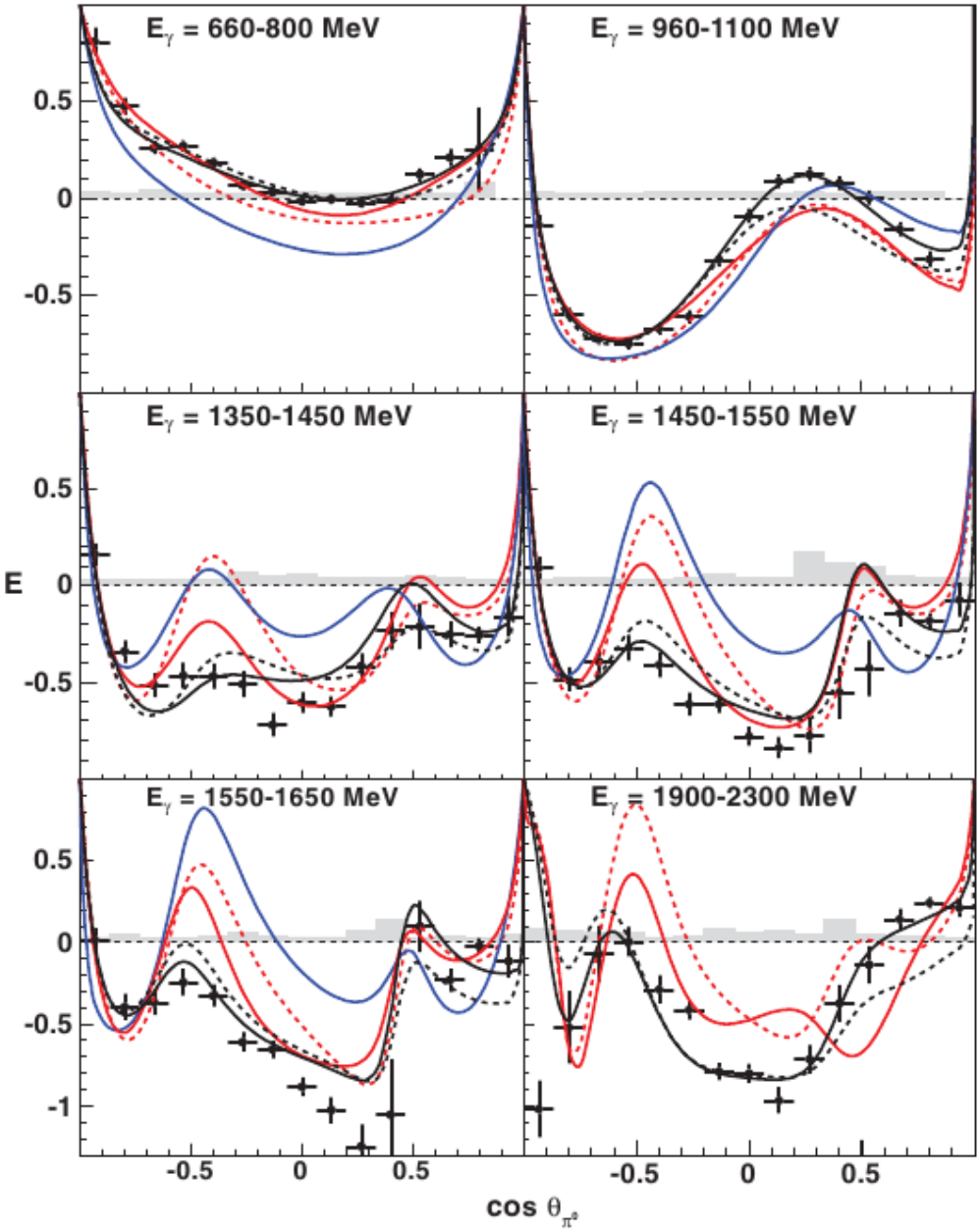

Figure 2.6: Helicity asymmetry E as a function of $\cos\theta_{\pi^0}$. PWA predictions: black dashed curves are BnGa2011-02, blue solid curves are MAID, red solid curves are SAID-CM12, red dashed curves are SAID-SN11 and black solid curve are the BnGa2011-02 fits to the data points [60].

Chapter 3

Experimental Setup

This chapter presents an overview of the experimental setup used this work. The experimental setup consists of: the electron accelerator, the Mainz Microtron (MAMI) discussed in 3.1; the photon tagging facility in section 3.2, and a set of reaction product detectors (the Crystal Ball and TAPS) in section 3.3 and the frozen spin target. The frozen spin target will be discussed in chapter 4 since the operation of the target and development of polarizing magnet was a substantial part of this thesis. The experimental trigger and data acquisition systems are described in sections 3.4 and 3.5, respectively. Lastly, an overview of beam-time conditions are presented in section 3.6.

3.1 The Mainz Microtron (MAMI)

MAMI is an electron accelerator facility located at the Johannes Gutenberg-University in Mainz, Germany. Figure 3.1 shows the floor plan for the MAMI accelerator and all of the experimental halls. It first came into operation in 1979, delivering an electron beam of 14 MeV, and has been upgraded several times. It consists of a cascade of three Race Track Microtron (RTMs), each with a single accelerating section and two 180°-deflecting recirculation magnets. The RTMs form the accelerator stage MAMI B, with a maximum extracted electron energy of 883 MeV [62, 63]. In addition to RTMs, the final accelerator stage is a Harmonic Double Sided Microtron (HDSM) with

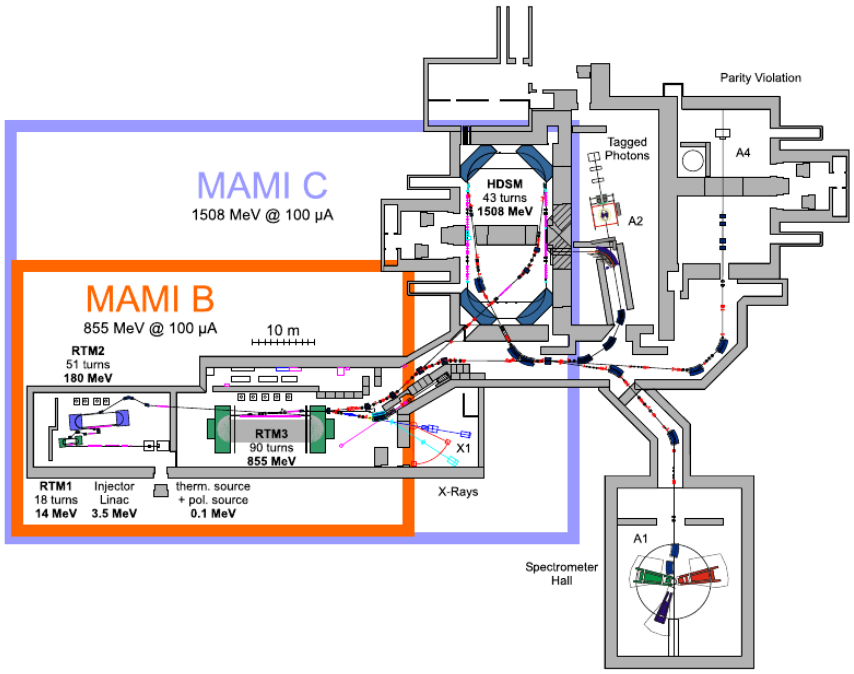

Figure 3.1: An overview of the MAMI floor plan and all the experimental halls [64, 65].

four 90°-bending magnets and two harmonic-frequency accelerating sections [66]. This upgrade for higher energy is known as MAMI C. The accelerator produces a continuous wave (cw) electron beam with nominal energies up to 1.6 GeV for both unpolarized and polarized beam. The beam is fed into one of the three experiment hall at a time: A1 (Electron scattering), A2 (Tagged photons) or X1 (X-rays). Experimental hall A4 was shutdown to pave way for the construction of MESA (Mainz Energy-Recovering Superconducting Accelerator). The present experiment was carried out in the Tagger hall (A2). The RTMs, HDSM, polarized electron beam and circularly polarized photon beam are briefly described in subsections 3.1.1 through 3.1.3.

3.1.1 The Race Track Microtron (RTM)

A Microtron is an accelerator that recirculates a beam of electrons through the same linear accelerator (linac) multiple times. It consists of a single linac between two large dipole magnets. The electrons are injected into the linac

where they pass through standing wave cavities powered by radio frequency (rf) klystrons. The electrons are recirculated in the RTMs several times with an energy gain ΔE delivered each pass [65]. The energy gain ΔE is given by:

$$\Delta E = \frac{ecB}{2\pi\nu_{rf}} \tag{3.1}$$

where e is the electron charge, c is the speed of light, B is the magnetic field and ν_{rf} is the frequency of the klystrons given as $\nu_{rf} = c/\lambda_{rf}$ [65].

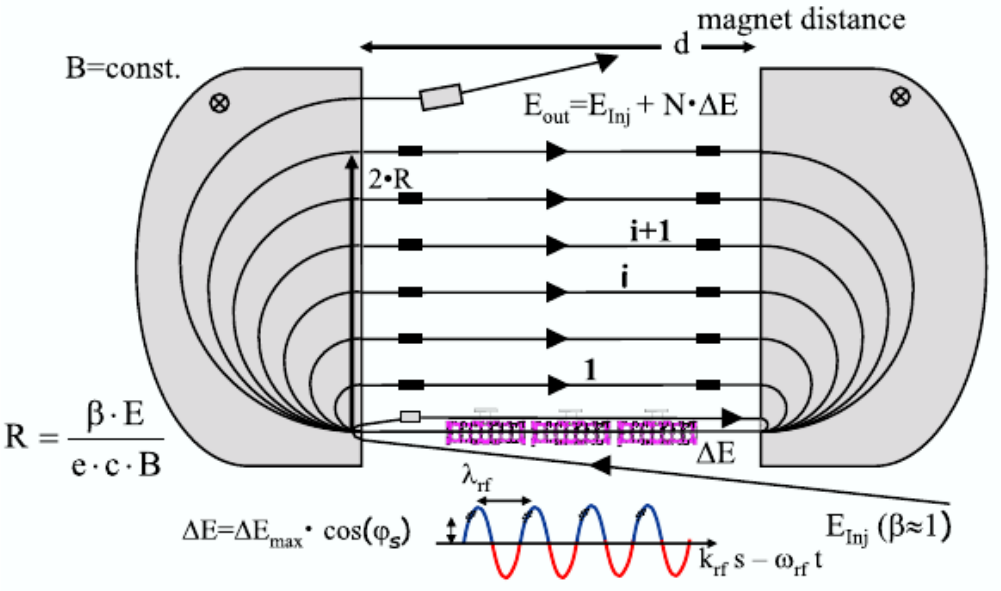

Figure 3.2: A schematic diagram of a race track Microtron [65].

The RTM provides good intrinsic energy resolution the electron path through the magnets is adjusted such that they arrive in phase with the accelerating field of the rf cavities. For electrons not in phase, the nominal energy gain ΔE is modified correspondingly. The energy gain per recirculation is of the order of 1 MeV/m. The accelerator operates with a 100% duty factor. The RTMs were designed in 1975 with the aim of attaining a electron beam energy of 800 MeV [65]. Figure 3.2 shows a schematic diagram of an RTM. The electrons are pre-accelerated in a separate linac to an energy of 4.10 MeV. RTMs 1, 2 and 3 then accelerate the electrons to 15.35 MeV, 185.9

MeV and 883.1 MeV, respectively. The energy extracted from each RTM is given by:

$$E_{out} = E_{Inj} + N \cdot \Delta E, \tag{3.2}$$

where E_{Inj} is the injected energy (the energy output from the preceding RTM) and N is the number of turns.

3.1.2 Harmonic Double Sided Microtron (HDSM)

A further energy upgrade using the RTM concept was not possible. This is because extremely large magnets would be required to produce the required magnetic field. Therefore, a HDSM proposed in 1979 by K. H Kaiser, was the best suited option for a higher energy electron beam due to its smaller sized magnets compared to RTM magnets [62, 63, 66]. The HDSM consists of four

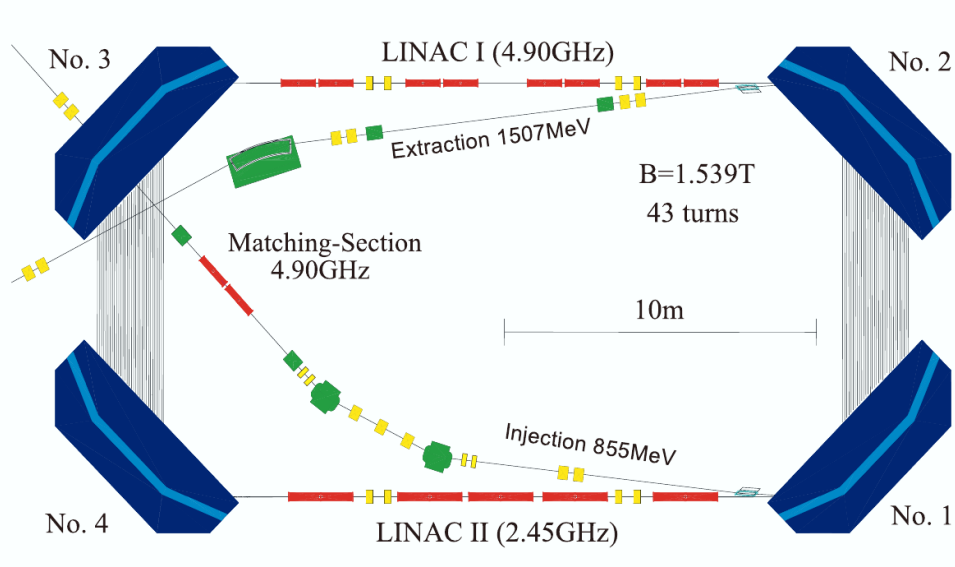

Figure 3.3: A schematic diagram of the harmonic double sided microtron [65].

dipole magnets at 90°, and two linear accelerators, with one linac operating at 4.9 GHz while the other operates at 2.45 GHz (figure 3.3). The pole face area of HDSM is reduced by a factor of $(\pi - 2)/\pi$ compared to an equivalent RTM. Therefore, each HDSM magnet has roughly the same weight as RTM

3 magnets and the energy gain ΔE changes to:

$$\Delta E = n \cdot \frac{ecB}{\pi - 2} \cdot \lambda_{rf}. \tag{3.3}$$

The different accelerating frequencies gave rise to the name "harmonic" [62, 65]. With the addition of the HDSM to the RTM cascade, a maximum electron beam energy of 1604 MeV is attainable. Table 3.1 gives an overview of the RTMs and HDSM parameters.

Stage	RTM1	RTM2	RTM3	HDSM
Injection E [MeV]	4.10	15.35	185.9	883.1
Extraction E [MeV]	15.35	185.9	883.1	1557.4
Magnetic Field [T]	0.106	0.573	1.326	1.428
$\Delta\sigma$ [keV]	1.2	2.8	13	110
Bending radius [m]	0.484	0.590	1.366	3.638
Number of turns	18	51	90	43

Table 3.1: MAMI RTM and HDSM parameters [64, 65].

3.1.3 Polarized Electron Beam

In MAMI, a strained GaAsP semiconductor is used as a polarized electron source. Longitudinally polarized electrons are produced when the GaAs is irradiated with circularly polarized laser light [67]. The helicity of the photons is reversed by reversing the sign of the voltage applied to the pockel cell, which, in turn changes the sign of the spin polarization of the electrons emitted. This spin flip occurs at a frequency of approximately 1 Hz, thereby reducing the systematic uncertainty which would result from a fixed beam polarization. The degree of electron beam polarization is measured regularly near the source at an energy of 3.5 MeV using a Mott polarimeter installed in the spin rotator of the beam-line [67].

Additionally, an independent measurement of the electron beam polarization was performed using a Møller polarimeter in A2 hall. The Møller polarimeter is based on $e^- + e^- \rightarrow e^- + e^-$ scattering. For a longitudinally polarized electron beam and target electrons, the cross section of this

reaction in the center of mass (c.m.) frame is given by:

$$\frac{d\sigma}{d\Omega} = \frac{d\sigma_0}{d\Omega}\{1 + P_t P_e A_{zz}(\theta)\} \tag{3.4}$$

where $\frac{d\sigma_0}{d\Omega}$ is the unpolarized cross section, P_t the target electron polarization, P_t the electron beam polarization and A_{zz} the analyzing power [68]. The degree of electron beam polarization P_e can be measured by comparing the cross section asymmetry for beam and target spins aligned parallel and anti-parallel with:

$$P_e = \frac{A}{P_t \cdot \cos\alpha \cdot a_{zz}} \tag{3.5}$$

where A is the asymmetry calculated from the total events with helicity $h = 1$ or $h = -1$ obtained during experiment[68, 69]. It is expressed as

$$A = \frac{N^+ - N^-}{N^+ + N^-} \tag{3.6}$$

where N^+ and N^- is the number of events for parallel and anti-parallel spin combinations, respectively. For $\gamma' \gg 1$[1], the analyzing power a_{zz} is given as

$$a_{zz} = \frac{-\sin^2\theta \cdot (8 - \sin^2\theta)}{(4 - \sin^2\theta)^2}$$

where θ is the scattering angle given by;

$$\theta = 2tan^{-1}\sqrt{\frac{E_e - E_{e'}}{E_{e'} - m_e}}$$

$E_{e'}$ is the electron energy detected in the Tagger, E_e is the incoming electron energy and m_e is the electron mass.

During the experiment, the electron beam impinges on the polarized Møller foil producing two Møller electrons. Two Tagger channels (see section 3.2) are used to detect these electron pairs in coincidence. A good Møller event is a coincidence of two focal plane detectors with the sum of the corresponding electron energies equal to the primary beam energy E_e. By

[1] $\gamma' = \gamma + 1; \gamma = 1/\sqrt{1 - v^2/c^2}$

coincidences in the two Tagger channels the asymmetry A can be measured. In this experiment the Møller foil polarization was $P_t = 0.080 \pm 0.002$ and the relative angle between the Møller foil and the direction of the electron beam is $\alpha = 25^o \pm 0.1^o$ [70].

3.1.4 Circularly Polarized Photon Beam

The degree of circular polarization of the photon beam was calculated from the polarization of the electron beam, photon energy and the incoming electron energy. Longitudinally polarized electrons partially transfer their polarization to the bremsstrahlung photons (see section 3.2) according to:

$$P_\gamma = P_e \cdot \frac{4x - x^2}{4 - 4x + 3x^2} \tag{3.7}$$

where $x = E_\gamma / E_e$, E_e is the energy of the incoming electron beam, P_e is the electron beam polarization measured using Mott/Møller polarimeter and E_γ is the photon beam energy [72]. The degree of circular polarization P_γ of the photons increases as the photon energy increases as shown in figure 3.4. At the highest values of photon beam energy, the degree of photon polarization is approximately equal to the electron's polarization ($P_\gamma \approxeq P_e$). For this work, a 1557 MeV electron beam energy with $77 \pm 2\%$ degree of longitudinal polarization (see 3.1.3) was used.

3.2 The Glasgow Photon Tagger

In order to produce a beam of photons, electrons of a constant beam energy E_0 impinges on a thin metal radiator to produce high energetic photons via bremsstrahlung. Since the mass of the radiator nucleus is much larger than the mass of the electron m_{e^-}, only a negligible amount of energy (of the order of a few keV) is transfered to the nuclei. From the principle of energy conservation, the energy of the emitted photons E_γ can be calculated as

$$E_\gamma = E_e - E_{e^-} \tag{3.8}$$

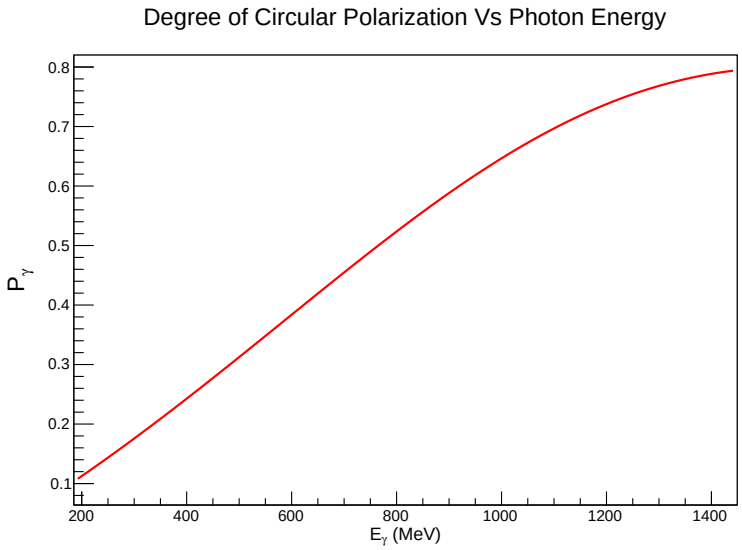

Figure 3.4: The degree of photon polarization as a function of the photon energy.

where $E_{e'}$ is the energy of the scattered electron. The bremsstrahlung cross section shows an energy and angular dependence given by:

$$\frac{d\sigma}{dE_\gamma} \propto \frac{1}{E_\gamma}, \tag{3.9}$$

$$\frac{d\sigma}{d\theta_r} \propto \frac{\theta_r}{(\theta_r^2 + \theta_c^2)^2} \tag{3.10}$$

where the characteristic angle θ_c, depends on the mass of the electron m_{e^-} and the energy of the incoming electron beam [73, 71]. It is defined as

$$\theta_c = \sqrt{\langle\theta_\gamma\rangle^2} \propto \frac{m_{e^-}}{E_e}. \tag{3.11}$$

During bremsstrahlung, 50% of the photons are emitted within the characteristic angle. The ratio of the electron mass and the incoming electron energy gives a very small characteristic angle. This means that most of the photons are emitted in the forward direction within θ_c having small angles θ_γ. The produced photon beam is collimated with a lead collimator of 2 mm in diameter in order have a better defined photon beam on the target.

The Glasgow Photon Tagger [74, 75, 76] is a magnetic electron spectrometer, determines the bremsstrahlung energy via tagging technique. The Tagger consists of a large dipole magnet that bends the electron's path depending on its energy [76] as shown in figure 3.5. Electrons that do not

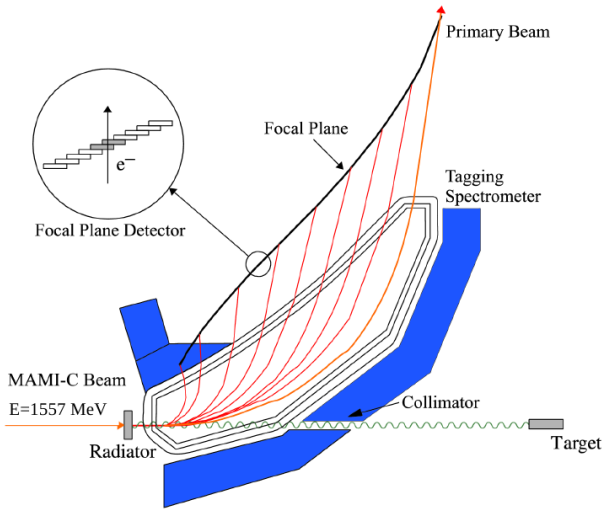

Figure 3.5: The Glasgow Photon Tagger spectrometer [77]. Electron beam enters from the left and strikes the radiator, the bremsstrahlung photon passes to the right through a collimator to interact with the target, while the electrons are bent by the spectrometer magnet to the FPD and beam damp.

undergo bremsstrahlung are bent into the beam dump, while those that do radiate are bent with a smaller radius of curvature to the Focal Plane Detector (FPD). The FPD ladder consists of 353 half-overlapping EJ200 plastic scintillators, each 80 mm long, 2 mm thick and 9 to 32 mm wide. The scintillator strips overlap by slightly more than half their width so that an electron hit is defined by coincident signals in adjacent detectors. In this way, the electron energy can be reconstructed with a resolution of 2-4 MeV. The covered photon energy range for an electron beam of 1557 MeV was between 110 and 1469 MeV. Figure 3.6 shows the distribution of the Tagger channel hits and the corresponding photon energies distribution.

The electron energy can be reconstructed with an appropriate calibration. The calibration of the electron energies in the Tagger is dependent

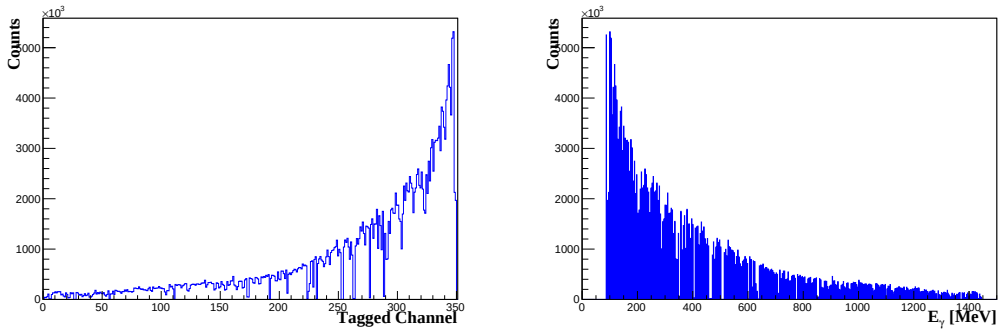

(a) (b)

Figure 3.6: The Tagger channel hits distribution (a) and the corresponding tagged photon energy distribution (b) shows a bremsstrahlung cross section of $1/E_\gamma$.

on the magnetic field strength of the Tagger dipole magnet and the incoming electron beam energy. The magnetic field is very stable but the exact electron beam energy vary between beam-times. Direct Tagger energy calibration measurements are performed using a low intensity electron beam which is made to pass through the Tagger without a radiator. The electrons are bent directly into the Tagger magnet to impinge on the focal plane detectors. Measurements using different electron energies and magnetic fields are performed in order to determine a linear relationship between the electron energies and the Tagger channel numbers. This can only be performed on a small range of energies and these measurements are then extrapolated to the complete energy range using a program called *ugcalv2ua* [76, 78].

During the experiment, the energy of the recoiling electron is reconstructed from its detected position in the Tagger FPD. The hit time is then used to correlate the hits in the FPD with events in the detectors. The analog signal from the FPD photomultiplier tubes (PMTs) is fed to the Tagger electronics via an amplifier/discriminator and a coincidence unit. If the signal passes the discriminators, a logical pulse is sent to Time to Digital Converter (TDC) [79] which records the timing of the multiple hits per event. In addition, the signals are sent to scalers which count the total number of hits in the FPD elements. The information from the scalers is used to get a spectrum of the

recoil electron which is then used in photon beam flux extraction.

3.2.1 Photon Flux

Due to collimation, not all bremsstrahlung photons reach the target. Therefore, the photon flux incident to the target can not be calculated directly from the measured recoil electron flux. To account for the photons which did not pass through the target, a correction to the photon flux is needed. This is done via the calculation of the tagging efficiency ϵ:

$$\epsilon = \frac{N_\gamma}{N_e}$$

where N_γ is the number of photons which pass through the collimator and N_e is the number of electrons measured in the FPD elements. A lead glass detector placed in the beam-line, 15 m downstream from the radiator, was used for the tagging efficiency measurement. The number of coincidence hits between the lead glass detector and each FPD element was measured and used to calculate ϵ for each element. The tagging efficiency measurement was performed at a lower beam intensity than used in the normal runs. This ensured that the lead glass detector is not damaged and that there are no multiple hits in the FPD elements. The lead glass detector was assumed to have 100% detection efficiency.

3.3 Detectors

The detector setup for the experiment includes: the Crystal Ball, Particle Identification Detector (PID), Multi Wire Proportional Chambers (MWPC) and TAPS (BaF_2-$PbWO_4$ and Veto). Each of them will be discussed in subsections 3.3.1 through 3.3.4. Figure 3.7 shows a schematic diagram of this setup in the A2 experimental hall.

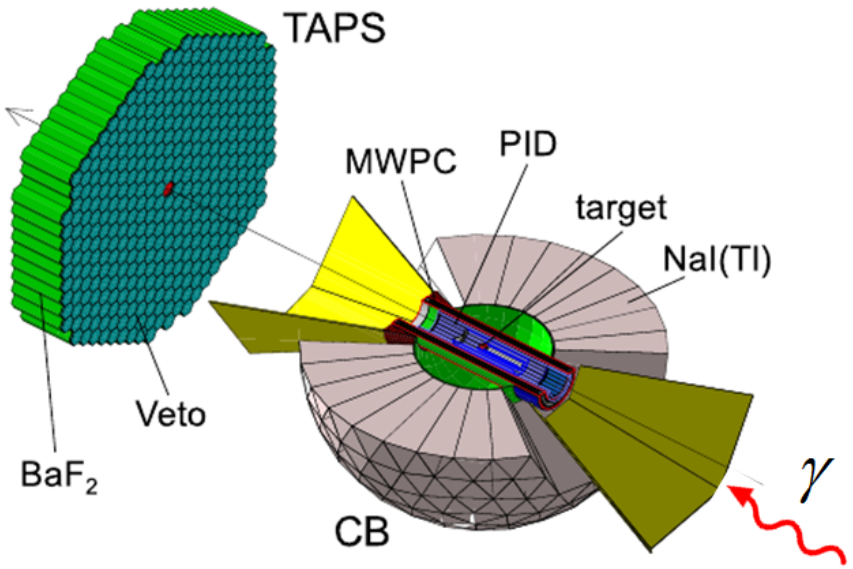

Figure 3.7: A schematic picture of the detector setup in the A2 hall with the upper half of the Crystal Ball removed [71].

3.3.1 The Crystal Ball

The detector was proposed a few months before the discovery of the J/ψ particle in 1974 (jointly by SLAC and Brookhaven national laboratory) and played a crucial role in making some of the first measurements of J/ψ and its excited states [80, 81, 82, 83]. It was then moved to Deutsches Elecktronen-Synchrotron (DESY) in Hamburg between 1982-1987 to facilitate the study of b-quarks. After a period of 8 years in storage at SLAC it was used to study strange and non-strange baryon resonances at Brookhaven National Laboratory from 1995 to 2002. In November 2002 it was moved to the current location in the A2 hall at MAMI.

The Crystal Ball calorimeter is a sphere consisting of 672 optically insulated NaI(TI) crystals shaped as truncated triangular pyramids, all pointing towards its center. The crystals are arranged in two hemispheres that cover 92.3% of 4π. It has a spherical cavity in the center with radius of 25 cm. The cavity is designed to hold a target and inner detectors. The crystal ball

has two cone-shaped tunnels, each close to 40° which serve as the entrance and exit of the beam [84]. Figure 3.8a shows the design of the Crystal Ball and 3.8b is the structure of a single Crystal Ball element.

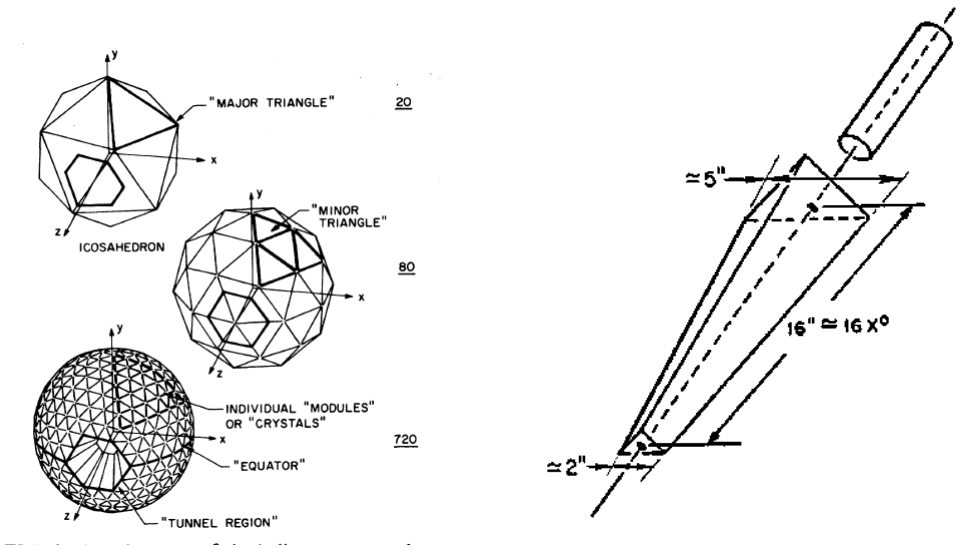

(a) (b)

Figure 3.8: (a) is the Crystal Ball design and (b) a single Crystal Ball element [83].

Each crystal measures 40.6 cm in length, corresponding to approximately 15.7 radiation lengths. Since NaI(Tl) is hygroscopic, the crystals are hermetically sealed and stacked in two separate hemispheres made of 1.5 mm thick of stainless steel. Each hemisphere has inner and outer radii of 25.3 cm and 66.0 cm, respectively [83]. The equator region between the hemispheres is 0.8 cm with an air gap of 5 mm. The mechanical separation of the two hemispheres allows easy access for mounting the targets and maintaining of the inner detectors. Figure 3.9 shows a picture of the Crystal Ball with its upper hemisphere lifted during a maintenance period. Each crystal is optically coupled to a SRCL50B01 photomultiplier tube with glass windows.

During a scattering reaction, reaction products deposit energy in the NaI(TI) via electromagnetic showers. Typically photons deposit $\approx 98\%$ of their energy in a cluster of maximum 13 adjacent crystals. From the elec-

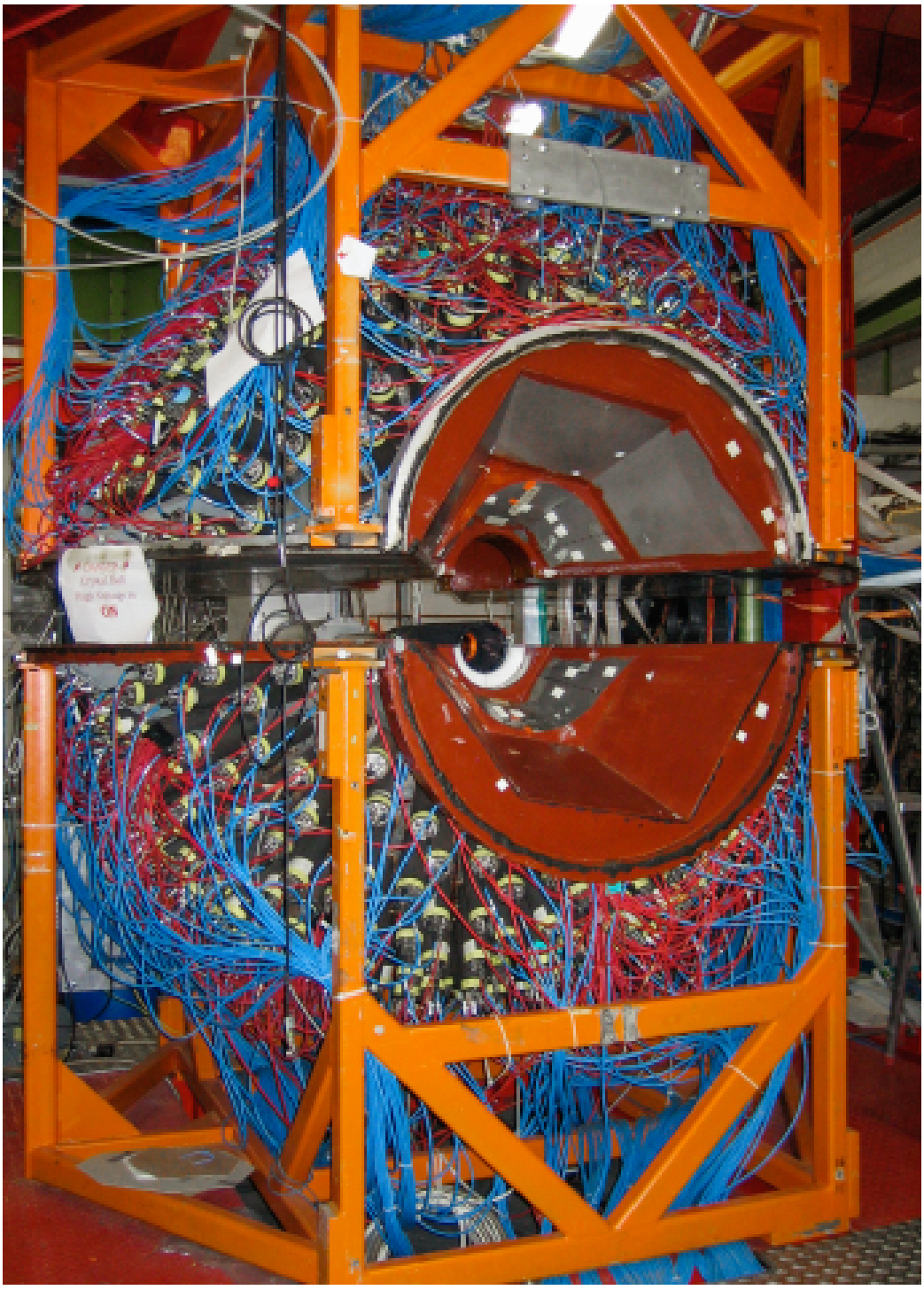

Figure 3.9: A picture of Crystal Ball detector with the upper hemisphere lifted for the purpose of maintenance.

tromagnetic shower in the Crystal Ball, the energy and direction of particles can be reconstructed. Table 3.2 summarizes the energy, timing, angular resolution and angular coverage of the Crystal Ball detector.

Photon energy resolution $\frac{\sigma E}{E}$	$\approx \frac{0.020}{(E(GeV))^{0.36}}$
Time resolution	$\sigma_t \approx 2ns$
Angular resolutions	
Polar	$\sigma_\theta \approx 2^o$-$3^o$
Azimuthal	$\sigma_\phi \approx \frac{2^o}{\sin\theta}$
Angular coverage	
Polar	$20^o \leq \theta \leq 160^o$
Azimuthal	$0^o \leq \phi \leq 360^o$

Table 3.2: Energy, spatial and time characteristics of Crystal Ball [85, 86].

During the experiment, the signals from the Crystal Ball detector elements are fed into fan-in fan-out unit with each unit handling a group of 16 channels. The output signal is split into three parts: the first signal is summed along with the other 15 signals and sent to the trigger electronics to measure the energy sum of all the crystals. The second signal is fed into the Leading Edge Discriminator (LED) with 16 input channels where the signals are compared with two thresholds. If the low threshold is passed the signal proceeds to the TDC and scaler module. The third signal is sent to the Sampling Analog to Digital Converter (sampling ADC) to measure the charge. A Sampling ADC with a frequency of 40 MHz is used to convert the analog signal from each PMT to a digital signal from which charge of the signal is measured. In principle, the shape of the entire pulse can be sampled and recorded. However, in order to reduce the dead-time of the system, the integral of the pulse is read in three different timing windows. These correspond to the pedestal (records the residual charge), the signal itself and the tail. In order to reduce pile-up, the pedestal is automatically subtracted from the signal on an event by event basis.

3.3.2 The Particle Identification Detector (PID)

The particle identification detector is part of the inner detectors of the Crystal Ball. It consists of 24 EJ-204 plastic scintillators arranged in a cylindrical barrel with an average diameter of 10.84 cm. Each element is 500 mm in length, 15.3 mm wide and 4 mm thick [85]. The cross section of each element is a right angled trapezium, which ensures gaps between elements are minimized. Its azimuthal angle coverage ranges from 15^o to 159^o which is larger than that of the Crystal Ball. Each element is wrapped in foil to ensure optical isolation. In addition, the entire detector is covered in black Tedlar (PVF) to provide light-proofing. Scintillation light induced in each scintillator travels through a light guide to a photomultiplier tube at one end of the PID [86]. Figure 3.10 shows a picture of the PID during a maintenance session.

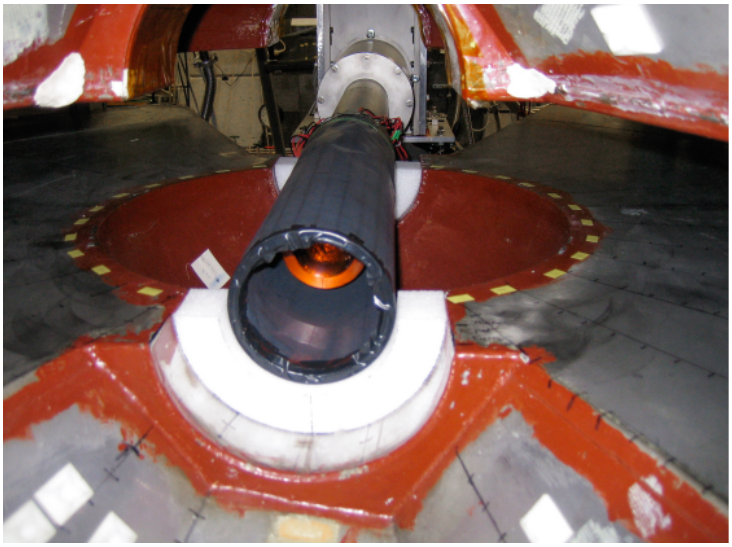

Figure 3.10: A picture of the particle identification detector [71].

The PID is used for the identification of charged particles in the Crystal Ball by employing the $\Delta E/dx$ technique. The energy loss of a particle as it traverses the PID is compared with the total energy that particle deposits in the Crystal Ball. Charged particles having similar kinetic energy but different masses tend to deposit different energies in the scintillator. Electrons and

charged pions deposit smaller fractions of their total energy in the scintillator as compared to protons. The PID takes advantage of this to differentiate between charged particles. A plot of the energy deposited in the PID as a function of the cluster energy in the Crystal Ball is shown in figure 3.11 .

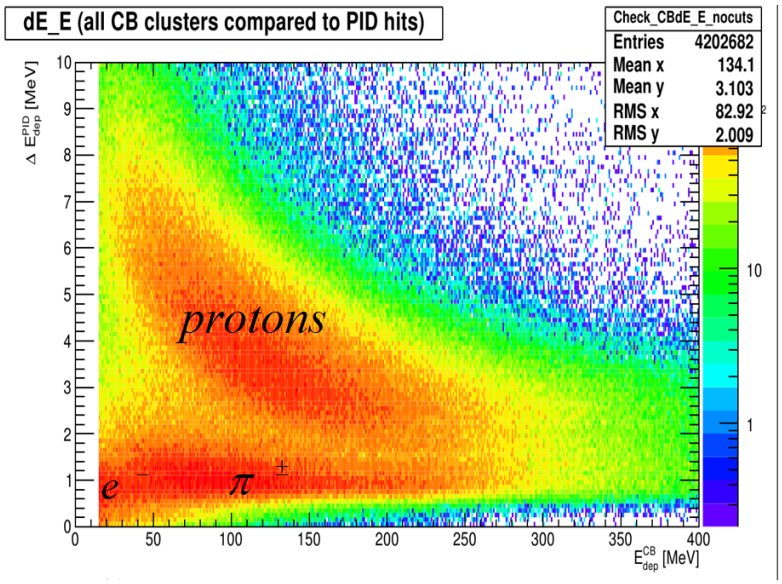

Figure 3.11: A $\Delta E - E$ plot of the particle identification detector showing how different charged particles deposit their energies. The top locus is the protons and the lower one is the charged pions.

3.3.3 Multi Wire Proportional Chambers (MWPC)

Due to the fact that a photon triggers several NaI crystals of the Crystal Ball, a weighted position method is used to retrieve information of the photons with a high resolution. However, this is not the case with the charged particles since they deposit their energy over only one or two crystals. Therefore, more precise information can be obtained by using two coaxial cylindrical MWPCs with cathode strip read out. The MWPCs [87, 88, 89] are gas filled enclosures, each consisting of a set of thin, equally spaced, anode wires sandwiched between two cathode planes as shown in figure 3.12a.

The cathodes are made from 1 mm thick cylindrical conductors covered with 25 μm Kapton foil and 0.1 μm thick aluminum coating on the external

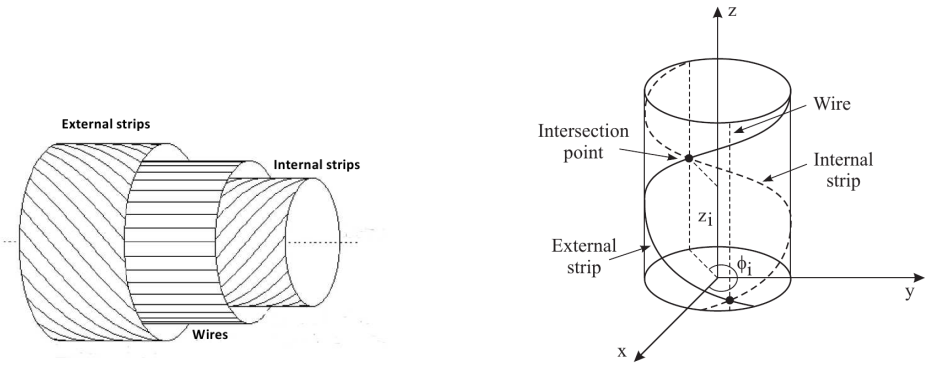

(a) (b)

Figure 3.12: MWPC diagram showing (a) position of the anode and cathodes and (b) the impact reconstruction of the charged particle trajectory in MWPCs [87].

surfaces of the chamber walls to enhance electrical screening. Both interior surfaces are laminated with 4 mm wide aluminum strips of 0.1 μm in thickness with a 0.5 mm gap between adjacent strips. At one of the cathode planes, the strip direction should be perpendicular to the anode wire direction to be able to determine the position of the avalanche in two dimensions. The cathode strips cross each other twice along the length of the chamber. Therefore, it is necessary to establish which anode wires has fired to identify the correct intersection point. Table 3.3 gives a summary of the MWPCs parameters used in this experiment.

MWPC	1	2
Length [mm]	560	560
Internal radius [mm]	70	90
External radius [mm]	78	98
Number of wires	232	296
Number of internal strips	69	89
Number of external strips	77	97

Table 3.3: The geometrical parameters of the MWPCs [87].

The MWPCs are filled with a gas mixture of 65.5% argon, 28% ethane 0.5% freon- CF_4 gases and 6% alcohol [90]. The mixture is a compromise

between charge multiplication and localization requirement imposed by the ionizing particle tracks [87]. A charged particle passing through the chamber will ionize the gas mixture leading to movement of the ionized electrons to the anode wires due to the potential difference between the anode and the cathodes. This creates an avalanche of electron-ion pairs through secondary ionization. The avalanche, which is collected on one or more wires, induces positive ions on both cathodes which in turn are accelerated to the cathodes.

Due to the center of gravity of the charge distribution induced on the cathode strips, the azimuthal angle ϕ and the longitudinal coordinate z of the impact point are evaluated. These values are defined in figure 3.12b. Once ϕ and z are known for each chamber, a straight line can be fitted through these coordinates and the polar angle θ and the azimuthal angle ϕ of the track can be determined by vertex reconstruction. The wire chambers used in this experiment have an angular coverage of $0^{\circ} - 360^{\circ}$ in azimuthal angle ϕ and $21^{\circ} - 159^{\circ}$ in polar angle θ which is 94% of 4π steradian coverage. In addition it has $\approx 2.4^{\circ} \cdot \sin\theta$ angular resolution in θ and $\approx 3^{\circ}$ in ϕ [87].

3.3.4 TAPS

To cover the downstream beam tunnel of the Crystal Ball, the Two Arms Photon Spectrometer (TAPS) [91, 92] calorimeter was installed. The TAPS is placed at the forward wall of the Crystal Ball $\approx$ 1.8 m from the center of the target, covering a polar region between 1° to 20°. It consists of 366 Barium Fluoride (BaF_2) crystals and 72 Lead Tungstate ($PbWO_4$) crystals [93, 94]. Figure 3.13 shows the wall of the TAPS detector with all six sectors and 438 elements.

Each BaF_2 crystal has a hexagonal shape with a front diameter of 5.9 cm, 22.5 cm (12 radiation lengths) long plus 2.5 cm of the cylindric end cap with a diameter of 5.4 cm. Charged pions can be stopped up to 185 MeV and protons up to 380 MeV. BaF_2 has a fast ($\tau \approx 0.9$ ns) and a slow ($\tau \approx 650$ ns) scintillation light component. The former provides a very good time resolution needed for time-of-flight measurements and allows particle identification, whereas the latter provides a good energy resolution because

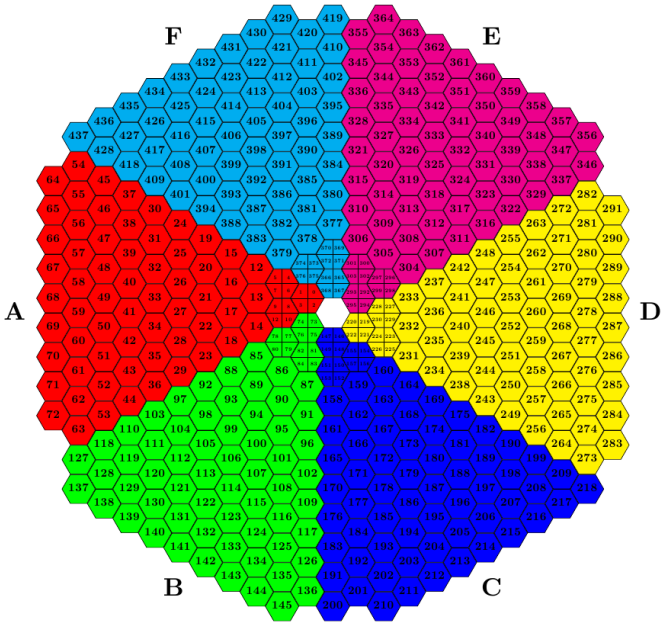

Figure 3.13: A rear view of the TAPS detector showing the six sectors and how the elements are numbered.

of the high light yield. To ensure that the BaF_2 crystals are light tight, each crystal is wrapped in 8 layers of 38 μm thick UV reflecting Teflon foil and one layer of 15 μm aluminum foil. Each crystal is connected to a photomultiplier tube of type Hamamatsu R2059-01 which is connected to electronics that record charge and timing information. Figure 3.14 shows a BaF_2 crystal coupled to a photomultiplier tube.

During the experiment, the signal from each BaF_2 crystal is split into seven parts. Four signals are sent to the charge to digital converters (QDCs). The fifth component is sent to a Constant Fraction Discriminator (CFD) while the remaining two are passed through the Leading Edge Discriminators (LEDs). If the threshold condition in the CFD is passed the TDC begins counting and is stopped by the experimental trigger.

The $PbWO_4$ crystals replaced 18 BaF_2 crystals of the inner two TAPS rings covering polar angles from 1° to 5°. This was to have a better handling of high intensity beams and improve angular resolution at smaller angles especially for fixed target experiments. The $PbWO_4$ crystals shown in figure

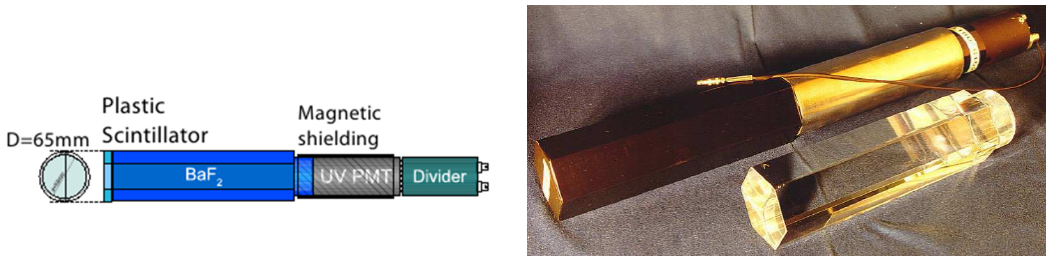

(a) (b)

Figure 3.14: Figure (a) is the schematic view of one BaF_2 module: crystal, photomultiplier tube, voltage divider and the plastic scintillator in front of the crystal [95] and (b) is a picture of a BaF_2 crystal before and after connected to a PMT [94].

3.15, have a trapezoidal shape so that a combination of four $PbWO_4$ crystals gives the geometry of one BaF_2 crystal, which allows an easy integration into the TAPS geometry [93, 94]. Each crystal measures 20 cm in length corresponding to 22.5 radiation lengths and has a 6 ns delay time. Each crystal is wrapped in 70 μm reflector foil VME 2000 with an additional layer of 20 μm aluminum foil to ensure that light stays within the crystal. Individual crystals are coupled to photonis XP 1911 photomultiplier tubes. The energy resolution of the TAPS calorimeter is expressed as $\Delta E/E =$

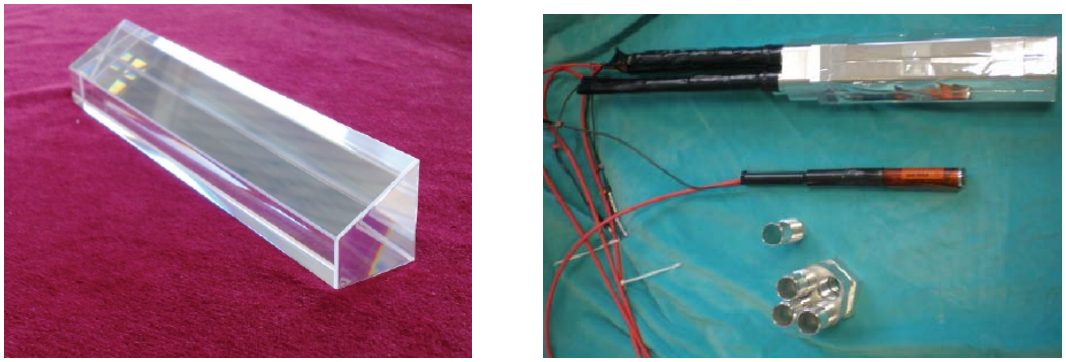

(a) (b)

Figure 3.15: 3.15a a picture of a $PbWO_4$ crystal and 3.15b a complete module of four $PbWO_4$ [94].

$0.018 + 0.008/(E(GeV))^{0.5}$. The angular resolution in polar angle θ is more than 1^{o} while in azimuthal angle ϕ it's better than $1/R$ radian, where R is

the distance in centimeters from the TAPS center to the point on the TAPS surface that corresponds to the θ angle [84].

In front of each BaF_2 crystal, and every group of four $PbWO_4$ crystals, a thin plastic scintillator is installed that is used for charged particle identification. Similar to the PID, a charged particle will deposit some portion of its energy in the scintillator before depositing its remaining energy in the calorimeter. Besides marking the event as charged, and possibly vetoing it, plotting $\Delta E - E$ allows for charged particle identification. The scintillators are made of 5 mm thick EJ-204 and have the same hexagonal shape as the face of the BaF_2 crystals as shown in figure 3.16. They are connected via BCF-92 wavelength shifting fibers to multi-anode photomultiplier tubes of the type Hamamatsu H6568 with 16 channels which allows for a direct correlation between a hit in a veto crystal and a hit in a $BaF_2/PbWO_4$ crystal [94]. The Veto detectors are held by a hexagonal frame that is placed infront of TAPS.

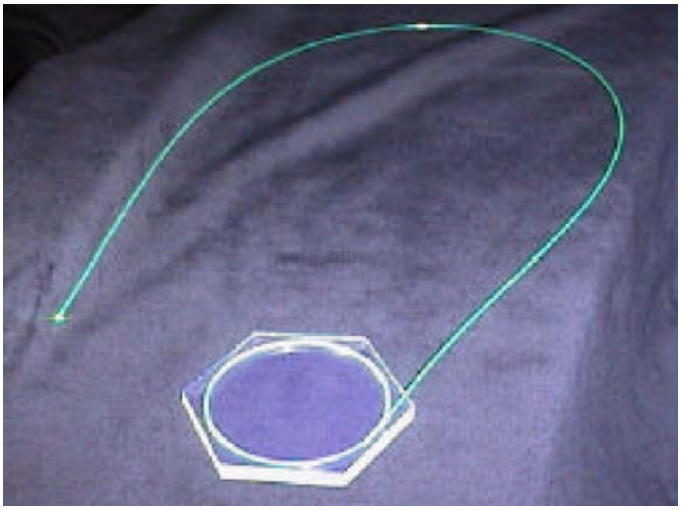

Figure 3.16: Picture of a veto plastic scintillator with the WLS-fiber embedded in a groove [94].

3.3.5 Cherenkov Detector

During the experiment, there is a large amount of background originating from electromagnetic reactions inside the target. Incoming photons interact with the target material possibly inducing pair production. The electrons and positrons produced are scattered by the Coulomb field of the atomic nuclei. This, as well as Compton scattering in the forward angles causes unnecessary triggers in the forward detectors. To suppress this background, a threshold Cherenkov detector [87, 96] was installed between the Crystal Ball and TAPS detectors. The detector covers polar angular region from 0^{o} to 18^{o}, where practically all electromagnetic events take place.

When a charged particle travels through a medium at a speed exceeding that of light in that medium, Cherenkov light is emitted. The direction under which this light is emitted is at a specific angle θ with respect to the direction of the particle. The angle depends on the particles speed v and the refractive index n of the traversed medium:

$$\cos\theta = \frac{1}{\beta n} \tag{3.12}$$

where $\beta = v/c$ with c as the speed of light in vacuum [87].

The refractive index n determines the speed of light in the material and hence, the threshold speed (c/n) for a particle to emit Cherenkov light. At the threshold $\beta_t = 1/n$, the Cherenkov effect occurs corresponding to Lorentz factor γ_t given as;

$$\gamma_t = \sqrt{\frac{1}{1-\beta_t^2}} = \sqrt{\frac{n^2}{n^2-1}}. \tag{3.13}$$

The threshold can be expressed as a function of the energy of the particle and its rest mass m_0 as;

$$E_t = \gamma_t \cdot (m_o c^2). \tag{3.14}$$

This shows that particles which are less massive have a lower energy threshold. Therefore, all particles exceeding their threshold energy are detected in the Cherenkov detector [96]. This makes it possible to suppress detector triggers of unwanted particles.

The main components of the Cherenkov detector used in this experiment include: a gas volume, a mirror and a photomultiplier tube (PMT). The gas volume is enclosed in a hermetically sealed aluminum casing which has an entrance and exit window on the front and back covers of the detector, respectively. Both windows consist of a mylar foil of 100 μm thickness and a TEDLAR-PVF foil which are light and gas tight. C_4F_8 gas is used as a Cherenkov radiator gas. It has a refractive index $n = 1.0013$ corresponding to an energy threshold of 10 MeV for electrons and 2.7 GeV for pions. In addition, the gas has a very good transparency for light in the ultra-violet (UV) range, where the Cherenkov radiation is emitted. Nitrogen gas is flushed into the detector before the radiator gas is filled to purge it of air and water vapor. The emitted Cherenkov light is collected and focused by a highly-reflective ellipsoidal mirror onto a photomultiplier tube. A Hamamatsu R1584-03 SEL photomultiplier tube, with a UV transparent entrance window and a peak quantum efficiency of 26% at 390 nm, is used [87, 96].

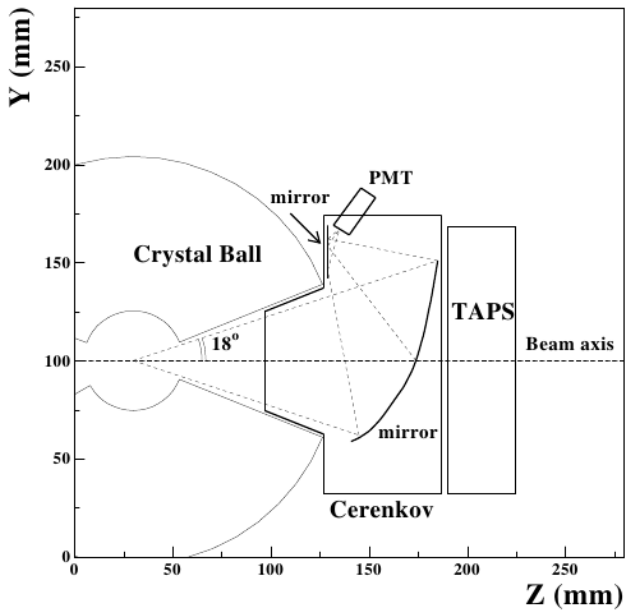

Figure 3.17: A schematic side view of the experimental setup including the Cherenkov detector [87].

The Cherenkov detector is designed in a way that it fits inside the down stream aperture of the Crystal Ball detector as shown in the schematic drawing of its geometry in figure 3.17. It has a volume of ≈ 1.3 m^3 and 70 cm light emission length along the beam direction. A black cloth was mounted inside the detector in order to avoid light from stray electrons reaching the mirror. To let the incoming photon pass through the mirror, a 5 cm diameter hole was made in the mirror and covered with a thin highly reflective mylar foil in order to avoid the loss of Cherenkov light. It has an efficiency of about 100% [87].

3.4 Experimental Trigger

In order to reduce the event rate and keep the dead time at a reasonable level during the experiment specific trigger conditions must be set. In this experiment, the total energy deposited in the Crystal Ball elements was used as a trigger condition for data readout. This is known as the energy sum trigger. The total energy in the Crystal Ball is calculated by summing up all analog signals from the photomultiplier tubes coupled to each NaI crystal. The summed analog signal is split into two parts; the first one is passed through a discriminator with set at low threshold. The second part is passed through a second discriminator set at a high threshold. The low threshold forms a first level trigger condition which initiates a trigger signal and inhibits the system from accepting more signals. The high threshold forms the final experimental trigger. If the energy sum signal passes the two thresholds, the information from all ADCs and TDCs in the detectors are read out and stored, after which the system is un-inhibited. If the energy sum signal passes the low threshold but not the high threshold, a "fast clear" signal is passed to all ADCs and TDCs. This resets the hardware and un-inhibits the system. The use of two thresholds instead of one gives a better timing resolution to the trigger. The overview of the experimental trigger and its components are presented in appendix A.2.

In the November 2013 beam-time, the low threshold was set to 48 mV and

the high threshold to 96 mV corresponding to an energy deposit of 20 MeV and 40 MeV, respectively. In the May 2014 beam-time, the low threshold was set to 48 mV and the high threshold to 200 mV corresponding to an energy deposit of 20 MeV and 90 MeV, respectively. The trigger rates with these energy sum settings were 1.5 kHz and 1.9 kHz for November 2013 and May 2014 beam-times, respectively. Figure 3.18 shows the energy sum for November 2013 and May 2014 beam-times.

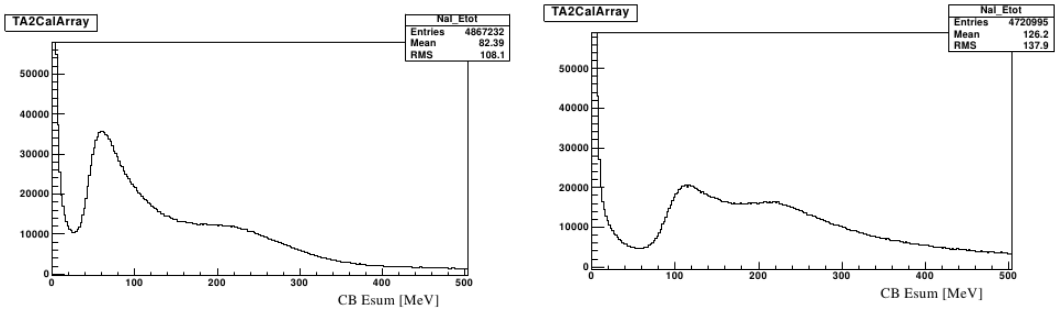

(a) (b)

Figure 3.18: Crystal Ball energy sum for November 2013 (3.18a) and May 2014 (3.18b) beam-times. High threshold energy sum is $E_{sum} \geq 40$ MeV and $E_{sum} \geq 90$ MeV for November 2013 and May 2014 beam-times, respectively.

3.5 Data Acquisition

Acqu a C++ based data acquisition framework is used for data readout. It consists of AcquDAQ and AcquRoot softwares. When a trigger condition is satisfied, the ADC and TDC information from all the detector elements is read out by AcquDAQ and AcquRoot is used to merge multiple data streams. AcquRoot is also used for offline analysis (see 5.1.1).

3.6 Beam-Times Summary

The data analyzed in this work was obtained in three beam-times. November 2013 and May 2014 used a butanol target while April 2014 and some part of November 2013 used a carbon target. Table 3.4 gives a summary of some important experimental parameters.

Parameter	**Nov 2013**	**April 2014**	**May 2014**
Electron Beam energy	1557 MeV	1557 MeV	1557 MeV
Electron beam current	3-6 nA	3-6 nA	3-6 nA
Electron Beam Polarization	78.63%	-	77.55%
Collimator	2 mm	2 mm	2 mm
Target Material	Butanol/Carbon	Carbon	Butanol
Target Length	2 cm	2 cm	2 cm
Average Target Polarization	63%	-	63%
Energy Sum	$>$ 40 MeV	$>$ 40 MeV	$>$ 90 MeV

Table 3.4: Overview of beam-time parameters.

Chapter 4

Frozen Spin Polarized Target

In this chapter, an overview of the polarized target will be presented. The theoretical background of the target polarization is described in section 4.1, the Mainz frozen spin polarized target in section 4.2 and the design and construction of an internal polarizing coil is presented in section 4.3.

4.1 Frozen Spin Target Polarization Principle

The energy levels of particles with spin S and magnetic moment μ split in magnetic field **B** into $2S+1$ sub-levels (Zeeman-effect). When such particles are placed in a high magnetic field and cooled to low temperatures they polarize. At thermal equilibrium the population of magnetic sub-levels is described by Boltzmann statistics as:

$$N_1 = N_2 \cdot exp\left(\frac{-\Delta E}{kT}\right) \tag{4.1}$$

where T is the temperature, k is the Boltzmann constant, $N_{1,2}$ are the corresponding population numbers of the magnetic sub-levels and $\Delta E = E_1 - E_2 = -\mu B$ is the energy difference between two sub-levels [97]. Here $\mu = g\mu_B$ where g is the g-factor and μ_B is the magnetic moment of the particle of interest. In thermal equilibrium the general form of the polarization degree

is given by the Brillouin function [98]

$$P_S = \frac{2S+1}{2S}\coth\left(\frac{2S+1}{2S}\frac{\mu BS}{kT}\right) - \frac{1}{2S}\coth\left(\frac{1}{2S}\frac{\mu BS}{kT}\right). \tag{4.2}$$

The degree of polarization for spin 1/2 (electrons and protons) and spin 1 (deuterons) particles is defined in:

$$P_{1/2} = \frac{N_+ - N_-}{N_+ + N_-} = tanh\left(\frac{\mu B}{2\kappa T}\right), \tag{4.3}$$

$$P_1 = \frac{N_+ - N_-}{N_+ + N_0 + N_-} = \frac{4tanh\left(\frac{\mu B}{2\kappa T}\right)}{3 + tanh^2\left(\frac{\mu B}{2\kappa T}\right)}. \tag{4.4}$$

Protons have a magnetic moment of $\mu_p = 5.0507866(17)\times10^{-27}J/T$ while that of deuteron is $\mu_d = 5.0507866(17)\times10^{-27}J/T$. The proton and deuteron g-factor are $g_p = 5.585694675(57)$ and $0.8574382329(92)$, respectively. Electrons have a magnetic moment and g-factor of $\mu_e = 92740.154(31)\times10^{-27}J/T$ and $g_e = 2.0023193043737(82)$, respectively. Due to the small magnetic moments of protons and deuterons compared to that of electrons, the degree of polarization for electrons is much higher than for protons and deuterons when exposed to the same conditions [99, 100]. From equation (4.2), it follows that, in a magnetic field of 2.5 T and a temperature of 1 K, electrons can be polarized up to 93% while protons reach a value of only 0.25% and deuterons less than 0.05%. To achieve a proton polarization of 47%, a magnetic field of 10 T and temperatures around 20 mK is required; with these conditions, the degree of polarization of deuterons is still only about 5% (Figure 4.1). This method of polarizing protons or deuterons is known as "brute force method".

Achieving reasonable proton polarization using this method is very difficult and expensive since high magnetic field and very low temperatures are necessary. In addition, the outgoing particles are affected by the high magnetic fields. Moreover, the build up time to obtain the final nuclear polarization under thermal equilibrium condition is of the order of several weeks due to the weak spin-lattice interaction[1]. To overcome these challenges, the

[1] *Spin-lattice interaction* is the interaction between a spin system and the lattice.

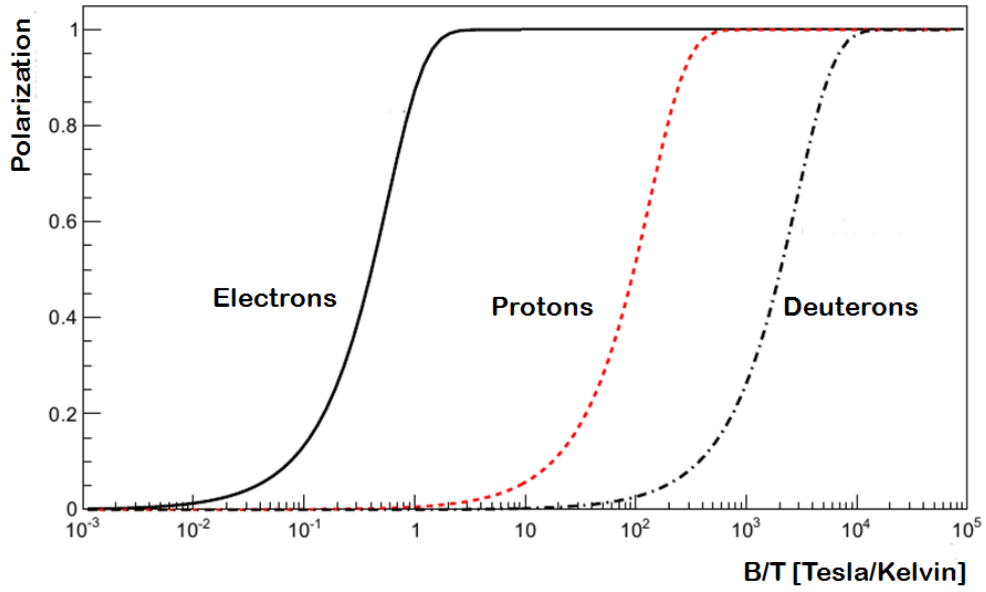

Figure 4.1: Degree of polarization as a function of magnetic field/temperature for electrons, protons and deuterons.

principle of Dynamic Nuclear Polarization (DNP) is used.

4.1.1 Dynamic Nuclear Polarization (DNP)

DNP was suggested by A W. Overhauser in 1953 [101] and was tested the same year by T R. Carver and C P. Slichter [102]. DNP takes advantage of good electron polarization and long proton relaxation time and uses external microwaves with the correct frequency to transfer the high electron polarization to the protons/deuterons. The electrons couple with the nucleons via dipole-dipole interactions to induce an electron-nucleon spin-flip transition and leave them with a fixed spin orientation. Four different states (figure 4.2 left) can be obtained depending on the spin combination of the particles:

$$\begin{aligned} |a\rangle &= |e\uparrow n\downarrow\rangle \\ |b\rangle &= |e\uparrow n\uparrow\rangle \\ |c\rangle &= |e\downarrow n\downarrow\rangle \\ |d\rangle &= |e\downarrow n\uparrow\rangle \end{aligned} \tag{4.5}$$

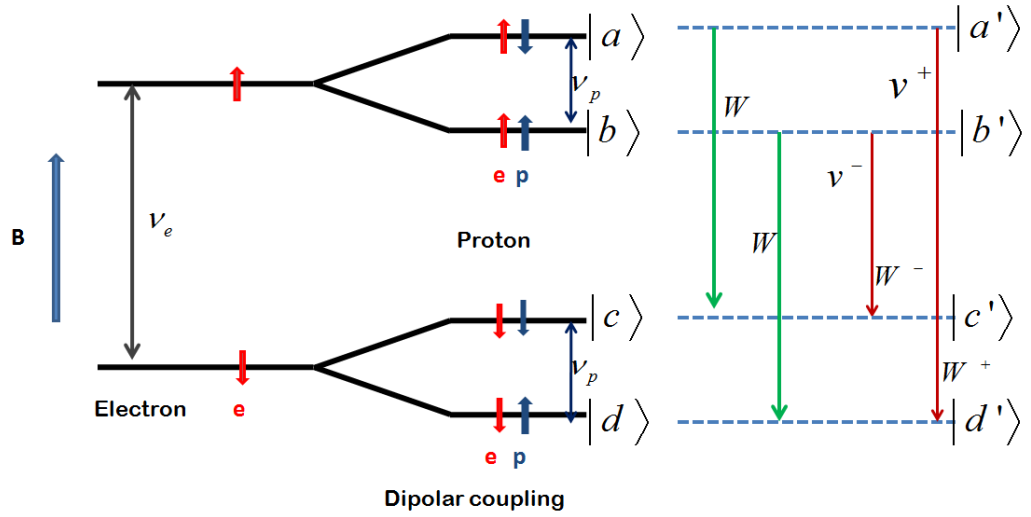

Figure 4.2: A schematic diagram of the energy levels of the coupled electron-nucleon system showing the spin flip transition when the microwave frequency ν^+ and ν^- are applied. $W^{\pm}$ and W are the probabilities of transition from one energy level to the other.

Taking into account the Zeeman effect, the selection rules for dipole radiation allows transitions in which only one spin flips at a time. This means that no double spin-flips are allowed. Therefore, for electron-nucleon spin coupling, the states in equation (4.5) can be written as linear combinations as:

$$\begin{aligned} |a'\rangle &= |e\uparrow n\downarrow\rangle + q|e\uparrow n\uparrow\rangle, \\ |b'\rangle &= |e\uparrow n\uparrow\rangle + q|e\uparrow n\downarrow\rangle, \\ |c'\rangle &= |e\downarrow n\downarrow\rangle + q|e\downarrow n\uparrow\rangle, \\ |d'\rangle &= |e\downarrow n\uparrow\rangle + q|e\downarrow n\downarrow\rangle \end{aligned} \tag{4.6}$$

with $q \approx 1\%$.

When the electron-proton system is irradiated with microwaves (discussed in 4.2.6) of frequency $\nu^+ = \nu_e + \nu_p$ (where ν_e and ν_e are the Larmor frequencies of the electron and the proton, respectively), a transition W^+ from $|a'\rangle$ to $|d'\rangle$ is induced as indicated in figure 4.2. The electron flips its orientation back in some milliseconds while the nucleon, at a temperature of about

300 mK and a magnetic field of 2.5 T, keeps it for several hours. The electron couples again with another nucleon and the process continues. By this, the polarization degree of the target material increases. Similarly, applying microwaves of frequency $\nu^- = \nu_e - \nu_p$, results in a transition W^- from $|b'\rangle$ to $|c'\rangle$. The transitions W^+ and W^- represent the two spin polarization orientations (positive and negative) of the target during this experiment [99].

To achieve a uniform transition, the target material has to be placed into a magnet with a field homogeneity better than 10^{-4} over the whole target sample, usually, a large superconducting solenoid magnet completely surrounding the target is used, which, however, strongly reduces the angular acceptance. To overcome the challenge of using a large magnet over the target, and to improve angular acceptance for observing scattered particles, the frozen-spin method was developed [103]. The principle of a frozen-spin target is as follows. Once the maximum polarization degree is achieved via the DNP process the microwaves are turned off. At this moment the temperature is driven down to about 50 mK (or below), where the spins become "frozen" and the relaxation time increases vastly. Then the field of the polarizing magnet is reduced and an internal holding coil keeps the magnetic field at about 0.5 T. The polarizing magnet is then removed and the detector is installed around the target for data taking.

4.2 Mainz Frozen Spin Target

Figure 4.3a shows a schematic diagram of the main components of the Mainz frozen spin target while figure 4.3b shows a picture of an assembled dilution refrigerator in the A2 experimental hall. It consist of the: dilution refrigerator, microwaves and Nuclear Magnetic Resonance (NMR) system, polarizing magnet, internal holding magnet, pumping and circulation system and control systems. A description of some of the components will be given in the following subsections.

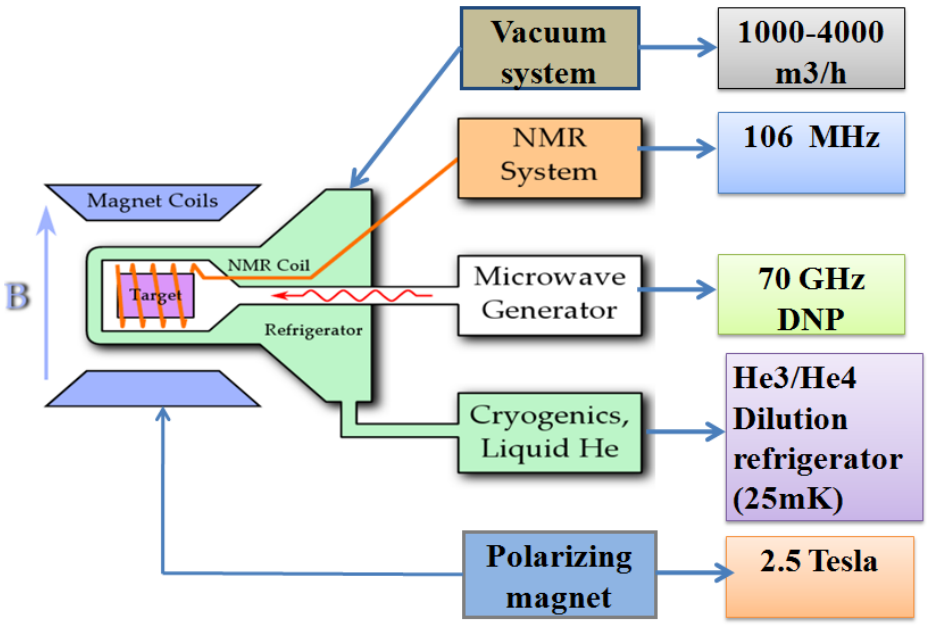

(a)

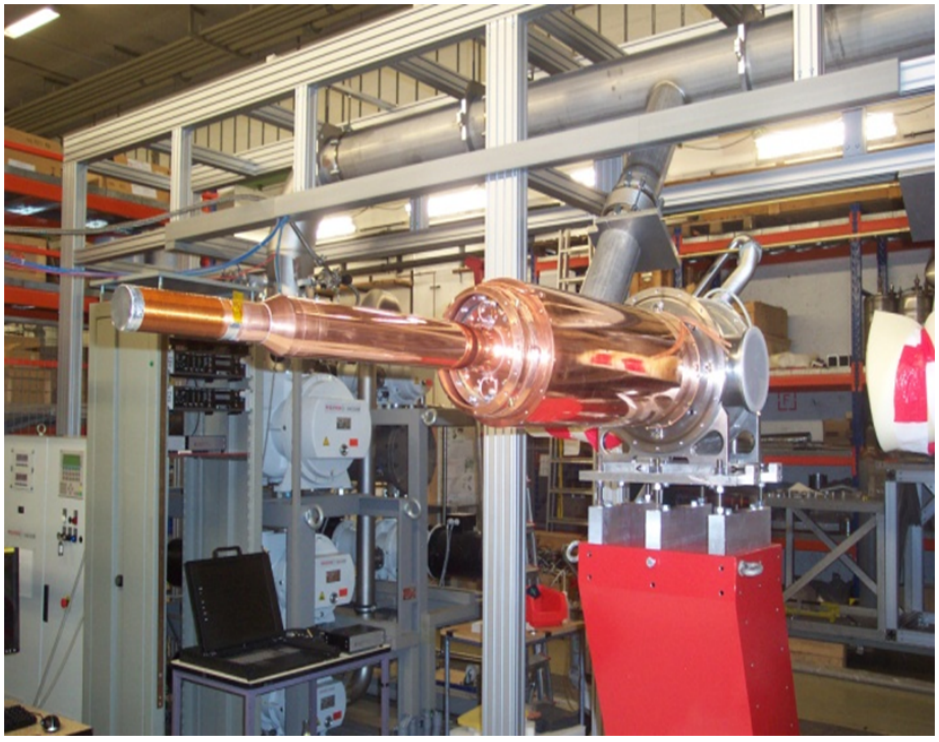

(b)

Figure 4.3: (a) is the schematic diagram showing main components of a frozen spin target and (b) is a picture of the Mainz frozen spin target.

4.2.1 Dilution Refrigerator

A central part of the frozen spin target apparatus is the ^{3}He/^{4}He dilution refrigerator. In order to fulfill the low temperature requirements and high cooling power in continuous operation, a horizontal refrigerator aligned along the direction of the photon beam is used. The Mainz frozen spin target dilution refrigerator was developed in close collaboration with the polarized target group of the Joint Institute for Nuclear Research (JINR) Dubna [104, 105, 106, 107, 108]. Figure 4.4 show a schematic view of the dilution refrigerator.

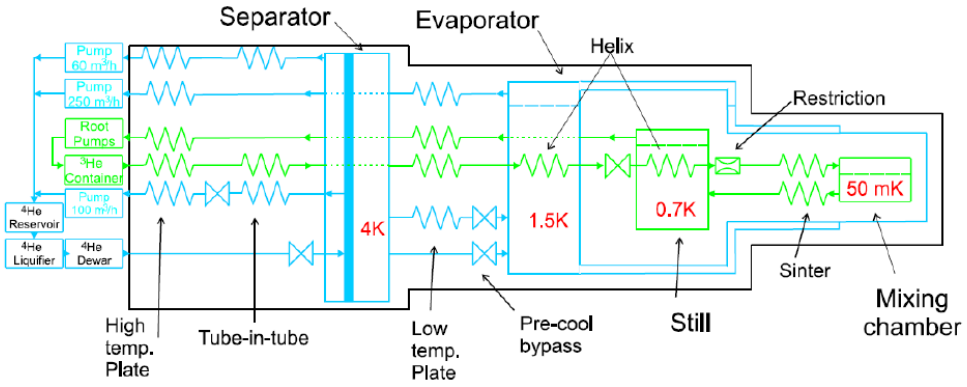

Figure 4.4: A schematic diagram of the dilution refrigerator showing its cooling stages [99].

The refrigerator has a total length of about 2 m and a diameter of 65 mm in the target area and 300 mm in the back part. To meet the requirement of a large thermal load in the DNP mode its cooling power at 200 mK is 10 mW. Cryogenic components are placed symmetrically around the beam tube which is a central part of the refrigerator. It operates by pumping helium through different stages, namely: the separator, evaporator, still and mixing chamber, in order to achieve the lowest temperature possible by forming a mixture of ^{3}He/^{4}He. Each part of the cryostat thermally isolates the subsequent inner stage. The outgoing vapor produced in the different parts is used as pre-cooling of the incoming gas by the employment of heat exchangers. Therefore, the mixture of helium is cooled from about 4 K in the separator

down to about 1.5 K in the evaporator, then to 0.7 K in the still, and finally to about 25 mK in the mixing chamber. Due to continuous circulation of the mixture of ^{3}He/^{4}He a constant temperature is maintained throughout the experiment. The refrigerator operates at a temperature of 25 mK with a high relaxation time of the order of 1000 hours for the target material in the frozen-spin mode. More details of the dilution refrigerator can be found in reference [99].

4.2.2 Target Materials

In this work a proton target material was used. An ideal proton target material would be molecular hydrogen, however, at low temperatures the transition from the ortho- to the para-state makes it impossible to polarize. Therefore, other materials have been developed for this purpose. A good polarized target material should have the following characteristics:

- short polarization build up time,
- high degree of polarization via dynamic nuclear polarization (DNP),
- high dilution factor (ratio of the number of polarizable free nucleons to the total number of nucleons),
- radiation hardness (necessary that the material does not considerably change its polarization properties during several days of irradiation with photon beam),
- long relaxation time,
- free from other polarizable nuclei,
- simple to handle and prepare

In this work a tempo doped butanol (C_4H_9OH) target (figure 4.5) was used. This is due to the fact that it has; a good dilution factor, high degree of polarization, long relaxation time and short polarization build up time. In addition, butanol is advantageous since the background nuclei, i.e., carbon and oxygen, are spin-less [109, 110]. The target is made of spherical beads, 2 mm in diameter which are filled in the target container (figure 4.7) measuring

2 cm in length by 2 cm in diameter. When the butanol beads are filled in the container they leave some spaces between them which lead to the loss of target volume. Thus a filling factor of $\approx 60.7 \pm 2.0\%$ needs to be used in analyses. The number of protons in the target is $9.18(56) \times 10^{22}$ $1/\mathrm{cm}^2$.

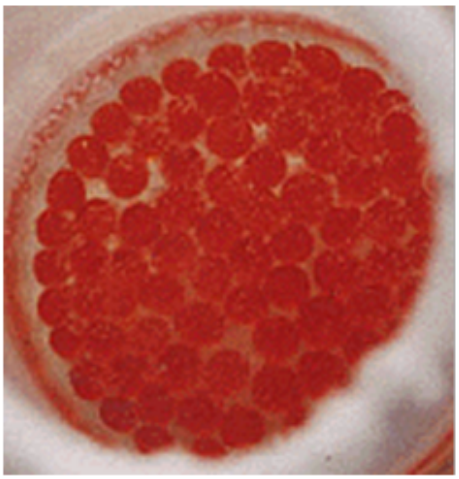

Figure 4.5: A picture of the tempo doped butanol target material.

Even though the carbon and oxygen nuclei in the butanol target are spinless, they are the main source of the background since they also participate in the reaction. Therefore, a separate data set was taken with a carbon target shown in figure 4.6 for the purpose of background subtraction. The total number of nucleons in the carbon target is approximately the same as the total number of ^{12}C and ^{16}O in the butanol target plus the ^{3}He/^{4}He mixture [111].

4.2.3 Insert

The target material (section 4.2.2) is placed in a cylindrical 6.28 cm^3 container made of Teflon. This container is mounted at the end of an insert (Figure 4.7) which allows the introduction of the target materials into the cold cryostat and to extract it at the end of the operation period. The insert also carries elements of the microwave and NMR systems, temperature

Figure 4.6: A picture of the carbon target material [111].

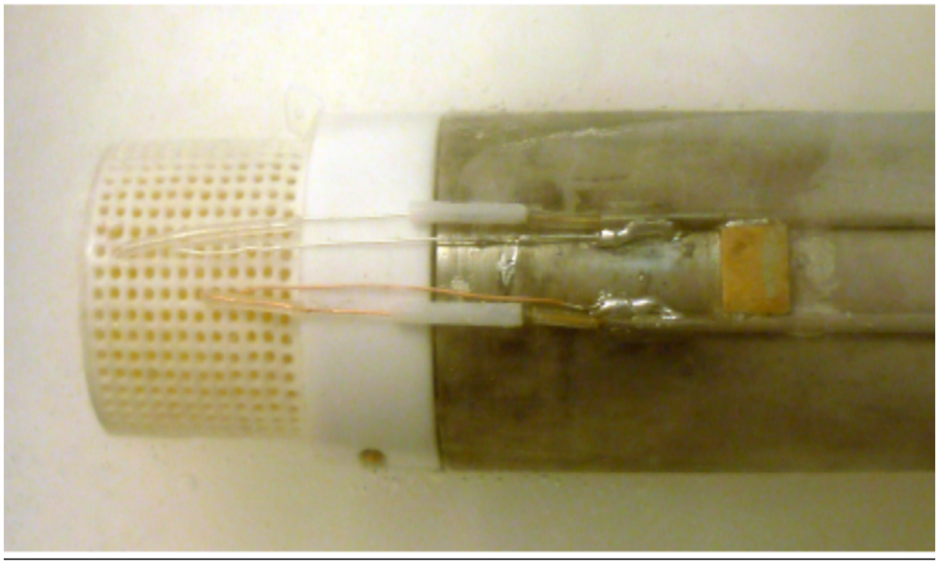

Figure 4.7: The target cell attached to the target insert with the NMR and microwave connections.

sensors, warm and cold vacuum seals, and radiation shields which minimize the heat load on the dilution stage by a room temperature radiation. In fact, the insert is one of the most complicated and important target elements which in many ways predetermines the physical and operational parameters of the frozen spin target.

4.2.4 Polarizing Magnet

In order to polarize the target material a superconducting magnet, capable of producing a magnetic field up to 5 T with a homogeneity $\leq 10^{-4}$, was used. A schematic view and the control system of the magnet is shown in Figure 4.8. A superconducting solenoid consists of a single block of multi-

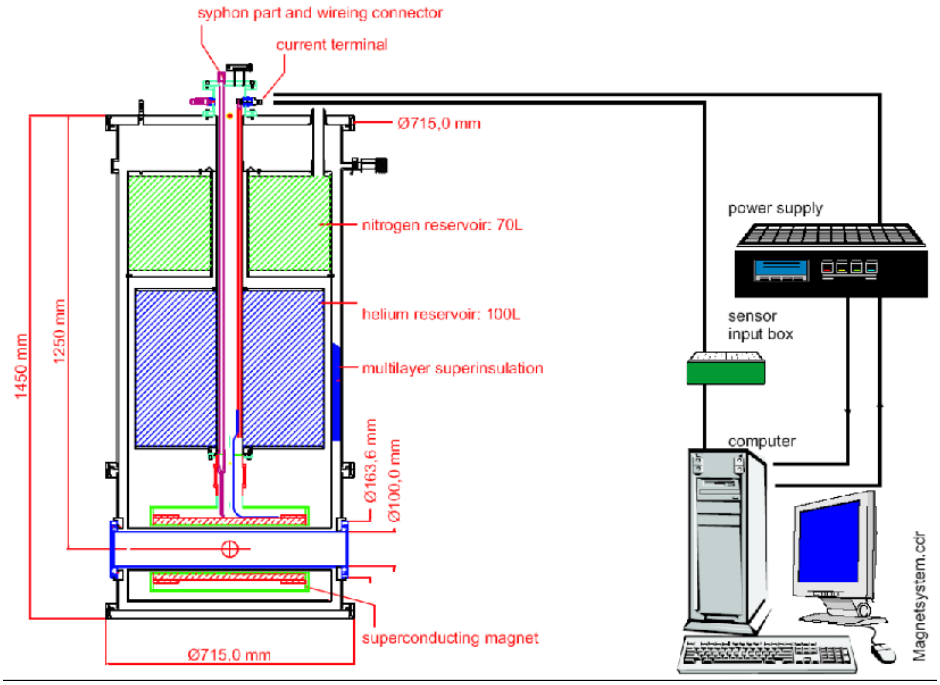

Figure 4.8: A schematic diagram of the polarizing magnet and its control system [112].

filamentary NbTi wire wound onto a stainless steel former. To prevent wire movements the conductor is cast in epoxy resin. The magnet cryostat contains a 70 L liquid nitrogen bath and a 100 L liquid helium bath. The magnet

cryostat has a 100 mm diameter warm bore which encloses the target material completely in the DNP mode. After switching to the frozen-spin mode the magnet is moved from the refrigerator in order to place the Crystal Ball detector in the data-taking position. The polarizing magnet and the detectors are mounted on a railway system which allows them to be placed into reproducible positions [99, 100].

The magnet control system was developed mainly by Cryogenic Limited. The power supply incorporates a sophisticated microprocessor unit, with all operations being monitored through the internal firmware. It is connected to a PC and is completely controlled by a LabView program. The ramping speed and maximum current can be set, and the induced magnetic field is continuously displayed. The temperature sensors and the helium level gauge are verified at any time by the program.

4.2.5 Internal Holding Magnet

A superconducting internal holding magnet placed inside the cryostat of the refrigerator maintains the target polarization in the frozen-spin mode when the external magnet is removed. In this work, a longitudinal internal holding superconducting magnet, shown in figure 4.9, was used. The holding magnet has a low magnetic field and is less homogeneous compared to the polarizing magnet. It is made of a multi-filament Nb-Ti wire type F54-1.35(0.20)TV of 0.227 mm in diameter. It has four layers with 600 turns per layer around a copper holder with a diameter of 48.0 mm and a length of 136 mm. In this work the holding coil was operated at a current of 36 A producing a magnetic field of 0.63 T.

The electrical current to the holding magnet is supplied via conductors refereed to as "current-leads". The current-leads are usually the main source of heat leaking into the dilution refrigerator. This heat leak largely determines the running cost of the magnet system, either in terms of coolant consumption or refrigerator power load. Therefore, caution must be taken when designing the current-lead system so that the Joule heating effect is as low as possible. The Joule heating effect depends on the ratio between the

Figure 4.9: A picture of the longitudinal internal holding superconducting coil.

length and the thickness of the wire and weakly on the material choice.

For the Mainz frozen spin target, the current-lead system consists of three types of conductors (copper, high and low temperature superconductors) at different stages. The copper-current leads are used from a temperature of 300 K down to around 70 K and a high temperature superconductor (HTS) from 70 K down to 4 K. From 4 K the HTS is connected to the low temperature superconductor (LTS) from the holding coil. The current-leads are guided directly through the isolation vacuum of the dilution refrigerator and are not in direct contact with any cryogenic liquid. They are cooled exclusively by thermal heat contact to the radiation shields of the dilution refrigerator. The copper lead is 57 cm long and has a cross section of 6 mm^2. The details on calculation and optimization of the current lead is in reference [100]. The HTS used is a multifilament TT-gold wire composed of BSCCO ceramic embedded in a Ag-Au matrix with an outer sheath of reinforced Ag-Au alloy. It is 4 mm wide and 0.25 mm thick. It can support currents up to 70 A and has a critical temperature around 100 K. Using this combination of conductors the heat conduction is significantly reduced in both copper and HTS segments, as well as the cold end heat load by a factor of 3-10

depending on the superconducting material used as compared to using normal conducting material like copper alone [113, 114, 115]. The HTS wire leads are then soldered to the LTS wire of the holding coil.

4.2.6 Microwave system

The microwave system was designed, tested and successfully used for the Mainz GDH experiment on the neutron. However, minor changes were made to suit the current frozen spin target setup [116]. Figure 4.10 shows a schematic picture of the microwave system used in this experiment. A Varactor IMPATT (IMPact ionization Avalanche Transit-Time) diode is used as a microwave source. It is able to deliver about 150 mW with a central frequency of 70 GHz (tunable around 200 MHz by an external power supply). This corresponds to the Larmor frequency of the electron in a magnetic field of 2.5 T. For a fast polarization build-up a microwave power of 2-3 mW/cm^3 is required which amounts to about 15 mW for a 6.28 cm^3 target. More details of the microwave system can be found in [116].

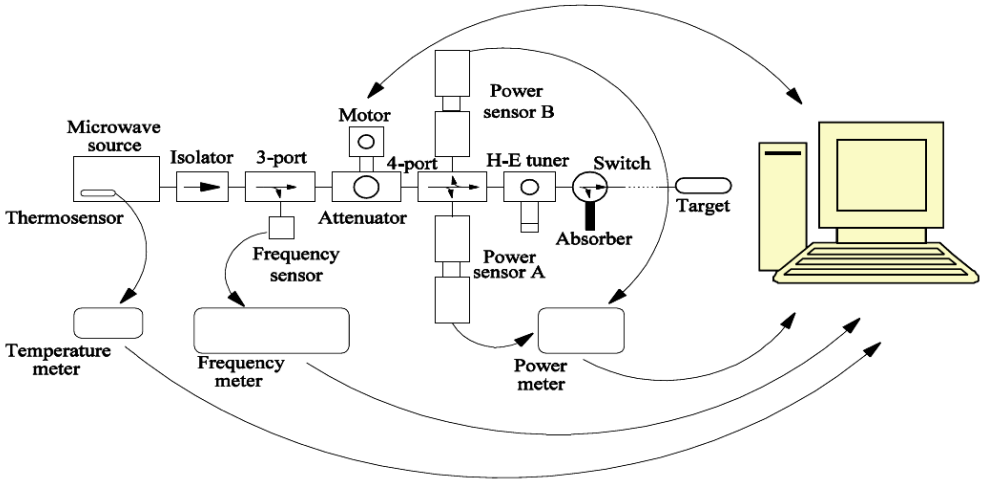

Figure 4.10: A schematic diagram of the microwave system [116].

In this experiment a microwave frequency of 70.04 GHz corresponding to the electron Larmor frequency at a temperature of 200 mK and a magnetic

field of 2.5 T was used. In addition, the proton Larmor frequency $\nu_p = \pm 106.4$ MHz was used. The target is polarized at 200 mK, after which the temperature is lowered to 25 mK ("spin frozen"), which is the operation mode during data taking. The target polarization can be oriented either in positive or negative direction by adding or subtracting the proton Larmor frequency from that of electrons ($\nu^{\pm} = \nu_e \pm \nu_p$ where ν_e and ν_p is the Larmor frequency of the electron and the proton, respectively).

4.2.7 NMR System for Polarization Measurement

The nuclear magnetic resonance technique can be used to measure the degree of polarization of a target material. The resonance frequency for the NMR circuit is adjusted to the Larmor frequency of the particle of interest. For protons this is typically 106 MHz at 2.5T. The main idea is to measure the probability of the transition shown in figure 4.2 and thus the degree of polarization.

When the target material is placed in an external magnetic field B, and irradiated with radio frequency (rf) energy at the Larmor frequency ω_L, the spins can absorb or emit this energy. The response of a spin system to rf irradiation is described by its magnetic susceptibility:

$$\chi(\omega) = \chi'(\omega) - i\chi''(\omega) \tag{4.7}$$

where the real part of the complex susceptibility (dispersion) χ' represents the resulting inductance, whereas the imaginary part (absorption) χ'' is determined by the energy exchange caused by the Zeeman transitions.

The spin polarization of the target material is given by the integral of the absorption function over the frequency ω:

$$P = \frac{2\hbar S}{g^2 \mu_N^2 \pi N} \int_0^{\infty} \frac{\omega_L \chi''}{\omega} d\omega \tag{4.8}$$

here S is the spin, g the g-factor, μ_N the nuclear magnetron, N the spin population and ω_L the Larmor frequency [110]. The absorption function is

measured by putting a coil of inductance L_c and resistance r_c around the target material. Through the inductive coupling between the spins and the coil, the impedance of the coil Z_c is given as:

$$Z_c = r_c + i\omega L_c(1 + 4\pi\eta\chi(\omega)) \tag{4.9}$$

where η is the effective filling factor of the target material in the coil.

The change of impedance is detected by a continuous wave, constant current Q-meter connected to a series LRC circuit as shown in figure 4.11. The LRC circuit consists of the NMR coil connected to the damping resistor

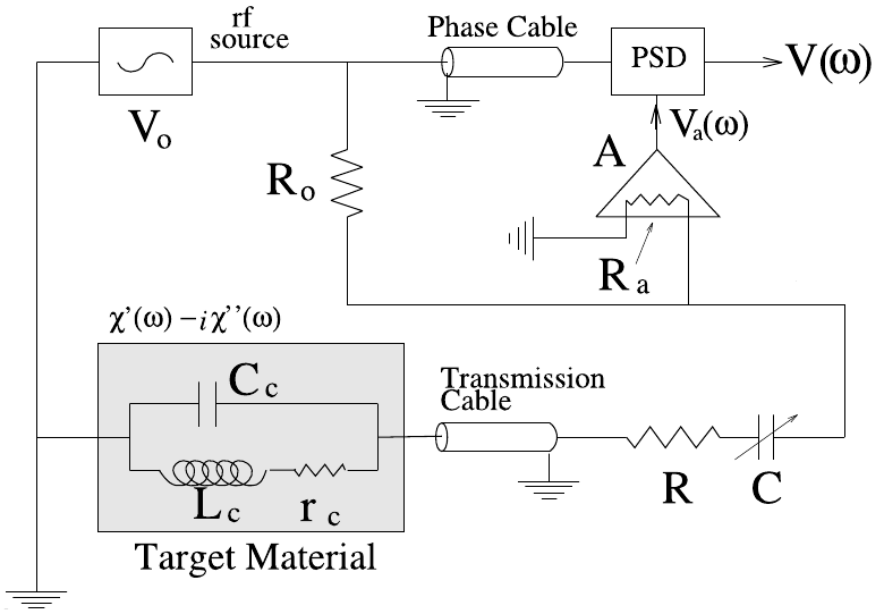

Figure 4.11: A schematic diagram of an NMR circuit [116].

R and the tuning capacitor C via a coaxial transmission line. A frequency synthesizer connected to the Q-meter sweeps the radio frequency ω over the values where $\chi(\omega)$ is non zero. A complex voltage $V(\omega, \chi)$, which is a function of Z_c, is generated if the current is constant. The voltage is a superposition of both the signal proportional to χ and the Q-curve (the response of the Q-meter to ω in the absence of χ). The last stage of the Q-meter selects the real part of the voltage by using the input rf signal as a reference. The Q-

curve is measured separately by changing the external magnetic field **B** such that ω_L is well outside the range of the frequency scan of the Q-meter [110]. In this case χ'' vanishes and χ' is negligible. The two signals are subtracted and the result is the NMR signal[2],

$$S(\omega) = Re\left[V(\omega,\chi) - V(\omega,0)\right] \propto \chi'' \propto P. \tag{4.10}$$

The degree of polarization in terms of the NMR signal is:

$$P = k\frac{\omega_L S(\omega)}{\omega}d\omega \tag{4.11}$$

where k is a constant that contains all the unknown frequency independent gains in the Q-meter. The proportional factor k for the polarization is obtained by a calibration measurement in thermal equilibrium (TE measurement) at a known temperature and magnetic field. Once k is known, the polarization can be calculated during the microwave pumping stage of the DNP. Figure 4.12 show a typical proton NMR signal obtained during a target polarization measurement.

In this work, the degree of polarization was measured in two steps. First, an NMR signal is taken at low temperature with a magnetic field of 2.3 T which is slightly different from that corresponding to the resonance. Secondly, the signal is taken at the polarization magnetic field of 2.5 T. The polarization signal is determined as the difference between the signal measured at 2.5 T, and the signal measured in step one (equation (4.10)). The degree of polarization is proportional to the area under the NMR signal. For calculation

[2]In this experiment, the NMR signal is obtained by a frequency sweep over the resonance Larmor frequency using a Rohde & Schwarz generator capable of producing frequencies from 5 kHz up to 1.5 GHz. In order to increase the signal to noise ratio many sweeps are accumulated (the noise reduces as a square root of the number of sweeps). Initially the NMR system with a so-called Liverpool Q-meter was used. However, the high frequency Liverpool NMR box is no longer commercially available, and it was replaced by Mini-circuits high frequency components. They create a circuit that amplifies the NMR signal and processes it (Figure 4.11). The processed signal goes via a PCI-68M I/O M-series board (National Instruments) to the computer, where it is read and analyzed.

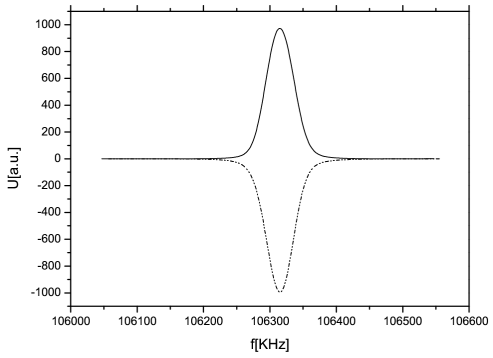

Figure 4.12: Proton NMR signal obtained during a target polarization measurement. The area under the signal is proportional to the degree of polarization.

of the polarization, the thermal equilibrium (TE) signal is used:

$$\frac{Polarization\ (DNP)}{Area\ Units\ (DNP)} = \frac{Polarization\ (TE)}{Area\ Units\ (TE)} \tag{4.12}$$

where the area unit in thermal equilibrium (TE) and in DNP are measured at the same magnetic field and temperature. The degree of polarization in TE is calculated from equation 4.3. Therefore, the degree of polarization in the DNP is:

$$Polarization\ (DNP) = Polarization\ (TE)\frac{Area\ Units\ (DNP)}{Area\ Units\ (TE)} \tag{4.13}$$

Target polarization measurements are not possible during data taking because the polarizing magnet and the Crystal Ball detector can not surround the target at the same time. Moreover, the magnetic field strength and homogeneity of the holding coil is not sufficient for a polarization measurement. Therefore, polarization is taken at the start and end of a data taking period for each target polarization orientation. During polarization measurement, a set of five values were measured from which an average value for the start and end degree of polarization P_i and P_f are calculated, respectively. The values are used in calculation of the relaxation time for each target polarization

orientation using:

$$P_f = P_i \times \exp^{\frac{-T}{\tau}} \tag{4.14}$$

where P_f is the polarization after a period of time t, P_i is the polarization at the start of data taking at time t_0, $T = t - t_0$ is the time difference and τ is the relaxation time. The degree of polarization before and after data taking and calculated values of the relaxation time for November 2013 and May 2014 beam-times are summarized in table 4.1.

Start Date	End Date	$P_i[\%]$	$P_f[\%]$	$\tau[hrs]$
16.11.13	25.11.13	63.00	59.25	3707
26.11.13	06.12.13	-64.49	-53.14	1223
20.05.14	28.05.14	-64.5	-54.17	1082

Table 4.1: Starting and ending values of target degree of polarization and relaxation times for November 2013 and May 2014 beam-times.

To calculate the degree of the target polarization for each run equation (4.14) and the parameters in table 4.1 were used. Each run was taken for a duration of between 30 to 60 minutes. Due to the long relaxation time the change in the degree of polarization within a file was negligible and the average value was used. The time t_{run} for each run was taken as the difference between the time when the file was recorded and the time when the starting polarization was measured. This was used to calculate the degree of polarization using:

$$P_{run} = P_i \times \exp^{\frac{-T_{run}}{\tau}}$$

where $T_{run} = t_{run} - t_0$. Figure 4.13 shows the target degree of polarization as a function of run number for November 2013 and May 2014 beam times. It's assumed that the degree of polarization decreases exponentially with time, meaning that each run has a different value of polarization depending on the time it was recorded. The drastic change in the polarization around run 800 in figure 4.13, corresponds to a period when no data was taken due to a technical problem with the accelerator.

The uncertainty in the degree of target polarization per run can be cal-

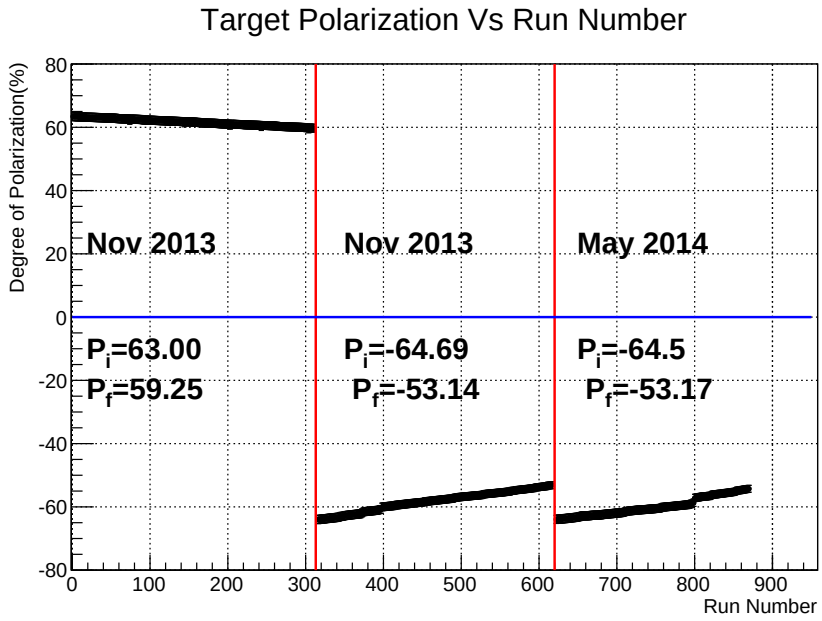

Figure 4.13: Degree of target polarization as a function of run number for November 2013 and May 2014 beam-times. The vertical red lines separate the different target polarization periods.

culated from combination of equations (4.14) and (4.2.7) to get:

$$P_{run} = P_i exp\left[\left(\frac{1}{T} ln \frac{P_f}{P_i}\right) T_{run}\right] \tag{4.15}$$

The uncertainty is basically a result of the error in the determination of P_i, P_f, the measurement of the duration of each polarization cycle T, and the time T_{run} in which the file was recorded. The error in T and T_{run} is negligible compared to the errors of P_i and P_f which is known to be 2% [117]. Therefore, the uncertainty in polarization for each run is given by:

$$\Delta P_{run} = \sqrt{\left(\frac{\partial P}{\partial P_i}\Delta P_i\right) + \left(\frac{\partial P}{\partial P_f}\Delta P_f\right)}$$

The error was determined to be $\approx 3\%$.

The low temperatures in the dilution refrigerator (4.2.1) and use of the internal holding magnet (4.2.5) allows for long periods of operation for the

frozen spin target. However, the target loses its polarization according to equation (4.14) resulting in a different degree of polarization at different times of the beam-time. In quest of tackling this challenge, an internal polarizing magnet (discussed in section 4.3) has been constructed. Unfortunately even though it was not finished in time to be used in the current experiment.

4.3 Internal Polarizing Magnet

As discussed in section 4.1, the development of the frozen spin target was proposed to solve the problem of using external holding magnets during experiments. This is because their large size and strong fringe field made them unsuitable for experiments where the detector components are placed close to the target. They were replaced with an internal holding superconducting magnet (see section 4.2.5) which can be used inside the cryostat and in combination with 4π detectors. Such coils have been developed and used in various labs: Electron Stretcher and accelerator (ESLA) [118] in Bonn, Jefferson lab (JLAB) [119] in the USA and Mainz Microtron (MAMI) [120] in Mainz.

The frozen spin target in Mainz operates at 25 mK (see 4.2.1) during data taking periods. This low operation temperature coupled with the holding magnet results in long relaxation times of $\approx$1000 hrs. However, this does not prevent the target from losing its polarization after a certain period of time. This results in data files with different degrees of target polarization depending on the time the file was recorded. Figure 4.14 shows a schematic diagram illustrating the process of target polarization and depolarization. At the start of a beam-time, the target is polarized via DNP to an initial maximum value P_i. After time t, the polarization decreases exponentially to a final value P_f such that $\Delta P = P_f - P_i$ (see section 4.2.7). At some point the detectors have to be moved in order to re-polarize the target. This leads to loss of beam time and detector positions are not perfectly reproduced. This results in an overall loss of efficiency during data taking. Therefore, using an internal polarizing magnet will provide an opportunity of having a constant

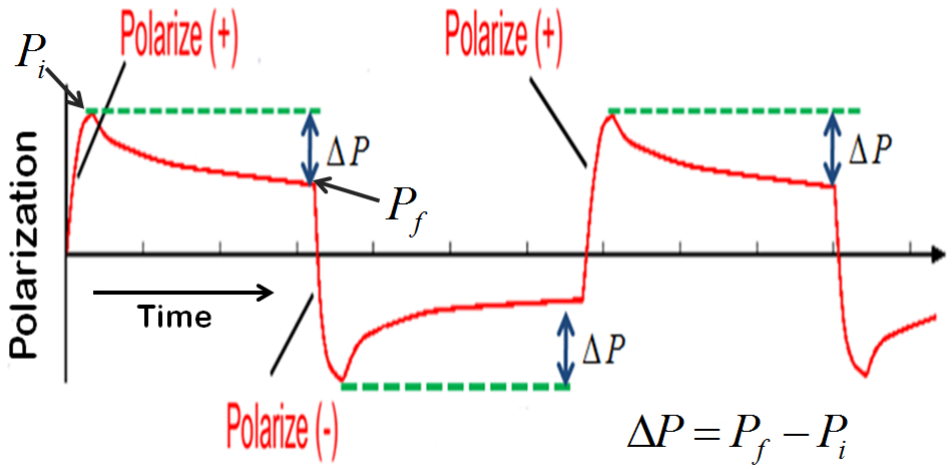

Figure 4.14: Schematic diagram showing polarization process during a standard data taking period.

target polarization ($P_i \approx P_f$) and minimize the detector movements during experiments.

In order to construct a good magnet, the choice of a good superconductor material which remain superconducting even at high current hence generating high magnetic fields is necessary. An example of such wire is niobium titanium (NbTi) which is made of niobium titanium filaments embedded in a copper matrix. It produces magnetic fields of up to 9 T at 4.2 K. In addition to high and homogeneous magnetic field, a choice of a simple and economical winding technique is important. Different winding and field homogeneity optimization methods for high magnetic field generation have been discussed in references [121] [122], [123] and [124]. They include: the use of Helmhotz doublet, notched coils and use of blind wires (plastic wires with a similar cross section area to the superconductor but carrying no current) at the center of the coil. The simplest method of producing fairly homogeneous fields is using the Helmholtz coils. However, due to its large size they are limited by cryogenics and detectors. On the other hand, notched coils can be used to generate a homogeneous field in a greater space around the center of the coil

than Helmholtz coils even though their winding technique is complicated. In this work, the design and construction of an outside notched coil with high and homogeneous field is presented. The notched coil was chosen so that the internal polarizing magnet is compatible with the current dilution refrigerator. The theory, design, construction, testing and the results of the coil will be described in subsections 4.3.1 through 4.3.5.

4.3.1 Magnetic Field Calculation of a Solenoid

Coil configurations of superconducting magnets with highly homogeneous magnetic fields in the central region has been discussed in references [125] and [126] where calculations of the magnetic field is based on power series of Legendre polynomials and error coefficients. The method described in reference [127] is used for the design of the internal polarizing coil in this work. It is based on superposition of magnetic fields of different sections of a notched solenoid. The magnetic field along the axis of the solenoid with a uniform current density is calculated using the Biot-Savart formula:

$$d\vec{B} = \frac{\mu_0}{4\pi}.\frac{Id\vec{l}\times\vec{r}}{r^3} \tag{4.16}$$

where I is the electric current, $d\vec{l}$ is the length element of the solenoid, μ_o is the permeability of free space and $r = \sqrt{a^2+z^2}$. Solving equation (4.16) for a simple solenoid of an internal radius a_1, external radius a_2 and length b, the magnetic field at the center is given as

$$B_z(0,0) = \mu_0 J a_1 F(\alpha,\beta) \tag{4.17}$$

where $F(\alpha,\beta) = \beta ln\left(\frac{\alpha+\sqrt{\alpha^2+\beta^2}}{1+\sqrt{1+\beta^2}}\right)$ is a field factor for a uniform current density coil, with $\alpha = \frac{a_2}{a_1}$, $\beta = \frac{b}{a_1}$ and J is the current density.

For an outside notched coil shown in figure 4.15, the magnetic field $\mathbf{B}(0,z)$ at a point z along the axis can be evaluated by dividing the coil into four notch-less coils with their cross-sections defined in 1 to 4:

1. ABDC(with $\alpha_1 = \frac{a_2}{a_1}$, $\beta_1 = \frac{b_1}{a_1}$ and $\gamma_1 = \frac{z}{a_1}$)

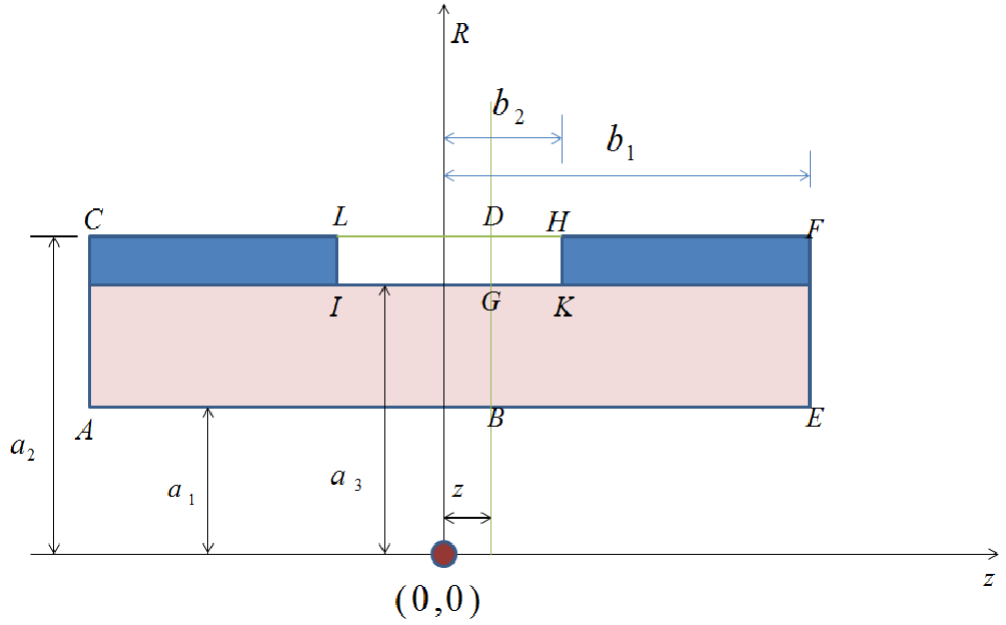

Figure 4.15: Schematic diagram for a notched coil.

2. BEFD(with $\alpha_1 = \frac{a_2}{a_1}$, $\beta_1 = \frac{b_1}{a_1}$ and $\gamma_1 = \frac{z}{a_1}$)

3. IGDL(with $\alpha_2 = \frac{a_2}{a_3}$, $\beta_2 = \frac{b_2}{a_3}$ and $\gamma_2 = \frac{z}{a_3}$)

4. GKHD(with $\alpha_2 = \frac{a_2}{a_3}$, $\beta_2 = \frac{b_2}{a_3}$ and $\gamma_2 = \frac{z}{a_3}$)

The magnetic field **B**(0,z) for solenoid 1, is half of the center field of a solenoid $2b = 2(b_1+z)$ long having the same values of a_1, a_2 and current density J. This is because the center field **B**(0,0) of a solenoid $2b$ long is the sum generated by one half of the solenoid (from 0 to $z = b$) and that generated by the second half (from $z = -b$ to 0). This implies that each half of the solenoid generates 50% of the total field at the center. Thus, using equation 4.17, the magnetic field for solenoid ABDC is expressed as:

$$B_z(0,z)_1 = \frac{1}{2} J a_1 F(\alpha_1, \beta_1 + \gamma_1). \tag{4.18}$$

In a similar way, the magnetic field for solenoid 2, 3, and 4 can be calculated. Therefore, using symmetry, the coil and superposition of the magnetic field of each solenoids, the total magnetic field for the notched solenoid at a point

z is:

$$\begin{aligned} B_z(0,z)_1 = \frac{1}{2}Ja_1 \left\{ ln\left(F(\alpha_1, \beta_1 + \gamma_1)\right) + ln\left(F(\alpha_1, \beta_1 - \gamma_1)\right)\right\} \\ -\frac{1}{2}Ja_3 \left\{ ln\left(F(\alpha_2, \beta_2 + \gamma_2)\right) + ln\left(F(\alpha_2, \beta_2 - \gamma_2)\right)\right\}. \end{aligned} \tag{4.19}$$

The negative sign in equation (4.19) is due to the fact that the current in solenoid 3 and 4 is in opposite direction to that in 1 and 2.

The magnetic energy of the solenoid was calculated using:

$$E = \frac{1}{2}LI^2 \tag{4.20}$$

where I is the current and L is the inductance of the coil. For a multilayer coil, inductance is calculated as the sum of coil self inductance and mutual inductance between them as discussed in [128];

$$\begin{aligned} L = 4\pi m n^2 \left\{ \frac{2a_o^4 + a_o l^2}{\sqrt{4a_o^2 + l^2}} - \frac{\delta a_o^3}{3\pi} \right\} + 8\pi^2 n^2 \left[(m-1)a_1^2 + (m-2)a_2^2 + \dots \right] \\ \left(\sqrt{a_1^2 + l^2} - \frac{7}{8}a_1 \right) + 4\pi^2 n^2 \left[m(m-1)a_1^2 + \dots \right] \left(\frac{a_1 \delta a}{\sqrt{a_1^2 + l^2}} - \delta a \right) \end{aligned} \tag{4.21}$$

where $n = N/l$ is the number of turns per unit length, a_0 is the internal radius, $a_1, a_2 \dots a_m$ is the radius of the m^{th} layer, l is the length of the coil, m is the number of layers and δa is the distance between two consecutive layers.

4.3.2 Magnet Design

The internal polarizing coil was designed to be used in the Mainz frozen spin target for nucleon polarization. Currently the dynamic nuclear polarization (DNP) method is used to polarize the nucleon using microwaves of 70 GHz corresponding to the Larmor frequency of electrons at 2.5 T (discussed in section 4.2.4 and 4.2.6). Therefore, the designed coil should be capable

of attaining a high magnetic field of 2.5 T which is equivalent to that of currently used external superconducting magnet. In addition, the magnetic field should be highly homogeneous since inhomogeneous fields result in non-uniform and low polarization of the target. The main objective was to design and construct a coil which has a high magnetic field of 2.5 T, high homogeneity in the target region of $\leq 10^{-4}$ and thin enough to allow particles to punch through. The target cell measures 20 mm in diameter and 20 mm in length. The volume covered by the target cell (target volume) will be the area of interest in our design. The magnetic field homogeneity in this volume is defined as:

$$Homogeneity = \left|\frac{\Delta B}{B_0}\right| = \frac{B(0,0) - B(r,z)}{B(0,0)} \tag{4.22}$$

where $B(0,0)$ is the magnetic field at the center of the coil and $B(r,z)$ is the magnetic field at any other point (r,z) in the target volume.

Parameter	Simple Solenoid	Notched solenoid
Inner radius(a_1)	24 mm	24 mm
Outer radius (a_2)	26.27 mm	26.72 mm
Notch radius (a_3)	-	26.27 mm
Coil length ($2b_1$)	136 mm	136 mm
Notch length ($2b_2$)	-	78 mm
Wire diameter(bare)	0.200 mm	0.200 mm
Wire diameter(insulated)	0.227 mm	0.227 mm
Current	46 A	46 A
Number of layers	10	10
Number of layers plus correction	-	12

Table 4.2: Internal polarizing coil parameters when uncorrected and corrected. Parameter definitions are as in figure 4.16.

The best coil parameters summarized in table 4.2 were determined from simulations. A 2D finite element method magnetics (FEMM) program [129] was used for this purpose. The magnetic field homogeneity of 5.37×10^{-3} and field strength of 2.5 T was attainable with a 10 layer simple solenoid at a current of 46 A. As expected, the axial field decreases along the axis while it increases in the radial direction as shown, in magenta, in figures 4.17a and

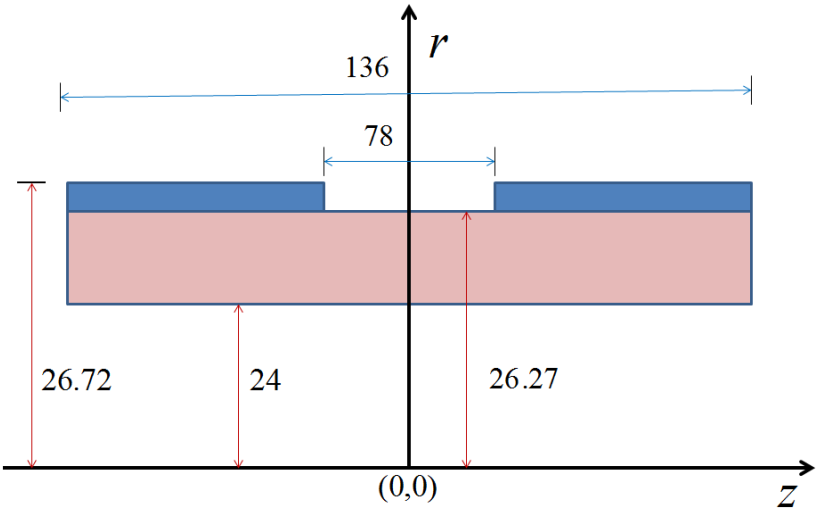

Figure 4.16: A schematic diagram showing the notched coil dimensions with a notch with of 78 mm. All dimensions are in mm.

4.18a, respectively. However, the magnetic homogeneity did not meet our requirement and had to be improved by creating a symmetric notch with an additional two layers.

To attain magnetic field homogeneity in the target volume, equation 4.22 was used to calculate homogeneity for coils with different notches at three different positions in the target volume. The homogeneity as a function of notch length for the three positions was plotted as shown in figure 4.19. The best magnetic field homogeneity of 5.9×10^{-5} was attained at a notch of 78 mm for the three positions. After the correction, the peak of the field in both axial (4.17a in blue) and radial directions (4.18a in blue) were flattened, hence increasing the homogeneity at the target region. Figures 4.17b and 4.18b show a zoom out of the magnetic field in the target region. Since this has shown a very good homogeneity of the magnetic field in the target volume, this notch width was used for the construction of the polarizing magnet.

In addition to the magnetic field strength and homogeneity, the coil thickness was another important condition considered since it affects the number of particles reaching the detectors. In order to compare different geometries,

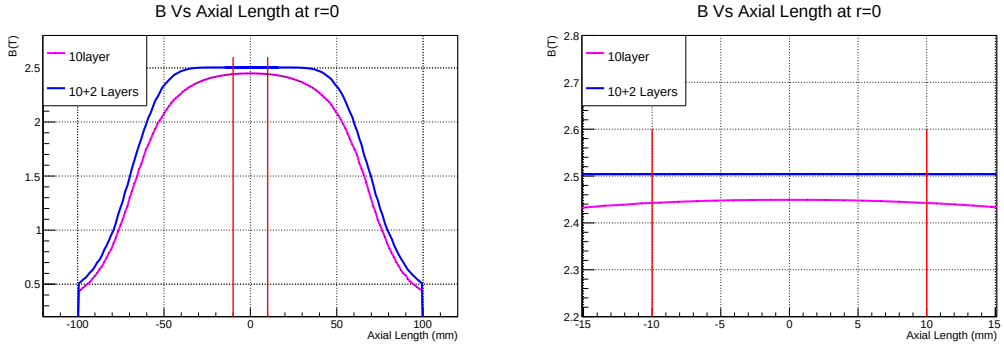

(a) (b)

Figure 4.17: Axial magnetic field as a function of axial length for a simple 10 layer coil in magenta and a notched coil in blue. (b) is the zoom out of (a) at the target region indicated by the vertical red lines.

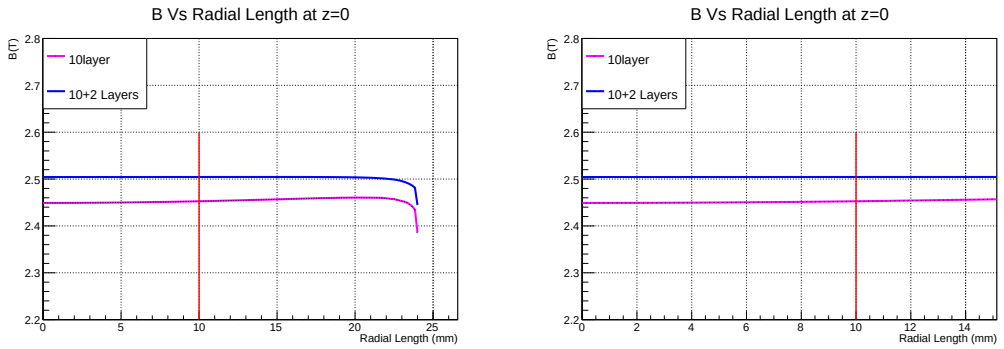

(a) (b)

Figure 4.18: Radial magnetic field as function of radial length for a simple 10 layer coil in magenta and a notched coil in blue. (b) is the zoom out of (a) at the target region indicated by the vertical red line.

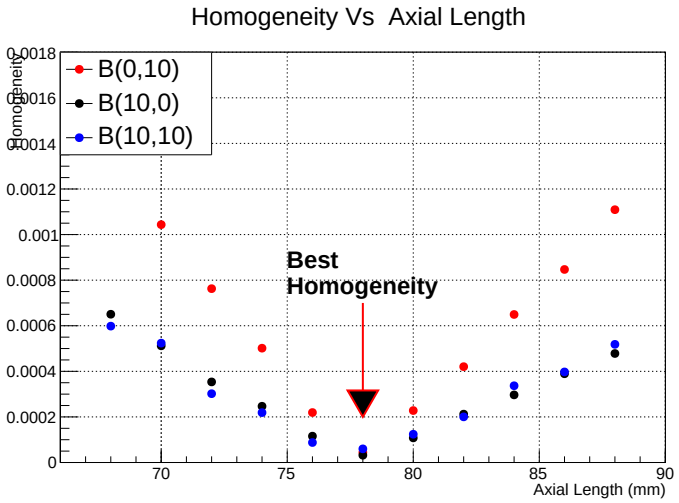

Figure 4.19: Homogeneity as a function of notch length. Three points in the target volume were considered in order of B(z,r): B(0,10), B(10,0) and B(10,10).

a calculation of the radiation length of the materials was done using:

$$X_0 = \frac{716.4}{Z(Z-1)ln\frac{287}{\sqrt{Z}}} g/cm^2 \tag{4.23}$$

where Z is the atomic mass of the material. The values of material density and radiation length is adopted from the Particle Data Group website [130]. The coil is made of a massive copper holder to provide good mechanical strength and thermal conduction, a thin niobium titanium superconductor (discussed in section 4.3.3) and epoxy for holding the wires together. Therefore, the number of radiation lengths for the complete coil was calculated by the sum of all the number of radiation lengths of all the materials used. The thickness of the niobium titanium used to make the coil, the coil holder and epoxy results in a total thickness of 2.7 mm which is approximately 24.55% radiation lengths. Table 4.3 summarizes the values of the radiation length of the materials used to construct the magnet.

Material	X_o (mm)	Thickness X (mm)	$\frac{X}{X_o}(\%)$
Copper	14.28	1.85	12.95
Niobium Titanium	19.21	2.2	11.45
Epoxy	387	0.6	0.15
Total			24.55

Table 4.3: A summary of the calculated radiation lengths of the material used in the construction of the internal polarizing magnet.

4.3.3 Magnet Construction

In order to fulfill the design conditions, construction materials had to be chosen carefully. In consideration of having a thin coil, a 200 μm multi-filament Niobium titanium (NbTi) superconducting wire[3] was chosen. Its characteristic parameters specified by the manufacturer are: alloy composition of Nb-47wt%Ti, 54 niobium-titanium filament embedded in a copper matrix and critical current at different magnetic fields at 4.2 K as shown in table 4.4.

Magnetic Field(B)	I_c (A)
1	60
2	45
3	38
4	34
5	29

Table 4.4: NbTi (Nb-47wt%Ti) critical current values at different magnetic fields.

Epoxy adhesive Araldite CY 221[4], a bisphenol-A epoxy resin with a viscosity of 300-500 cPs at 25^0C and Aradur HY 2954 BD[5] amine hardener with a viscosity of 70-120 cPs at the same temperature were used. The epoxy was prepared by mixing the resin and the hardener in the ratio 100:25 parts by weight(pbw). During the mixing process, the mixture was put in a vacuum chamber and evacuated in order to remove the air bubbles. The gluing was

[3]Bruker EAS GmbH -Hanau
[4]T-E- Klebetechnick Hannover
[5]Huntsman Advanced materials Belgium

done by wet winding after which the coil was allowed to rotate on a motor to allow for uniform drying of the epoxy.

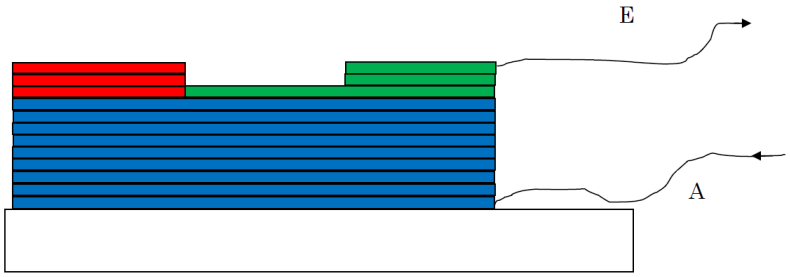

Figure 4.20: Schematic diagram showing how the coil is supposed to be wound to avoid wire crossing at the notch.

The greatest challenge during design was the choice of the best coil winding technique during construction to avoid a wire passing through the notch, as this affects the magnetic field homogeneity. Additionally, an even number of layers was chosen to make sure that the current input and output leads are on the same side of the coil. Since the coil has ten and two correction layers as shown in figure 4.20, the winding was done as follows:

(i) the first nine layers (in blue) were wound first to completion,

(ii) the 10^{th}, 11^{th} and 12^{th} layers (in red) were wound up to where the correction point starts,

(iii) the 10^{th} layer (in green) was completed and allowed to dry, and,

(iv) the remaining part of the 11^{th} and 12^{th} layers (in green) on the right side of the coil were wound.

In all winding steps the coil was glued and allowed to rotate on a motor for 48 hrs for the epoxy to dry uniformly to avoid an inhomogeneous epoxy geometry due to drops of glue at the lower part of the coil. After the epoxy

was tested and the coil winding technique chosen, Jelonnek Transformatoren und Wickelgut GmbH [6] was contracted to construct the coil, as they have better winding machines compared to what we have in our laboratory and they are more experienced in winding complicated magnets. Figure 4.21 shows a picture of the completed internal polarizing coil. Table 4.5 shows the deviation of actual number of turns per layer compared to the calculated turns per layer. The actual number of turns of the coil are $\approx 4\%$ less than the calculated. The difference may be a result of production imperfections (discussed in section 4.3.4).

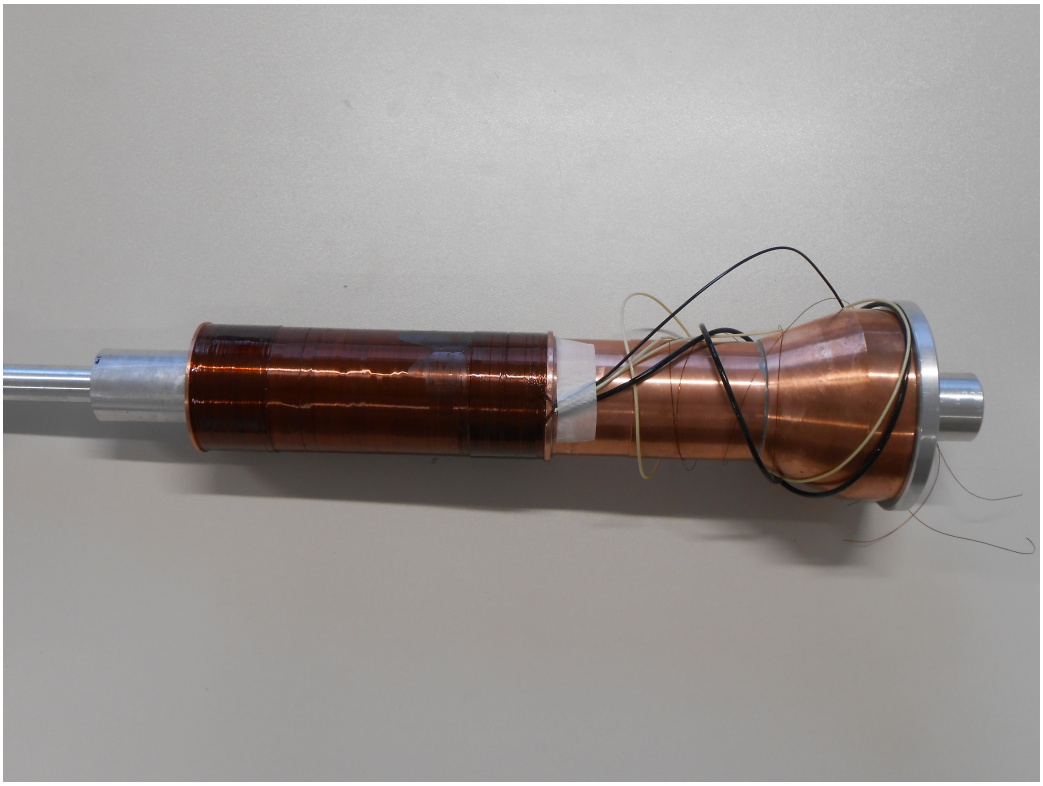

Figure 4.21: A picture of the completed internal superconducting polarizing magnet.

[6] Roechlingstraße 7 73447 Oberkochen

Layer	Calculated turns	Actual turns
1	595	576
2	595	572
3	595	572
4	595	571
5	595	573
6	595	570
7	595	571
8	595	568
9	595	556
10	595	564
11	252	239
12	252	235
Total	6454	6167

Table 4.5: Comparison of calculated to actual number of turns in the coil. The actual number of turns are 4% less than the calculated.

4.3.4 Magnet Testing

The internal polarizing coil was tested in a liquid helium dewar at a temperature of 4.2 K. An insert made of stainless steel was used to suspend the coil in the dewar. A carbon pipe fitted to the Hall probe holder was used to move the Hall probes longitudinally while in fixed positions in the radial direction. This enabled measurements to be performed at a distance of ± 70 mm longitudinally and ± 14 mm in the radial direction. Further measurements in the radial direction were not possible due to limitations of the coil holder and the adapter. Figure 4.22 shows the Hall probes, the coil fixed on the adapter and the carbon pipe for moving the Hall probes. Figure 4.23 shows the adapter inside the helium dewar during coil testing.

The input and output current-leads for the Hall probes were passed through the carbon pipe. Two Hall probes of the type HGCA -3020[7] were used to measure axial and radial magnetic field. The characteristics of the Hall probes were: a mean load sensitivity of 0.827 mv/kG at 298 K, nominal current of 100 mA and an offset voltage of 3.1 μV. The Hall probes

[7]Cryophysics GmbH Darmstadt, Germany

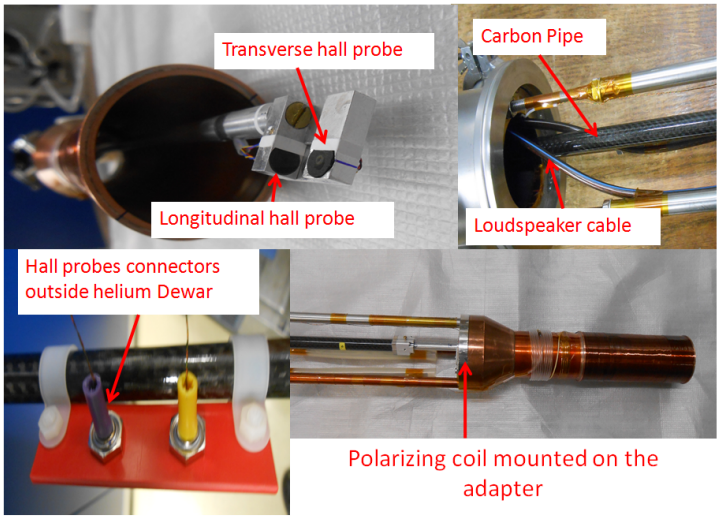

Figure 4.22: The magnet test setup pieces: adapter, coil, carbon pipe and Hall probes.

were operated at the nominal current throughout the test. The final value of measured magnetic field was calculated as $B = \sqrt{B_z^2 + B_r^2}$.

To prevent the Hall probes from moving, they were each fixed in a hole on the holder (4.22) as described in the manufacturer's manual [131]. Two thermo-resistors (Pt 100 and Carbon resistor) were placed on top of the coil holder to monitor the temperature during the experiment. The resistance was constant throughout the measurement period which is an indication of stable temperature in the dewar. Helium was filled in the dewar up to a height of 45 cm, 12 cm more than the total length of the coil and the holder. This served as a reserve in case of a quench and ensured that the temperature of the coil was at 4.2 K throughout the measurement.

After helium was filled to the required level and the pressure in the dewar had stabilized, a test on the maximum current attainable was performed. In this case, the Hall probe was held at the center of the coil and the current was ramped up at an interval of 1 A up to 45 A, at which point quench occurred. This measurement was repeated twice and the same value of current was attained. In addition, the current was ramped down at similar intervals to test the possibility of magnetic hysteresis. The results were compared

Figure 4.23: The internal polarizing magnet test setup.

with calculated values as shown in figure 4.24a. In both cases, a linear relationship between current and magnetic field, as expected, was observed and no hysteresis effects were observed.

After the linearity of field versus current was established, the current was held constant at 25 A and the Hall probes moved along the axis at different radial positions. The current of 25 A was chosen because the current-leads were heating up at higher currents. However, in the standard experimental setup, the coil will be mounted in the ^{3}He/^{4}He-dilution refrigerator of the frozen spin target which has specially designed current leads to carry high current (to maximum current $I_{max} = 70$ A). The measurements were taken in steps of 5 mm starting from the center of the coil to ±70 mm to ensure that the full length of the coil is mapped. This was done along the axis at different fixed radial positions *(z,0)*, *(z,7.6)* and *(z,14)*. The results are presented in figures 4.24b, 4.25a and 4.25b, respectively in comparison to calculations. The magnetic field at the center of the coil is flat as expected

and then decreases as the Hall probe is moved further from the center.

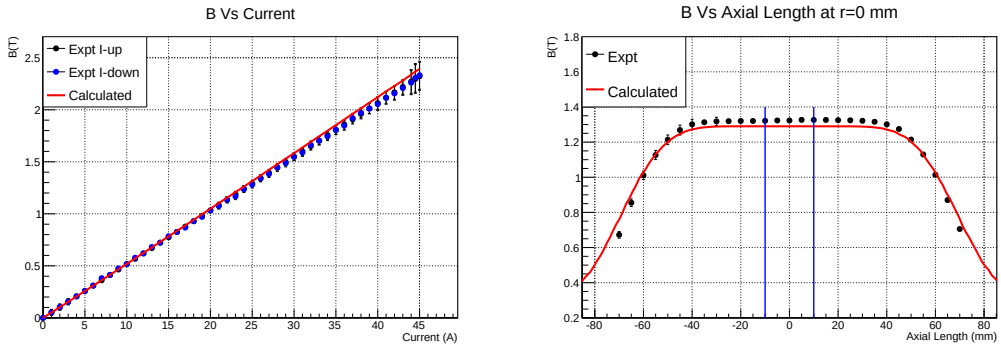

(a) (b)

Figure 4.24: (a) shows the magnetic field versus current, where a linear relationship is observed and (b) is a figure of magnetic field versus axial length (4.24b) at radial position $r = 0$.

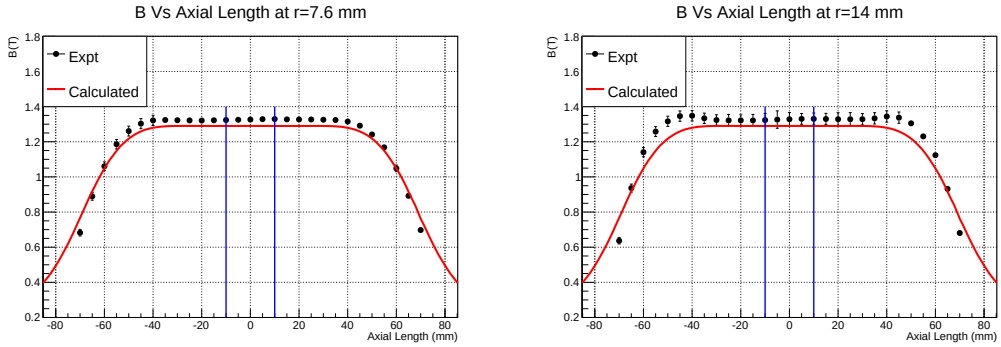

(a) (b)

Figure 4.25: Magnetic field versus axial length at the radial position $r = 7.6$ mm (a) and at $r = 14$ mm (b) from the center of the coil.

It is important to note that, the Hall probe outputs voltage from which the magnetic field is calculated using:

$$V_H = \gamma_B B \sin\theta \tag{4.24}$$

where V_H is Hall voltage (mV), γ_B is the magnetic sensitivity (mV/kG) (at a fixed current), B is the magnetic field flux density (kG) and θ is the angle between the magnetic flux vector and the plane of the Hall generator [131].

The angle was taken as $90^o \pm 5^o$ since the Hall probes were placed perpendicular to the magnetic field. The effect of field orientation with respect to the plane of the Hall probe must be taken into account when evaluating the error. This error is given in the application guide as:

$$Error\% = (1 - \cos\theta)100\% \tag{4.25}$$

where θ is the angular deviation from the perpendicular plane of magnetic field by the Hall probe. The error in the angle deviation of $\theta \pm 5^o$ was determined to be $\approx 0.38\%$. The Hall sensor output is not perfectly linear

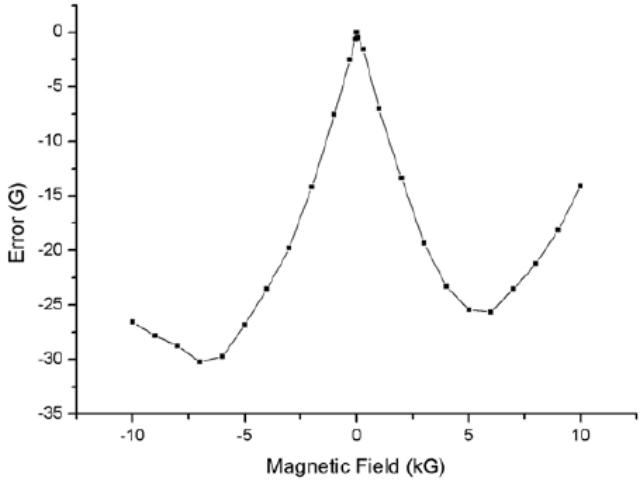

Figure 4.26: Error plot for the HGCA-3020 sensor with mean loaded sensitivity of 0.827 mV/kG [131].

with magnetic field, because the magnetic sensitivity is not constant. For example, at 4.2 K, the Hall probe sensitivity is 0.05% of the given value. The full error values can be evaluated using a single sensitivity value provided by the supplier [131]. Figure 4.26 shows the error plot for magnetic fields between -10 kG and 10 kG for the HGCA-3020 sensor used in the experiment.

4.3.5 Discussion and Outlook

The internal polarizing magnet attained a magnetic field of 2.3 T at a current of 45 A which is 96.27% of the projected value of 2.4 T. This can be attributed to the fact that the actual number of turns in the coil was 4.5% less than expected, as indicated in table 4.5, which affects the total magnetic field strength. In addition, at the current of 45 A the coil experienced a quench and no measurement was possible above this current (see table 4.4). At the temperature of 4.2 K and current of 45 A, a maximum magnetic field of 2 T can be achieved according to the supplier calibration even though a higher value was measured. This shows that there is hope to get higher current inside the dilution refrigerator at 1.5 K. The measured values are in agreement with calculations as shown in figure 4.24a except at high current values which shows a slight deviation from the calculation. This is due to the fact that the Hall probe sensitivity decreases with a current increase [131].

Using equations (4.21) and (4.20), the inductance of the coil was calculated to be 0.22 H and the magnetic energy stored in the coil as 224.73 J at a current of 45 A. When the critical current or magnetic field of the wire shown in table 4.4 was exceeded a quench occurred. At quench point, the stored energy of 224.73 J is converted into heat causing a small temperature increase on the copper holder. At this point the superconductor losses it superconducting ability and becomes resistive leading to joule heating.

Measurement of the magnetic field as a function of axial position in the target region was performed at a constant current of 25 A throughout the experiment because the temperature of the current leads remained stable at this current in the test setup. However, in the dilution refrigerator the coil can be operated at higher currents without heating of the current leads as discussed in 4.2.5. The axial magnetic field profile at different radial positions is shown in figures 4.24b, 4.25a and 4.25b for *(z,0)*, *(z,7.6)* and *(z,14)*, respectively. The calculated and measured values show good agreement except at position *(z,14)* from the center where it displays some symmetric bumps at around 40 mm from the center of the coil. This is due to the effect of winding imperfections and since this point is close to end of the notch there

is a high field strength due to the additional coil. However, this will not affect target polarization since this point is 14 mm from the center of the coil which is outside the target region. To ascertain if the bumps are a result of winding imperfections, simulation was performed by creating imperfections in the coil. This was done by introducing some regions without wires on the coil. As a result there were bumps at around 40 mm as shown in figure 4.27. This was then compared to the measured magnetic field at position *(z,14)*. The experimental results show agreement with the calculation, an indication that the winding imperfections may be one of the causes of the bumps at this point.

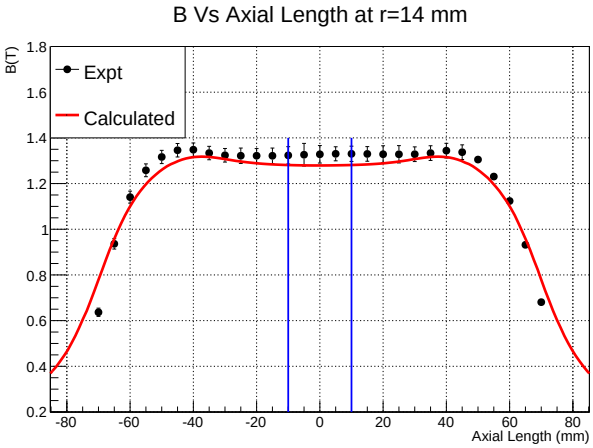

Figure 4.27: Magnetic field versus axial length for a coil with some winding imperfections compared to experimental values at $(z, 14)$.

The measured magnetic homogeneity in the target region was found to be 1.22×10^{-3}, higher than the calculated homogeneity of 5.9×10^{-5}. This was due to imperfections during the coil winding process, for example layer 9 has 556 turns and 10 has 564 turn as shown in table 4.5. This clearly shows that there are large spaces between the wires. It is also important to note that, during winding of layers 11 and 12 (in green in figure 4.20), the coil fell down and the wire was broken. Thus, this part was wound on top of the other coil as a separate coil which was later soldered together during testing. Since this was our first prototype of the internal polarizing coil, it is possible to construct a better coil by using a wire with a higher critical current and

winding machine mounted with monitoring cameras. This will prevent early quenching and reduce winding imperfections.

Chapter 5

Data Analysis I: Detector Calibration

The extraction of the helicity asymmetry E for the reaction

$$\gamma + p \rightarrow \pi^0 p \rightarrow \gamma\gamma p$$

requires that the reaction is reconstructed before the asymmetry is extracted. However, before any analysis can be undertaken, the raw signals from the detectors need to be converted into real physical formats (time (ns), energy (MeV) and position) through calibrations. Therefore, the first step in the data analysis is the conversion of the raw QDC and TDC values into energies (MeV) and times (ns), respectively through calibrations. The experimental setup consists of several detectors systems with many elements requiring calibration. Therefore, the calibration work was divided out between various members of the collaboration. The author's main responsibility was to calibrate the Crystal Ball and PID detectors (except PID energy calibration which was performed by a colleague at the University of Edinburgh [132]). The TAPS and Veto calibrations were performed by colleagues from the University of Bonn [133]. This chapter describes the analysis software, the determination of hits clusters in the calorimeter and time and energy calibration steps for the detectors.

5.1 Analysis Software

This section describes the data analysis software used in this work. They include: Acquroot, Calib, GoAT and A2Geant.

5.1.1 AcquRoot

The AcquRoot software [134] is written in C++ and based on the CERN ROOT framework [135]. AcquRoot has three components: AcquDAQ, which is used for data acquisition; AcquRoot, which is used for on-line and off-line data analysis and AcquMC, which is used as a Monte Carlo event generator. AcquRoot processes the raw data produced by AcquDAQ for each detector system by converting it into meaningful kinematic information of the detected particles. In AcquRoot, all detectors are modeled in classes, which are derived from base classes that incorporate common features and properties. For example, an apparatus like the Crystal Ball consists of NaI, PID, and MWPC that work together to produce particle tracks. In addition to detector and apparatus classes, physics analysis classes that are written to analyze specific decay channels can be added to access the detector information.

5.1.2 CaLib

CaLib is a detector calibration software [71] developed in the ROOT framework and contains modules to create almost all of the calibrations during analysis. It is based on an SQL database system where calibration parameters for each detector element are saved and can be accessed during data analysis. CaLib has classes that provide interaction with the SQL database, reading and writing of AcquRoot calibration files, reading headers of ACQU raw data files as well as importing and exporting calibrations. In order to simplify and accelerate the calibration process, CaLib has a graphical user interface shown in figure 5.1.

The TA2MyCaLib physics class is used in the AcquRoot framework to produce root files which are used as input for CaLib. Depending on the time frame, and experimental conditions, data can be divided into various

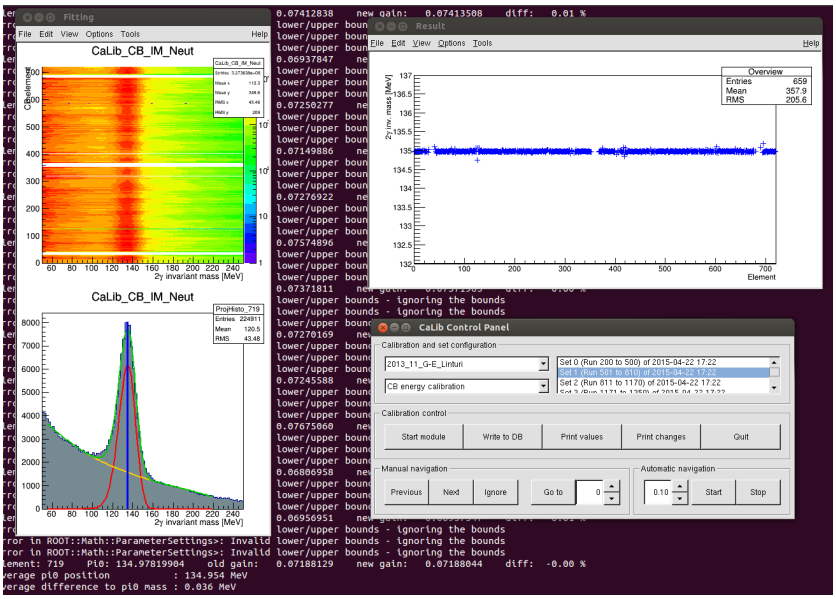

Figure 5.1: The CaLib User Graphical Interface (GUI) during the Crystal Ball energy calibration.

sets which are calibrated independently. This enables data that have similar conditions to be merged and calibrated together to get the best result. In CaLib the user has the possibility to process all the elements automatically or to check the results of each element. This helps to estimate the accuracy and status of the calibration. After an iteration the newly determined calibration parameters for all elements are saved to the database and read for the next iteration. This process is repeated until the best values are attained. The details on the calibration for each detector is described in 5.3.

5.1.3 GoAT

Generation of Analysis Trees (GoAT) [136, 137] is developed in the ROOT framework. It was developed as a tool to generate generic analysis trees. It uses a TA2GoAT physics class incorporated in AcquRoot to produce trees with all detector information. The TA2GoAT physics class is linked to the CaLib database via an SQL access class which makes it possible to access and include calibration information from the CaLib database to the output

trees. The output trees from AcquRoot are then run in GoAT where particle and meson reconstruction is performed. This is achieved through different detector and particle reconstruction classes. A global configuration file is used to setup all the reconstruction and sorting choices of different decay channels. After the sorting of the required reaction channel, analysis is done using a user physics class which is incorporated in GoAT.

5.1.4 A2Geant

The A2Geant [138, 139] software is written in C^{++} using the Geant4 software packages [140] and was developed by colleagues at the University of Edinburgh. AcquMC is used to generate pseudo events which serve as an input for A2Geant. The reaction parameters such as the photon beam energy and distribution and the target length, width and offset can be specified in AcquMC. In addition, the type and number of reaction particles produced can also be set. The output from AcquMC is passed through A2Geant where the particles are tracked and the physics process of interest modeled. The files produced contains the energy and timing information associated with each detector hit. These files are analyzed using the same physics class used for analyzing experimental data to test the reconstruction efficiency.

5.2 Detector Cluster Algorithm

Particles interacting with calorimeters create electromagnetic showers which have a transversal spread. The calorimeters are segmented in a way that the shower is deposited in multiple crystals, thus, improving the spatial resolution. The neighboring crystals into which the showers deposit energy is referred to as a cluster. As discussed in 3.3.1, 98% of photon energy is on average deposited over 13 Crystal Ball crystals and 7 TAPS crystals. Therefore, clustering is performed in two steps; first, the element with maximum energy is searched and marked as the center of a cluster and second, the 12 nearest crystals in the Crystal Ball and 6 in TAPS are checked for energy deposits above a certain cut off threshold. If their energy is above threshold,

they are added to the cluster and removed from the list of hits. This ensures that each detector element is only allowed to contribute to one cluster. The procedure is repeated until all crystals are assigned to a cluster. Figure

(a) (b)

Figure 5.2: The topology of the crystals in a cluster. (a) is the Crystal Ball cluster of 13 crystals and (b) is the TAPS BaF_2 cluster. The crystal marked with blue is the crystal with maximum energy deposit, where the particle likely hit.

5.2 shows the topology of the crystals in a cluster in the Crystal Ball (5.2a) (with 12 neighbors) and in the TAPS (5.2b) with the maximum energy crystal marked in blue. At the inner rings of the TAPS where some of BaF_2 were replaced by $PbWO_4$, the clusters have more than 6 neighbors depending on the number of $PbWO_4$ adjacent to the BaF_2 crystal. This is because four $PbWO_4$ crystals occupy the space of one BaF_2 crystal.

Once all the neighbors are processed, the total energy of the cluster E_{cl} is calculated as:

$$E_{cl} = \sum_{i=1}^{n} E_i \tag{5.1}$$

where E_i is the energy of the i^{th} detector element that contributes to the cluster of n elements($n \leq 13$ and $n \leq 7$ for the Crystal Ball and the TAPS BaF_2 crystals, respectively[1]). If the total cluster energy is below the energy threshold of 15 MeV the event is rejected. The position of the cluster, which determines the position of the incident particle, is calculated by the weighted

[1]For $PbWO_4$ crystals next to the BaF_2 crystals $n > 7$.

mean position $\vec{r}_{cl}$ of the cluster as:

$$\vec{r}_{cl} = \frac{\sum_{i=1}^{n} \sqrt{E_i} \cdot \vec{r}_i}{\sum_{i=1}^{n} \sqrt{E_i}} \tag{5.2}$$

where $\vec{r}_i$ is the cluster center of gravity of individual crystals. Figure 5.3 shows the number of crystals participating in a cluster for the Crystal Ball (5.3a) and the TAPS (5.3b) detectors.

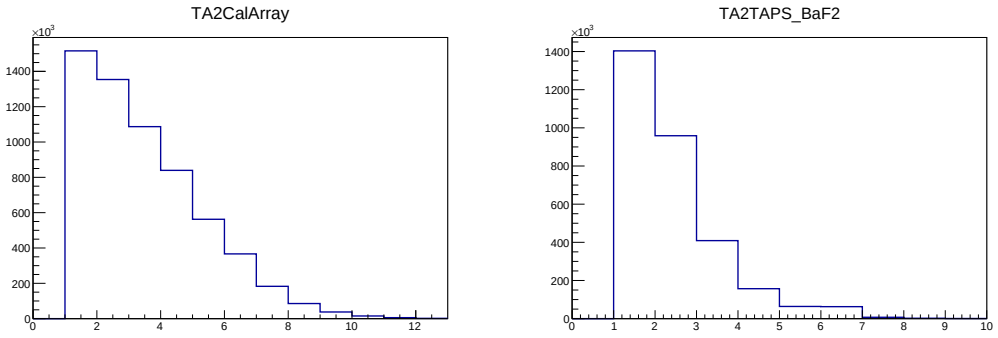

(a) (b)

Figure 5.3: Number of crystals participating in a cluster in the Crystal Ball (5.3a) and (5.3b) in TAPS.

5.3 Detector Calibrations

The analog signal from each photomultiplier tube coupled to each detector element is fed into an analog-to-digital converter, ADC, and a time-to-digital converter, TDC. The ADCs and TDCs, store digital values approximately proportional to the energy and time of the analog signal respectively. Hence, the ADC and TDC digital values can be discretized in terms of the ADC and TDC channel $\mathbf{C}$. The channels can be converted into energy or time using the relations:

$$E = \mathbf{k_E}(C - P) \tag{5.3}$$

$$T = \mathbf{k_T}(C - O) \tag{5.4}$$

where C is the digital ADC or TDC channel, P is the pedestal channel of the ADC, and O is the offset channel of the TDC. $\mathbf{k_E}$ and $\mathbf{k_T}$ are the energy and time conversion gain factors for the channel's energy and time, respectively. The ADCs and TDCs channel do not change during an experiment. Therefore, detector calibrations are performed to obtain the correct values of pedestal, P, offset, O, and the energy gain conversion factor $\mathbf{k_E}$. The time gain conversion factor $\mathbf{k_T}$ for the TDC is not calibrated since it does not change during an experiment. The calibration steps for all detectors are discussed in subsections 5.3.1 through 5.4.

5.3.1 Crystal Ball Energy Calibration

The energy calibration of the Crystal Ball detector is done in two stages; a low and high energy calibration.

Low Energy Calibration

As discussed in 3.4, various thresholds are applied to all of the Crystal Ball detector element signals. To ensure that all signals are discriminated equally, a relative gain calibration for all photomultiplier tubes (PMTs) coupled to each element is necessary. This is performed by using an ^{241}Am/^{9}Be source which is placed inside the Crystal Dall. Americium decays by emitting an α particle which interacts with beryllium to produce an excited state of $^{13}C^{*}$. The excited state of carbon decays by emitting a neutron, leaving an excited state of $^{12}C^{*}$ which in turn decays to the ground state of ^{12}C via emission of a photon of energy 4.438 MeV. The energy of the photon is used as a common calibration point of all the Crystal Ball PMTs. The calibration is done by adjusting the gains and high voltage of all photomultiplier tubes such that the resulting photon peak is at the same position for all the ADCs spectra [141, 142]. Figure 5.4 shows a typical ADC raw energy spectrum for a single NaI crystal where the full energy was deposited in one element.

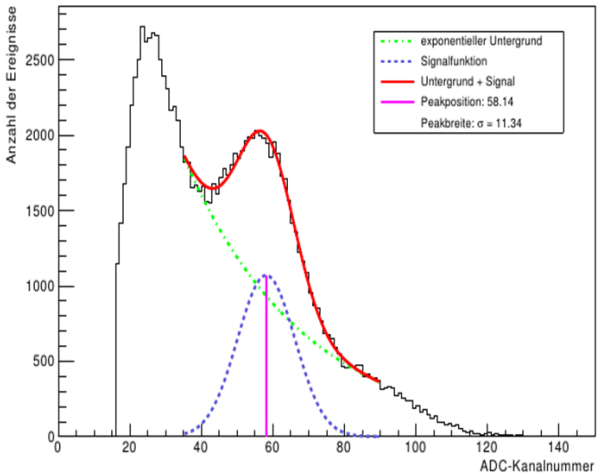

Figure 5.4: A typical raw energy spectrum for a single NaI crystal obtained from an ^{241}Am/^{9}Be source. The green curve is the exponential fit of the neutron background, blue is the Gaussian fit for the photon peak, the red curve is the total fit function for the spectrum and the magenta line show the photon peak position [142].

High Energy Calibration

Since the photons detected during data taking in the Crystal Ball have energies higher than the ones used for the low energy calibration, it is important to use photons with higher energies for this calibration. Therefore, high energy calibrations for the Crystal Ball detector are performed by analyzing neutral pion photoproduction decaying into two photons. This is because the $\gamma p \to \pi^0 p \to \gamma\gamma p$ reaction is kinematically overdetermined, i.e., the mass of π^0 and consequently the energies of the decay photons can both be calculated and measured with precision. Using the information of energy deposited in the crystals and the momentum of the photons a reconstruction of the π^0 mass can be performed:

$$M_{\gamma\gamma} = \sqrt{2E_{\gamma 1}E_{\gamma 2}(1 - \cos\vartheta_{\gamma 1\gamma 2})} \tag{5.5}$$

where $E_{\gamma 1}$ and $E_{\gamma 2}$ are the energies of the first and the second gamma, respectively and $\vartheta_{\gamma 1 \gamma 2}$ is the opening angle between the two photons. The ADC gain for each crystal is corrected using:

$$\mathbf{k'_E} = \mathbf{k_E} \frac{\pi^0_M}{\pi^0_{IM}} \tag{5.6}$$

where $\mathbf{k_E}$ is the uncorrected gain factor, $\mathbf{k'_E}$ is the corrected gain, $\pi^0_M = 134.98$ MeV is the nominal mass of π^0 and π^0_{IM} is the reconstructed invariant mass of π^0 [71]. Since the π^0 is from two photon clusters, and the energy of the photons in the crystals comes from the contribution of neighboring crystals, changing the gain of one element directly influences the other elements. Therefore, correction of the element gains has to be performed iteratively until the correct values are achieved. The invariant mass peak position was determined by fitting the spectrum with a combined fit of a polynomial for the background and a Novosibirsk fit function[2] for the peak. The mean position of the peak was taken as the invariant mass. Figure 5.5 shows the π^0 invariant mass spectra for a single element (5.5a) and all elements (5.5b). The vertical blue line is the π^0 peak position. Figure 5.6 shows a comparison of the π^0 mass peak position for a single Crystal Ball element before (red) and after (blue) calibration. After calibration the peak position of the spectra is aligned at the π^0 mass.

[2] A Novosibirsk fit function is defined as

$$(x) = Aexp\left[-0.5\left(\frac{ln^2[1+\Lambda\tau(x-\mu)]}{\tau^2}+\tau^2\right)\right]$$

where

$$\Lambda \equiv \frac{Sinh(\tau\sqrt{ln4})}{\sigma\tau\sqrt{ln4}}$$

with μ as the peak position, σ the peak width, τ the tail parameter, and A is the normalization constant [143]. The function was used instead of a Gaussian because the reconstructed π^0 mass does not follow a normal distribution.

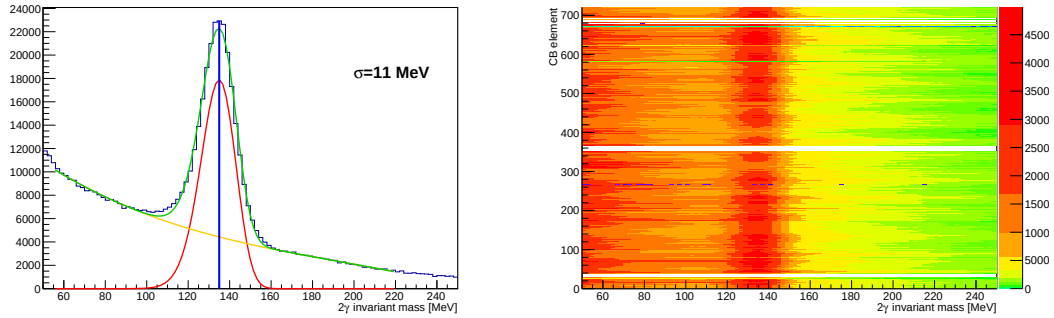

(a) (b)

Figure 5.5: The Crystal Ball high energy calibration using π^0 invariant mass spectrum. (a) is a spectrum from a single crystal. The green fit is the total fit for the signal and background, yellow is the background fit and red the signal fit. The blue vertical line shows the position of the π^0 mass. (b) shows the π^0 mass spectrum from all the Crystal Ball crystals aligned around its nominal mass (134.98 MeV).

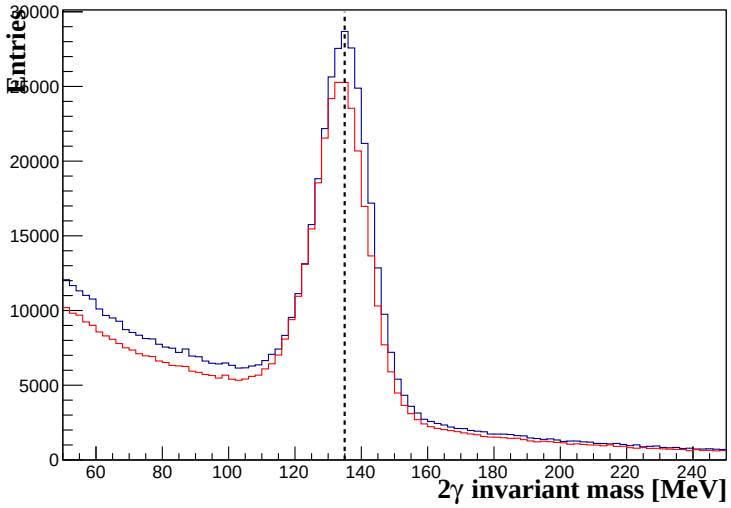

Figure 5.6: The π^0 mass for a single crystal before (red) and after (blue) energy calibration for the May 2014 beam-time.

5.3.2 Crystal Ball Time Calibration

The Crystal Ball time calibration was performed in two steps: time alignment and time walk correction discussed in 5.3.2 and 5.3.2, respectively.

Time alignment

The Crystal Ball TDC time offsets are determined by the time difference between all cluster hit combinations in the Crystal Ball using the central channel of a cluster as a reference. The Crystal Ball elements are then plotted as a function of these time difference. The resulting spectrum for each element is fitted with a Gaussian with the vertical blue line showing the time peak position as shown in figure 5.7a. Figure 5.8 show as single Crystal Ball element hits time before (red) and after (blue) calibration. The mean

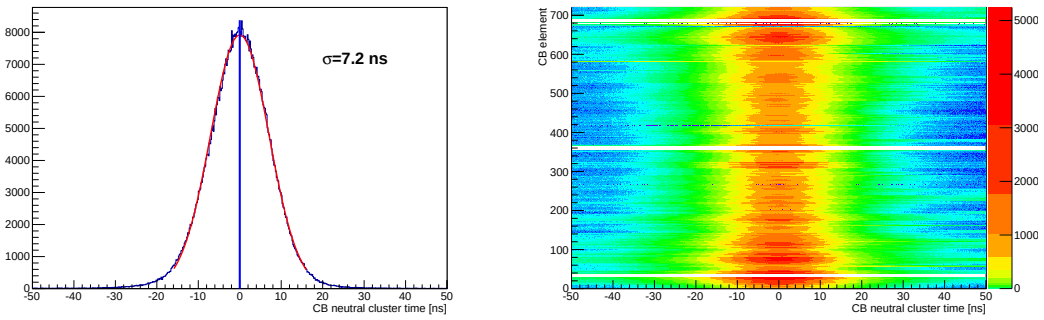

(a) (b)

Figure 5.7: An overview of the NaI crystal hits time. (a) is the time spectrum of a single NaI crystal with the blue line as the peak position while (b) is the alignment of all the Crystal Ball crystals time to zero for the May 2014 beam-time.

value m_i from the fit is used in the calculation of the new offset o_i':

$$O_i' = O_i + \frac{m_i}{\mathbf{k_T}} \tag{5.7}$$

where O_i is the old offset for the i$^{\text{th}}$ detector element. The calibration is performed iteratively until the mean values of all elements are aligned to zero.

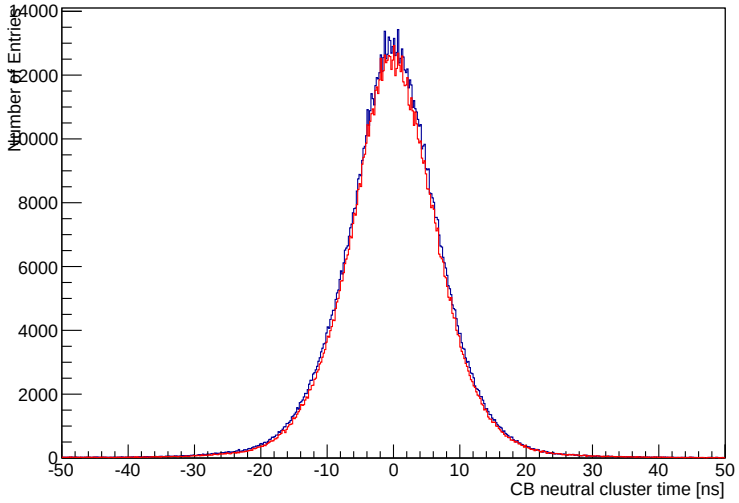

Figure 5.8: A comparison of the time peak position for a single Crystal Ball element before (red) and after (blue) calibration.

Time Walk Correction

NaI crystal pulses have a rise time of $\tau \approx 30$ ns. This produces a shift in timing between small and large pulse height events in the Crystal Ball and should be corrected to improve the time resolution in NaI crystals. Therefore, a time walk correction is required to account for the difference in time for two signals with different amplitudes but the same time difference value. This is done by plotting the Crystal Ball time as a function of energy for each element which is then fitted with the function:

$$t_{E_{dep}} = a + \frac{b}{(E_{dep} + c)^d} \tag{5.8}$$

where a, b, c and d are fit parameters which are determined for each detector element and E_{dep} is the deposited energy in that crystal. Using these parameters the time walk is then corrected using:

$$t' = t - \left(a + \frac{b}{(E_{dep} + c)^d} \right). \tag{5.9}$$

The time of all detector elements of the two photon cluster was calculated relative to the Tagger time. Therefore, the corrected time t' for each element was centered at zero with respect to the Tagger time. Figure 5.9 shows a time walk spectrum of a single NaI crystal time as a function of energy and figure 5.10 is the fit to the time walk spectrum.

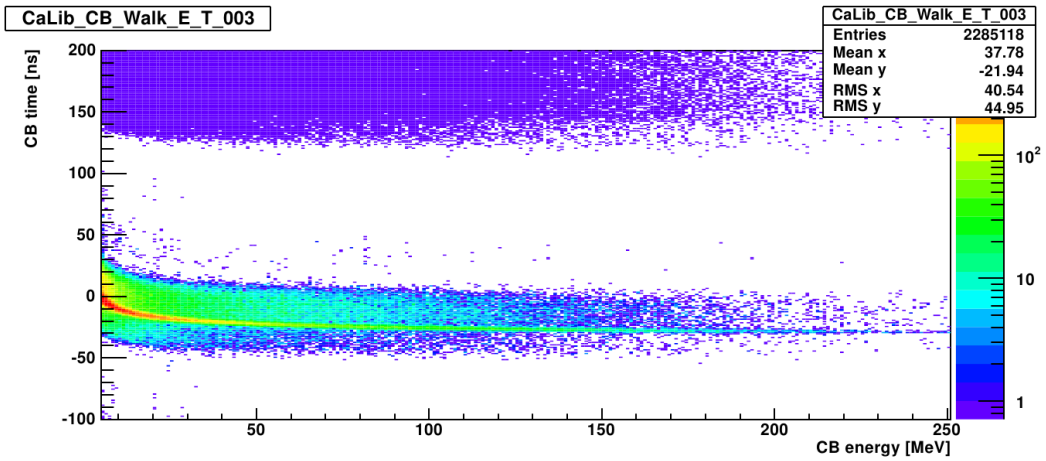

Figure 5.9: An overview of the Crystal Ball showing the time walk effect. Data from the May 2014 beam-time.

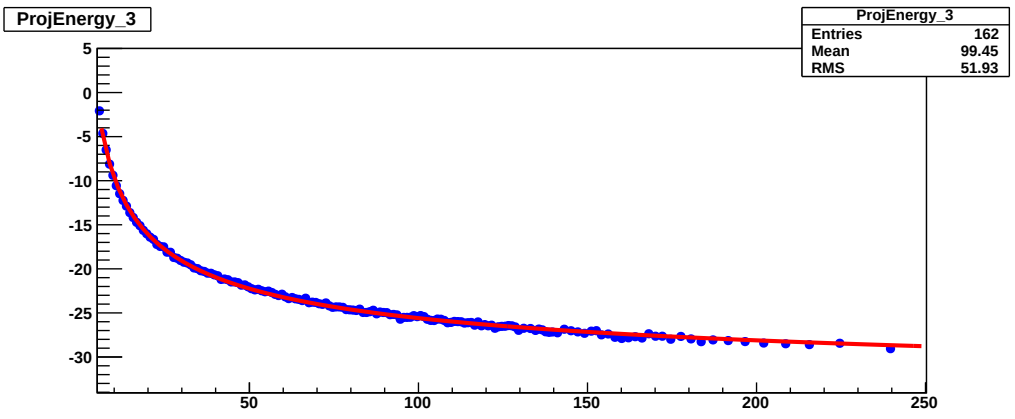

Figure 5.10: The time walk spectrum fitted with the function in equation (5.8). Data from the May 2014 beam-time.

5.3.3 PID-Crystal Ball ϕ Alignment

The PID allows the separation of charged and neutral particles in the Crystal Ball by identifying angular correlations between charged hits in the PID element and the the Crystal Ball clusters. Therefore, its correlation with the Crystal Ball elements is necessary to get the correct correlation parameters during analysis. The correction is performed by selecting exactly one hit in the Crystal Ball and one in the PID in order to extract the coincidence signal with minimal background. The PID ϕ parameters are then obtained by plotting the PID element hit as a function of the Crystal Ball cluster ϕ as shown in figure 5.11b. The projection of each element onto the x-axis is fitted with a Gaussian (Fig. 5.11a). The mean values of the Gaussian of the Crystal Ball-ϕ angle are plotted as a function of the PID element and fitted with a line.

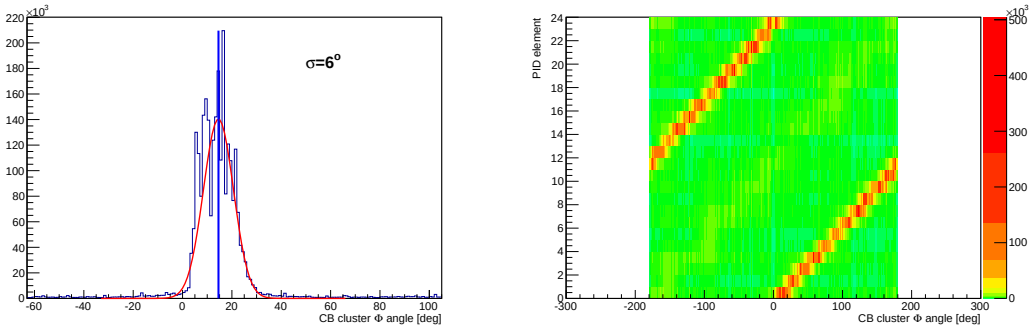

(a) (b)

Figure 5.11: The Crystal Ball-PID ϕ angle correlation alignment. (a) is the projection of one element onto the x-axis while (b) is the spectrum for all PID elements aligned at different angles.

5.3.4 PID Time Alignment

The PID TDC gains are fixed at 0.117ns/channel as in the Crystal Ball and Tagger. Therefore, the PID TDC offset correction is determined using the method described in 5.3.2 . However, the PID element is plotted as a function of the difference in time between two charged hits in the PID instead

of two neutral hits in the Crystal Ball. Figure 5.12a shows the time spectrum of a single element while figure 5.12b shows the time alignment of all PID elements to zero.

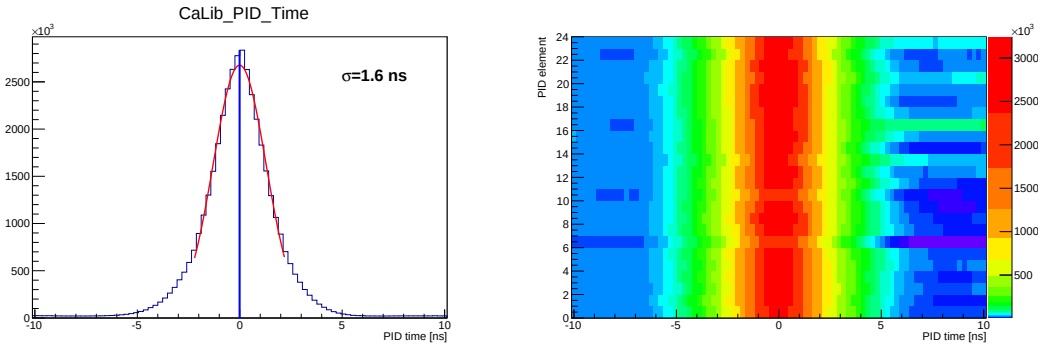

(a) (b)

Figure 5.12: An overview of the PID element hits time. (a) is the time spectrum of a single element fitted with a Gaussian. The blue line is the hits time peak position. (b) is the alignment of all PID element hits time to zero.

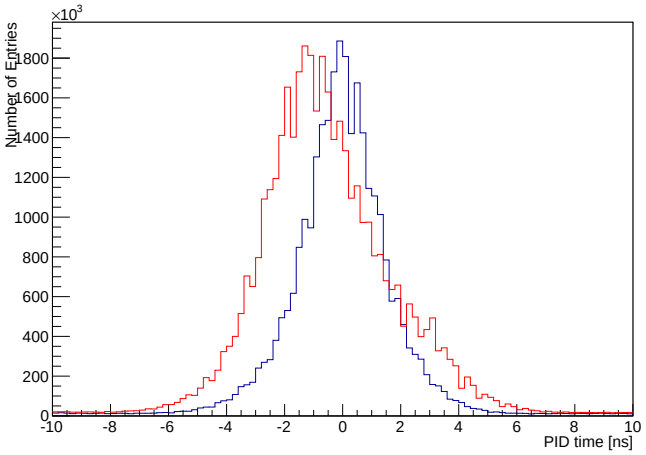

Figure 5.13: A comparison of PID time before (red) and after (blue) calibration. The time was aligned around zero after calibration.

5.3.5 TAPS Calibrations

As discussed in section 3.3.4, TAPS consists of BaF_2-$PbWO_4$ and plastic scintillators (Veto) detector elements. The BaF_2-$PbWO_4$ are calibrated together while the Veto is calibrated separately.

TAPS BaF_2-$PbWO_4$ Energy Calibration

The analog signal of the TAPS BaF_2-$PbWO_4$ elements is fed into two different ADCs. One going into long and the other into short integration gates (referred herein to as Long Gate (LG) and Short Gate (SG), respectively). The LG energy calibrations was performed in the same way as in Crystal Ball NaI ADCs since the LG ADCs work in a similar way. However, due to insufficient statistics in TAPS, the BaF_2-$PbWO_4$ element hits were plotted as function of $M_{\gamma\gamma}$ by considering either two photons in TAPS or one photon in TAPS and one in the Crystal Ball. This makes the TAPS energy calibration dependent on the Crystal Ball energy calibration. Thus, the Crystal Ball calibration has to be finished before the TAPS calibration is started. Figure 5.14 shows the LG energy calibration of a BaF_2-$PbWO_4$ element.

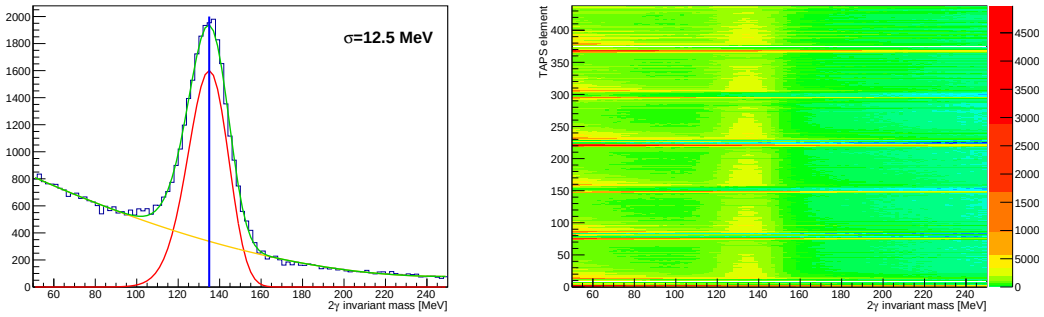

(a) (b)

Figure 5.14: TAPS BaF_2-$PbWO_4$ LG energy calibration. (a) is a spectrum for a single element. The green fit is the total fit for the signal and background, yellow is the background fit and red the signal fit. The blue vertical line shows the position of the π^0 mass. (b) the spectrum from all elements aligned at the π^0 invariant mass is shown.

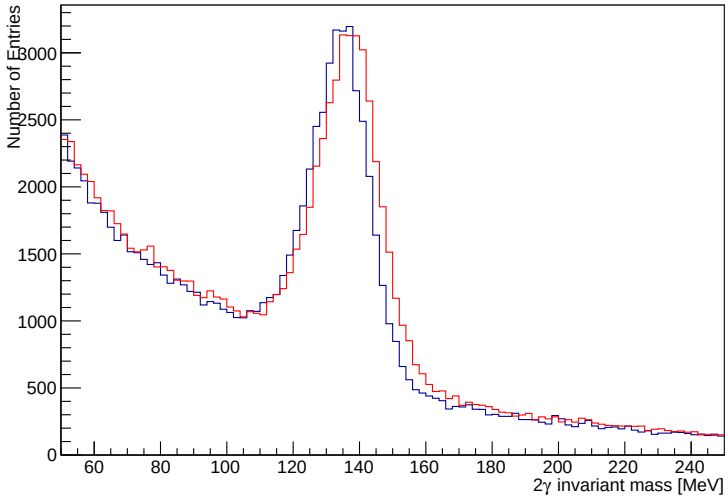

Figure 5.15: The π^0 mass for a single BaF_2-$PbWO_4$ crystal before (red) and after (blue) energy calibration for the May 2014 beam-time.

After the energy calibration of the LG energy, the gain of the short gate ADCs need to be calibrated. The calibration was performed by comparing the energies of the SG to that of the already calibrated LG by using the following transformation:

$$r_{PSA} = \sqrt{E_{LG}^2 + E_{SG}^2} \tag{5.10}$$

$$\theta_{PSA} = tan^{-1}\left(\frac{E_{SG}}{E_{LG}}\right) \tag{5.11}$$

where E_{LG} and E_{SG} is the energy in LG and SG ADCs, respectively, r_{PSA} and θ_{PSA} are the pulse shape analysis (PSA) radius and angle [71]. When the PSA radius is plotted as a function of PSA-angle band like structures can be seen for different particles as shown in figure 5.16. The SG energy is calibrated such that photon energy in SG equals the energy in LG ADC ($E_{LG} = E_{SG}$). This means that photons should be located at PSA-angles of 45 degrees for all PSA-radii. Protons have smaller PSA-angles and their PSA-radii show a typical dependence on the PSA-angles (banana shape structures). This is

due to the fact that a large fraction of their analogue signal is integrated in the LG ADCs.

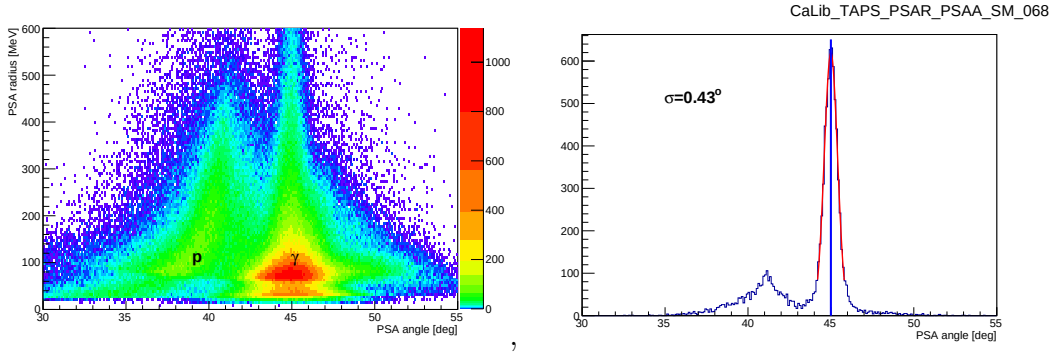

(a) (b)

Figure 5.16: TAPS BaF_2-$PbWO_4$ SG energy calibration spectrum for a single element. The banana shape shows the location of the protons while photons are aligned around angle of 45^o in (a). (b) is a projection on the θ_{PSA}-axis fitted with a Gaussian to determine the parameters.

During the calibration process, all clusters in TAPS are selected and their r_{PSA} and θ_{PSA} calculated from the SG- and LG-energies of their central crystal. The spectrum for each element is then filled. The positions of the photon bands are determined within two r_{PSA}-intervals at low and high PSA-radii, respectively, using Gaussian fits to the interval projections on the θ_{PSA}-axis as shown in figure 5.16b. From the two estimated PSA-angles, and the two mean PSA-radii of the projected intervals, new values for the pedestal and gain were calculated requesting $E_{LG} = E_{SG}$. The procedure was iterated until the correct values were attained. Figure 5.17 shows a comparison of SG energy projection before (red) and after calibration. Before calibration the peak position is around 38^o but after calibration the position is at 45^o as required.

TAPS BaF_2-$PbWO_4$ Time Calibration

Before data taking the TAPS TDC hardware was calibrated using a series of cables of known length in order to measure known time differences which determines the gains. The time offset alignment calibration of BaF_2-$PbWO_4$ is

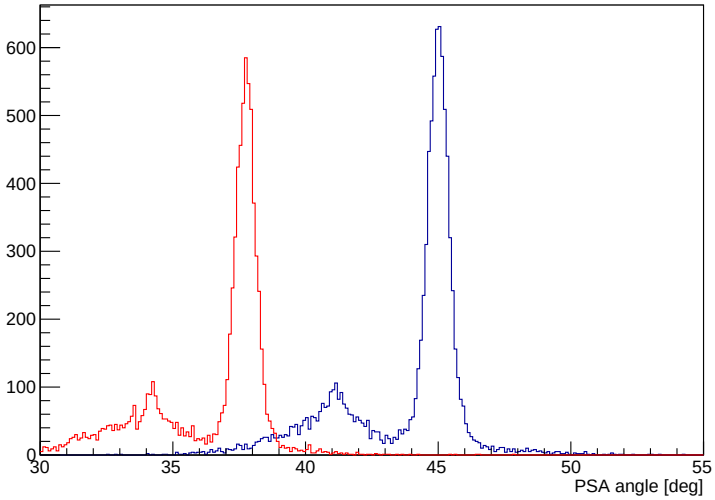

Figure 5.17: TAPS BaF_2 SG energy projection on the θ_{PSA}-axis for a single element before (red) and after (blue) calibration.

performed in a similar way as in the Crystal Ball time alignment calibration. Figure 5.18 shows a plot of TAPS element as a function of TAPS neutral cluster time. All the element hits time are aligned around zero.

TAPS Veto Energy Calibration

Veto ADC calibration was determined by plotting Veto energy (ΔE) as a function of TAPS cluster energy *(E)* as shown in figure 5.20a. A projection of this histogram onto the y-axis for Veto energy is fitted with a Gaussian as shown in figure 5.20b and the centroid of the peak determined. The data peak positions were fitted to simulation to get the correct values.

TAPS Veto Time Calibration

The Veto TDC offsets were calibrated using the same procedure to that of the PID by aligning the relative coincidence peaks of the individual detectors around zero. Figure 5.21a shows a spectrum of Veto hits time for a single element and figure 5.21b is the spectrum for all Veto elements aligned at zero. Figure 5.22 shows a comparison of Veto hits time for a single element

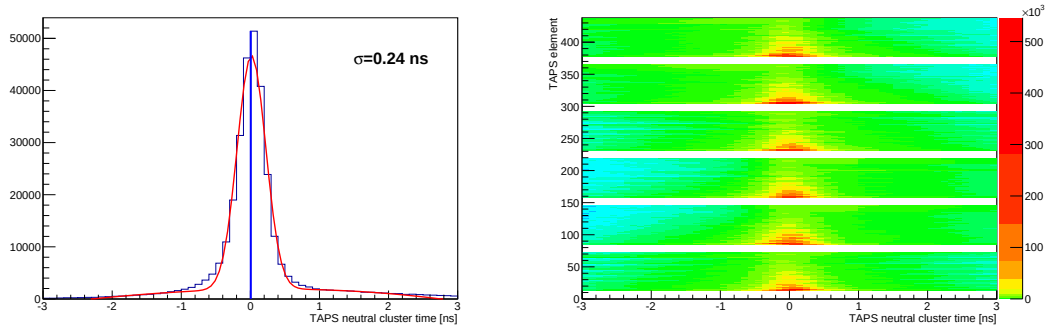

(a) (b)

Figure 5.18: TAPS BaF_2-$PbWO_4$ time calibration. (a) is a spectrum for a single TAPS element fitted with a Gaussian is shown. The vertical blue line shows the peak position. In (b) TAPS element as a function of TAPS neutral cluster time for all elements aligned around zero is shown.

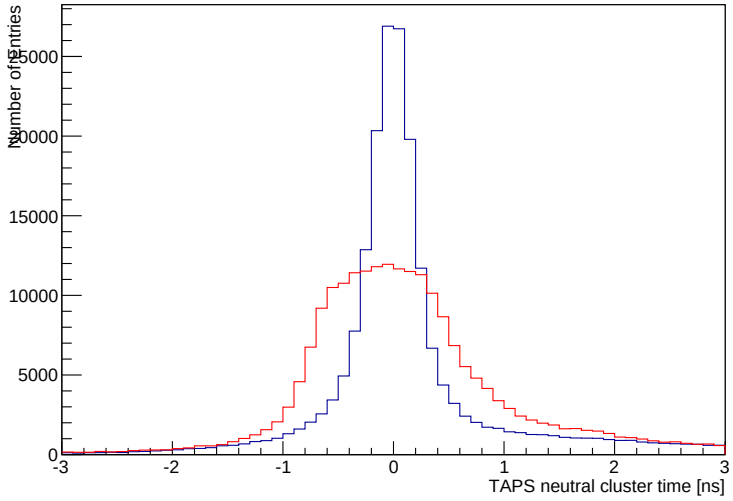

Figure 5.19: TAPS hits BaF_2-$PbWO_4$ time spectrum for a single element before (red) and after (blue) calibration.

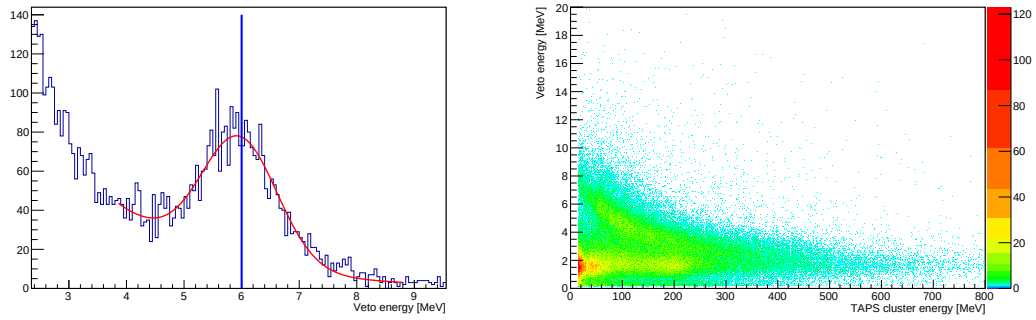

(a) (b)

Figure 5.20: Veto energy as a function of TAPS cluster energy.

before (red) and after (blue) calibration.

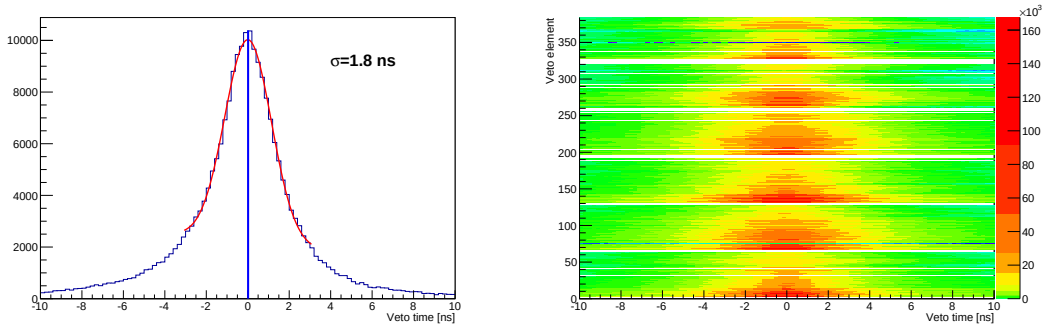

(a) (b)

Figure 5.21: Veto hits time spectrum. (a) is the spectrum for a single element fitted with a Gaussian. The blue line shows the peak position. (b) is the spectrum for all Veto elements aligned around zero.

5.4 Tagger Time Calibration

Like the Crystal Ball and PID TDCs, the Tagger TDCs also have a fixed conversion rate of 0.117ns/channel. Therefore, it is only the TDC offsets that need to be calibrated to eliminate difference in timing due to different cable length and other hardware timing difference. Time alignment was performed after the TAPS was fully calibrated since TAPS was used for the

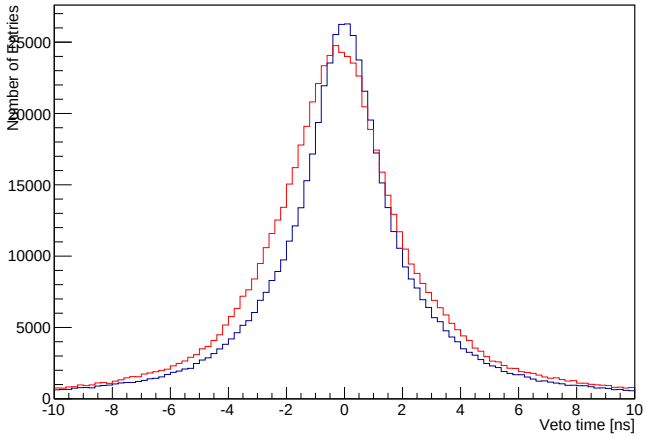

Figure 5.22: A comparison of Veto hits time for a single element before (red) and after (blue) calibration.

time correction due to its good resolution. This was performed by subtracting TAPS time from Tagger time and the result is plotted against each Tagger channel as shown in figure 5.23b. A projection onto the x-axis for each individual Tagger element is then fitted with a Gaussian as shown in 5.23a. The alignment was done in a similar way as in the Crystal Ball using equation (5.7). Since there is no dependence between Tagger channels one iteration was enough to align the Tagger time around zero. After all detectors were calibrated, the reconstruction of the physics reaction was started (discussed in chapter 6).

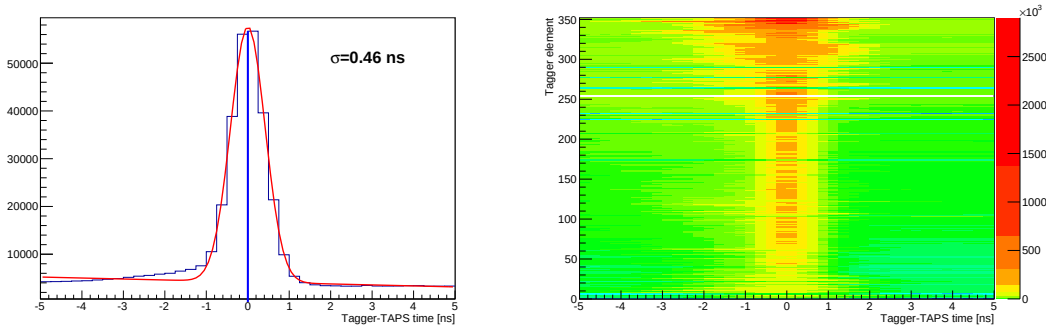

(a) (b)

Figure 5.23: Difference in Tagger and TAPS time alignment. (a) the time for a single element fitted with a Gaussian and (b) is the spectrum for all Tagger elements.

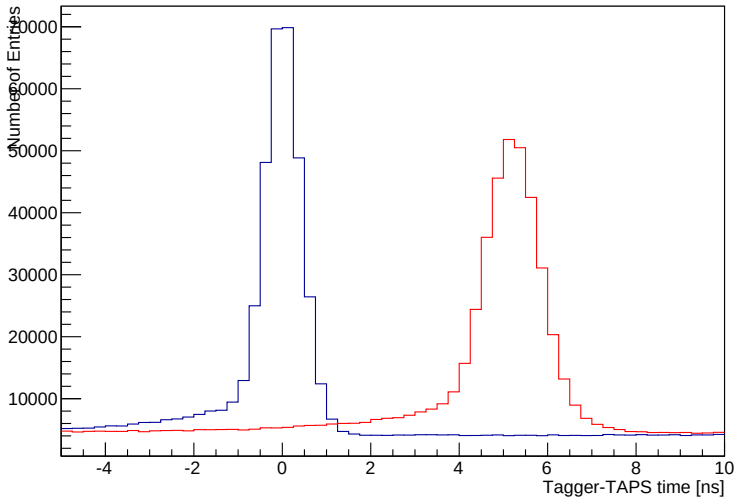

Figure 5.24: A comparison of Tagger-TAPS hits time for a single element before (red) and after (blue) calibration. Before calibration the peak was broader and centered around 5 ns. After calibration it is aligned at zero.

Chapter 6

Data Analysis II: Reconstruction of the Physics Reaction

This chapter presents the steps taken in the analysis of the physics reaction $\gamma p \rightarrow \pi^0 p \rightarrow \gamma\gamma p$ in the energy range $E_\gamma = 210 - 1410$ MeV. Section 6.1 describes the subtraction of the tagger random background. The selection of the π^0 is described in section 6.2. The description of the extraction of the helicity asymmetry E is presented in section 6.3 and the estimates of the systematic and statistical uncertainties are presented in section 6.4.

6.1 Tagger Random Background Subtraction

During the experiment, not all electron hits that are recorded in the Tagger are associated with photons that participate in a reaction with the target. This is due to the fact that some photons are lost due to the collimation of the beam and many photons pass through without interacting with the target. The events hits in the Tagger which correspond with a timing coincidence to the photons interacting with the target are refereed to as "prompt events" while those that are uncorrelated are "random events". The random events contribute to the background which has to be subtracted during analysis. However, it is not possible to identify the contribution of random background on an event-by-event basis from the incoming photon beam en-

ergy. Therefore, a statistical subtraction of the random background has to be performed on all quantities calculated in the analysis that uses the information of the incoming photon.

The method used in this work for background subtraction uses the coincidence time spectrum between the calorimeters and the photon Tagger for a sideband subtraction, i.e., quantities calculated using photons from the random windows on either side of the prompt window are subtracted from the quantities calculated from prompt window events [144]. It uses the fact that a coincidence should be seen in the timing between the photon Tagger and the calorimeters for the events which interacted with the target. The prompt peak is distributed around 0 ns for detector element hits corresponding to photons which interacted with the target as shown in figure 6.1.

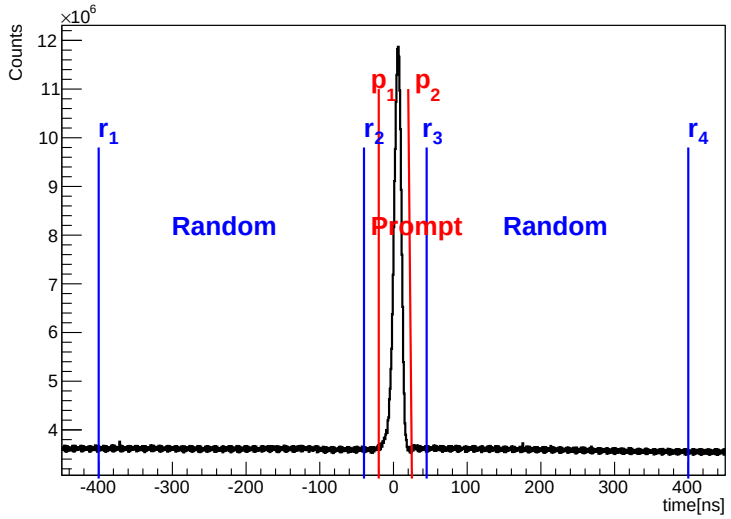

Figure 6.1: Time difference between the Tagger and π^0 time. The region between the red lines represent the prompt events while those between the blue lines represent the random event samples used for the sideband subtraction.

Figure 6.1 shows a time spectrum where the prompt and random windows are marked by red and blue lines, respectively. The distribution of the true coincidences in the prompt interval $[p_1, p_2]$ can be calculated by subtracting the normalized random distributions obtained in the intervals $[r_1, r_2]$ and

$[r_3, r_4]$ from the total distribution in the interval $[p_1, p_2]$. The subtraction of the random coincidences was performed by filling the same histograms with different weights for events from the prompt and the two random intervals:

$$N_t = N_p - w_r N_r \tag{6.1}$$

where N_t is the number of true prompt entries, and N_p and N_r are the number of prompt and random entries, respectively. The weight w_r was calculated from the normalization of the time intervals as

$$w_r = \frac{p_2 - p_1}{(r_2 - r_1) + (r_4 - r_3)}. \tag{6.2}$$

Subtraction of the weighted events of the random windows from the prompt window allows the removal of the random events under the prompt peak. In order to improve statistical accuracy, the random window should be as large as possible. In this work the random window was ≈ 18 times the width of the prompt window.

6.2 Selection of π^0 Events

The π^0 is the lightest meson with a mass of 134.9766 ± 0.0006 MeV and a lifetime of $(8.52 \pm 0.18) \times 10^{-17}$. Due to its very short lifetime, it is not possible to detect it directly within the calorimeters. Therefore, its presence is inferred from the reconstruction of two decay photons which are combined to get its mass. Therefore, the electromagnetic decay of $\pi^0 \to 2\gamma$, which has a branching ratio of $98.823 \pm 0.034\%$ [4], will be studied. In order to select photons participating in the reconstruction of a π^0, a cut on the number of hits in the calorimeters (cluster multiplicity) (Figure 6.2) is first applied to reduce the event sample into the most probable events for the reaction. This was done by requiring a events with a maximum of three clusters in the calorimeters. Events with more than three clusters in the calorimeters were rejected in order to cut on other competing processes and eliminate false clusters due to split-off within the crystals. The cluster were classified

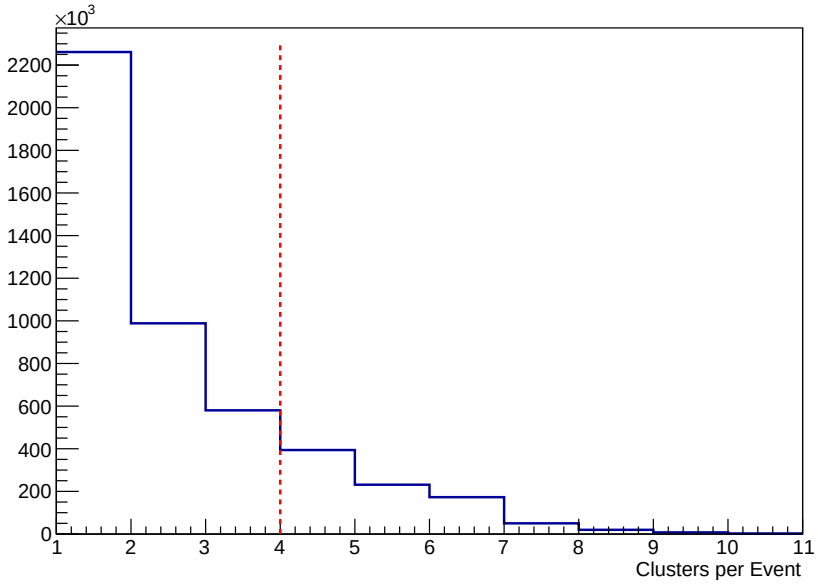

Figure 6.2: The number of clusters per event. The dotted red line shows the position of the highest cluster used. Events with clusters above the red line were rejected.

either as charged or neutral. Two separate event classes were, considered; event class 1 and event class 2, refereed to as inclusive and exclusive analysis respectively, depending of the number of neutral and/or charged particles. In the inclusive analysis two neutral particles with/without charged particle in the final state were considered while in the exclusive analysis two neutral particles and a proton in the final state were considered.

Using the information from the calorimeters, the mass of π^0 was reconstructed using the energies and momenta of its two decay photons:

$$M_{\gamma\gamma} = \sqrt{(p_{\gamma 1} + p_{\gamma 2})^2} = \sqrt{p_{\gamma 1}^2 + p_{\gamma 2}^2 + 2p_{\gamma 1}p_{\gamma 2}} \tag{6.3}$$

where p_1 and p_2 are the four vectors of the photons. In terms of the energy and the opening angle between the two photons, the invariant mass can be expressed as in equation (5.5). The invariant mass of the π^0 was reconstructed by treating all particles in a cluster as photons and combining then in order to get the mass of the π^0. The best combination was determined by

using a weighted factor χ:

$$\chi = \frac{|M_{i,j} - M_{\pi^0}|}{\omega}, \quad i \neq j \tag{6.4}$$

where $M_{i,j}$ is the reconstructed invariant mass from γ_i and γ_j, M_{π^0} is the nominal mass of a π^0-meson ($M_{\pi^0} = 134.98$ MeV) and ω is the width of the cut. The width ensures that the $M_{i,j}$ is within $M_{\pi^0} \pm \omega$. For this analysis, a width of $\omega = 22$[1] MeV was applied and only photon combinations with $\chi \leq 1$ were considered. If the condition of reconstruction in equation (6.4) is met, the π^0 is reconstructed and stored. Events that satisfied the cut were used for other subsequent analysis steps. Figure 6.3 shows the reconstructed π^0 mass $M_{i,j}$ spectra at different photon beam energies with the vertical red lines indicating the position of the cuts. At the beam energy $E_\gamma = 255 \pm 15$ MeV there is some background on the left which arises from the nucleon Fermi motion which is predominant in negative z-direction close to threshold. This will be subtracted later during background subtraction discussed in 6.2.3. The number of events per energy bin decreases with higher energies due to the $1/E_\gamma$ dependency of the bremsstrahlung photon cross section and $\gamma p \to \pi^0 p$ cross section.

6.2.1 Missing Proton Mass Reconstruction

During the experiment, not all protons produced in the reaction are fully detected in the calorimeters. This is due to the fact that high energy protons will punch through the calorimeter's crystals without fully depositing their energy, while some low energy protons do not reach the calorimeters due to energy loss in the PID and the target. Therefore, the recoil proton can be reconstructed using the missing particle technique. Using this method solves the problem of low proton detection efficiency, hence, increasing the statistics for analysis since the low acceptance regions can be accessed.

[1]The choice of the cut width was determined by performing reconstruction of π^0 using different cut widths and comparing the number of events. It was shown that a cut of 25 MeV included more background events while that of 20 MeV rejected some useful events. Therefore a safe cut of 22 MeV was used.

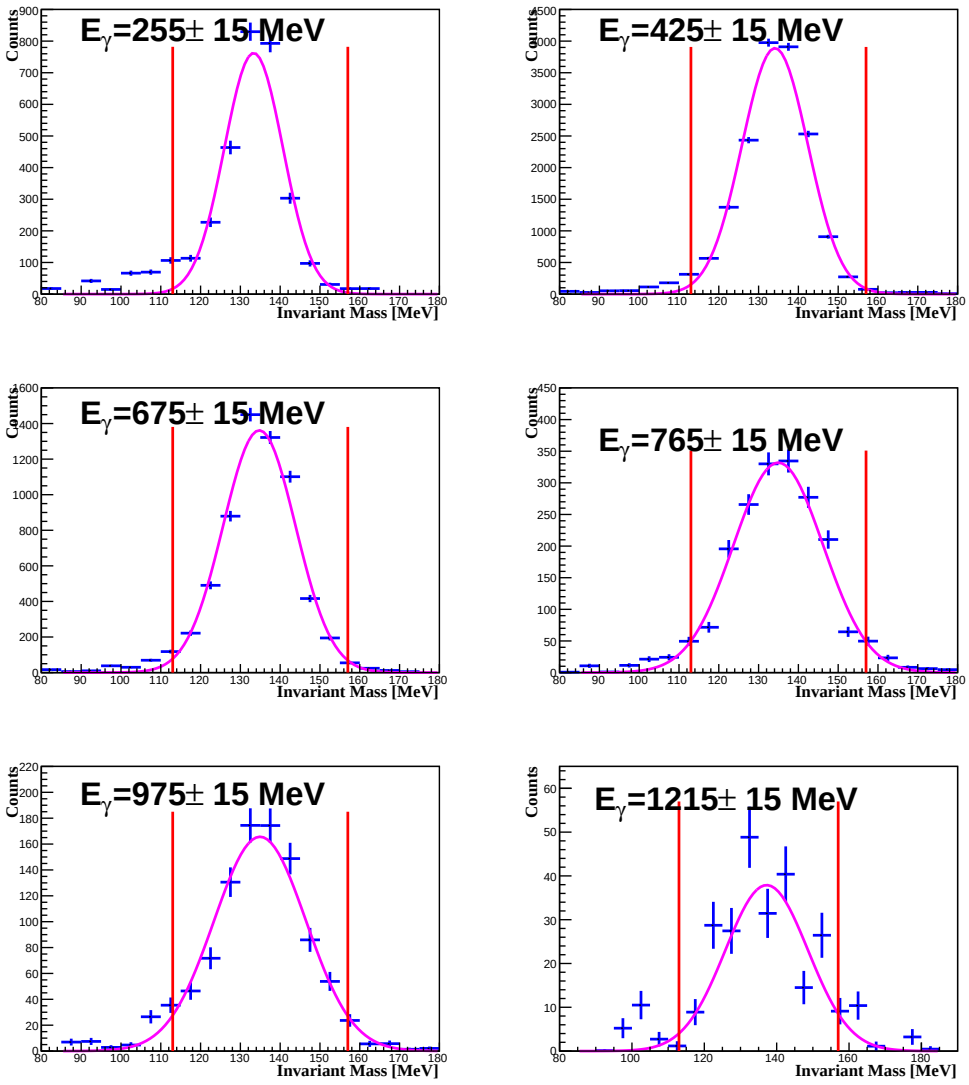

Figure 6.3: Reconstructed π^0 invariant mass spectra at different photon beam energies. Vertical red lines indicate the position of the cut limits.

The missing proton mass is reconstructed using the 4-vector information of the reconstructed π^0, the incoming photon and the target. In this case the target is assumed to be at rest. Using the principle of four momenta conservation the missing proton mass can be calculated:

$$(E_\gamma, \vec{p}_\gamma) + (E_{p_{in}}, \vec{p}_{p_{in}}) = (E_{miss}, \vec{p}_{miss}) + (E_{\pi^0}, \vec{p}_{\pi^0}) \tag{6.5}$$

where $(E_\gamma, \vec{p}_\gamma)$ and $(E_{p_{in}}, \vec{p}_{p_{in}})$ are the four vectors of the initial state of the photon and proton, respectively and $(E_{\pi^0}, \vec{p}_{\pi^0})$ is the four vector of π_0 . Therefore, the missing proton mass can be expressed as:

$$M_{miss} = \sqrt{(E_\gamma + m_p - E_{\pi^0})^2 - (\vec{p}_\gamma - \vec{p}_{\pi^0})^2}. \tag{6.6}$$

The reconstructed missing proton mass is usually distributed around the proton mass (938.27 MeV). However, the proton mass was subtracted from the reconstructed missing proton mass (Eq. 6.7) so that the signal is distributed around zero as shown in figure 6.4.

$$\Delta M = |M_{miss} - M_p|. \tag{6.7}$$

The missing mass spectrum is asymmetric as shown in figure 6.4b, i.e., the proton peak is on a broad background which is skewed to the right. The background originates from the photoproduction processes from the bound nucleons such as carbon and oxygen in the butanol target. The background have to be subtracted in order to get the contribution of the free proton. Figure 6.4b shows a reconstructed proton peak compared to a proton peak from the Monte-Carlo (MC) simulation. The reconstructed proton mass agrees well with the MC simulation except on the right side of the peak where some background is still remaining. This background will be eliminated through a cut applied to the missing proton mass later in the analysis. The procedure of the background event subtraction is described in section 6.2.3.

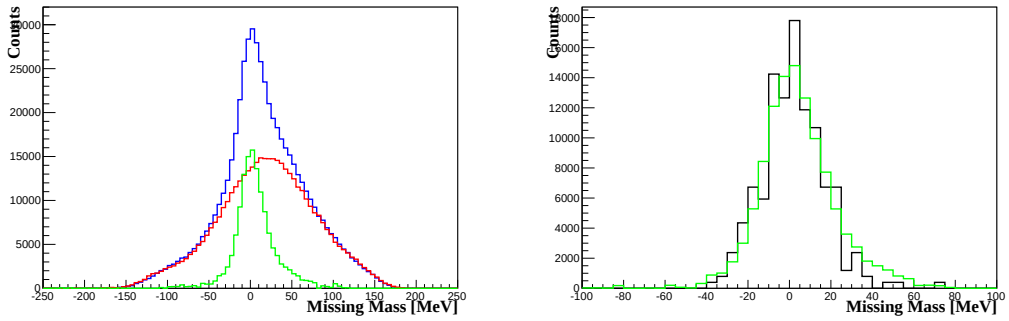

(a) (b)

Figure 6.4: The missing proton mass for the reaction $\gamma p \to \pi^0 p$ distributed around zero for $E_\gamma = 315$ MeV and $\cos\theta_{\pi^0} = -0.08$. In figure (a) the blue line is the missing proton mass distribution from the butanol target, the red line is the distribution from the carbon target and the green line is the difference between the carbon and butanol spectra (see 6.2.3). Figure (b) shows a comparison of the reconstructed proton mass (green) to that from MC simulation.

6.2.2 Angular Cuts

In addition to the invariant and missing mass cuts, angular cuts were applied where the presence of a proton was required (exclusive analysis). This was performed by using the angular information of the measured proton and that of the reconstructed proton and meson. Two variables were calculated; coplanarity and polar angle difference. Figure 6.5 shows a kinematic diagram of the reaction $\gamma p \to \pi^0 p$ where a photon along the z-direction interacts with a proton at rest to produce a pion at angle θ. Coplanarity was calculated from the difference $|\phi_{\pi^0} - \phi_p|$, where ϕ_p is the azimuthal angle of the recoil proton and ϕ_{π^0} is the azimuthal angle of the π^0 meson. The polar angle difference was calculated from the difference $|\theta_p^{calc} - \theta_p^{meas}|$, where θ_p^{calc} is the polar angle of the proton calculated from the photon and π^0 information and θ_p^{meas} is the measured polar angle. Each of them is discussed separately in the following:

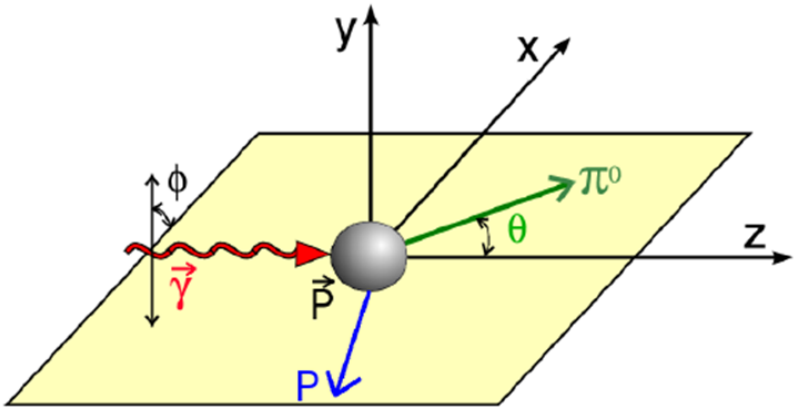

Figure 6.5: A schematic diagram of the kinematics of the reaction $\gamma p \rightarrow \pi^0 p$ where a photon along the z-direction interacts with a proton at rest to produce a pion at angle θ.

Coplanarity

If the π^0 and recoil proton are originating from $\gamma p \rightarrow \pi^0 p$, then the recoil proton and π^0 must lie in the same reaction plane that is spanned by the incoming photon in the center of mass frame due to momentum conservation. Therefore, the difference in the azimuthal angle of π^0 and recoil proton are supposed to satisfy the condition:

$$\Delta\phi = |\phi_{\pi^o} - \phi_p| = 180^o. \tag{6.8}$$

A plot of $\Delta\phi$ shows a peak centered around 180^o. The method described in 6.2.3 was used to determine the cut width for the coplanarity. A plot of $\mathcal{M} \pm \sigma$ as a function of photon energy shown in figure 6.6 indicates minimal energy dependence of the coplanarity spectra. Therefore, a fixed cut around $\Delta\phi = 180 \pm 20^o$ was applied on the reconstructed hydrogen spectra as shown in figure 6.7 for a few selected energy bins. To show the quality of data before and after the coplanarity cut, the missing mass spectrum before and after the cut is applied is plotted as shown in figure 6.8. Before the cut, the

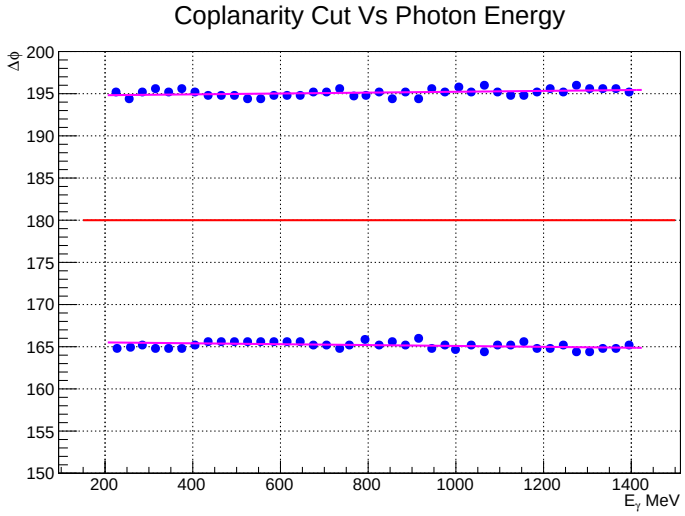

Figure 6.6: Coplanarity cut positions as a function of photon energy. The blue points represent the lower and upper cut position. The magenta line is a polynomial fit to the cut position.

proton peak shows up on a large background, which is significantly reduced after the cut is applied as shown in figure 6.8 in red.

Polar Angle Difference

After the coplanarity cut, there is still a significant amount of events which fulfill the coplanarity condition but do not correspond to the reaction $\gamma p \rightarrow \pi^0 p$ due to the Fermi motion or combinatorics within the given event. Therefore, a cut on the polar angle difference $|\theta_p^{calc} - \theta_p^{meas}|$ helps in reduction of these events. Monte Carlo (MC) simulation was performed to determine the width of the cut to be applied. Moreover, the calculated proton angle θ_p^{calc} is ideally the same as the measured proton angle θ_p^{meas} resulting in a difference close to zero. The MC spectrum shows that the different $|\theta_p^{calc} - \theta_p^{meas}|$ peak distribution is primarily less than 6^o. Therefore, a safe cut on the polar angle difference $|\theta_p^{calc} - \theta_p^{meas}| < 10^o$ was used to avoid rejection of good events. A spectrum of $|\theta_p^{calc} - \theta_p^{meas}|$ for the data is compared to simulation in figure 6.9. The vertical red line indicates the position of the cut. Missing mass spectrum before (red) and after the polar angle cut (blue) shown in figure

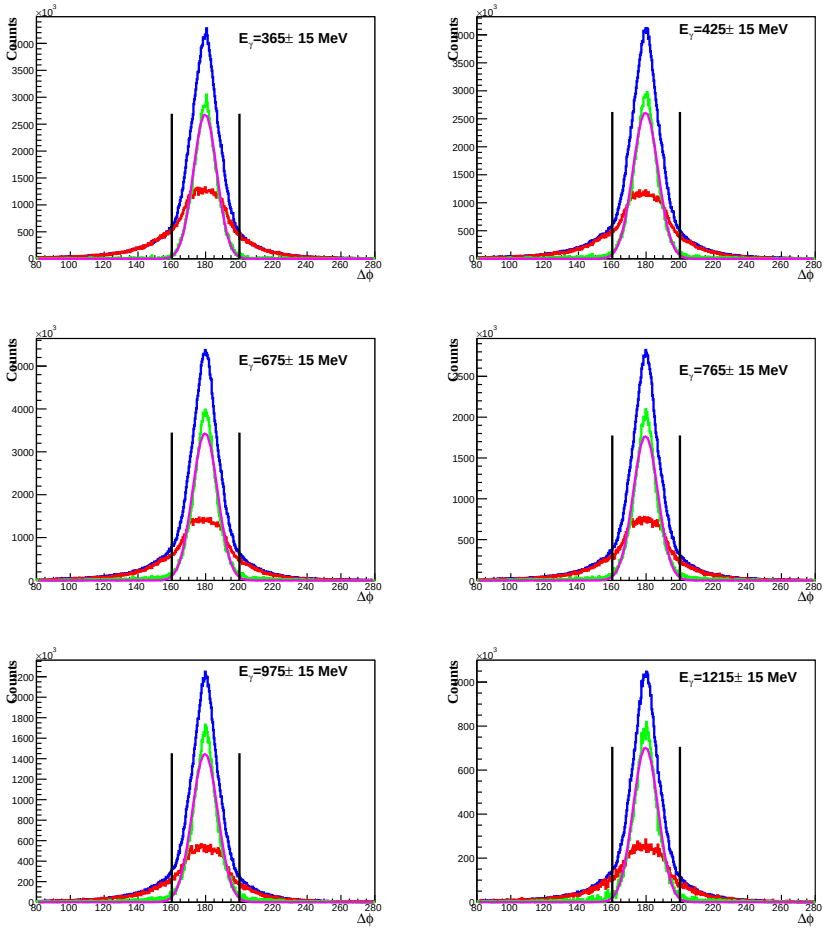

Figure 6.7: Coplanarity spectra for butanol (blue), carbon (red) and reconstructed hydrogen (green) for selected energy bins. The coplanarity spectra shown here are after the polar angle difference cut. In magenta is the Gaussian fit of the reconstructed hydrogen and the black vertical lines show the cut positions.

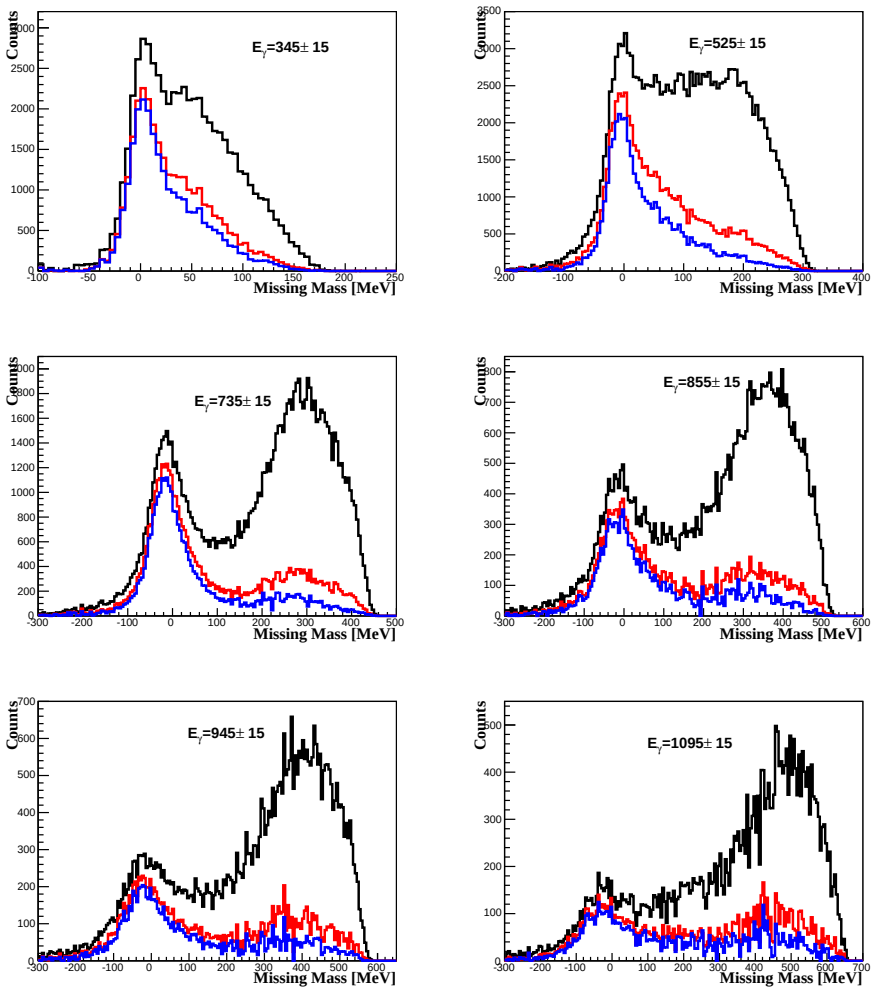

Figure 6.8: The missing mass spectrum before coplanarity cut (black) and after the cut (red). The blue spectrum is obtained after polar angle cut (see 6.2.2).

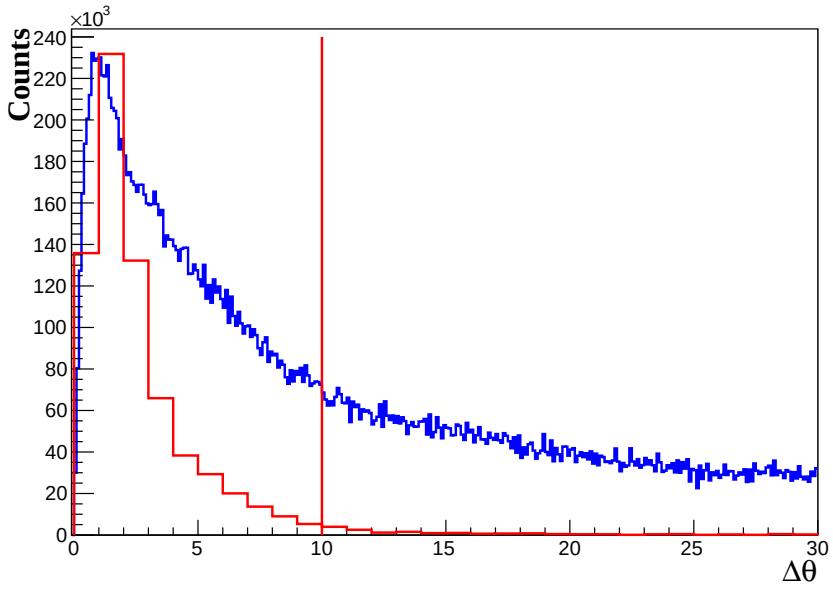

Figure 6.9: The polar angle difference spectrum between the detected and the calculated proton from data (blue) and MC simulation (red). The vertical red line shows the cut position.

6.8 shows a significant reduction of background. The remaining background was subtracted as described in 6.2.3.

6.2.3 Background Events Subtraction

The butanol target consists of hydrogen, carbon and oxygen nuclei which participate in the reaction. The reconstructed missing mass spectrum from butanol target in figure 6.4a shows a peak around zero on top of a broad background. The broad background arises mainly from the Fermi momentum of the struck nucleon. This is because the nucleons inside the butanol target are not at rest as assumed in the calculation of the missing proton mass. Thus, a separate data set taken with a carbon target (see 4.2.2) was analyzed and the contribution of the carbon and oxygen nuclei to the data was subtracted to get rid of the background. This was performed by comparing the missing proton mass spectra obtained using butanol and carbon target data sets. The missing mass spectrum from carbon data was scaled (discussed in

6.3.1) in order to correctly describe the broad background. A symmetric proton mass (expected from hydrogen) was reconstructed from the subtraction of the spectrum from carbon target from that of the butanol target (figure 6.4a).

However, the background contribution on the reconstructed hydrogen does not completely vanish, especially at high energies as shown in figures 6.11 and 6.12. This can be attributed to the fact that at high energies other reaction channels, such as $\pi^0\pi^0 p$ and $\pi^+\pi^0 n$, open up and contribute to the background. For example, at $E_\gamma = 735 \pm 15$ MeV, there is a bump at the double pion production threshold. Therefore, a cut on the reconstructed hydrogen spectra was performed in order to eliminate the remaining background. To determine the width of the cut to be applied, the reconstructed hydrogen missing mass spectra was fitted with a Gaussian to estimate the peak position and the mean ($\mathcal{M}$) and sigma (σ) values were calculated. A cut around the mean value was performed using:

$$\mathcal{M}(E_\gamma, \theta) \pm f \cdot \sigma(E_\gamma, \theta)$$

where f is a factor to define the size of the cut width.

In the exclusive analysis the background is more suppressed due to the fact that the recoil proton were detected and additional cuts (see 6.2.2) were applied. Therefore, f was taken as 2 in the exclusive analysis while in the inclusive analysis, a value of 1.5 was used in order to minimize contamination from the broad background distribution. Figures 6.10a and 6.10b show plots of the cuts applied as a function of photon energy and $\cos\theta_{\pi^0}$, respectively. As the photon beam energy increases, the missing mass spectra broadens because the calorimeters resolution becomes poorer as the energy increases. Hence, energy dependent cuts were applied for each energy bin. Even though there is no strong dependence of missing mass on $\cos\theta_{\pi^0}$, independent cuts for each bin were applied to improve the quality of the event selection. Figures 6.11 and 6.12 show the reconstructed hydrogen spectra for different energy bins for inclusive and exclusive analyses (additional cuts discussed in 6.2.2 were applied on the spectra), respectively with the black vertical lines indicating

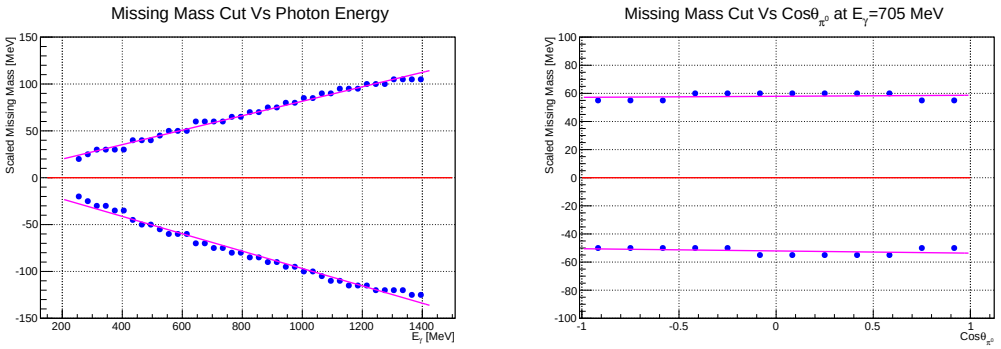

(a) (b)

Figure 6.10: Reconstructed hydrogen missing mass cuts. 6.10a is the cut as a function of the photon beam energy and 6.10b is a cut as a function of $\cos\theta_{\pi^0}$. The blue points represent the lower and upper cut positions. The magenta line is a polynomial fit to the cut position.

the cut positions. The events between the cuts are used for the extraction of the helicity asymmetry discussed in 6.3.

6.3 Extraction of the Helicity Asymmetry E

The helicity asymmetry E is obtained by studying the photoproduction reaction using a circularly polarized photon beam and a longitudinally polarized target. Helicity is defined as the projection of the spin vector of a particle to its momentum vector. The incoming photon and the proton target have spin 1 and 1/2, respectively. During the experiment, the helicity of the photon beam is flipped between positive and negative direction at a frequency of 1 Hz while target spin orientation either parallel or anti-parallel to the direction of the photon beam is fixed for a certain period of data taking. Table 6.1 summarizes beam-time information for data taken with different target polarization orientations. The photon and target spin can be combined either in parallel or anti-parallel configurations resulting in four total spin combinations of $\pm 1/2$ or $\pm 3/2$. Due to parity conservation, there are only two total spin configurations, i.e., parallel (3/2) and anti-parallel (1/2). The events from the two helicity configurations were used in the reconstruction

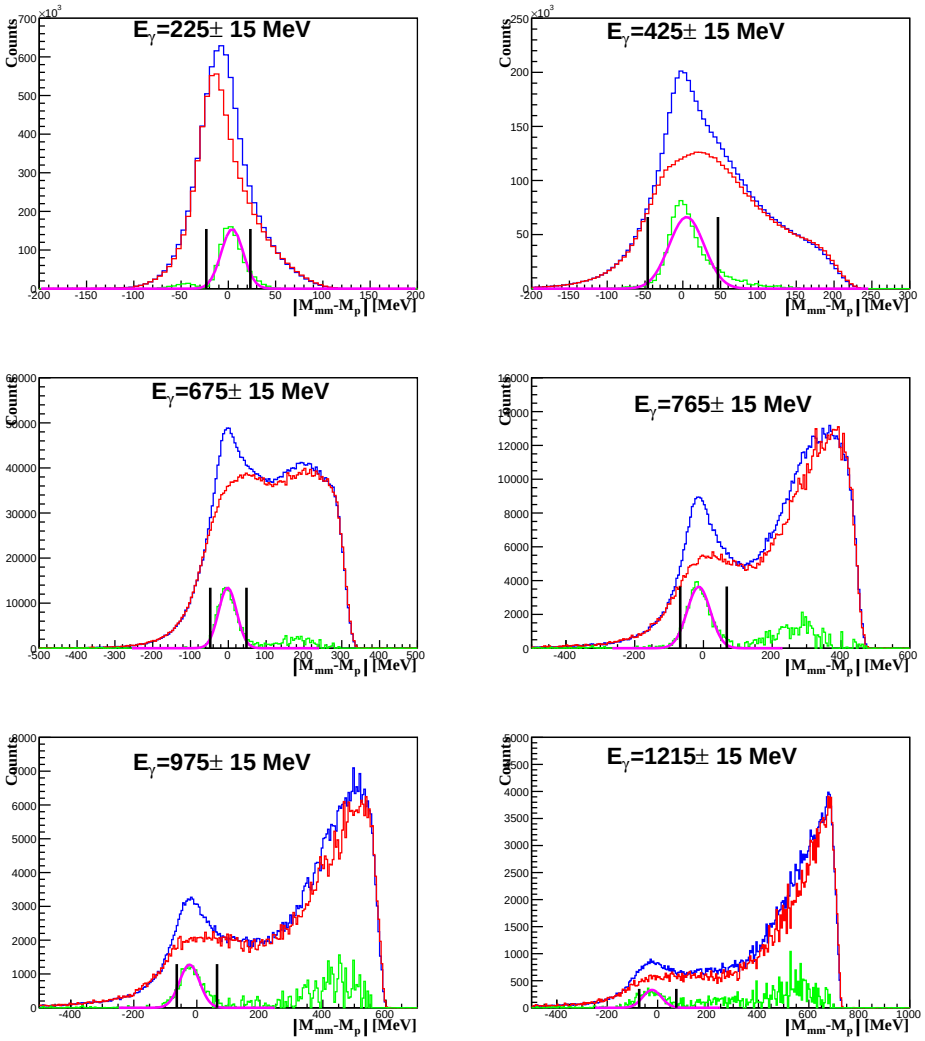

Figure 6.11: Missing mass spectra for butanol (blue), scaled carbon (red) and reconstructed hydrogen (green) at different energy bins for the inclusive analysis. The two black vertical lines define the cut positions.

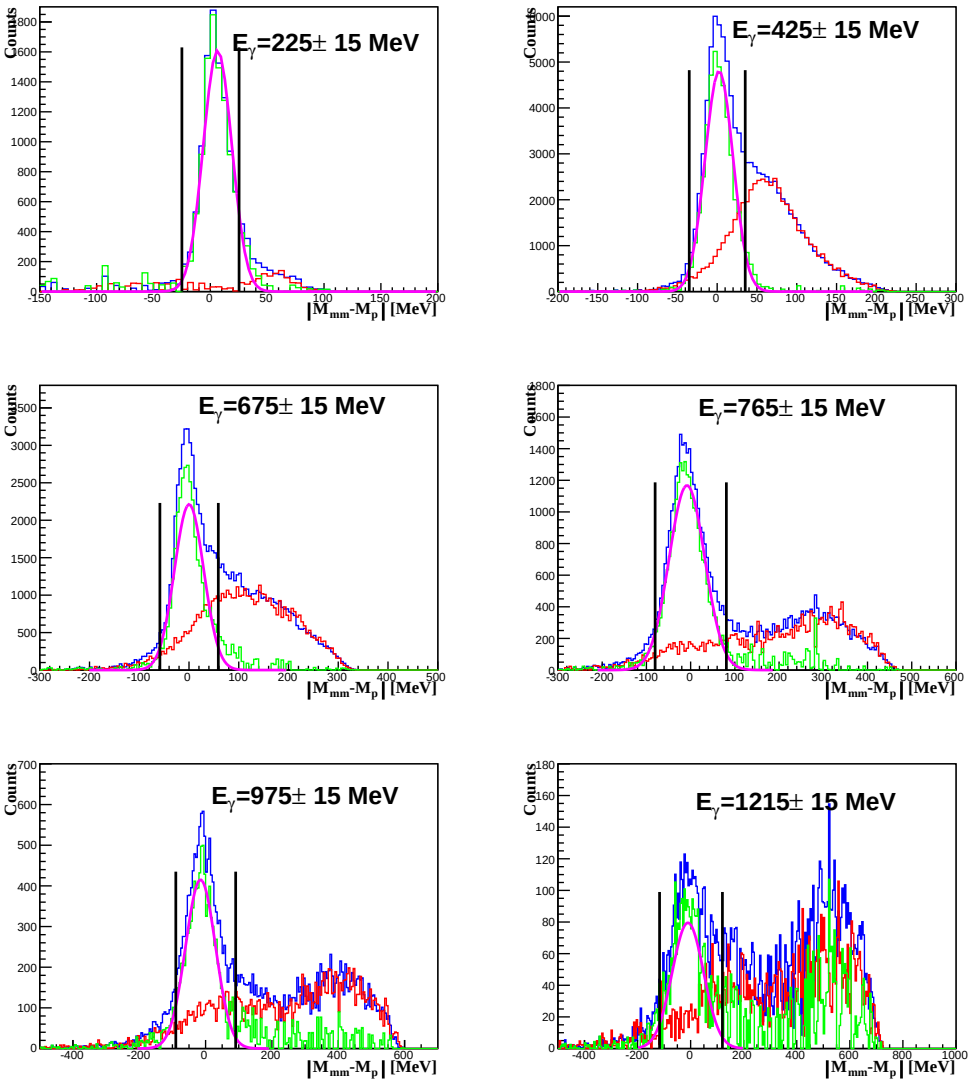

Figure 6.12: Missing mass spectra for butanol (blue), scaled carbon (red) and reconstructed hydrogen (green) at different energy bins for the exclusive analysis. The two black vertical lines define the cut positions. Angular cuts were performed on this analysis.

Beam-time	Run No.	Target	Target Pol.	No. of Files	Time [hrs]
Nov 2013	322-787	Butanol	Positive	264	132
Nov 2013	860-1348	Butanol	Negative	276	138
Nov 2013	1358-1483	Carbon		79	38.5
April 2014	3139-3381	Carbon		124	62
May 2014	4188-4508	Butanol	Negative	166	83

Table 6.1: Beam time information showing the target polarization orientation and the number of files used in extraction of the helicity asymmetry E.

of kinematic variables such as invariant and missing mass of π^0 as shown in figure 6.13. It is clear from figure 6.13 that there are no obvious systematic errors that could arise if the helicity was maintained in one direction. Also, the spectrum from the difference between parallel and anti-parallel helicity combinations is symmetric and centered at zero. This means that all the background events have been subtracted.

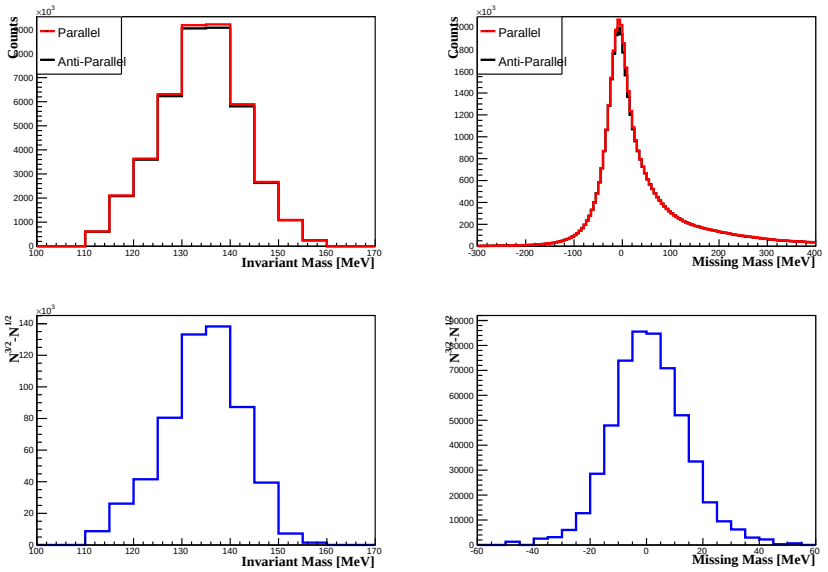

Figure 6.13: Invariant mass (top left) and the missing mass (top right) histogram filled with events from parallel (blue) and anti-parallel (red) configurations of the photon beam and target spin. The bottom row is the difference between parallel and anti-parallel for invariant mass (left) and missing mass (right).

As discussed in section 2.2, the spin dependent cross section in equation (2.28) reduces to (6.9) in case of helicity asymmetry due to the orientation of the photon beam and target polarization.

$$\frac{d\sigma^h}{d\Omega} = \frac{d\sigma_o}{d\Omega}(1 \mp p_z^T p_{cir}^\gamma E) \tag{6.9}$$

where h is the total helicity configuration and the $\mp$ is the overall sign of the target and photon beam polarization alignment. If the spin is aligned in the beam direction, which corresponds to the momentum direction, the sign of the helicity is positive, else it is negative. The spin dependent differential cross-section for parallel and anti-parallel configurations can be written in terms of the polarizable (hydrogen) and unpolarizable (carbon and oxygen) parts of butanol as [145]:

$$\frac{d\sigma^{\frac{3}{2}}}{d\Omega_B} = \frac{d\sigma}{d\Omega_H}(1 - p_z^T p_{cir}^\gamma E) + \frac{d\sigma}{d\Omega}_C, \tag{6.10}$$

$$\frac{d\sigma^{\frac{1}{2}}}{d\Omega_B} = \frac{d\sigma}{d\Omega_H}(1 + p_z^T p_{cir}^\gamma E) + \frac{d\sigma}{d\Omega}_C. \tag{6.11}$$

Dividing the difference of equations (6.10) and (6.11) with their sum we get:

$$\frac{\frac{d\sigma^{\frac{1}{2}}}{d\Omega_B} - \frac{d\sigma^{\frac{3}{2}}}{d\Omega_B}}{\frac{d\sigma^{\frac{1}{2}}}{d\Omega_B} + \frac{d\sigma^{\frac{3}{2}}}{d\Omega_B}} = p_z^T p_{cir}^\gamma E \cdot \frac{\frac{d\sigma}{d\Omega_H}}{\frac{d\sigma}{d\Omega_H} + \frac{d\sigma}{d\Omega}_C} \tag{6.12}$$

with

$$\frac{\frac{d\sigma}{d\Omega_H}}{\frac{d\sigma}{d\Omega_H} + \frac{d\sigma}{d\Omega}_C} = D_f$$

as the dilution factor.

The differential cross-section is defined as

$$\frac{d\sigma}{d\Omega} = \frac{N}{AN_\gamma \rho_t \Delta\Omega}\frac{\Gamma_{total}}{\Gamma} \tag{6.13}$$

where ρ_t is the target area density, N is the number of reconstructed events

in each $(E_\gamma, \cos\theta_{cm})$ bin, A is the acceptance in $(E_\gamma, \cos\theta_{cm})$ bin, N_γ is the number of photons in an E_γ bin, $\Delta\Omega$ is the solid-angle interval $\Delta\Omega = 2\pi\Delta\cos(\theta_{cm})$ and $\frac{\Gamma_{total}}{\Gamma}$ is the decay branching ratio [50].

Using equation (6.12) and (6.13) and assuming that the photon flux for the two spin configurations is approximately the same (the helicity flips at a frequency of 1 Hz hence having the same number of events for the two orientations), the helicity asymmetry E can be redefined as:

$$\mathbf{E} = \frac{1}{P_z^T \cdot P_{cir}^\gamma} \cdot \frac{1}{D_f} \cdot \frac{N^{\frac{1}{2}} - N^{\frac{3}{2}}}{N^{\frac{1}{2}} + N^{\frac{3}{2}}} \tag{6.14}$$

where the dilution factor D_f is

$$D_f = \frac{N_H}{N_H + N_C},$$

$N^{\frac{3}{2}}$ and $N^{\frac{1}{2}}$ is the number of events for parallel and anti-parallel spin configuration, respectively, P_z^T is the target polarization (discussed in 4.2.7) and P_{cir}^γ is the photon beam polarization (discussed in 3.1.4). The dilution factor will be described in 6.3.1.

6.3.1 Dilution Factor

The extraction of the helicity asymmetry E requires that the dilution factor (the ratio of polarizable nucleons to total number of nucleons in the target) is first evaluated. The dilution factor accounts for the non-vanishing carbon part in the sum of spin 1/2 and 3/2 differential cross sections in equation (6.12). A static dilution factor D_f of the butanol target can be obtained from the ratio of the number of hydrogen nucleons to the total number of nucleons in a butanol molecule as in:

$$D_f = \frac{H_N}{B_N} = \frac{10}{74} \approx 0.135 \tag{6.15}$$

where H_N is the number of hydrogen nucleons in butanol and B_N is the total number of nucleons in butanol molecule.

The kinematic cuts applied during analysis affect the number of nucleons at each energy and angular bin. Therefore, an effective determination of the dilution factor D_{eff} is necessary. This is performed by analyzing a separate data set obtained using the carbon target in order to subtract the background contribution (see 6.2.3) from carbon and oxygen nuclei in the butanol target and ^{3}He/^{4}He from target cooling. Assuming that the energy and angle dependent yield is the same for the bound nucleons of butanol and for those of carbon target, the spectra from the carbon target can be scaled by a factor (scaling factor) so as to describe the background contribution in the butanol target correctly. The effective dilution factor D_{eff} is defined as:

$$D_{eff}(E,\theta) = \frac{N_B(E,\theta) - S_f(E,\theta) \cdot N_C(E,\theta)}{N_B(E,\theta)} \tag{6.16}$$

where S_f is the scaling factor, $N_B(E,\theta)$ and $N_C(E,\theta)$ are the number of counts from butanol and carbon target, respectively. $N_B(E,\theta)$ and $N_C(E,\theta)$ are accessible from the data but the scaling factor had to be determined for each energy bin from missing mass spectra obtained using the butanol and carbon targets.

The missing mass spectra obtained with the butanol target was divided by missing mass spectra obtained with the carbon target in order to determine the scaling factor [146]. A combination of a Gaussian and a constant was fitted to the resulting spectrum as shown in figure 6.14. The Gaussian described the peak position while the magnitude of the constant describes the baseline. The fit parameter of the constant was used as the scaling factor. The carbon spectrum is then scaled with the scaling factor and subtracted from the spectrum taken with the butanol target to get a clean proton peak.

Figure 6.15a shows missing mass spectra from butanol and carbon target data before scaling while figure 6.15b shows missing mass spectra from butanol and scaled carbon. The background in the missing mass spectrum obtained using butanol target is well-described by the scaled missing mass spectrum obtained using the carbon target.

Due to the dependence of missing mass spectra on the energy of the

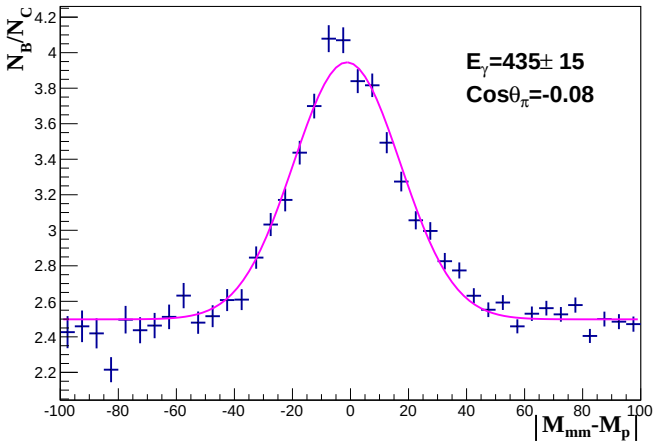

Figure 6.14: A spectrum from the ratio of the missing proton mass taken with butanol and carbon targets. The magenta line is a combined fit of a Gaussian and a constant. The parameter of the constant defines the baseline of the spectrum and, thus, used as the scaling factor.

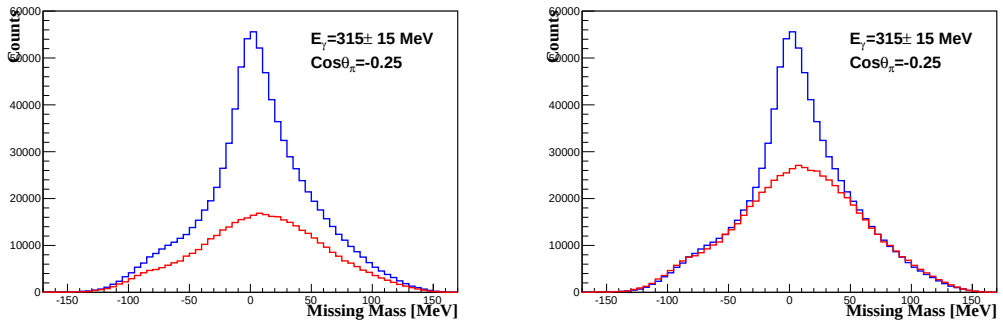

(a) (b)

Figure 6.15: Missing mass spectra from butanol and carbon target before (a) and after (b) carbon is scaled. The background in the butanol target is well-described by the scaled spectra.

incoming photon and the scattering angle of the meson, the scaling factor was determined independently for each energy and angular bin. Figure 6.16 shows the scaling factor as a function of $\cos\theta_{\pi^0}$ bin at selected photon energies. In the subsequent analysis, the scaling factors were used to scale carbon data for background subtraction and account for variations in photon energy and the π^0 scattering angle.

The scaled missing mass spectrum from carbon was subtracted from that of butanol. The resulting spectra (reconstructed hydrogen spectra) were fitted with a Gaussian and cuts described in 6.2.1 were applied. The events within the cuts were used in calculation of the dilution factor and the helicity asymmetry E for all energy and angular bins. Due to the dependence of the dilution factor on the photon energy and the scattering angle of the meson (π^0), the dilution factor and the helicity asymmetry E were calculated independently for each energy and angle bin. Figure 6.17 shows the missing mass spectra as a function of $\cos\theta_{\pi^0}$ for selected energy bins. Figure 6.18 shows the dilution factor as a function of $\cos\theta_{\pi^0}$ for selected photon energy bins. From figure 6.18 it is clear that the dilution factor is not constant as suggested by the simple calculation of 0.135 for the static case. Rather it depends on both the meson polar angle and the photon energy. This is due to the fact that different cuts applied at different energies affect the number of nucleons. The dilution factor in the exclusive analysis is higher than that obtained in an inclusive analysis because the angular cuts applied on the former suppressed much of the background, hence reducing the total number of the nucleons.

6.3.2 Data Merging

Data analyzed in this work were taken in three beam-times; November 2013 (butanol+carbon), April 2014 (carbon) and May 2014 (butanol). Extraction of the helicity asymmetry E was performed independently for November 2013 and May 2014 beam times using carbon data sets for November 2013 and April 2014, respectively. Therefore, the final values of the helicity asymmetry E were calculated from the weighted average of the values from the two beam

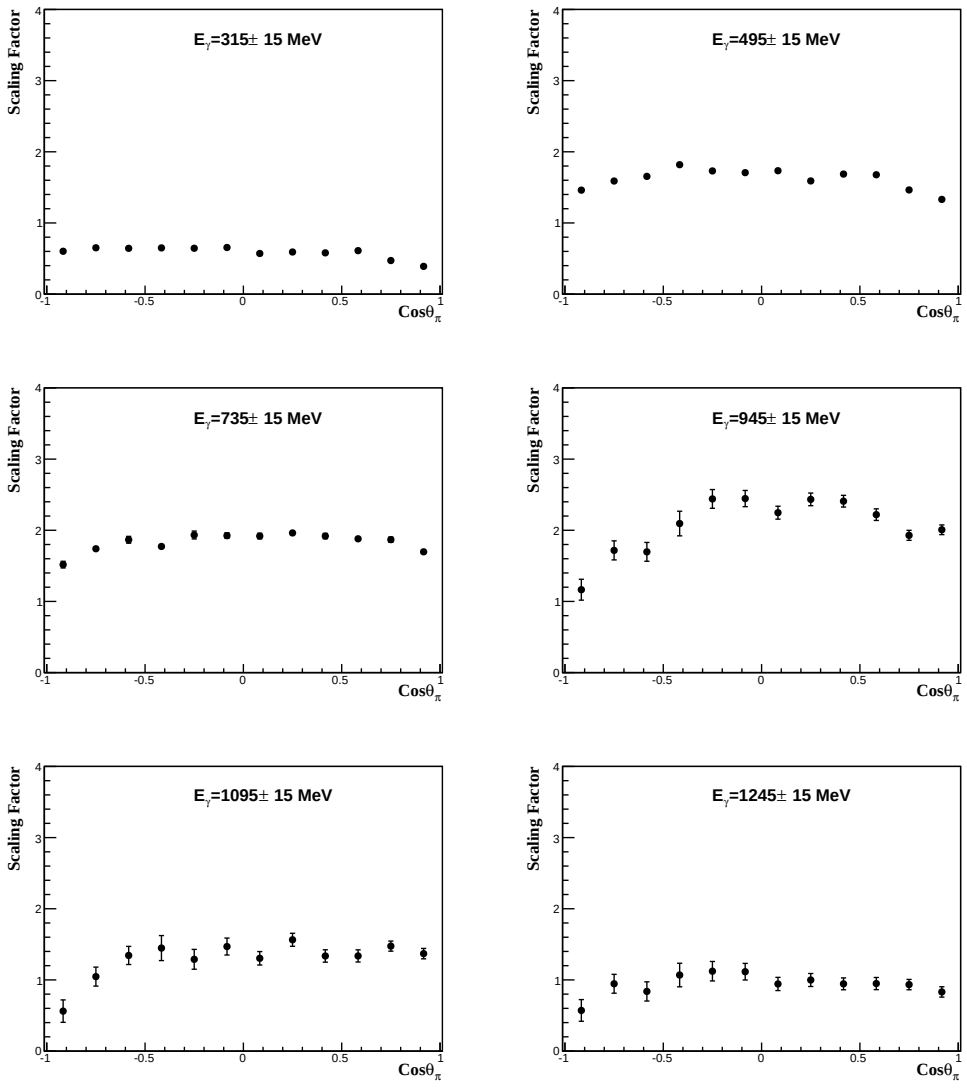

Figure 6.16: Scaling factor as a function of $\cos\theta_{\pi^0}$ for selected photon energy bins. The error bars represent the statistical uncertainty.

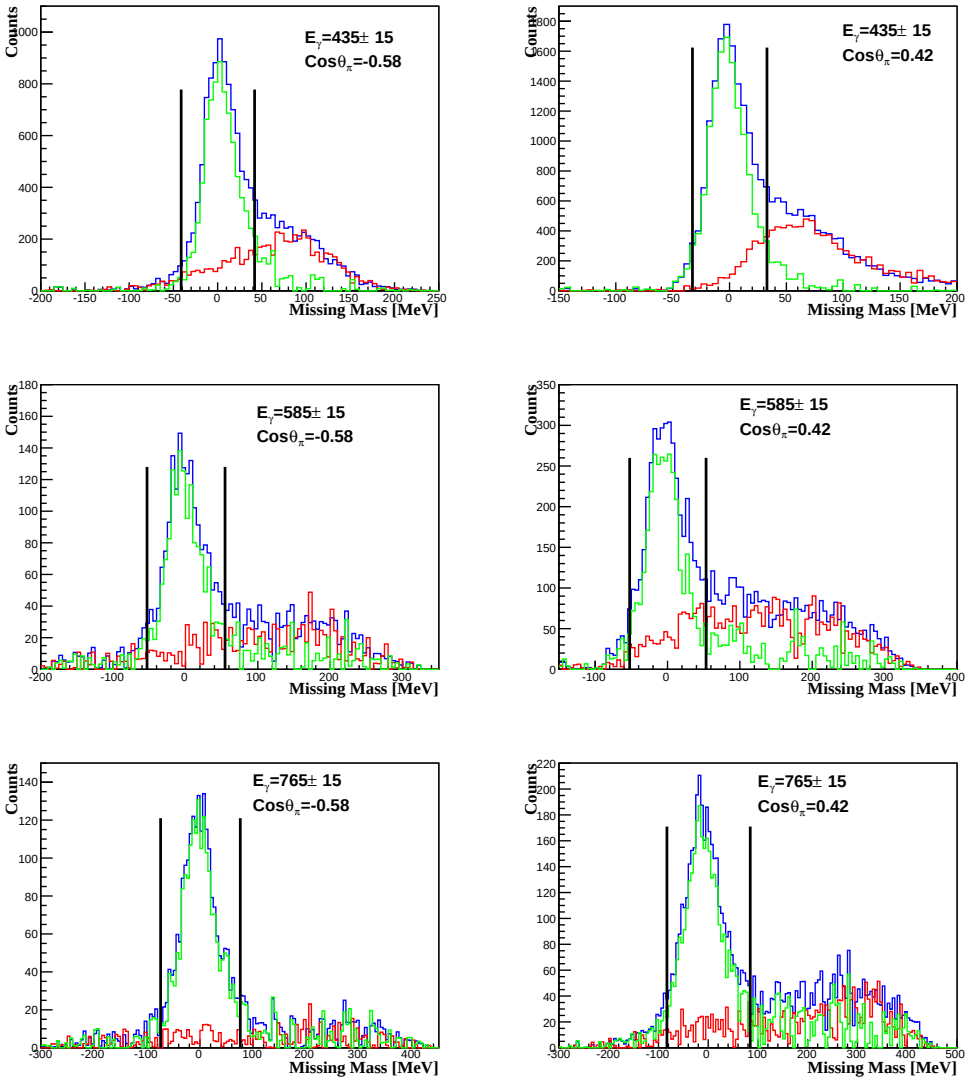

Figure 6.17: Missing mass spectra for butanol (blue), scaled carbon (red) and reconstructed hydrogen (green) for selected energy and $\cos\theta_{\pi^0}$ bins. The vertical black lines shows the cut limits.

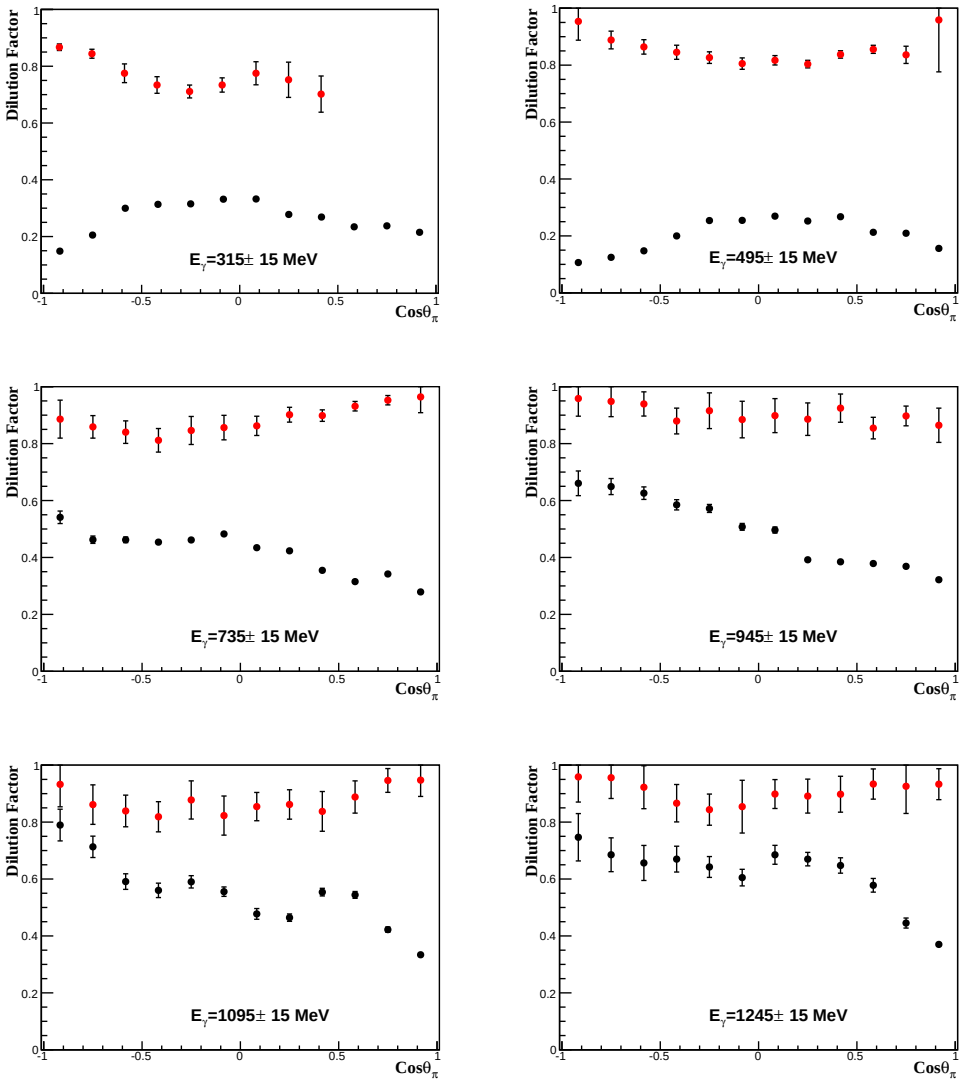

Figure 6.18: Dilution factor as a function of $\cos\theta_{\pi^0}$ for selected photon beam, energies. Red and black dots represent results for exclusive and inclusive analyses, respectively. The error bars represent the statistical uncertainty.

times. A weighted average formula was used:

$$\bar{E} = \frac{\sum(E_i/\Delta E_i^2)}{\sum(1/\Delta E_i^2)} \tag{6.17}$$

where E_i and ΔE_i are the helicity asymmetry E and its associated statistical error, respectively [147]. The weighted error $\Delta\bar{E}$ is given by:

$$\Delta\bar{E} = \frac{1}{\sqrt{\sum(1/\Delta E_i^2)}}. \tag{6.18}$$

6.4 Statistical and Systematic Uncertainties

This section presents estimation of the associated statistical and systematic errors in the extraction of the helicity asymmetry E.

6.4.1 Statistical Uncertainties

The calculation of the statistical error for the dilution factor and the helicity asymmetry E was calculated using the error propagation method [147] equation:

$$\sigma_x = \sqrt{\sum(\sigma_{N_i})^2 \left(\frac{\partial x}{\partial N_i}\right)^2} \tag{6.19}$$

where N_i is the measured variables of x and $\sigma_{N_i}^2$ is its uncertainty. Using equation (6.14) for helicity asymmetry E and (6.16) for the dilution factor, a simplified form of the helicity asymmetry E is defined as:

$$\mathbf{E} = \frac{1}{P_z^T \cdot P_{cir}^{\gamma}} \cdot \frac{N_{\frac{1}{2}} - N_{\frac{3}{2}}}{N_{\frac{1}{2}} + N_{\frac{3}{2}} - S_f N_c}. \tag{6.20}$$

Only the number of events for two helicity configurations from the butanol target and from the carbon target were considered in evaluation of the statistical errors. The contribution of the scaling factor, target and photon beam polarization were considered in the systematic uncertainties. Therefore, the

statistical uncertainty in E was calculated as;

$$\Delta E = \sqrt{(\Delta N_{1/2})^2 \left(\frac{\partial E}{\partial N_{1/2}}\right)^2 + (\Delta N_{3/2})^2 \left(\frac{\partial E}{\partial N_{3/2}}\right)^2 + (\Delta N_c)^2 \left(\frac{\partial E}{\partial N_c}\right)^2} \tag{6.21}$$

and dilution factor as;

$$\Delta D_f = \sqrt{(\Delta N_B)^2 \left(\frac{\partial D_f}{\partial N_B}\right)^2 + (\Delta N_c)^2 \left(\frac{\partial D_f}{\partial N_c}\right)^2} \tag{6.22}$$

where $\Delta N_{1/2} = \sqrt{N_{1/2}}$, $\Delta N_{2/2} = \sqrt{N_{3/2}}$, $\Delta N_B = \sqrt{N_B}$ and $\Delta N_c = \sqrt{N_c}$ were used.

6.4.2 Systematic Uncertainties

Some of the sources that contribute to the systematic uncertainties include: target and photon beam polarization, determination of the scaling factor, analysis cuts applied and the choice of event selection method (inclusive and exclusive). Different cuts were applied during the analysis, however, only the effect of the missing mass cut will be described since its spectrum was used in the extraction of the helicity asymmetry E. A brief description of each of them will be given in the following sub headings.

Target and Photon Beam Polarization

The uncertainty in the degree of target polarization basically arises from the uncertainty in the measurement of the starting and ending polarization values as explained and evaluated in 4.2.7. The uncertainty in the target polarization was evaluated to be $\approx 3\%$. The beam polarization was measured using a Møller polarimeter and compared to the measurement from a Mott polarimeter. The deviation between the Møller and Mott measurements was used as the systematic uncertainty. This deviation was $\approx 2\%$.

Scaling Factor

In order to scale the carbon data set, a scaling factor was determined by fitting the ratio of butanol and carbon target data with a combination of a Gaussian and constant. Therefore, the source of the systematic arose mainly from the choice of fitting range. The fitting range was varied from ±150 MeV to ±200 MeV from the mean position of the spectrum. The average deviation of the asymmetry E was evaluated in both cases and used to determine the systematic uncertainty $\approx 3.5\%$.

Missing Mass Cuts

In the evaluation of the helicity asymmetry E, cuts on the missing proton mass distribution were used. The reconstructed hydrogen missing mass spec-

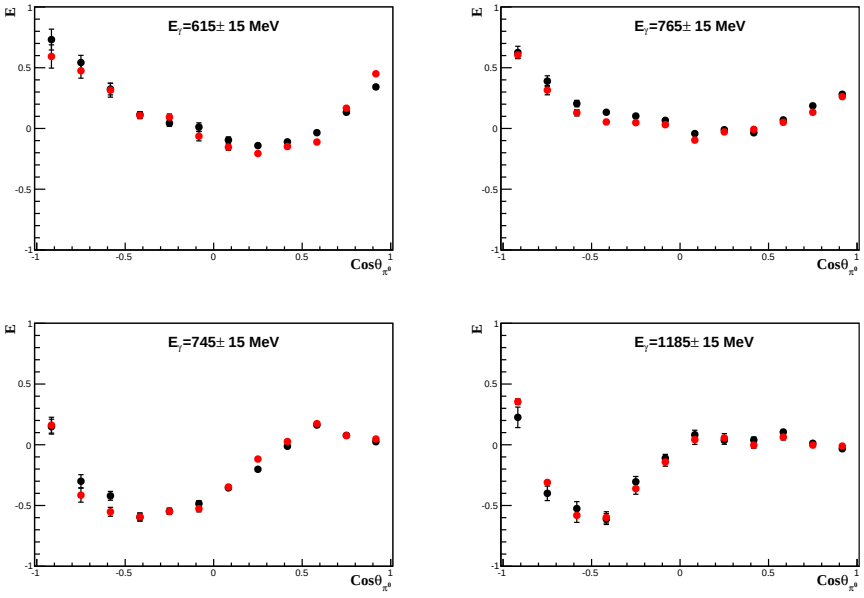

Figure 6.19: Helicity asymmetry E as a function of $\cos\theta_{\pi^0}$ obtained using 3σ (black) and 2σ (red) cuts on reconstructed missing mass spectra. The error bars represent the statistical uncertainty.

tra were fitted with a Gaussian and the mean and sigma values used to determine the cut limits. The variation of the cut limits caused a change in

the event selection with a narrow cut reducing more background but also resulting in a loss of some useful events. A wider cut retains more events, but has a higher possibility of including more background. Therefore, events from 2σ and 3σ cuts on the reconstructed hydrogen missing mass spectra were used to extract the helicity asymmetry E. The results were compared to estimate the systematic uncertainty by calculating the average deviation of the helicity asymmetry E obtained from the two cuts. This uncertainty was determined to be $\approx 3.70\%$. Figure 6.19 shows a plot of the helicity asymmetry E as a function of the photon energy obtained using 2σ and 3σ cuts on the reconstructed hydrogen missing mass.

Event Selection Method

Two event classes were used in the extraction of the helicity asymmetry E: inclusive and exclusive selection. The inclusive analysis has a higher number

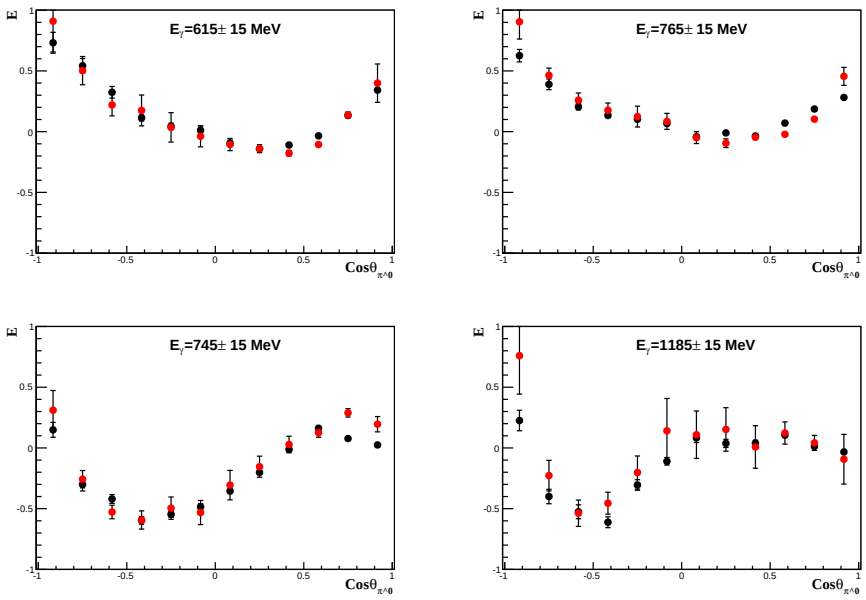

Figure 6.20: Helicity asymmetry E as a function of $\cos\theta_{\pi^0}$ for inclusive (black) and exclusive (red) analysis. The error bars represent the statistical uncertainty.

of events but at higher energies there is more background as compared to the

exclusive analysis. Therefore, analyses were performed using the two methods and the average deviation of the helicity asymmetry E was used to determine an uncertainty of $\approx 3.4\%$. Figure 6.20 shows the helicity asymmetry E as a function of $\cos\theta_{\pi^0}$ for four selected energy bins for the inclusive and exclusive analyses.

Summary

The systematic uncertainties from all sources described above were summed up quadratically to determine the total uncertainty. Table 6.2 summarizes possible sources of systematic uncertainty. The resulting total uncertainty was multiplied by the helicity asymmetry E data to get the absolute errors.

Uncertainty	Value
Target polarization	2.00%
Beam polarization	2.00%
Scaling factor	3.50%
Missing mass Cuts	3.70%
Event selection method	3.40%
Total	7.10%

Table 6.2: Summary of the systematic uncertainties.

Chapter 7

Results and Discussions

This chapter presents the results of the helicity asymmetry E for the reaction channel $\gamma p \rightarrow \pi^0 p \rightarrow 2\gamma p$ extracted using the method described in chapter 6. Section 7.1 presents the results obtained from the count rate difference between anti-parallel and parallel helicity configurations ($N^{1/2} - N^{3/2}$). A discussion on the helicity asymmetry E results is presented in section 7.2 and the interpretation of the present results is presented in section 7.3.

7.1 Count-rate Difference $N^{1/2} - N^{3/2}$

First information on the helicity asymmetry E can be gained from the numerator ($N^{1/2} - N^{3/2}$) in equation 6.14. The difference gives the information on the dependence of the polarized events on the photon energy and the scattering angle of the meson (π^0). This is achieved by filling histograms with the values from different kinematic variables (missing and invariant mass among others) independently with events from either parallel or anti-parallel configurations of the photon and target spins. The histograms from different beam-times are summed up and the difference between the anti-parallel and parallel calculated. Figure 7.1 shows the π^0 invariant mass and missing proton mass histograms (top row) for parallel and anti-parallel spin combinations. The bottom row is the difference $N^{1/2} - N^{3/2}$ of invariant and missing mass spectra.

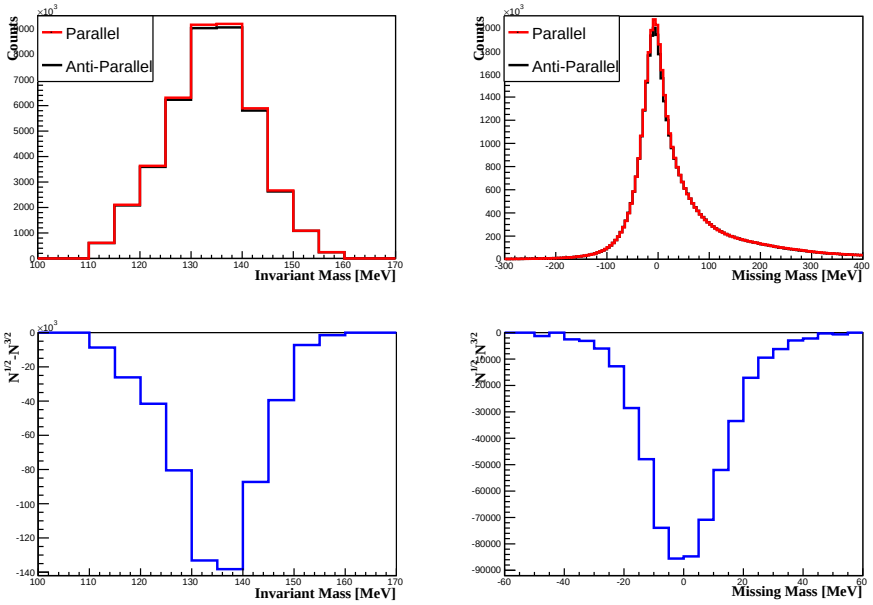

Figure 7.1: Invariant and missing mass histograms filled with events from parallel (red) and anti-parallel (black) spin configurations (top row). The count-rate difference for invariant and missing mass (bottom row).

The count-rate difference for both the invariant and missing mass shows a negative peak around the π^0 mass and zero, respectively, an indication of an overall dominance of total spin 3/2 in π^0 photoproduction. Similarly, events from the two helicity configurations were filled in a histogram as a function of photon energy as shown in figure 7.2. The energy dependent spectrum is not smooth at all energy bins as expected due to tagger inefficiencies. The count-rate difference plotted in figure 7.3 was calculated using the difference in missing mass spectra for each energy bin for the anti-parallel and parallel helicity configurations. Considering the count-rate difference as a function of photon energy shown in figure 7.3, various peaks are visible around 300 MeV, 700 MeV and 1 GeV. These peaks correspond to contributions of different nucleon resonances extracted from experimental data and predicted by models [49, 15, 16, 17, 19]. The first negative peak correspond to the Δ-resonance region $\Delta(1232)3/2^+$ dominated by the total spin 3/2. At the second resonance region a positive peak is visible at around 700 MeV as

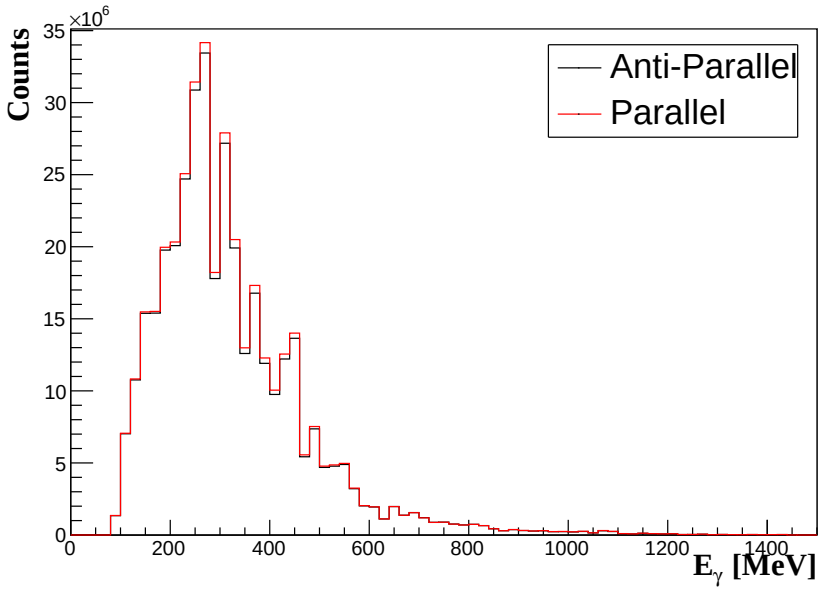

Figure 7.2: Histogram filled with events from parallel (red) and anti-parallel (black) spin configurations as a function of photon energy. The energy spectrum is not smooth at all energies due to the tagger inefficiencies.

shown in figure 7.3b. This region is dominated by several nucleon resonances with N(1535)$1/2^-$ and N(1520)$3/2^-$ having the largest contributions. In this region a positive peak is visible, an indication of helicity 1/2 dominance. The third negative peak around 1 GeV corresponds to the third resonance region. In this region, the main contributions are due to N(1700)$3/2^-$, N(1680)$5/2^+$ and N(1650)$1/2^-$ resonances, each contributing $\approx 35\%$, $\approx 25\%$ and $\approx 20\%$, respectively.

7.2 Helicity Asymmetry E Results

In this section results of the helicity asymmetry E are presented in the energy range $E_\gamma = 210 - 1410$ for 40 energy bins. Each energy bin is 30 MeV wide and includes 12 bins in the π^0 polar angle. Due to low proton detection at low reaction energies and high background contribution at high energies, the helicity asymmetry results presented in this work are for the inclusive

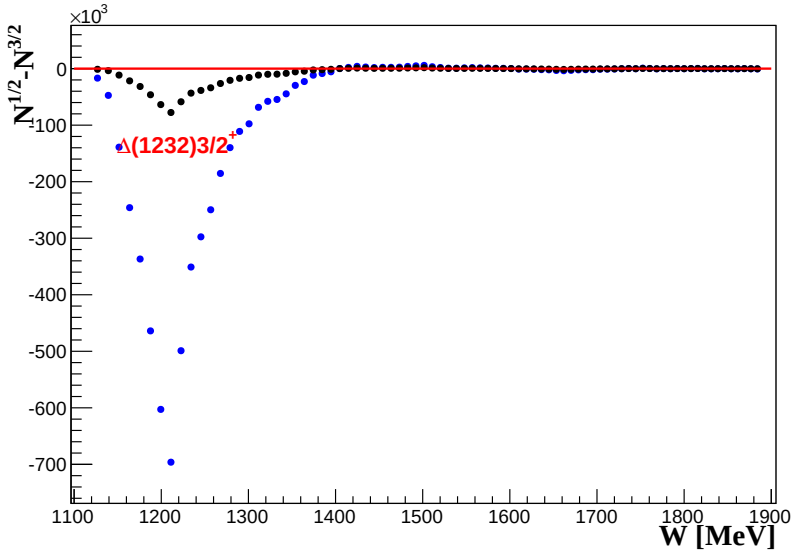

(a)

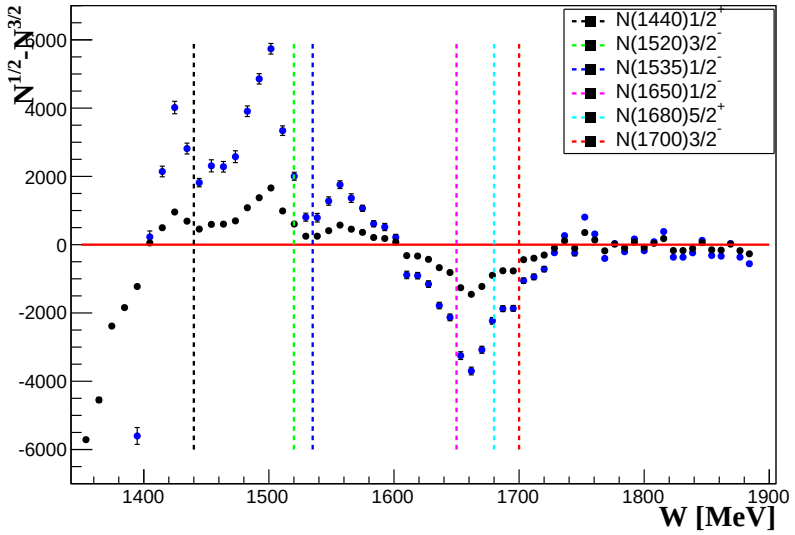

(b)

Figure 7.3: The count-rate difference as a function of energy for $W = 1120 - 1885$ MeV for the reaction $\gamma p \rightarrow \pi^0 p$. (a) shows the spectra for the complete energy range studied while (b) is a zoom out of the same figure from 1350 MeV. The blue symbols are the count-rate difference scaled with the target and beam polarization $(1/P_\gamma P_T)$ while the black ones are the unscaled spectrum. The dotted line shows the position of the known resonances.

analysis in the range $E_\gamma < 570$ MeV and for the exclusive analysis in the range $E_\gamma > 570$ MeV. In all plots, the error bars represent the statistical uncertainties while the gray bars represent the systematic uncertainties. The present results are compared to data from CBELSA/TAPS [148] in the energy range $E_\gamma = 600 - 1230$ MeV. Figures 7.4 through 7.7 show the helicity asymmetry E as a function of the $\cos\theta_{\pi^0}$ at different energy bins.

Depending on the contribution of different partial waves to a given resonance, the asymmetry shows various angular shapes at different energy bins. In the Δ-resonance region $\Delta(1232)3/2^+$, the asymmetry shows a strong contribution from the $J^P = \frac{3}{2}^+$ partial wave. The asymmetry in this region is mainly negative. In the energy range $E_\gamma = 450-850$ MeV, several resonances contribute to the reaction. The main contributions are from the N(1520)3/2$^-$ and N(1535)1/2$^-$ resonances while $\Delta(1232)3/2^+$ and N(1440)1/2$^+$ contribute weakly. Due to the dominance of $J^P = \frac{1}{2}^-$ the values of the helicity asymmetry E are positive especially for the energy range $E_\gamma = 600 - 800$ MeV. In the energy range $E_\gamma = 870 - 1260$, the N(1680)5/2$^+$ and N(1650)1/2$^-$ resonances dominate the asymmetry. A W-shape like structure is observed in the asymmetry as shown in figure 7.6 and 7.7, an indication of contribution of both $J^P = \frac{5}{2}^+$ and $J^P = \frac{1}{2}^-$ partial waves as observed in [60]. In the energy range $E_\gamma = 1250-1410$ MeV, the asymmetry shows a wavy shape, an indication of contributions from interference of several resonances including N(1700)3/2$^-$, N(1710)1/2$^+$ and N(1720)3/2$^+$.

The present results show a general agreement with the CBELSA/TAPS data [148]. However, for energy above 800 MeV there is a discrepancy for the values between $\cos\theta_{\pi^0} = \pm\ 0.5$. At these angles the present asymmetry is smaller than the CBELSA/TAPS results. This may be as a result of systematics arising from the experimental setup and analysis method for both CBELSA/TAPS and A2Mainz.

In addition, our data are compared to the model predictions (see section 2.3) of MAID (MAID2007) [15], Bonn-Gatchina (BnGa 2014-02) [17] and SAID (SAID-CM12) [16]. In the Δ-resonance region, our result generally agrees with the three models simply because only one resonance ($\Delta(1232)3/2^+$) contributes in this region. In the energy range $E_\gamma = 470 - 840$ MeV (the

second resonance region), the PWA model of SAID and BnGa gives a good description of our data except at the backward angles where the present data is smaller. For the energy range $E_\gamma = 700 - 1020$ MeV, the MAID model shows a large asymmetry compared to our data and other models. This could be explained by the fact that the SAID and BnGa models have been fitted with the most recent data sets of cross sections and polarization observables which were not available at the time when the MAID2007 solution was released. The SAID and BnGa results and our data show reasonable agreement for the angular range $\cos\theta_{\pi^0} \leq 0.0$ but slightly differs for other angles. For $E_\gamma \geq 850$ MeV, our results tends to favor the BnGa and MAID models. The asymmetry E results for each $\cos\theta_{\pi^0}$ bin have been plotted as a function of photon beam energy and compared to the models as shown in figure 7.8.

7.3 Interpretation of the Results

This section presents the interpretation of the results both by expansion of the polarized cross section in terms of Legendre polynomial (7.3.1) and by simultaneous fitting of cross section and polarization observables in a combined fit to extract multipole information (7.3.2).

7.3.1 Legendre Polynomial Fits

Photoproduction observables in equation (2.28) can be expanded in terms of Legendre polynomials up to a maximum angular momentum (L_{max}) as explained in 2.2. The helicity cross section $\hat{E} = E \cdot \frac{d\sigma_0}{d\Omega}$ can be expressed in the following way:

$$\hat{E}(W,\theta) = \sum_{j=0}^{j_{max}} A_j(W) P_j(\cos\theta) \tag{7.1}$$

where A_j are the Legendre polynomial coefficients representing a series of bilinear products of electromagnetic multipoles and $P_j(cos\theta)$ are Legendre polynomials of order j [23]. The asymmetry E was multiplied with the experimental unpolarized cross section for $\gamma p \rightarrow \pi^0 p$ reaction from our collaboration [19]. j_{max} in equation (7.1) is related to the maximum orbital

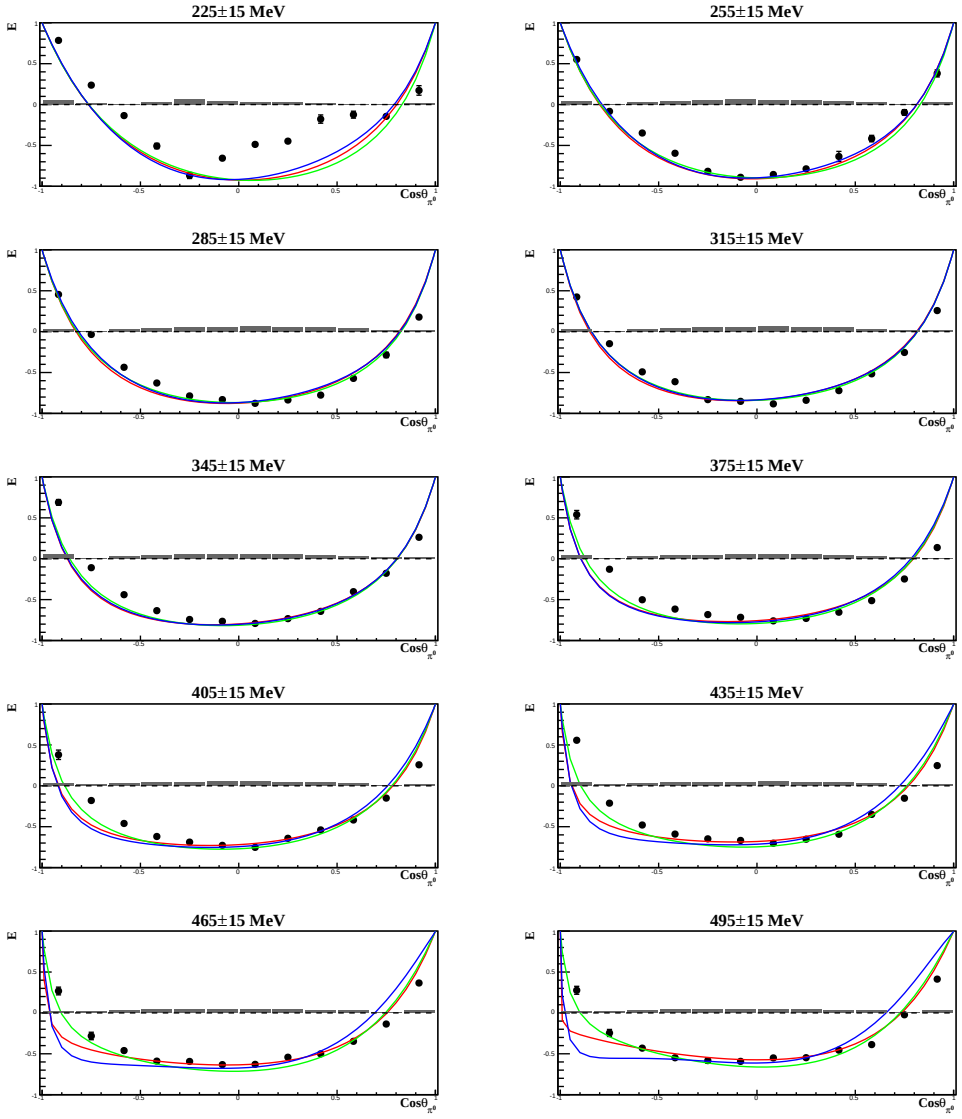

Figure 7.4: Helicity asymmetry E as a function of $\cos\theta_{\pi^0}$ for $E_\gamma = 210 - 510$ MeV. The symbols and lines represent the data and model predictions, respectively. • present data, MAID2007 (red), BnGa 2014-02 (green) and SAID-CM12 (blue). Grey bars are the systematic uncertainties.

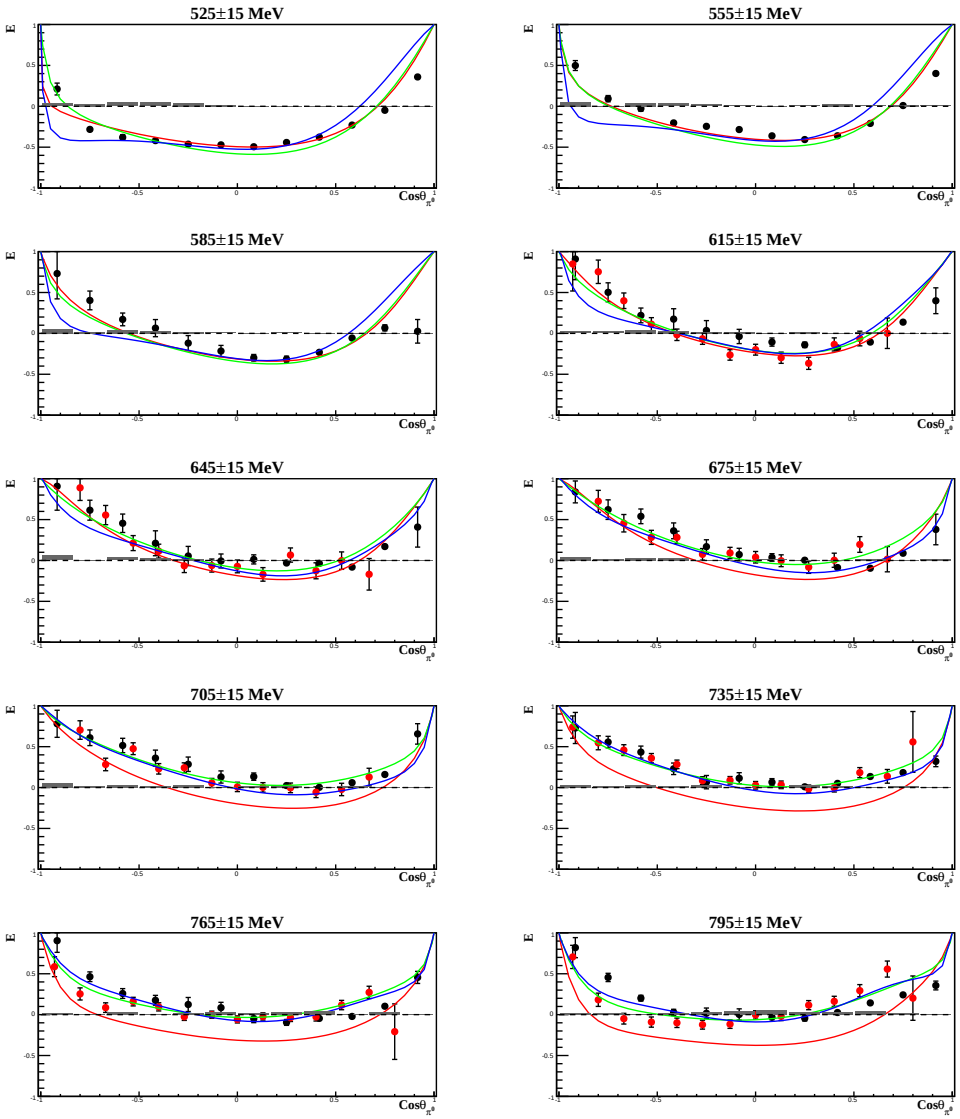

Figure 7.5: Helicity asymmetry E as a function of $\cos\theta_{\pi^0}$ for $E_\gamma = 510 - 810$ MeV. The symbols and lines represent the data and model predictions, respectively. • present data, • CBELSA/TAPS data, MAID2007 (red), BnGa 2014-02 (green) and SAID-CM12 (blue). Grey bars are the systematic uncertainties.

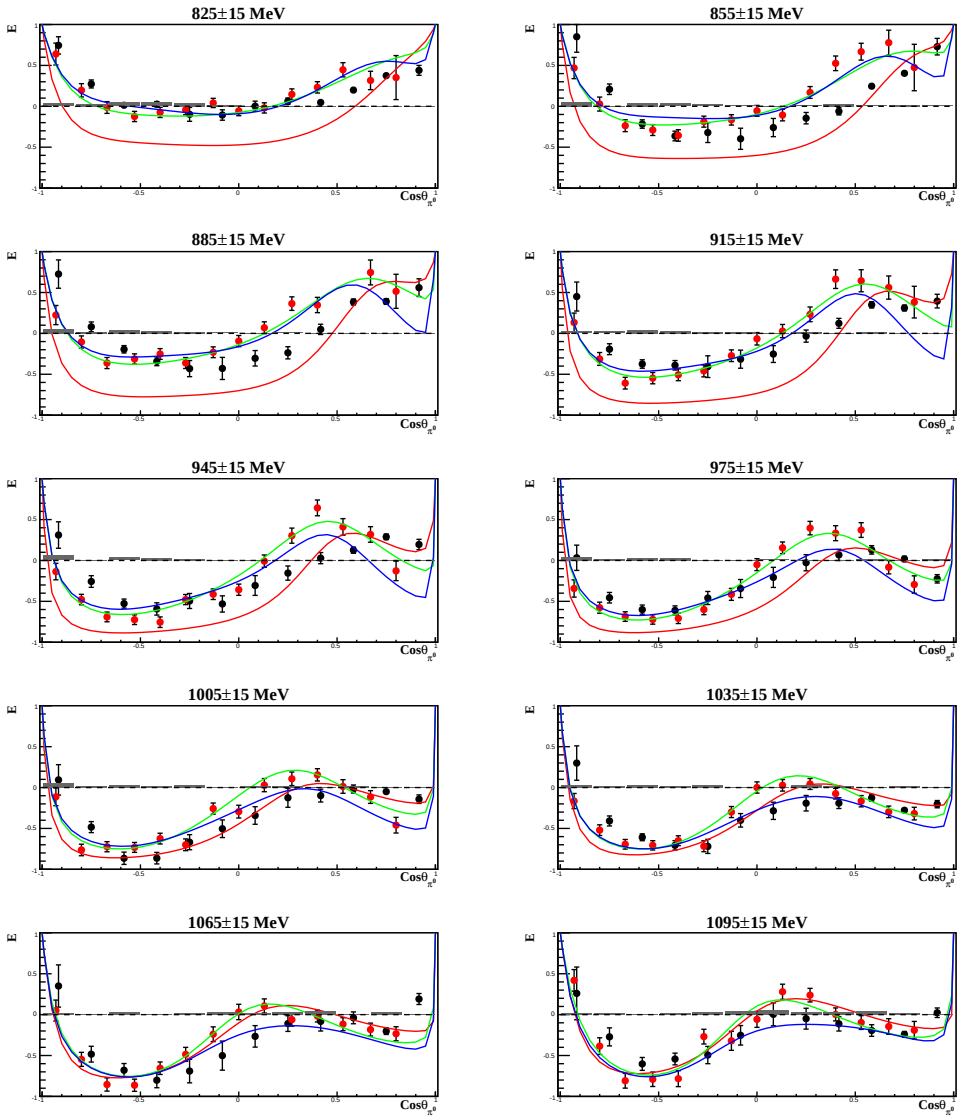

Figure 7.6: Helicity asymmetry E as a function of $\cos\theta_{\pi^0}$ for $E_\gamma = 810-1110$ MeV. The symbols and lines represent the data and model predictions, respectively. • present data, • CBELSA/TAPS data, MAID2007 (red), BnGa 2014-02 (green) and SAID-CM12 (blue). Grey bars are the systematic uncertainties.

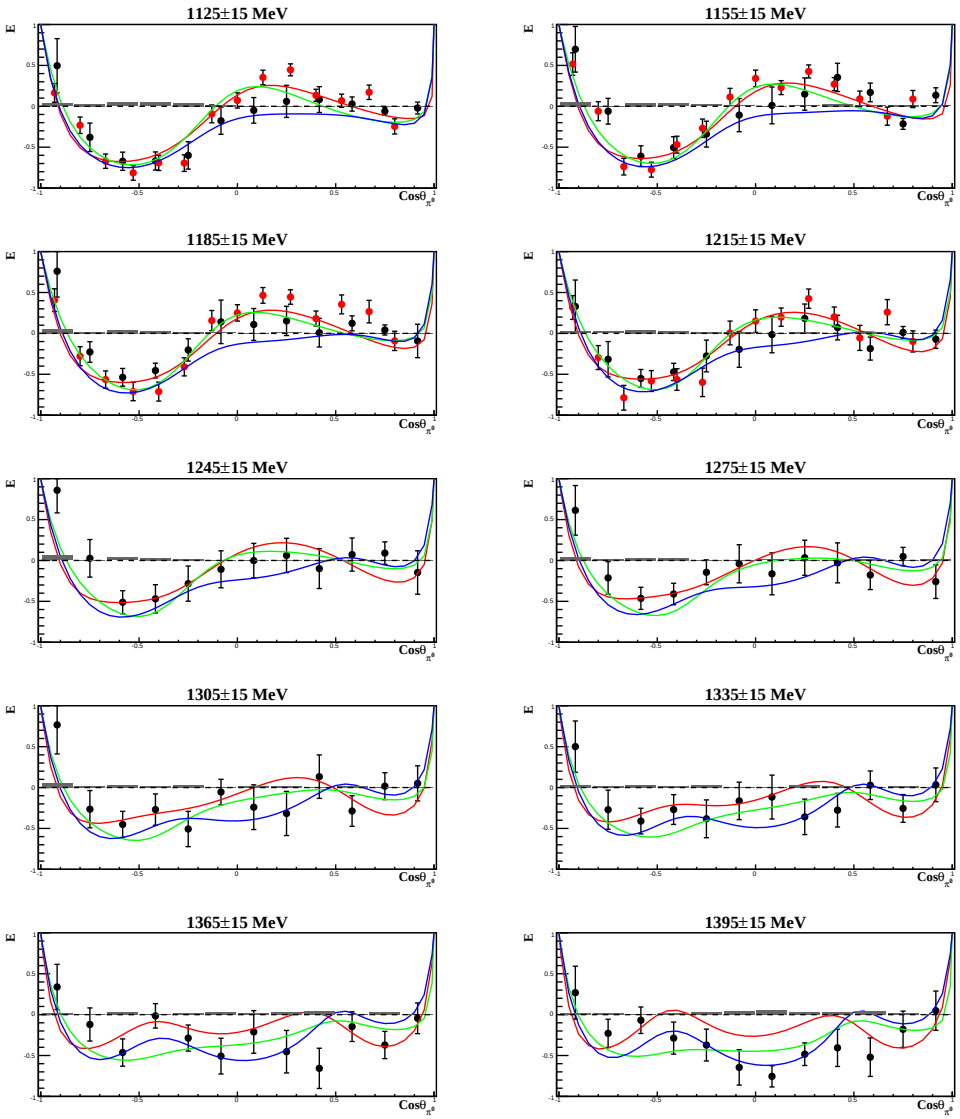

Figure 7.7: Helicity asymmetry E as a function of $\cos\theta_{\pi^0}$ for $E_\gamma = 1110-1410$ MeV. The symbols and lines represent the data and model predictions, respectively. • present data, • CBELSA/TAPS data, MAID2007 (red), BnGa 2014-02 (green) and SAID-CM12 (blue). Grey bars are the systematic uncertainties.

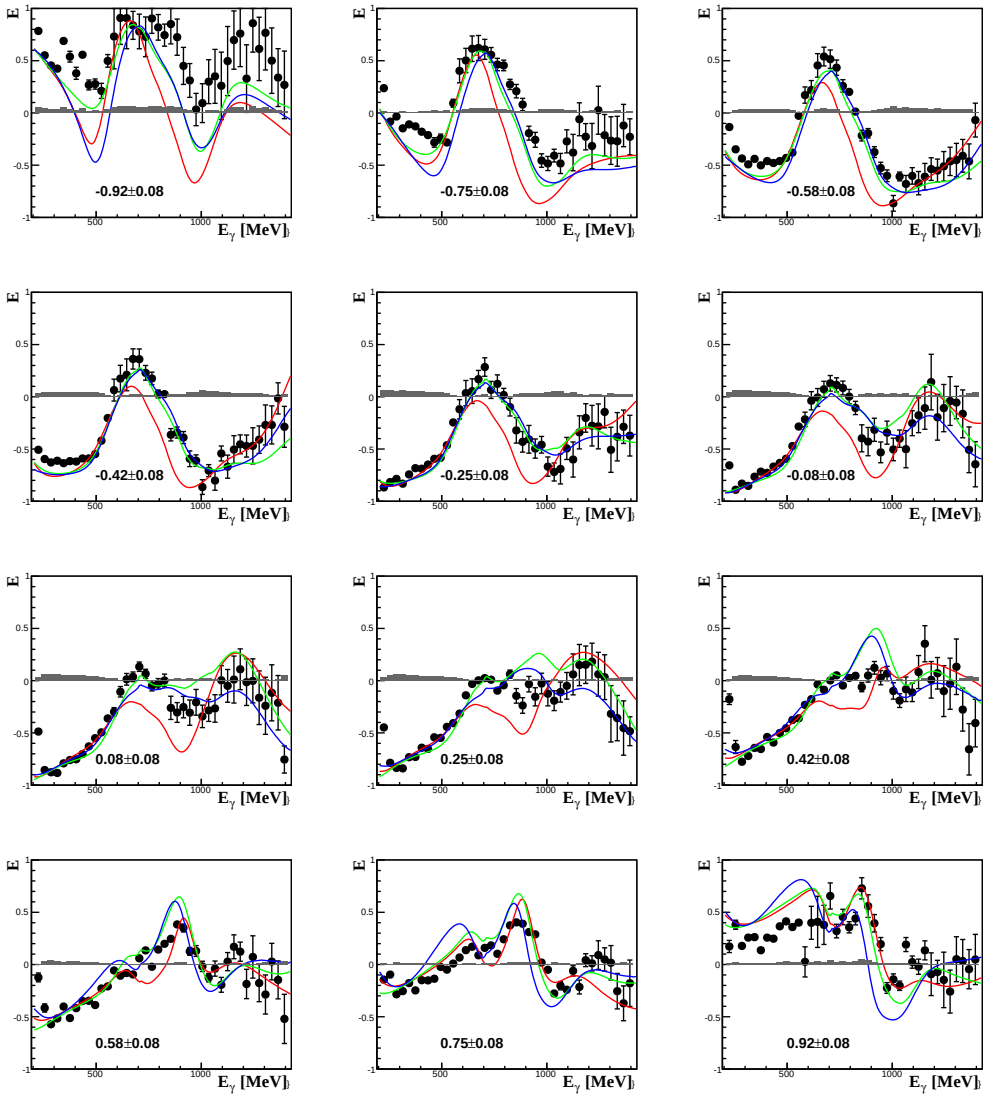

Figure 7.8: Helicity asymmetry E as a function of photon beam energy for different $\cos\theta_{\pi^0}$ bins. The symbols and lines represent the data and model predictions, respectively. • present data, MAID2007 (red), BnGa 2014-02 (green) and SAID-CM12 (blue). Grey bars are the systematic uncertainties.

angular momentum L_{max} of the $p\pi$ system ($j_{max} = 2L_{max}$). For example, if $L_{max} = 1$ then $j_{max} = 2$, meaning that only S- and P-waves will contribute to the resonances. The number of terms required in the Legendre series, j_{max}, depends on the orbital angular momentum of the partial wave amplitude or the highest spin of the resonances existing in the studied energy range, e.g., an isolated resonance with spin $J = (2L_{max} + 1)/2$ can contribute to coefficients A_j only with even j up to $j = 2L_{max}$ and to other coefficients via interference with the background amplitudes [19]. In addition, j_{max} is limited by the quality of the data being fitted, e.g., data with high statistics can be well-described with fits of higher orders of j_{max}.

In this work, the $\hat{E}$ was fitted with Legendre polynomials of order $j_{max} = 4, 6, 8$ and 10 to determine the best fit to the data. The reduced χ^2, i.e., χ^2/NDF was plotted as a function of energy for each energy bin as shown in figure 7.9a and a zoom out in figure 7.9b. A comparison of the reduced χ^2 for the fits with different values of j_{max} shows that there is no significant difference in the χ^2 for $j_{max} = 8$ and 10. Using $j_{max} = 8$ would have been the best choice but due to low statistics of our data it was not used. Instead $j_{max} = 6$ was used in order to get a reasonable fit to the data. Low order fits such as $j_{max} = 4$ were not used because they could only describe the data well for energies ≤ 1 GeV but not for energies above 1 GeV. In the $\Delta(1232)3/2^+$ region, the χ^2 values are large (between 2-35) compared to those in energy ≥ 570 MeV due to very small statistical uncertainties arising from high statistics in the $\Delta(1232)3/2^+$ region.

Figures 7.10 through 7.11 show a fit on the $\hat{E}$ data up to $j_{max} = 6$. This resulted in seven coefficients which are plotted as a function of photon beam energy as shown in figure 7.12. The errors in the coefficients represent the uncertainties obtained from the fits that took into account only the statistical uncertainties of the polarized cross section $\hat{E}$. The coefficient A_j results show some bumps corresponding to different resonance regions. The first coefficient A_0 shows a clear structure in the Δ-resonance region and first resonance region. A_1 and A_3 show peaks in the third-resonance region while A_4 and A_5 show peaks in the fourth-resonance region. The coefficients are compared to results obtained by fitting MAID, BnGa and SAID models prediction with

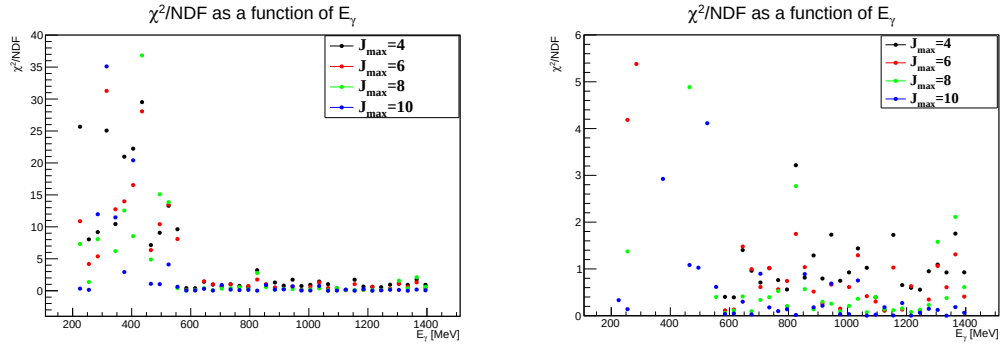

(a) (b)

Figure 7.9: The χ^2/NDF for the Legendre polynomial as a function of the photon energy for $j_{max} = 4$, 6, 8 and 10. (b) is a zoom out of figure (a).

Legendre polynomials up to $j_{max} = 6$. The fits from all model predictions reproduce fairly well only the coefficient A_0 as shown in figure 7.12. Other coefficients ($A_1 - A_6$) show large discrepancies especially in the Δ-region. The expansion of the present polarized cross section only serves as a first step towards a full single energy partial wave analysis. A direct extraction of the partial wave amplitudes by simultaneously fitting the present data, other polarization observables and cross sections is discussed in section 7.3.2. However, the expansion of the polarized cross section in terms of Legendre polynomials shows the sensitivity of the data to partial wave amplitudes up to F-waves ($L_{max} = 3$).

7.3.2 Multipole Analysis

In addition to Legendre expansion, a multipole analysis using the present data in combination with other experimental data (differential cross sections and polarization observables) was performed. A single energy fitting program [149], based on MINUIT [135] was used to determine the electromagnetic multipoles of pseudoscalar meson photoproduction from experimental cross sections and observables. The multipole fits are performed on fixed energy positions using the energy information of the unpolarized cross section σ_o. This is because σ_o have higher data points as compared to polarization ob-

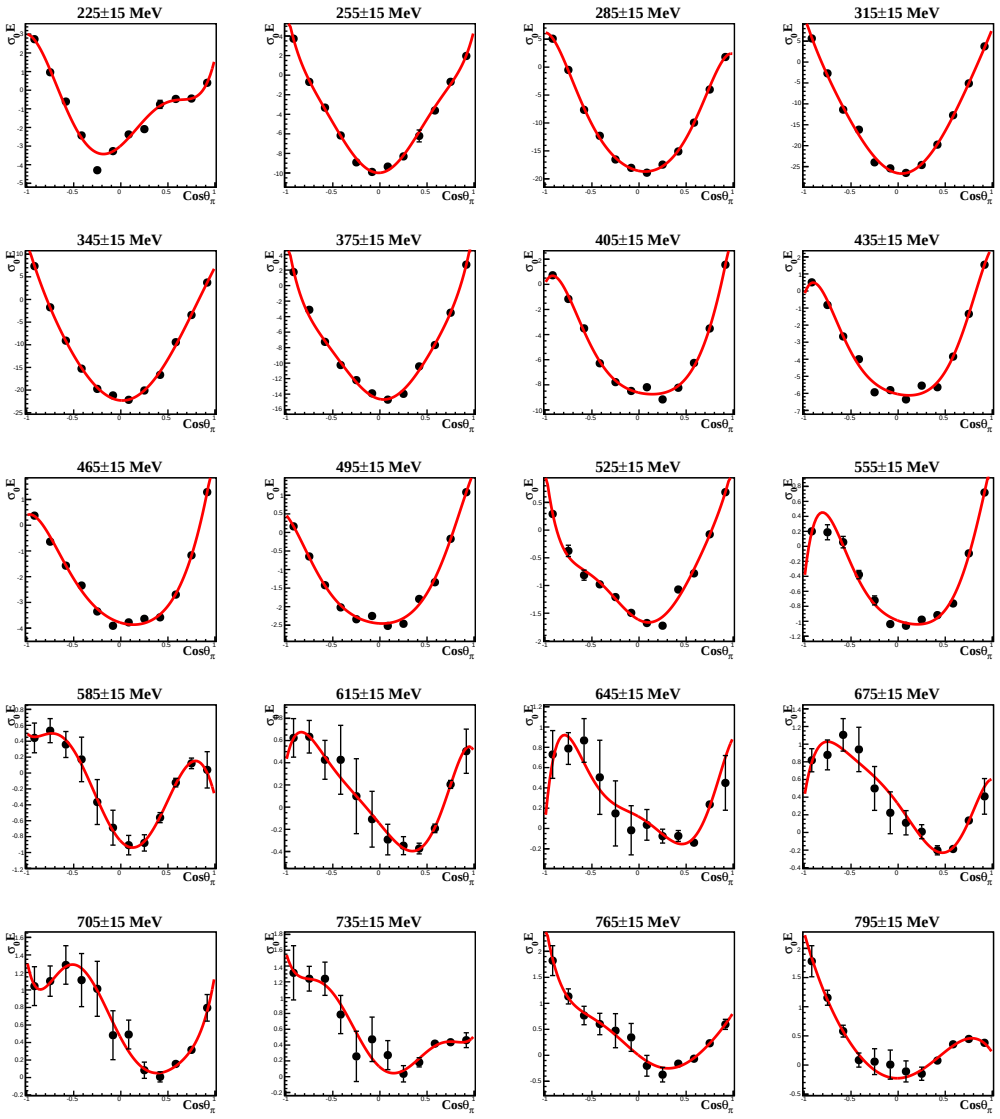

Figure 7.10: Legendre polynomial fit for $\hat{E}$ as a function of $\cos\theta_{\pi^0}$ for $E_\gamma = 210 - 810$ MeV.

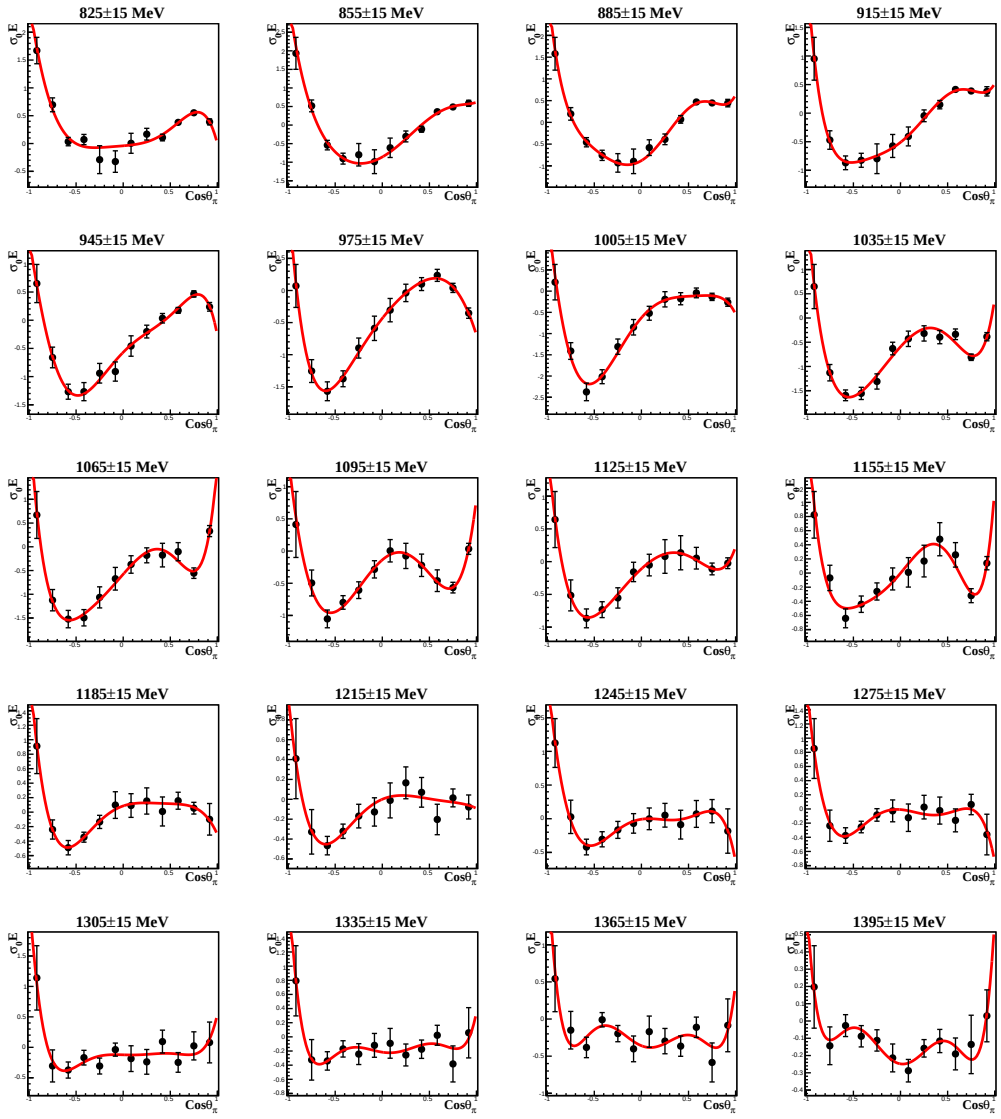

Figure 7.11: Legendre polynomial fit for polarized cross section $\hat{E}$ as a function of $\cos\theta_{\pi^0}$ for $E_\gamma = 810 - 1410$ MeV.

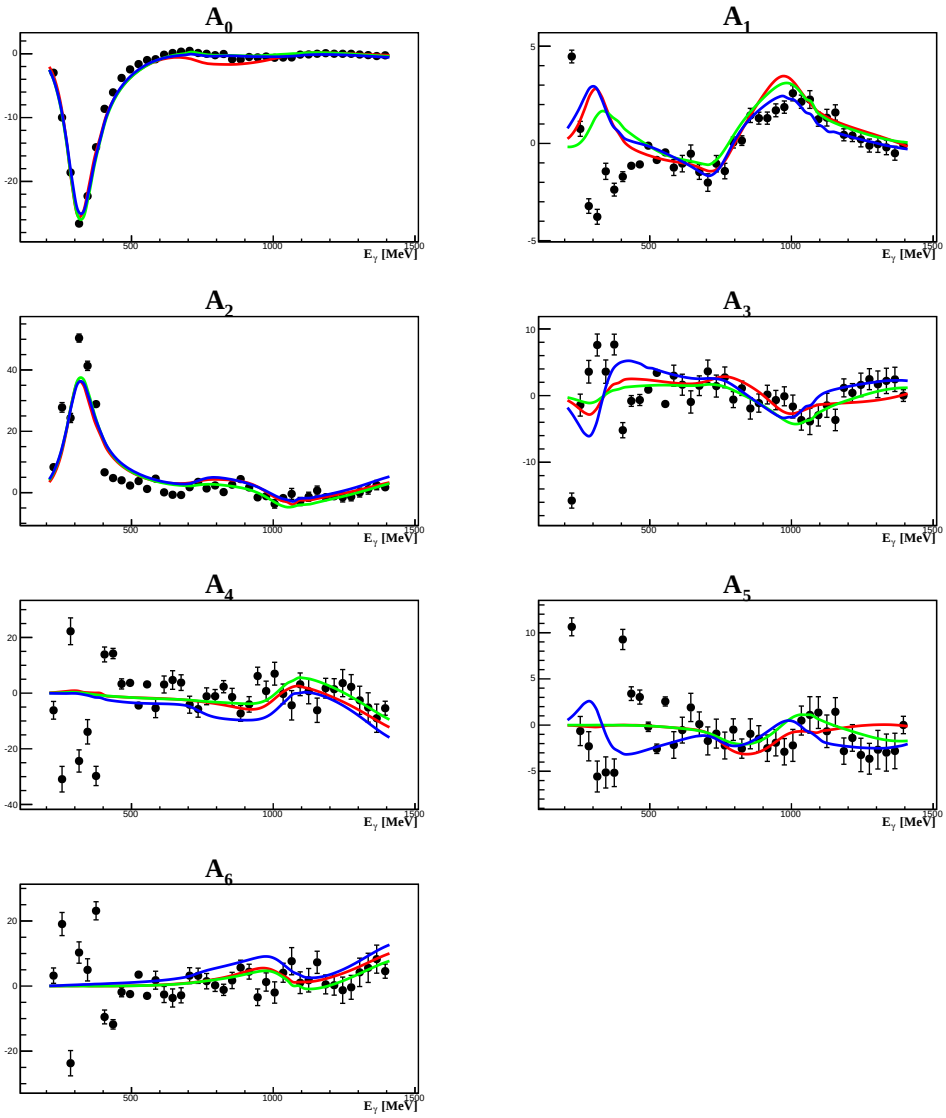

Figure 7.12: Legendre coefficients up to $j_{max} = 6$ for polarized cross section $\hat{E}$ (•) compared to MAID2007 (red), BnGa-2014-02 (green) and SAID-CM12 (blue) models.

servables data which are mostly available in wider energy binning and with low statistics [150]. The multipoles are extracted using a χ^2 minimization with a possibility of adding an additional constraints.

The differential cross section and the polarization observables can be expressed in terms of CGLN amplitudes (see equation (2.18)) which depend on the electromagnetic multipoles $E_{L_\pm}$ and $M_{L_\pm}$ for multipoles of order L up to L_{max} and the derivatives of the Legendre polynomials describing their angular dependencies. Therefore, the observables from the beam-target polarization in equation (2.28) can be expressed in terms of the four CGLN amplitudes $\mathcal{F}_i$ as follows:

$$
\begin{aligned}
\sigma_0 &= \mathbf{Re}(|\mathcal{F}_1|^2 + |\mathcal{F}_2|^2 - 2\cos\theta\mathcal{F}_1\mathcal{F}_2 + \tfrac{1}{2}\sin^2\theta(|\mathcal{F}_3|^2 + |\mathcal{F}_4|^2 + 2\mathcal{F}_2\mathcal{F}_3 \\
&\quad +2\mathcal{F}_1\mathcal{F}4 + 2\cos\theta\mathcal{F}_3\mathcal{F}_4)) \cdot \rho \\
\sigma_o\Sigma &= -\tfrac{1}{2}\sin^2\theta\mathbf{Re}\{|\mathcal{F}_3|^2 + |\mathcal{F}_4|^2 + 2(\mathcal{F}_2\mathcal{F}_3^* + \mathcal{F}_4\mathcal{F}_1^* + \cos\theta\mathcal{F}_4\mathcal{F}_3^*)\} \cdot \rho \\
\sigma_o T &= \sin\theta\mathbf{Im}\{\mathcal{F}_1^*\mathcal{F}_3 - \mathcal{F}_2^*\mathcal{F}_4 + \cos\theta(\mathcal{F}_1^*\mathcal{F}_4 - \mathcal{F}_2^*\mathcal{F}_3) - \sin^2\theta\mathcal{F}_4\mathcal{F}_3^*)\} \cdot \rho \\
\sigma_o P &= \sin\theta\mathbf{Im}\{\mathcal{F}_2^*\mathcal{F}_4 - 2\mathcal{F}_1^*\mathcal{F}_2 - \mathcal{F}_1\mathcal{F}_3 + \cos\theta(\mathcal{F}_2^*\mathcal{F}_3 - \mathcal{F}_1^*\mathcal{F}_4) + \sin^2\theta\mathcal{F}_4\mathcal{F}_3^*)\} \cdot \rho \\
\sigma_o E &= \mathbf{Re}\{|\mathcal{F}_1|^2 + |\mathcal{F}_2|^2 - 2cos\theta\mathcal{F}_2\mathcal{F}_1^* + \sin^2\theta(\mathcal{F}_1\mathcal{F}_4^* + \mathcal{F}_2\mathcal{F}_3^*)\} \cdot \rho \\
\sigma_o F &= \sin\theta\mathbf{Re}\{\mathcal{F}_1^*\mathcal{F}_4 - \mathcal{F}_2^*\mathcal{F}_4 + \cos\theta(\mathcal{F}_1^*\mathcal{F}_4 + \mathcal{F}_2^*\mathcal{F}_3)\} \cdot \rho \\
\sigma_o G &= \sin^2\theta\mathbf{Im}\{\mathcal{F}_2^*\mathcal{F}_3 + \mathcal{F}_1^*\mathcal{F}_4\} \cdot \rho \\
\sigma_o H &= \sin\theta\mathbf{Im}\{\mathcal{F}_1^*\mathcal{F}_2 + \mathcal{F}_1^*\mathcal{F}_3 - \mathcal{F}_2\mathcal{F}_4 - \cos\theta(\mathcal{F}_2^*\mathcal{F}_3 - \mathcal{F}_1^*\mathcal{F}_4)\} \cdot \rho
\end{aligned}
$$

where $\rho = \frac{q}{k}$ is a phase space factor given by meson and photon momenta q and k.

From the relationship between the observables and the electromagnetic multipoles, a χ^2 function with multipoles as fit parameters and physical observables as experimental input can be created. In this work, the experimental results listed in 7.1 from our collaboration were used. The fitting algorithm uses a start parameter from an existing photoproduction or partial wave analysis (PWA) model. In this work the Bonn Gatchina (BnGa) PWA model was used. The starting values for all fitting parameters are changed slightly by random numbers within an adjustable band around the model solution.

The multipole fits were performed in the energy range $E_\gamma = 210 - 1410$

Observable	Energy Range [MeV]	Number of data points
σ_0	218-1443	7380
σ_F	145-419	4500
σ_T	145-419	4500
F	425-1445	465
T	425-1445	466
Σ	146-206	528
E	210-1410	480

Table 7.1: A summary of the experimental photoproduction data used for multipole fitting. σ_o is the unpolarized cross sections [19], $\sigma_T = \sigma_o \cdot T$ and $\sigma_F = \sigma_o \cdot F$ are the polarized cross section [151], and F [152], T [152], Σ [153] and E are experimental polarization observables data from A2Mainz.

MeV for maximum orbital angular momentum $L_{max} = 3$. This results in twelve multipoles: E_{0+}, E_{1+}, M_{1+}, M_{1-}, E_{2+}, E_{2-}, M_{2+}, M_{2-}, E_{3+}, E_{3-}, M_{3+} and M_{3-}. The phase of the fitted multipole was not fixed to the models. The results of some multipoles: E_{0+}, E_{1+}, M_{1+}, M_{1-}, E_{2-} and M_{3-} are shown in figures 7.13 through 7.15 (other multipole results are in appendix A.3). From the results, it is not clear if the data fits well to the multipoles

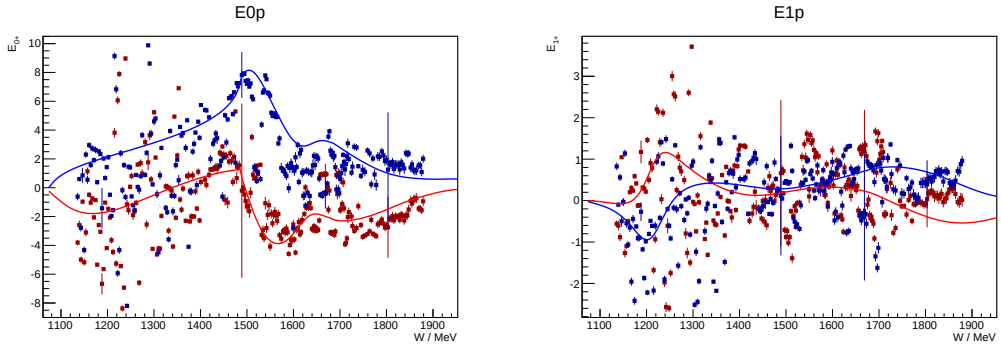

(a) (b)

Figure 7.13: Multipole fit results for E_{0+} (a) and E_{1+} (b). The blue and red colors represent the real and the imaginary parts of the multipoles, respectively.

since the data points are spread over a large region without a definite shape. Therefore, no meaningful information of the multipoles can be extracted. This may be due to the fact that the observables data are limited in energy

and have wide angular bins. In order to have a better fit, an additional constraint was introduced in the form of a "penalty term" to the χ^2 such that the minimization is implemented using a function:

$$f_{FCN} = \chi^2 + Q \tag{7.2}$$

where Q is the "penalty term". Q is designed in a way that it gets larger if

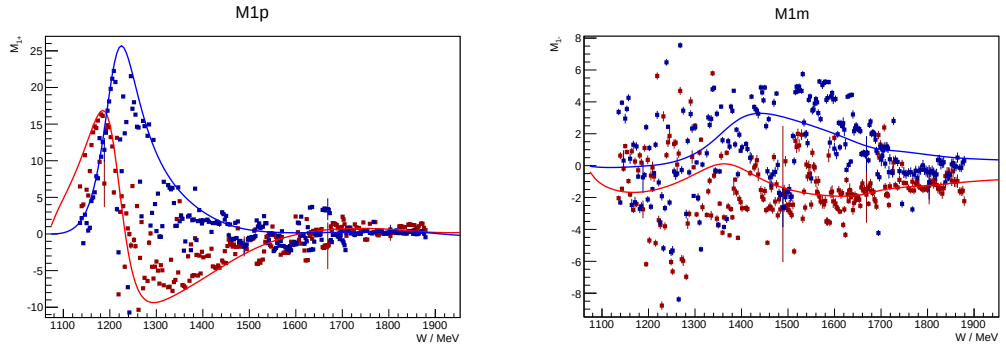

(a) (b)

Figure 7.14: Multipole fit results for M_{1+} (a) and M_{1-} (b). The blue and red colors represent the real and the imaginary parts of the multipoles, respectively.

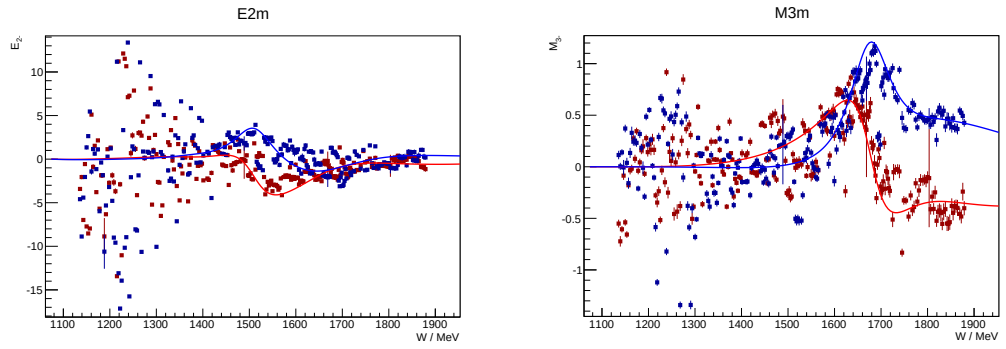

(a) (b)

Figure 7.15: Multipole fit results for E_{2-} (a) and M_{3-} (b). The blue and red colors represent the real and the imaginary parts of the multipoles, respectively.

the fit parameter deviates from the model solution. Any deviation from the

model is "penalized" in the fitting. This ensures that the single energy fits at different energies fulfill a smooth energy dependence constraint especially where the experimental data are too few (in-terms of number of observables or angular coverage) or have limited precision.

The algorithm supports different penalty terms as explained in [150]. However, in this work CGLN amplitudes $\mathcal{F}_i, i = 1...4$ in equation (2.18) were used to calculate the "penalty term". A weighting factor of $f_i = 0.5$ for each CGLN amplitude $\mathcal{F}_i$ was applied. The weighting factor adjust the size of the penalty contribution Q relative to χ^2. Figures 7.16 through 7.18 show the

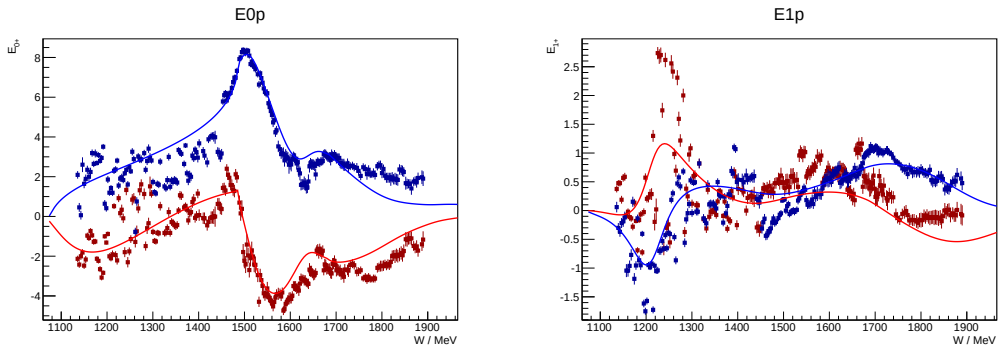

(a) (b)

Figure 7.16: Multipole fit results for E_{0+} (a) and E_{1+} (b). The blue and red colors represent the real and the imaginary parts of the multipoles, respectively.

multipole fit results after a "penalty term" was included. In this case, the M_{1+} multipole fits well to the data in the whole energy range while other multipoles show reasonable fits only above the Δ-resonance region. The fit to the data depends on the choice of the model for starting parameters and the "penalty term". A change of the model, (e.g., to MAID or SAID) or the "penalty term", (e.g., use helicity amplitudes) will affect the fit parameters and also the smoothness of the fit. This explains the importance of more experimental data (of which the helicity asymmetry E will be part) to unambiguously extract the multipole information. It is expected that when more polarization observable data is available, it will be possible to extract the multipoles information without much model dependence.

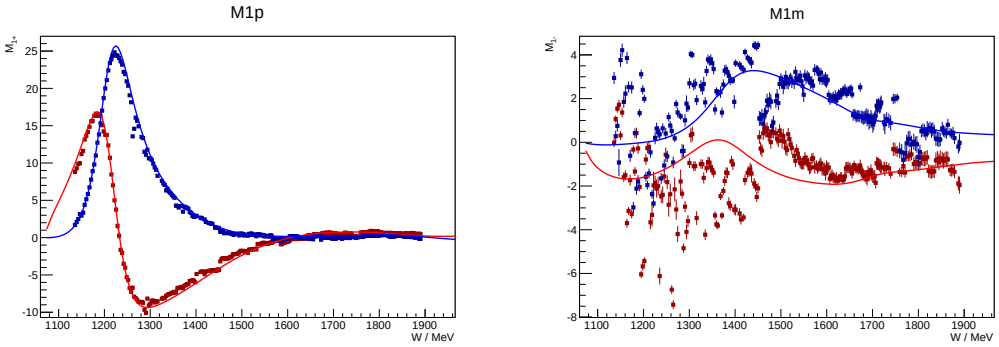

(a) (b)

Figure 7.17: Multipole fit results for M_{1+} (a) and M_{1-} (b). The blue and red colors represent the real and the imaginary parts of the multipoles, respectively.

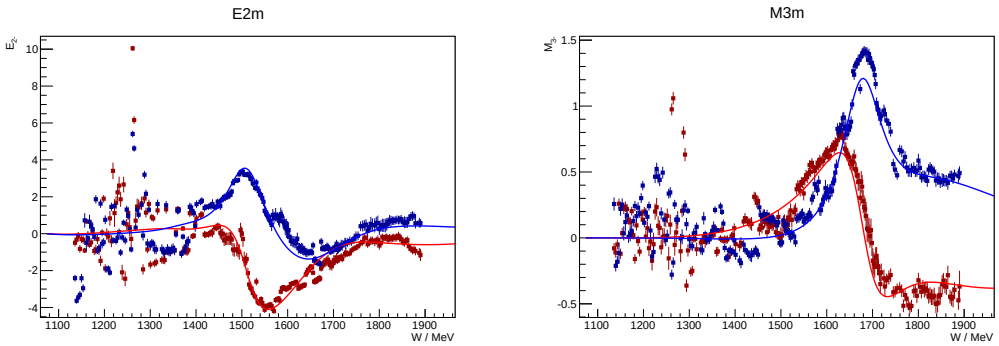

(a) (b)

Figure 7.18: Multipole fit results for E_{2-} (a) and M_{3-} (b). The blue and red colors represent the real and the imaginary parts of the multipoles, respectively.

Chapter 8

Summary and Conclusions

The main aim of this thesis was to study the helicity dependence of π^0 photoproduction on protons with the Crystal Ball at MAMI. This was motivated by the quest of gaining better understanding of the baryon resonances decaying to $\pi^0 p$. The resonances are broad and overlapping, making their interpretation a challenge since most of the existing data are from cross sections only. Therefore, measurement of the polarization observables for different final states of mesons provides a way of constraining the scattering amplitudes. In this work the helicity asymmetry E was extracted from experimental data taken in three beam-times.

The experiment was run with an electron beam of 1557 MeV with $77.55 \pm 2\%$ degree of polarization. The beam impinges on a radiator to produce photons via bremsstrahlung. The energy of the photons was determined by the difference between the energy of the incoming electron beam and scattered electron detected in the tagger focal plane detector. A circularly polarized photon beam and a longitudinally polarized butanol target was used in combination with a set of detectors (Crystal Ball and TAPS). The internal polarizing superconducting magnet for the Mainz frozen spin target has been developed and tested at liquid helium temperatures. The measured field at the center of the coil was 2.32 T at a current of 45 A which is close to the projected value of 2.4 T. The homogeneity of the coil is 1.22×10^{-3} which is higher than the calculated value of 5.9×10^{-5} mainly due to production

imperfections. Since the magnet was a first prototype, there is hope that it can be improved to attain the required magnetic field and homogeneity. This can be achieved by using a superconducting wire with higher critical current to avoid early quenching and by using a winding machine, mounted with cameras to monitor the winding of the coil, to avoid imperfections which affect the homogeneity.

In the extraction of double polarization observable E, the effective dilution factor was calculated independently for each $\cos\theta_{\pi^0}$ bin for a given photon energy bin. The results were compared to CBELSA/TAPS data and partial wave analysis models of MAID, BnGa and SAID. The present results show a general agreement with the CBELSA/TAPS data. However, at angles between $\cos\theta_{\pi^0} = \pm 0.5$ the present asymmetry is smaller than the CBELSA/TAPS results. The models describe well the data in the Δ-resonance region (only one resonance ($\Delta(1232)3/2^+$) contributes) but discrepancies in both the data and the models are observed in the second and third-resonance regions.

The helicity asymmetry was multiplied by the unpolarized cross section and expanded in terms of Legendre polynomials up to a maximum orbital angular momentum $L_{max} = 3$. The extracted polynomial coefficients were plotted as a function of photon energy and compared to model predictions. The fits from all model predictions reproduce fairly well the coefficient A_0 but other coefficients ($A_1 - A_6$) show large discrepancies especially in the Δ-resonance region. However, the expansion of the polarized cross section in terms of Legendre polynomials shows the sensitivity of the data to partial wave amplitudes up to F-waves ($L_{max} = 3$) even though this was only a first step towards a full single energy partial wave analysis. The present helicity asymmetry data was simultaneously fitted with the cross section and other polarization observables (from A2Mainz data) in a combined fit to extract multipole information. A fit was done only up to F-waves ($L_{max} = 3$) using the BnGa model for the starting parameters and the CGLN amplitudes to calculate the penalty term. No meaningful extraction of multipoles is possible when data is fitted directly without penalty term. However, after introduction of a penalty term the results show good fit of the data to multi-

poles at higher energies but show large deviations at the Δ-resonance region except for M_{1+}. It is expected that when more polarization observable data is available, it will be possible to extract the multipoles information without much model dependence.

In conclusion, the helicity asymmetry E has been measured in the energy range $E_\gamma = 210 - 1410$ MeV. The results in the energy range $E_\gamma = 210 - 600$ MeV has been measured for the first time. Expansion of the polarized cross section in terms of Legendre polynomials shows the sensitivity of the data to partial wave amplitudes. In addition, the extraction of electromagnetic multipoles indicates that the data will provide a significant contribution in the extraction of the nucleon resonances.

Appendix A

Appendix

A.1 Polarization Observables Expanded in Terms of Other Amplitudes

In addition to the CGLN amplitudes discussed in section 2.1, helicity amplitudes H_i and transversity amplitudes b can be used to describe further the photoproduction reaction beyond unpolarized cross section. In a meson photoproduction reaction given by equation (2.1), the helicity of the incident photon is $\lambda = \pm 1$ while that of the target nucleon in initial and final states is $\nu_i = \pm 1/2$ and $\nu_f = \pm 1/2$ respectively. Therefore a linear combination of these helicities yields eight matrix combinations given by

$$H_{\nu_f}, \mu = \langle \nu_f | T | \lambda_\gamma v_i \rangle \tag{A.1}$$

with μ as the final state helicity [28]. However, due to parity conservation they reduces to four independent helicity amplitudes given as

$$\begin{aligned} H_1 &= H_{+1/2,+3/2} = H_{-1/2,-3/2} \\ H_2 &= H_{+1/2,+1/2} = H_{-1/2,-1/2} \\ H_3 &= H_{-1/2,+3/2} = H_{+1/2,-3/2} \\ H_1 &= H_{+1/2,-1/2} = H_{-1/2,+1/2} \end{aligned} \tag{A.2}$$

The helicity amplitudes can be expressed in term of the CGLN as in equation (A.3). [154];

$$\begin{aligned} H_1(\theta,\phi) &= \frac{-1}{\sqrt{2}} e^{i\phi} \sin\theta \cos\left(\frac{\theta}{2}\right)(F_3+F_4) \\ H_2(\theta,\phi) &= \sqrt{2}\cos\left(\frac{\theta}{2}\right)\left[(F_2-F_1)+\frac{1}{2}(1-\cos\theta)(F_3-F_4)\right] \\ H_3(\theta,\phi) &= \frac{1}{\sqrt{2}} e^{2i\phi} \sin\theta \sin\left(\frac{\theta}{2}\right)(F_3-F_4) \\ H_4(\theta,\phi) &= \sqrt{2} e^{i\phi} \sin\left(\frac{\theta}{2}\right)\left[(F_1+F_2)+\frac{1}{2}(1+\cos\theta)(F_3+F_4)\right] \end{aligned} \tag{A.3}$$

Additionally, helicity amplitudes can be expressed in terms of electromagnetic multipoles as in equation (A.4) [28];

$$\begin{aligned} H_1 &= \frac{1}{\sqrt{2}}\cos\frac{\theta}{2}\sin\theta\sum_{l=1}^{\infty}\left[E_{l+}-M_{l+}-E_{(l+1)-}-M_{(l+1)-}(P''_l-P''_{l+1})\right], \\ H_2 &= \frac{1}{\sqrt{2}}\cos\frac{\theta}{2}\sum_{l=1}^{\infty}\left[(l+2)E_{l+}+lM_{l+}+E_{(l+1)-}-(l+2)M_{(l+1)-}(P'_l-P'_{l+1})\right], \\ H_3 &= \frac{1}{\sqrt{2}}\sin\frac{\theta}{2}\sin\theta\sum_{l=1}^{\infty}\left[E_{l+}-M_{l+}+E_{(l+1)+}-M_{(l+1)-}(P''_l+P''_{l+1})\right], \\ H_4 &= \frac{1}{\sqrt{2}}\sin\frac{\theta}{2}\sum_{l=1}^{\infty}\left[(l+2)E_{l+}+lM_{l+}-E_{(l+1)-}+(l+2)M_{(l+1)-}(P'_l-P'_{l+1})\right]. \end{aligned} \tag{A.4}$$

From equation (A.4) transversity amplitudes described in [25] can be constructed as;

$$\begin{aligned} b_1 &= \frac{1}{2}[(H_1+H_4)+i(H_2-H_3)], \\ b_2 &= \frac{1}{2}[(H_1+H_4)-i(H_2-H_3)], \\ b_3 &= \frac{1}{2}[(H_1-H_4)-i(H_2+H_3)], \\ b_4 &= \frac{1}{2}[(H_1-H_4)+i(H_2-H_3)]. \end{aligned} \tag{A.5}$$

A bilinear product of helicity or transversity amplitudes results to sixteen polarization observables listed in table A.1.

Observable	Helicity representation	Transversity representation	Group
σ_o	$\frac{1}{2}(\lvert H_1\rvert^2+\lvert H_2\rvert^2+\lvert H_3\rvert^2+\lvert H_4\rvert^2)$	$\frac{1}{2}(\lvert b_1\rvert^2+\lvert b_2\rvert^2+\lvert b_3\rvert^2+\lvert b_4\rvert^2)$	
$\Sigma\sigma_o$	$Re(H_1H_4^*-H_2H_3^*)$	$\frac{1}{2}(-\lvert b_1\rvert^2-\lvert b_2\rvert^2+\lvert b_3\rvert^2+\lvert b_4\rvert^2)$	$\mathcal{S}$
$T\sigma_o$	$Im(H_1H_2^*+H_3H_4^*)$	$\frac{1}{2}(\lvert b_1\rvert^2-\lvert b_2\rvert^2-\lvert b_3\rvert^2+\lvert b_4\rvert^2)$	
$P\sigma_o$	$-Im(H_1H_3^*+H_2H_4^*)$	$\frac{1}{2}(-\lvert b_1\rvert^2+\lvert b_2\rvert^2-\lvert b_3\rvert^2+\lvert b_4\rvert^2)$	
$G\sigma_o$	$-Im(H_1H_4^*+H_2H_3^*)$	$2Im(-b_1b_3^*-b_2b_4^*)$	
$H\sigma_o$	$-Im(H_1H_3^*-H_2H_4^*)$	$-2Re(b_1b_3^*-b_2b_4^*)$	$\mathcal{BT}$
$E\sigma_o$	$\frac{1}{2}(-\lvert H_1\rvert^2+\lvert H_2\rvert^2-\lvert H_3\rvert^2+\lvert H_4\rvert^2)$	$-2Re(b_1b_3^*+b_2b_4^*)$	
$F\sigma_o$	$Re(H_1H_2^*+H_3H_4^*)$	$2Im(b_1b_3^*-b_2b_4^*)$	
$O_{x'}\sigma_o$	$-Im(H_1H_2^*-H_3H_4^*)$	$-2Re(-b_1b_4^*+b_2b_3^*)$	
$O_{z'}\sigma_o$	$Im(H_1H_4^*-H_2H_3^*)$	$-2Im(-b_1b_4^*-b_2b_3^*)$	$\mathcal{BR}$
$C_{x'}\sigma_o$	$-Re(H_1H_3^*+H_2H_4^*)$	$2Im(b_1b_4^*-b_2b_3^*)$	
$C_{z'}\sigma_o$	$\frac{1}{2}(-\lvert H_1\rvert^2-\lvert H_2\rvert^2+\lvert H_3\rvert^2+\lvert H_4\rvert^2)$	$2Re(b_1b_4^*+b_2b_3^*)$	
$T_{x'}\sigma_o$	$Re(H_1H_4^*+H_2H_3^*)$	$-2Re(-b_1b_2^*+b_3b_4^*)$	
$T_{z'}\sigma_o$	$Re(H_1H_2^*-H_3H_4^*)$	$-2Im(b_1b_2^*-b_3b_4^*)$	$\mathcal{TR}$
$L_{x'}\sigma_o$	$-Re(H_1H_3^*-H_2H_4^*)$	$-2Im(-b_1b_2^*-b_3b_4^*)$	
$L_{z'}\sigma_o$	$\frac{1}{2}(\lvert H_1\rvert^2-\lvert H_2\rvert^2-\lvert H_3\rvert^2+\lvert H_4\rvert^2)$	$Re(-b_1b_2^*-b_3b_4^*)$	

Table A.1: Polarization observables for pseudoscalar mesons expressed in terms of helicity and transversity amplitudes [25, 26, 27].

A.2 Experimental Trigger

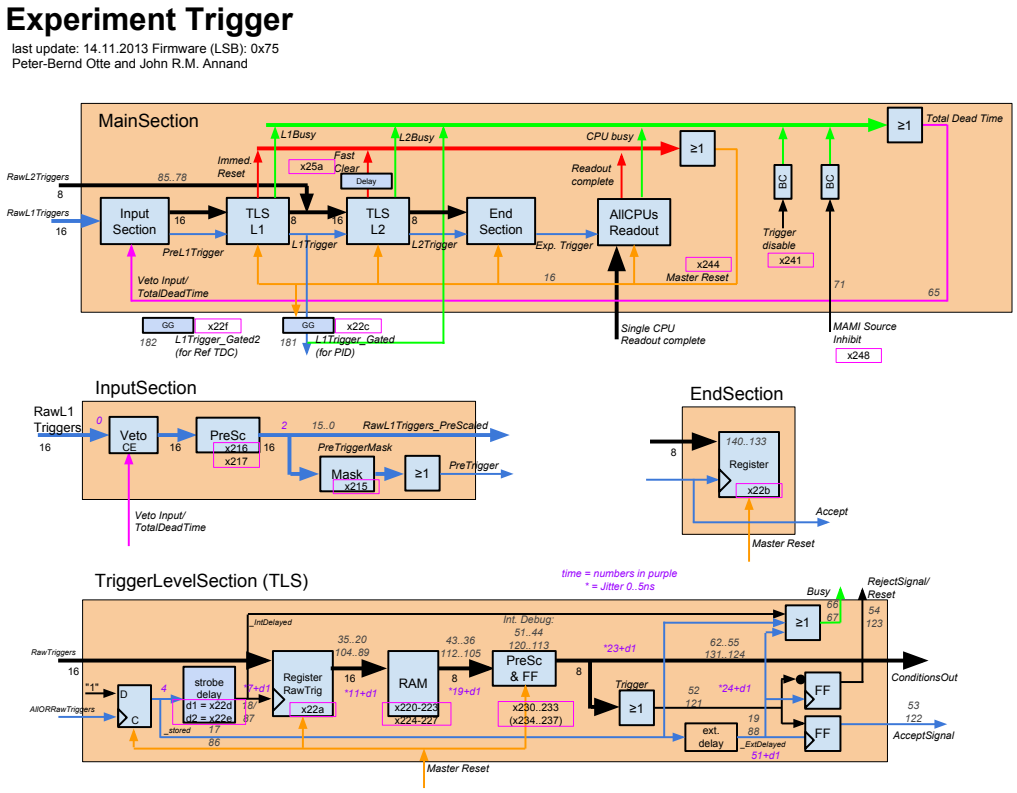

Figure A.1: A schematic diagram of the experimental trigger [155].

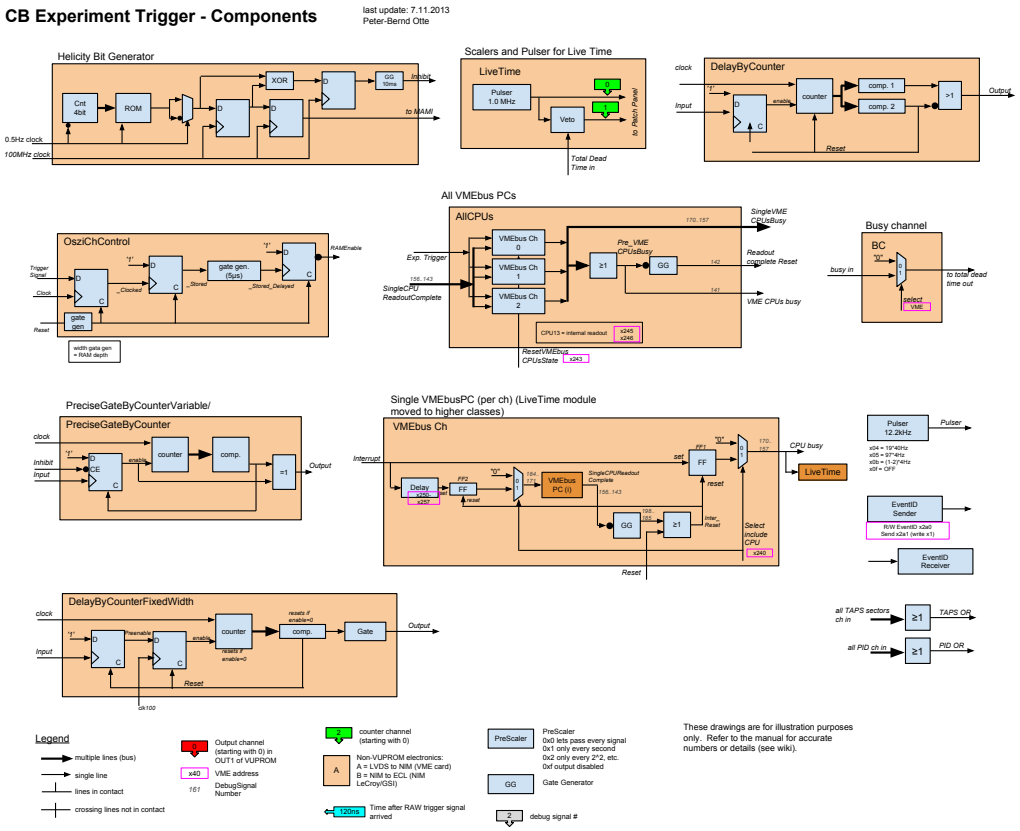

Figure A.2: A schematic diagram of the experimental trigger components [155].

A.3 Multipoles Analysis Fits

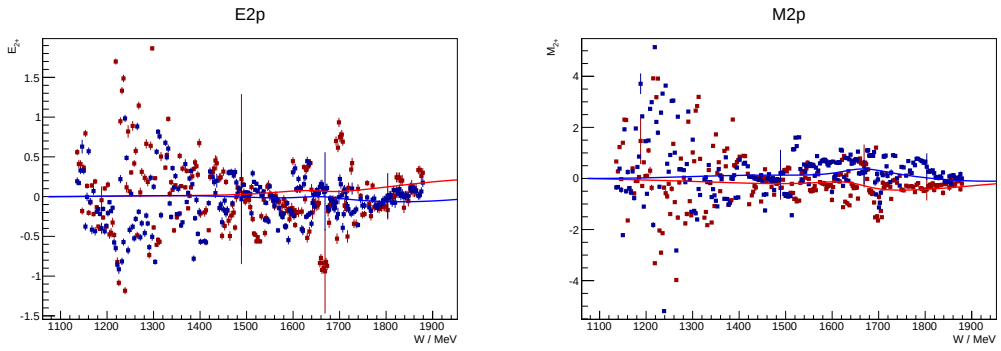

(a) (b)

Figure A.3: Multipole fit results for E_{2+} (a) and M_{2+} (b) without penalty term. The blue and red colors represent the real and the imaginary parts of the multipoles, respectively.

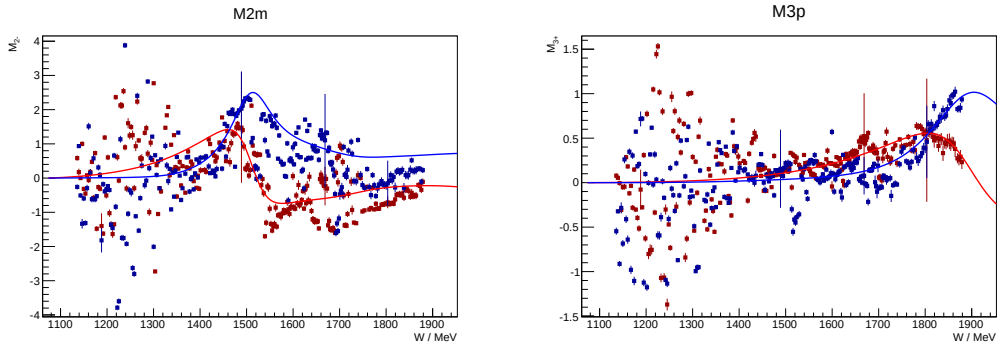

(a) (b)

Figure A.4: Multipole fit results for M_{2-} (a) and M_{3+} (b) without penalty term. The blue and red colors represent the real and the imaginary parts of the multipoles, respectively.

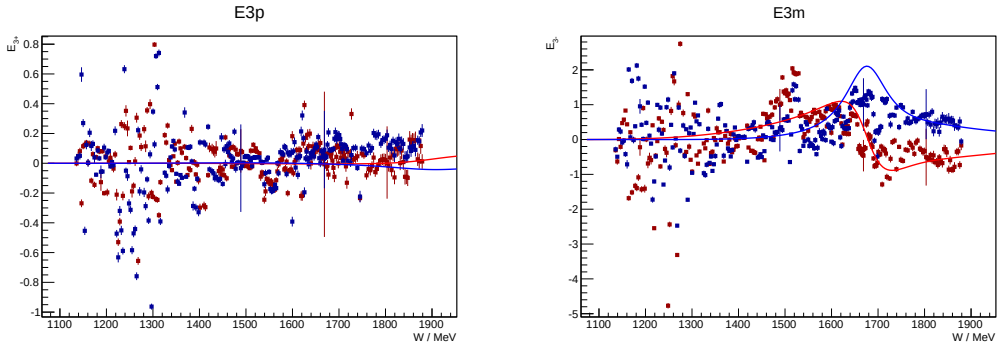

(a) (b)

Figure A.5: Multipole fit results for E_{3+} (a) and E_{3-} (b) without penalty term. The blue and red colors represent the real and the imaginary parts of the multipoles, respectively.

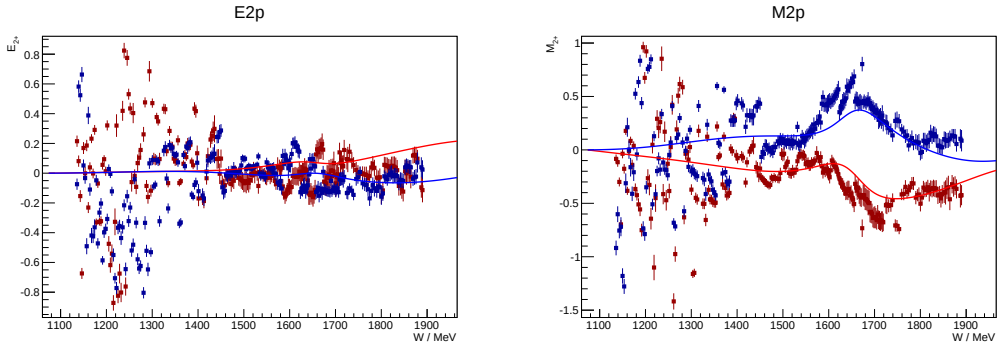

(a) (b)

Figure A.6: Multipole fit results for E_{2+} (a) and M_{2+} (b) with penalty term. The blue and red colors represent the real and the imaginary parts of the multipoles, respectively.

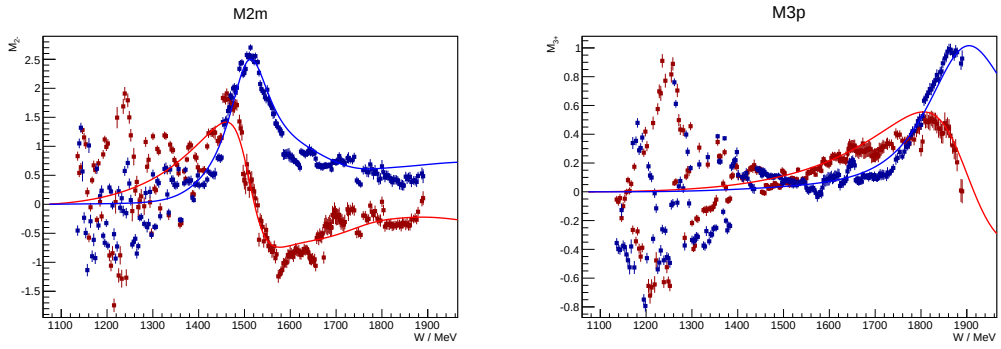

(a) (b)

Figure A.7: Multipole fit results for M_{2+} (a) and M_{3+} (b) with penalty term. The blue and red colors represent the real and the imaginary parts of the multipoles, respectively.

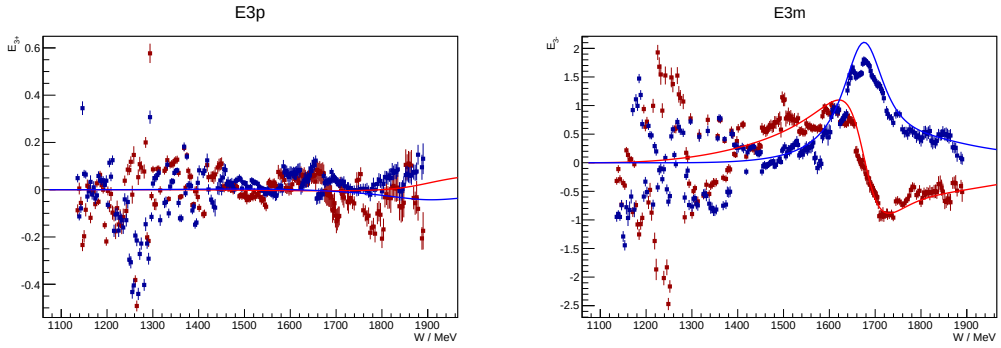

(a) (b)

Figure A.8: Multipole fit results for E_{3+} (a) and E_{3-} (b) with penalty term. The blue and red colors represent the real and the imaginary parts of the multipoles, respectively.

Bibliography

[1] I. G. Aznauryan et al., *Studies of Nucleon Resonance Structure in Exclusive Meson Electroproduction*, arXiv:1212.4891v2 [nucl-th] 3 Apr 2013.

[2] W. M. Yao et al., *The Review of Particle Physics*, J. Phys. G **33**, (2006).

[3] Kenneth G. Wilson, *Confinement of Quarks*, Phys. Rev. D **10** 8, (1974).

[4] K. A. Olive et al., *Review of Particle Physics*, Chin. Phys.C **86** 090001, (2014).

[5] R. G Edwards et al., *Excited State Baryon Spectroscopy from Lattice QCD*, Physical Review D **84** 074508, (2011).

[6] Volker D. Burkert, *Evidence of New Nucleon Resonances from Electromagnetic Meson Production*, arXiv:1209.2402 [nucl-ex], (2012).

[7] A.V. Anisovich et al., *Properties of Baryon Resonances from a Multichannel Partial Wave Analysis*, Eur. Phys.J. A **48** 15, (2012).

[8] V. Crede and W. Roberts, *Progress Towards Understanding Baryon Resonances*, Rep. Prog. Phy. **76**, (2013).

[9] B. Krusche and S. Schadmand, *Study of Non-strange Baryon Resonances with Meson Photoproduction*, Prog. Part. Nucl. Phys. **51**, (2003).

[10] M. Gell-Mann, *A Schematic of Model of Baryons and Mesons*, Phys. Let. Vol. **8** No. 3, (1964).

[11] G. Zweig, *An SU_3 Model Strong Interaction Symmetry and its Breaking*, CERN libraries, Geneva, (1964).

[12] O. W. Greenberg, *Spin and Unitary-Spin Independence in a Paraquark Model of Baryons and mesons*, Phys. Rev. Lett. Vol. **13** No. 20, (1964).

[13] S. Capstick and W. Roberts. *Quark Models of Baryon Masses and Decays. Progress in Particle and Nuclear Physics*, **45** 241–331, (2000).

[14] U Löring et al., *The Light-Baryon Spectrum in a Relativistic Quark Model with Instanton-Induced Quark Forces*, Eur. Phys. J. A **10**, 395–446, (2001).

[15] http://portal.kph.uni-mainz.de/MAID/

[16] http://gwdac.phys.gwu.edu/

[17] http://pwa.hiskp.uni-bonn.de/

[18] A.V. Anisovich et al., *Pion- and Photo-Induced Transition Amplitudes to ΛK Σk and $N\eta$*, Eur. Phys. J. A **48** 88, (2012).

[19] P. Adlarson et al., *Measurement of π^0 Photoproduction on Proton at MAMI C*, arXiv:1506.08849v1[hep-ex] 29 Jun 2015.

[20] Benmerouche et al., *Effective Lagrangian Approach to the Theory of η Photoproduction in the N*(1535) region*, Phys. Rev. D **57** 3237-3265, (1995).

[21] G. F. Chew et al., *Relativistic Dispersion Relation Approach to Photomeson Production.* Phys. Rev. **106** 1345-1355, (1957).

[22] R. M. Davidson, *Photo- and Electro-Production of Mesons*, Czech. J. Phys. **44** 365–403, (1995).

[23] Lothar Tiator. *Complete Experiment for Pion Photoproduction*, arXiv:1211.3927v1[nucl-th] 16 Nov 2012.

[24] A. M. Sandorfi et al., *Determining Pseudoscalar Meson Photoproduction Amplitudes from Complete Experiments*, J. Phys. G: Nucl. Part. Phys. **38** 053001, (2011).

[25] I. S. Barker, A. Donnachie and J. K. Storrow, *Complete Experiments in Pseudoscalar Photoproduction*, Nucl. Phys. B **95** 347-356, (1975).

[26] Y. Wunderlich, R. Beck, and L. Tiator, *The Complete-Experiment Problem of Photoproduction of Pseudoscalar Mesons in a Truncated Partial-Wave Analysis*, Phys. Rev. C **89**, (2014).

[27] W. Chiang and F.Tabakin, *Completeness Rules for Spin Observables in Pseudoscalar Meson Photoproduction*, Phys. Rev. C **55** 2054. (1997).

[28] R. L. Workman, *Single-Energy Amplitudes for Pion Photoproduction in the First Resonance region*, Phys. Rev. C **83**, (2011).

[29] G. Keaton and R. Workman, *Ambiguities in the Partial-Wave Analysis of Pseudoscalar-Meson Photoproduction*, Phys. Rev. C **54** 1437, (1996).

[30] G. Keaton and R. Workman, *Amplitude Ambiguities in Pseudoscalar Meson Photoproduction*, Phys. Rev. C **54** 1434, (1996).

[31] D. Drechsel et al., *A unitary isobar model for pion photo- and electroproduction on the proton up to 1 GeV*, Nucl. Phys. A **645** 145-174. (1999).

[32] L. Tiator and S. Kamalov, *MAID Analysis Techniques.* arXiv:nucl-th/0603012v1 6 Mar 2006.

[33] D. Drechsel, S.S Kamalov and L. Tiator, *Unitary Isobar Model - MAID2007*, Eur. Phys. J. A **34** 69–97, (2007).

[34] L. Tiator et al., *Baryon Resonance Analysis from MAID*, Chin. Phys. C **33** (12) 1069—1076, (2009).

[35] R. A. Arndt et al., *Partial-Wave Analysis of Pion Photoproduction*, Phys. Rev. C. **42** 5, (1990).

[36] R. A. Arndt et al., *Updated Analysis of πN Elastic Scattering Data to 2.1 GeV: The Baryon Spectrum*, Phys. Rev. C. **52** 4, (1995).

[37] M. W. Paris and R. L. Workman, *Toward a Unified Description of Hadro- and Photoproduction: S-wave π- and η-Photoproduction Amplitudes*, Phys. Rev. C. **82** 035202, (2010).

[38] R. L. Workman et al., *Updated SAID Analysis of Pion Photoproduction Data*, Phys. Rev. C. **85** 025201, (2012).

[39] A. V. Anisovich et al., *Partial-Wave Decomposition of Pion and Photoproduction amplitudes*, Eur. Phys. J. A **24** 111–128, (2005).

[40] A. V. Anisovich and A. V. Sarantsev, *Partial Decay Widths of Baryons in the Spin-Momentum Operator Expansion Method*, Eur. Phys. J. A **30** 427–441 (2006).

[41] G. Penner and U. Mosel, *Vector Meson Production and Nucleon Resonance Analysis in a Coupled-Channel Approach for Energies $M_N < \sqrt{s} <$ 2 GeV. I. Pion-induced Results and Hadronic Parameters*, Phys. Rev. C. **66** 055211 (2002).

[42] G. Penner and U. Mosel, *Vector Meson Production and Nucleon Resonance Analysis in a Coupled-Channel Approach for Energies $M_N < \sqrt{s} <$ 2 GeV. II. Photon-induced Results*, Phys. Rev. C. **66** 055212, (2002).

[43] A. Matsuyama et al., *Dynamical coupled-channel model of meson production reactions in the nucleon resonance region*, Phys. Rep. **439** 193–253, (2007).

[44] B. J. Diaz et al., *Dynamical Coupled-Channels Effects on Pion Photoproduction*, Phys. Rev. C. **77** 045205, (2008).

[45] R Beck et al., *Measurement of the $p(\gamma, \pi^0)$ Cross Section at Threshold*, Phys. Rev. Lett.**65** 15, (1990).

[46] R Beck et al., *Measurment of the $E2/M1$ Ratio in $N \rightarrow \Delta$ Transition using the reaction $p(\gamma, p)\pi^0$*, Phys. Rev. Lett. **78** 4, (1997).

[47] M. Fuchs et al., *Neutral Pion Photoproduction from the Proton near Threshold*, Phys. Let. B **368** 20-25, (1996).

[48] J Ahrens et al., *Helicity Amplitude $A_{1/2}$ and $A_{3/2}$ for the $D_{13}(1520)$ Resonance Obtained from the $\gamma p \rightarrow p\pi^0$ Reaction*, Phys. Rev. Lett. **88** 23, (2002).

[49] O Bartholomy et al., *Neutral-Pion Photoproduction off Protons in the Energy Range $0.3GeV < E_\gamma < 3GeV$*, Phys. Rev. Lett. **94** 012003, (2005).

[50] H. van Pee et al., *Photoproduction of π^0-Mesons off Protons from the $\Delta(1232)$ Region to $E_\gamma = 3$ GeV*, Eur. Phys. J. A **31** 61-77, (2007).

[51] M Dugger et al., *π^0 Photoproduction on the Proton for Photon Energies from 0.675 to 2.875 GeV*, Phys. Rev.C **76** 025211, (2007).

[52] V. Crede et al., *Photoproduction of Neutral Pions off Protons*, Phys. Rev. C **84** 055203, (2011).

[53] N. Sparks et al., *Measurement of the Beam Asymmetry Σ in the Forward Direction for $\gamma p \rightarrow p\pi^0$*, Phys. Rev. C **81** 065210, (2010).

[54] M Dugger et al., *Beam Asymmetry Σ for π^+ and π^0 Photoproduction on the Proton for Photon Energies from 1.102 to 1.862 GeV*, Phys. Rev.C **88** 065203, (2011).

[55] O. Bartalini et al., *Measurement of π^0 Photoproduction on the Proton from 550 to 1500 MeV at GRAAL*, Eur. Phys. J. A **26** 399–419, (2005).

[56] S. Schumann et al., *Threshold π^0 Photoproduction on Transverse Polarized Protons at MAMI*, Paper submitted to Phys.Lett. B, (2015).

[57] J. Hartmann et al., *$N(1232)3/2^+$ Helicity Amplitudes from an Energy-Independent Multipole Analysis Based on New Polarization Data on Photoproduction of Neutral Pions*, Phys. Rev. Lett. **113**, 062001, (2014).

[58] A. Thiel et al., *Well-Established Nucleon Resonances Revisited by Double-Polarization Measurements*, Phys. Rev. Lett. **109** 102001, (2012).

[59] J Ahrens et al., *Helicity dependence of the $\gamma p \to N\pi^0$ channels and multipole analysis in the Δ region*, *Eur. Phys. J. A* **21**, *323–333*, (2004).

[60] M. Gottschall et al., *First Measurement of the Helicity Asymmetry for $\gamma p \to p\pi^0$ in the Resonance Region*, Phys. Rev. Lett. **112** 012003, (2014).

[61] H. Iwamoto, *Helicity Asymmetry Measurement for π^0 Photoproduction with FROST*, Ph.D Thesis, The George Washington University, (2011).

[62] H. Herminghaus et al., *The design of a Cascaded 800 MeV Normal Conducting C.W. Race Track Microtron*, Nucl. Instr. Meth. **138** 1, (1976).

[63] H. Herminghaus, K. H. Kaiser and U. Ludwig-Mertin, *The Design of Double Sided Microtons*, Proceedings of the 1981 Linear Accelerator Conference, Santa Fe, New Mexico, USA.

[64] M. Dehn et al., *The MAMI C: The Beauty of Normal Conducting Multiturn Recirculators*, Eur. Phys. J. Special Topics **198** 19-47, (2011).

[65] A. Jankowiak, *The Mainz Microtron MAMI-Past and Future*, Eur. Phys. J A **28** 149-160, (2006).

[66] K. H. Kaiser et al., *The 1.5 GeV Harmonic Double-sided Microtron at Mainz University*, Nucl. Instr. Meth. A **593** 159, (2008).

[67] K. Aulenbacher et al., *The MAMI Source of Polarized Electrons*, Nucl. Instr. and Meth. in Phys. Res. A **391** 498-506, (1997).

[68] M. Hauger et al., *A High Precision Polarimeter*, Nucl. Instr. and Meth. in Phys. Res. A **462** 382-392. (2001).

[69] P. B. Otte, *Aufbau und Test eines Moellerpolarimeters fuer das Crystal-Ball-Experiment an MAMI-C*, Diploma Thesis, Universität Mainz, (2008).

[70] https://wwwa2.kph.uni-mainz.de/intern/daqwiki/experiment/detectors/moeller

[71] D. Werthmueller, *Experimental Study of Nucleon Resonance Contributions to η-Photoproduction on the Neutron*, Ph.D Thesis, Universität Basel, (2014).

[72] H. Olsen and L. C. Maximon. *Photon and Electron Polarization in High-Energy Bremsstrahlung and Pair Production with Screening*, Phys. Rev. **114** 3, (1959).

[73] H. W. Koch and J. W. Motz, *Bremsstrahlung Cross-Section Formulas and Related Data*, Rev. Mod. Phys. **31** 920, (1959).

[74] I. Anthony et al., *Design of a Tagged Photon Spectrometer for use with the Mainz 840 MeV Microtron*, Nucl. Inst. and Meth. Res. A **301** 230-240, (1991).

[75] S. J. Hall et al., *A Focal Plane System for the 855 MeV Tagged Photon Spectrometer at MAMI-B*, Nucl. Instr. and Meth. Phys. Res. A **368** 698-708, (1995).

[76] J. C. McGeorge et al., *Upgrade of the Glasgow Photon Tagging Spectrometer for Mainz MAMI-C*, Eur. Phys. J. A **37** 129–137, (2008).

[77] V. L. Kashevarov, *Baryon Spectroscopy at MAMI*, A Presentation on the 7^{th} International Conference on Quarks and Nuclear Physics. 2-6 March 2015, Valparaíso, Chile.

[78] D. Middleton, ugcalv2ua. 2013.

[79] G. Braun et al., *TDC Chip and Readout Driver Developments for COMPASS and LHC-Experiments*, Fourth Workshop on Electronics for LHC-Experiments ArXiv:hep-ex/9810048, (1998).

[80] E. D. Bloom and C. W. Peck, *Physics with Crystal Ball Detector*, Ann. Rev. Nucl. Part. Sci. **33** 143-97, (1983).

[81] R. Partridge et al., *Decay of $J/\psi \to 3\gamma$ and a Search for a η_c*, Phys. Rev. Let. **44** 11, (1980).

[82] R. Partridge et al., *Observation of an η_c, Candidate State with Mass 2978 ± 9 MeV*, Phys. Rev. Let. **45** 14, (1980).

[83] M. Qreglia et al., *Study of the Reaction $\psi' \to \gamma\gamma J/\psi$*, Phys. Rev. D **25** 2260-2277, (1982).

[84] S. Prakhov et al., *Measurement of the Slope Parameter α for the $\eta \to 3\pi^0$ Decay with the Crystal Ball Detector at the Mainz Microtron (MAMI-C)*, Phys. Rev. C **79** 035204, (2009).

[85] T. Jude, *Strangeness Photoproduction off the Proton at Threshold Energies* Ph.D Thesis, University of Glasgow, (2010).

[86] R. Jamie, *Two Proton Knockout from Carbon using Linearly Polarized Photons*, PhD Thesis, University of Glasgow, (2010).

[87] P. A. Bartolome, *First Doubly Polarized Photoproduction on ^{3}He at the Photon Beam of MAMI*, Ph.D Thesis, Universität Mainz, (2010).

[88] F Sauli, *Principles and Operation of Multi Wire Proportional and Drift Chambers*, Geneva, (1977).

[89] D. Vernekohl, *Measurements with a Multi-Wire Proportional Chamber for Small Animal Positron Emission Tomography*, Diploma Thesis, Universität Munster, (2010).

[90] F. Cividini. Private communication.

[91] A.R. Gabler et al., *Response of TAPS to Monochromatic Photons with Energies Between 45 and 790 MeV*, Nucl. Instr. and Meth. Phys. Res. A **346** 168-176, (1994).

[92] R. Novotny, *Performance of the BaF2-Calorimeter TAPS*, Nucl. Phys. B. Proc. Suppl. **6IB** 137-142, (1998).

[93] S. Bender, *Aufbau und Test eines Bleiwolframat-Kalorimeters für das Crystal Ball/TAPS-Experiment an MAMI*, Diploma thesis, Universität Mainz, (2009).

[94] M. Thiel, *In-medium Properties of the ω-Meson Studied in Photonuclear Reactions near the Production Threshold*, Ph.D. Thesis, Universität Giessen. 2010.

[95] P. B. Otte, *Erste Messung der π^0-Photoproduktion an Transversalpolarisierten Protonen nahe der Schwelle*, Ph.D Thesis, Universität Mainz, (2015).

[96] T. A. Rostomyan, *Experimental Verification of the GDH Sum Rule on the Neutron*, Ph.D Thesis, University of Ghent, (2005).

[97] D. G. Crabb and W. Mayer, *Solid Polarized Target for Nuclear and Particle Physics*, Annu. Rev. Nucl. Part. Sci. 47 67–109, (1997).

[98] K. Koptzki, *Einfuehrung in die Festkoerperphysik*, Teubner, (1986).

[99] M. M. Fabregate, *Study of the Helicity Dependence of Single Pion Photoproduction on the Deuteron*, Ph.D Thesis, University of Mainz, (2007).

[100] H. S Ortega, *Design of Superconducting Holding Magnets for a Polarized Solid Target*, Diploma Thesis, University of Mainz, (2009).

[101] A. W. Overhauser, *Polarization of Nuclei in metals*, Phys. Rev. **92** 411, (1953).

[102] T. R. Carver and C. P. Slichter, *Polarization of Nuclear Spins in Metals*, Phys. Rev. **92** 212, (1953).

[103] T.O. Niinikoskii and F. Udo, "Frozen Spin" Polarized Target, Nucl. Inst. Met. **134** 219-233, (1976).

[104] B. S. Neganov, N. S. Borisov and M. Yu. Liburg, *Frozen Spin Polarized Target*, JETP **50** 1445, (1966).

[105] B. S. Neganov, Vestn. Akad. Nauk. SSSR 12 49. 1968.

[106] F. Lehar et al., *The Movable Polarized Target as Basic Equipment for High Energy Spin Physics Experiments at the JINR-Dubna Accelerator Complex*, Nucl. Instr. and Meth. A **356** 58, (1995).

[107] N. A. Bazhanov et al., *Frozen Spin Solid Targets Developed at the Laboratory of Nuclear Problems (JINR, Dubna)*, Nucl. Instr. and Meth. A **402** 484, (1998).

[108] Y. Usov., *Frozen Spin Solid Targets Developed at JINR Dubna*, Nucl. Instr. and Meth. A **526** 153, (2004).

[109] M. Pliickthun et al., *Polarization Measurements of TEMPO-doped Butanol Targets*, Nucl. Instr. and Meth. in Phys. Res. A **400** 133-136, (1997).

[110] St. Goertz, W. Meyer and G. Reicherz, *Polarized H, D and ^{3}He Targets for Particle Physics Experiments*, Nucl. Phys.**49** 403, (2002).

[111] P. Martel, *Measuring Proton Spin Realizabilities with Polarized Compton Scattering*, Ph.D Thesis, University of Massachusetts, (2012).

[112] N. S. Borisov et al., *Frozen-Spin Target for Experiments at MAMI C*. Paper in preparation.

[113] J. R. Hull, *High Temperature Superconducting Current-Leads*, IEEE Trans. on Appl. Sup. **3** 869, (1992).

[114] H. M. Chang and S. W. Van Sciver, *Thermodynamic Optimization of Conduction Cooled HTS Current-Leads*, Cryogenics **38** 729, (1998).

[115] Y. Iwasa and H. Lee, *High Temperature Superconducting Current-Lead Incorporating Operation in the Current-sharing Mode*, Cryogenics **40** 209, (2000).

[116] M. M. Fabregate, *Setup and test of a 70 GHz Microwave Apparatus for a Polarized Target*, Diploma Thesis, University of Mainz, (2003).

[117] G. Reicherz et al., *The Bonn Polarized Target NMR-system*, Nucl. Inst. and Meth. in Phys. Res, A **356** 74-78, (1995).

[118] H. Dutz et al., *An Internal Superconducting "Holding-coil" for Frozen Spin Targets*, Nucl. Inst. and Met. in Phys. Res. A **356** 111-115, (1995).

[119] P.N. Seo et al., *Development of a Superconducting Transverse Holding Magnet for the HIγS Frozen Spin Target*, Nucl. Inst. Met. **618** 43-47, (2010).

[120] A. Thomas, *Polarised Targets for 4 π Detectors at MAMI*, Eur. Phys. J., Special Topics **198** 171-180, (2011).

[121] L. Cesnak and D. Kabat, *A Cylindrical Coil with Graduated Current Density for very Homogeneous Magnetic Fields*, J. Phys. E: Sci. Instrum. **5**, (1972).

[122] L.S.J.M Henkens et al., *Development of Superconductin Split-Coil Magnets Generating High and Homogeneous Fields*, J. Phys. E: Sci. Instrum. **10**, (1977).

[123] D. Kabat et al., *Optimization of Inner-Notch-Corrected Superconducting solenoids and their Comparison with other Coil Configurations*, J. Phys. E: Sci. Instrum. **12** (1979).

[124] Gerd F. Nowack, *A Novel Design Approach to Superconducting Magnet Coil Systems for High-Resolution NMR-Spectroscopy*, Proceedings of the International Conference on Modeling and Simulation. July 2 - 4, 2007, Algiers, Algeria.

[125] D.B. Montgomery, *Solenoid Magnetic Design: The magnetic and Mechanical Aspects of resistive and superconducting systems*, Willy-Interscience, New York, (1969).

[126] M. N. Wilson, *Superconducting Magnets*. Oxford University Press inc., New York, (1983).

[127] Y. Iwasa, *Case Studies in Superconducting Magnets: Design and Operational Issues*. Plenium Press, New York, (1994).

[128] L. Cohen, *Self Inductance of a Solenoid of any Number of Layers*, Bulletin of the Bureau of Standards **4** 3, (1907).

[129] D. Meeker, *Finite Element Method Magnetics User's Manual*, (2010).

[130] http://pdg.lbl.gov/2009/AtomicNuclearProperties/

[131] Lake Shore Cryogenics inc., *Application note Hall generators user manual 2010 edition.*

[132] Lorenzo Zana. Private communication.

[133] F. N. Afzal and K. Spieker. Private communication.

[134] J.R.M. Annand, Data *Analysis within an AcquRoot Framework*, AcquRoot Version 4v3, University of Glasgow, (2008).

[135] R. Brun and F. Rademakers, *ROOT-An Object Oriented Data Analysis Framework*, Nucl. Inst. Meth. A **389** 81, (1997).

[136] C. Collicott, *Probing Proton Structures Through Single Polarization Observables of Compton Scattering and π^0 Photoproduction Within the $\Delta(1232)$ Region*, Ph.D Thesis, Dalhousie University Halifax, Nova Scotia, (2015).

[137] https://github.com/A2-Collaboration-dev/a2GoAT

[138] D. Glazier, *A Geant4 simulation for the Crystal Ball@MAMI setup Internal Report. Technical report*, Univeristy of Edinburgh, (2007).

[139] https://wwwa2.kph.uni-mainz.de/intern/daqwiki/analysis/tutorials/simulation/geant4/

[140] S. Agostinelli, *GEANT4 A simulation toolkit*, Nucl. Instrum. Meth. A **506** 250, (2003).

[141] M. Unverzagt, *Energie-Eichung des Crystal Ball-Detektors am Mainz*, Diploma Thesis, Universität Mainz, (2004).

[142] J. Wetting, *Aufbau und Inbetriebnahme einer neuen HV-Versorgung fuer den Crystal Ball-Detektors am MAMI*, Diploma Thesis, Universität Mainz, (2014).

[143] C. Adloff et al., *Shower Development of Particles with Momenta from 1 to 10 GeV in the CALICE Scintillator-Tungsten HCAL*, JINST **9** P01004, (2014).

[144] R. O. Owens, *Statistical Treatment of Tagged Photon Experiments*, Nucl. Inst. and Meth. in Phys Res A **288** 574-584, (1990).

[145] F. N. Afzal, *Measurement of the Double Polarization Observable E in the Reaction $\gamma p \to \eta' p$*, Master Thesis, University of Bonn, (2012).

[146] P. E. H. Barrientos, *First Measurement of F Double Polarization Observable in Pion Photoproduction*, PhD Thesis, University of Edinburgh, (2012).

[147] P. R. Bevington and D. K. Robinson, *Data Reduction and Error Analysis for Physical Science*, 3rd Edition, McGraw-Hill, (1992).

[148] M. Gottschall, *Bestimmung der Doppelpolarisationsobservablen E fuer die Reaktion $\gamma p \to p\pi^0$ am CBELSA/TAPS-Experiment*, Ph.D Thesis, Universität Bonn. 2012.

[149] Sven Schumann. https://github.com/MainzPWA/PWA. May 2015.

[150] Sven Schumann, *Using the Mainz Multipole Fitter PWA manual*, (2015).

[151] S. Schuman and P. B. Otte. Private comunacation. 2015.

[152] V.L. Kashevarov. Private comunacation. 2015.

[153] D. Hornidge, *Accurate Test of Chiral Dynamics in the $\gamma p \to \pi^0 p$ Reaction*, Phys. Rev. Lett. **111** 062004, (2013).

[154] R. L. Walker, *Phenomenological Analysis of Single Pion Photoproduction*, Phys. Rev. **182** 1729-1748, (1969).

[155] http://wwwa2.kph.uni-mainz.de/intern/daqwiki/trigger/experiment/start. 2015.